Doctoral Dissertation
Doctoral Program in Aerospace Engineering (36.th cycle)

Impact of posture and gravity on the cardiovascular system: a validated multiscale modeling approach for ground-based and spaceflight applications

Matteo Fois

* * * * *

Supervisors
Prof. Stefania Scarsoglio, Supervisor
Prof. Luca Ridolfi, Co-supervisor

Doctoral Examination Committee:
Prof. Jordi Alastruey Arimon, Referee, King's College London
Prof. Gabriele Mascetti, Referee, Agenzia Spaziale Italiana
Prof. Marco Donato de Tullio, Politecnico di Bari
Prof. Raffaella Ricci, Università degli Studi di Torino
Prof. Diego Gallo, Politecnico di Torino

Politecnico di Torino
Month day, 2024

I hereby declare that, the contents and organization of this dissertation constitute my own original work and does not compromise in any way the rights of third parties, including those relating to the security of personal data.

. . . .
Matteo Fois
Turin, month day, 2024

Summary

The present thesis is aimed at exploring the response of the human cardiovascular system to a number of ground-based clinical and spaceflight-related applications, by resorting to a mathematical model calibrated and validated *in vivo*. The numerical framework developed for the purpose of this work encompasses a 1D representation of the arterial circulation linked to a 0D circuital analog of the remaining systemic (peripheral and venous return) and cardiopulmonary circulations. In addition, lumped parameter models of the cerebrovascular and ocular circulations, as well as specific models of short-term homeostatic control, are considered to inquire into the specific response of such compartments to different gravity conditions and postures. The model is then applied to several cases of interest to inquire into hidden or unknown mechanisms shaping the overall hemodynamic response. The computational model was used to characterize the global cardiovascular and hemodynamic response to numerically simulated varying posture under normal Earth gravity (1g), to varying gravity experienced during a numerically simulated parabolic flight trajectory, and to numerically simulated acute exposure to head-down tilt position assumed as ground-based analogue of human spaceflight. Additionally, from a clinical point of view, we employed the model also to explore a clinical problem related to the detrimental implications of atrial fibrillation onto perfusion of the myocardium, showing the validity of the presented numerical tool to conduct medical investigations.

To the purpose of validating our computational framework, the present work includes also two distinct experimental campaigns whose goal was to investigate the human physiological response to different scenarios. A first series of head-up tilt experiments was conducted, aimed at evaluating the impact of orthostatic stress onto the overall cardiovascular response; then, a second experimental study was carried out to the end of exploring the acute (up to one hour) effects of head-down tilt position onto the ocular and cardiovascular parameters.

The main findings presented in the following highlight that gravity - either through posture variation or due to actual modification of the gravity vector magnitude - induces marked responses of the human cardiovascular system that can be related, at first, to blood migration across the different body pools. Secondly, a series of control regulation mechanisms activates such to preserve the system's

homeostasis, by promoting cardiac chronotropic and inotropic control, regulation of vascular tone, and autoregulation of specific dependent vasculature (e.g., cerebrovascular bed). As observed in our studies, the extent of the autonomic response elicited by posture or gravity changes and of the overall cardiovascular response is strictly related to the extent of the corresponding posture/gravity magnitude change, as shown, for instance, in the investigation of the different cardiovascular parameters changes with respect to each simulated tilt angle or to the different phases of a parabolic flight. In addition, the implications of such gravity-driven hemodynamics changes elicited at different levels of the cardiovascular system are responsible for a number of additional observed behaviors, ranging from wave dynamics phenomena, to the insurgence of possible cerebrovascular and ocular consequences. Furthermore, the application of the model to the clinical scenario of atrial fibrillation shows how this conditions affects to gradually worse extents the different layers of the myocardium, at increasingly higher ventricular frequency.

The present work, thus, not only highlights the importance and noticeable usefulness of novel, *in vivo* calibrated and validated computational frameworks in the context of clinical diagnostics and prognostics strategies, but shows also promising insights into a number of so far poorly explored topics strictly related to the fields of bioastronautics and space medicine. In particular, our results help shed light onto the functioning principles of autonomic responses in combination with posture changes on Earth, contributing to the overall understanding of dysautonomias and orthostatic tolerance under normal Earth gravity. Furthermore, altered-gravity environments and ground-based analogues of spaceflight provides information regarding the human cardiovascular, cerebrovascular and ocular systems coping to hyper- and microgravity, leading to a better comprehension of microgravity-induced cardiovascular deconditioning, of potentially dangerous ocular diseases, and to the design of future, successful countermeasures to enable long-term human spaceflight.

Ai nonni,
qui e altrove, per tutto.
A mamma e papà,
a mio fratello.

Contents

Introduction

Human space travels and interplanetary exploration have always aroused enormous fascination and interest among researchers and within the scientific community in general. Starting from the first manned space missions back in the last century, the current, open challenges of sending humans in space, surviving from long permanence in a altered-gravity environment - among other existing spaceflight-related hazards - brought to the development of new scientific disciplines known as space medicine and bioastronautics. The main objective of such branches of life sciences is to ensure human survival and well-being during and after missions into space, putting in place a set of pre-flight, in-flight and post-flight countermeasures to mitigate and prevent from major risks connected to human permanence in the space environment.

Among the different human systems, the cardiovascular physiology is particularly challenged by altered-gravity environments, both from a short- and a long-term point of view. Indeed, the human circulation is particularly susceptible to changes of the gravity acceleration as blood tends to migrate across the body under the action of the external gravitational pull. To fully grasp the mechanisms determining the human cardiovascular physiology and behavior in space, and thus in response to altered-gravity environments, it is of primary importance to understand the mechanisms associated with hemodynamics and cardiovascular changes on Earth, under normal Earth gravity, during posture changes (*e.g.*, from supine to upright standing and *vice versa*). It is widely believed in fact that long permanence in space can be compared to prolonged bed rest with the head slightly tilted downward (by about 6°) in terms of cardiovascular response and long-term adjustments (refer for example to Pavy-Le Traon *et al.* 2007, *'From space to Earth: advances in human physiology from 20 years of bed rest studies (1986-2006)'*, Eur. J. Appl. Physiol. 2007). These evidences further underline the importance of conducting ground-based experimental campaigns aimed at reproducing cardiovascular changes similar or analogue to those observed in actual spaceflight, exploiting the different possibilities currently available in the field (head-down bed rest, parabolic flight, etc.).

In this context, numerical modeling is gaining larger popularity in the simulation of blood motion, vascular mechanics and related behavior to allow for a cheap, feasible and completely non-invasive exploration of a number of cardiovascular conditions, diseases and responses to different stimuli. In this PhD thesis, we propose a novel multiscale, 1D-0D closed-loop mathematical model of the human circulation, encompassing the large arteries of the arterial tree departing and branching out from the human aorta, down to downstream arterioles, capillary and venules representing the peripheral microcirculation, including also large veins and venae cavae of the venous return circuit. In addition, the model accounts for a mathematical description of the four contractile cardiac chambers, the arterial and venous pulmonary circulation, a specific and detailed scheme of the cerebrovascular circulation, and the ocular compartment. The model is then integrated with mechanisms of autonomic regulation control, such as a baroreflex control, a cardiopulmonary reflex control, and a cerebral autoregulation mechanism for the maintenance of the overall system's homeostasis over a number of different working conditions (*i.e.*, posture changes, altered-gravity). In the context of possible applications of a numerical tool such as the one described in the present thesis, aerospace and clinical are only a sub-set of a number or different options. One plausible common trait is however the ease of applicability to case studies that are far from being easily accessible - or even considered as extreme. Indeed, the spaceflight environment as also medical conditions such as atrial fibrillation are two examples in which the usefulness of a numerical tool of investigation at reduced costs and completely free from invasiveness may make a substantial change to the scope of the research.

The model has been calibrated on the basis of currently available literature considering changes of posture and gravity alterations commonly experienced during ground based experiments (change of posture) and analogues of actual altered-gravity (parabolic flight) or microgravity (head-down tilt). Furthermore, the model has also been validated *in vivo* during two different experimental campaigns of head up tilt (change of posture from supine to upright standing) and head-down tilt (to -6° as analogue of microgravity and human spaceflight). To the end of the present thesis, the model has therefore been used to investigate a number of (simulated) clinical and spaceflight-related scenarios, ranging from the study of the impact of cardiac arrhythmias on the perfusion of the myocardium, to the cardiovascular, cerebrovascular and ocular responses elicited by posture changes, gravity alteration and longer permanence at -6° (one-hour head-down tilt).

The contents of the present thesis are organized as follows. Chapter 1 is devoted to introducing the readers to the human cardiovascular physiology and functioning, providing a brief summary of the most important cardiovascular system functions, components and roles. Furthermore, a description of the heart and of the coronary circulation is also reported, while an introduction to some basic hemodynamic parameters, arterial wave dynamics and to the main regulatory mechanisms acting to preserve system's homeostasis is proposed in the following of the chapter. Chapter 2 reports a detailed survey of the state-of-the-art literature in terms of gravity-driven effects onto the human cardiovascular physiology. The aim of this chapter is to inform the readers on the currently known effects of posture and gravity magnitude changes both on Earth and on orbit, including also other ground-based solutions to elicit altered-gravity environment (*e.g.*, lower body negative pressure, parabolic flights, etc.). Then, Chapter 3 reports the overall mathematical description of the multiscale, closed-loop model of the human cardiovascular system used to conduct the numerical simulations and investigations reported in the following parts of the present thesis. All the detailed equations incorporated in the model are reported in Chapter 3, together with all related parameters introduction and description, whereas full parameters calibrating values are enclosed in Appendixes A and B. Following Chapters 4-7 are devoted to presenting the results of the numerical investigations conducted throughout the whole PhD research activity. In particular, Chapter 4 reports the results of the numerical investigation of the effects of atrial fibrillation on the perfusion of the myocardium, considered as a clinical case study to test the applicability of the model and explored through an inter-layer vs. inter-frequency analysis. Then, starting from Chapter 5 the focus is transferred to exploring the impacts of gravity on the cardiovascular physiology, with a first set of studies showing the results of the passive posture changes investigation. Chapter 5 describes thus the most interesting responses in terms of overall cardiovascular changes, oxygen consumption and energy supply-demand balance, cardiac perfusion and arterial wave dynamics in response to simulated head-up tilt from supine to upright standing. Chapter 6 presents our numerical investigations of parabolic flight as ground-based analogue of microgravity where actual free falling (or weightlessness) can be reproduced, although for few seconds only. Our study focuses particularly on the overall cardiovascular response elicited during the whole flight maneuver (thus including both hyper- and microgravity phases) simulated at different postures, as well as on the oxygen demand vs. supply balance, and on the response of the cerebrovascular circulation. Finally, Chapter 7 presents our results on acute (up to 60 minutes) permanence at 6° head-down tilt (*i.e.*, head -6° below horizontal) in terms of cardiovascular, cerebrovascular, and ocular responses, especially in association with spaceflight-associated neuro ocular syndrome (SANS) and its possible insurgence and development in astronauts undergoing long-term missions in space.

The present thesis thus points out how powerful and versatile numerical modeling could be, suggesting promising future applications to the diagnostics and prognostics of clinical and space medicine-related scenarios. With the nearly unlimited development margin of such computational tools at accessible costs (compared to actual on orbit experiments or to the level of invasiveness and risk associated with *in vivo* clinical measurements), the present PhD thesis aims at underlying the importance of pushing further the limit of computational empowerment, setting the base for future multi-purpose, high fidelity and widely accessible platforms for clinical and bioastronautics research.

Chapter 1

Basics of human cardiovascular physiology

The cardiovascular system (CVS) - or cardio-circulatory system - is the system of organs devoted to the transport of different substances throughout the human body by means of blood motion in blood vessels. The essential components of the human CVS are:

- blood, the fluid medium in charge of carrying the various substances along with its motion;
- blood vessels, the numerous conduits accommodating blood and allowing for blood motion to transport all substances throughout the whole body;
- heart, the pump forcing blood motion through vessels by continuous beating action.

The main functions of the human CVS can be summarized as (i) transport of nutrients, oxygen and hormones to all tissues and organs in order to provide the essential life energy supply to the body; (ii) carry away and remove all metabolic waste products, other pathological agents, and carbon dioxide; (iii) regulate body temperature by heat convective transport, regulate body pH, maintain a suitable body fluids equilibrium and, in general, maintain an appropriate environment for optimal survival and functioning of cells [92, 132, 19, 117].

In this chapter we will provide a brief overview of the human CVS with its main components and functioning principles, in order to understand the mechanism of blood motion through blood vessels and how it is regulated under different working conditions and stimuli. In the following, we will first present a description of the human circulation, covering the basis of blood motion and blood vessels characteristics. Then, we will introduce the heart, its role and functioning and the annexed coronary circulation, we well address the basic principles of hemodynamics, and, lastly, we will give details about the homeostatic control of blood pressure and flow responsible for regulating an appropriate CVS functioning.

1.1 The human circulation

The human circulatory system encompasses a network of vessels originating from the heart, reaching all the body tissues and organs, and returning back in a closed loop circuit. Generally, two main categories of large blood vessels are identified: arteries and veins [92, 132, 19, 117]. By artery are identified all vessels departing from the heart and directed towards the periphery, via multiple branching and progressive tapering. By contrast, veins are all vessels returning to the heart, usually through connections and anastomoeses. Table 1.1 summarizes other characteristics or arterial and venous vessels, based upon their general shape or appearance, blood pressure, wall thickness and oxygen transport. Arteries are the high pressure side of the circulation (around 80/120 mmHg), with blood directly ejected from the heart at nearly ventricular pressure to be pumped towards the body periphery with sufficiently high energy. Thus, arterial walls are thicker than venous and they also keep a nearly perfect circular cross-section shape, as they have to sustain higher intravascular pressure upon blood motion. Veins are instead the low pressure side of the circulation (few mmHg), with blood flowing at much lower pressure than compared to arteries. For this reason, venous vessels walls are generally thinner and their cross-sectional shape is often irregular and far from circular, with occasional vessel collapse (*i.e.*, partial/total vessel occlusion) whenever venous intra-vascular pressure should fall below local extra-vascular pressure.

Arteries and veins are connected through the microcirculation. This smaller type of vessels can be subdivided in arterioles, capillaries and venules. While arterioles and venules are the smallest peripheral tracts of arteries and veins, respectively, encountered at the level of body tissues after numerous bifurcations and consequent vessels downsizing, capillaries are the fundamental microcirculatory districts where gas exchange with adjacted organs takes place. This is an osmotic process during which oxygen is transferred from the intra-vascular to the extra-vascular space and carbon dioxide travels the opposite way, or *vice versa* [92, 117].

1.1.1 Systemic and pulmonary circulations

The human circulation is considered two-fold, being divided into a systemic circulation and a pulmonary circulation [92, 117]. Figure 1.1 illustrates schematically the two distinct circuits, with systemic circulation - the largest of the CVS, containing around 84% of total blood volume - departing from the left part of the heart with the aorta (the largest human artery) and reaching the body periphery through successive bifurcations and branching forming the so-called arterial tree. At the end of systemic arteries we find systemic microcirculation, perfusing all

Table 1.1: General characteristics of human arteries and veins. Reproduced from [19].

Feature	**Arteries**	**Veins**
Blood flow direction	away from the heart	towards the heart
General appearance	circular cross-section	irregular, collapsible
Pressure	high	low
Wall thickness	thick	thin
Oxygen concentration	systemic: high pulmonary: low	systemic: low pulmonary: high
Notes	no valves	presence of valves

body tissues and organs with blood carried from the heart and allowing for gas exchange to provide the needed energy supply. Then, through systemic veins and venae cavae, systemic circulation closes at the right part of the heart. Systemic circulation transports oxygenated blood from the heart to all depending tissues and organs through systemic arteries, while deoxygenated blood flows back through systemic veins carrying carbon dioxide and other metabolic waste products produced by the organism (Table 1.1). According to data reported in Figure 1.1, systemic arteries contains about 13% of total blood volume, whereas systemic arterioles and capillaries contain about 7% of total blood volume. Systemic veins and venules, instead, contain up to 64% of total blood volume, as venous vessels are considered to be good blood reservoirs thank to their highly compliant properties. More specific blood volume subdivision across systemic vessels and districts, including also absolute volume values referred to a total blood volume content of about 5 l, can be found in Table 1.2 or in [19].

Pulmonary circulation instead originates from the right heart, with large pulmonary arteries carrying deoxigenated blood (Table 1.1), reaching the lungs (notice that pulmonary arterial pressure is typically lower than systemic arterial pressure, usually around 15/25 mmHg), bronchial circulation and eventually down to the alveoli. The pulmonary alveoli are wrapped by pulmonary microcirculation vessels and pulmonary capillaries, where the reverse gas exchange takes place with oxygen flowing towards the intra-vascular space and carbon dioxide being transferred outside and then expelled by expiration. New oxygenated blood flows then back to the left part of the heart through pulmonary veins (Table 1.1), providing thus the energy supply for the entire organisms [92, 117]. Pulmonary circulation contains around 9% of total blood volume, which is subdivided as 2.6% in pulmonary arteries, 2.2% in pulmonary capillaries, and 4% in pulmonary veins (Table 1.2).

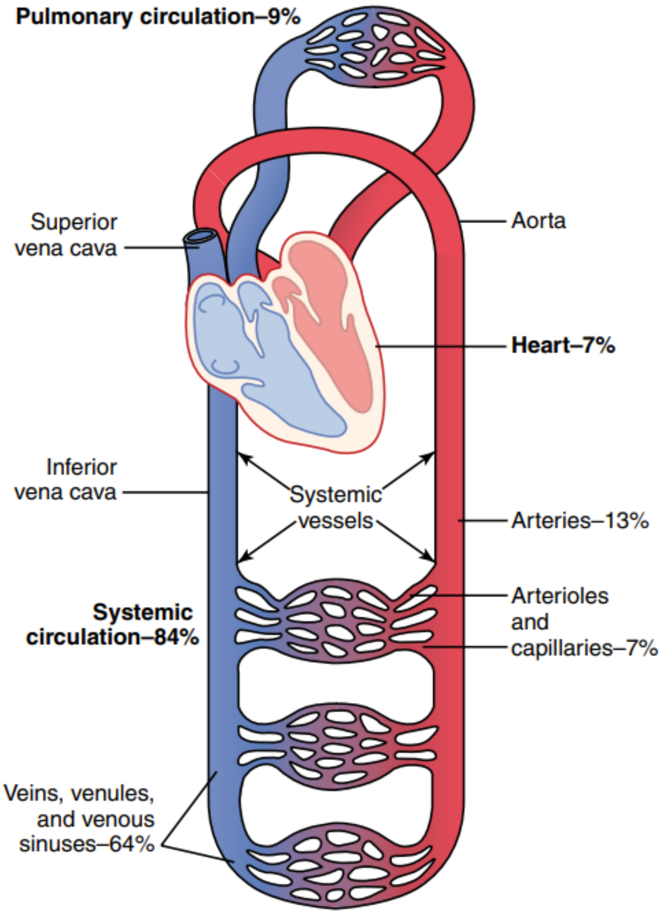

Figure 1.1: Human circulation divided into systemic (below) and pulmonary (above) circulations. Image taken from [92].

1.1.2 Blood motion and vessels mechanical properties

Blood motion in human vessels occurs thank to several factors which in turn determines the characteristics of blood flow [151, 293, 278]. The main determinant of blood flow in human vessels is pressure, which can be distinguished into three primary components: (i) the dynamic pressure imposed by the pumping heart, (ii) the visco-elastic component related to the local vessel wall mechanical properties, and (iii) the hydrostatic component (when applicable) depending on blood specific weight [24]. Among these, pressure imposed by the pumping heart is by far the most important contributor to blood pressure, determining the characteristic pulsatile regime of arterial blood flow [151, 293]. Figure 1.2 taken by [117] illustrates how pulsating pressure generated by the pumping heart (left ventricle) is transmitted to the aorta, where blood flows at a pulsating pressure oscillating typically between 80 mmHg and 120 mmHg in a healthy subject. As a consequence, blood flow and

Table 1.2: Absolute and relative blood volume distribution across the human vasculature. Reproduced from [92, 19, 177].

Location	**Absolute Volume [ml]**	**Relative Volume [%]**
Systemic Circulation		
Aorta and large arteries	300	6.0
Small arteries	400	8.0
Capillaries	300	6.0
Small veins	2300	46.0
Large veins	900	18.0
Pulmonary Circulation		
Arteries	130	2.6
Capillaries	110	2.2
Veins	200	4.0
Heart	360	7.2
Total	5000	100

blood velocity are also pulsatile along the aorta and in all large arteries (Figure 1.2, in the middle), at least until the peripheral microcirculation districts are reached. Notice that also pulmonary arterial blood flow and pressure are pulsatile, although with lower amplitude, as imposed by the beating action of the right part of the heart (right ventricle).

Flow regime - whether laminar or turbulent, stationary or pulsatile - is crucial to determine the flow velocity profile at each cross-section of the CVS vessels [151, 117]. In large arteries, being characterized by high velocity blood flow (Figure 1.2) and large radius, the local Reynolds number[1] can reach values sufficiently high to allow for turbulent flow to take place. However, the non-dimensional parameter describing the most of the flow profile behavior is the Womersly parameter[2]. In large arteris at highly pulsatile flow, the local Womersley parameter can rise up to 10-14, determining larger inertial effects over viscous ones. Therefore, the typical (mean) velocity profile is flatter than the standard parabolic Poiseuille profile where viscosity forces are of the same order of magnitude as inertial effects. Thus, along the aorta and in most large arteries the mean flow velocity profile can be assumed as flat, as shown in Figure 1.4, with steep transition to zero wall velocity (adherence)

---

[1] $Re = \rho U r/\mu$, with ρ blood density, U blood velocity, r vessel radius, and μ blood dynamic viscosity.

[2] $Wo = \sqrt(\rho \omega r/\mu)$, with ω pulsation of the oscillatory flow.

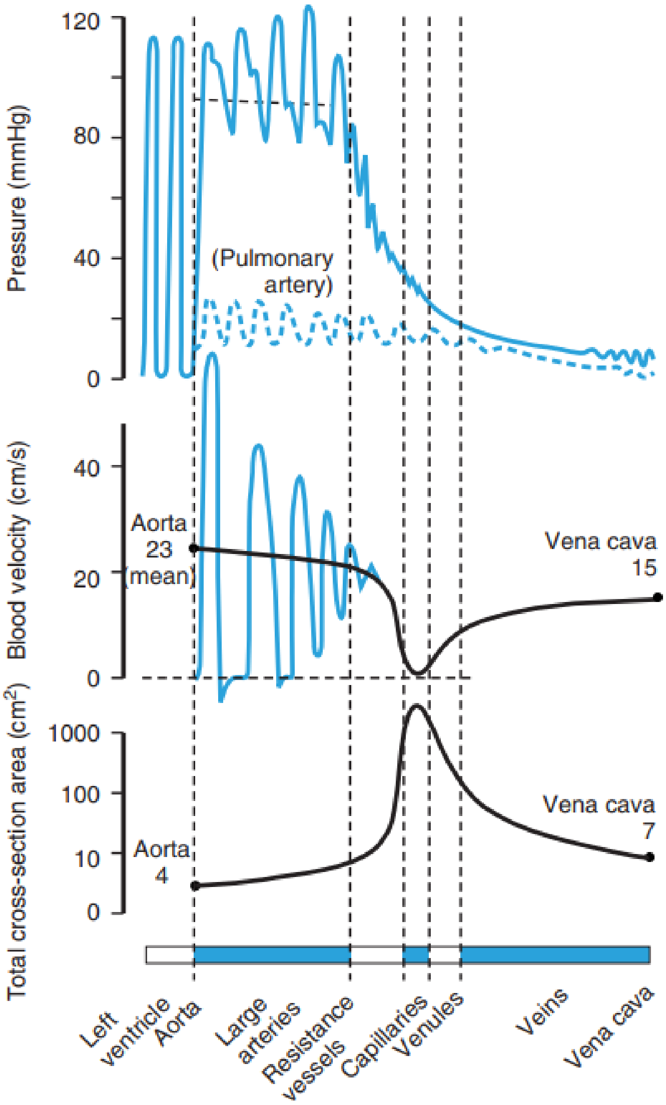

Figure 1.2: Blood pressure, velocity and total cross-section area throughout the human systemic vasculature (dashed line indicates pulmonary circulation vasculature). Image taken from [117].

in the proximity and onto vessels wall. Conversely, as arteries become narrower towards the periphery and microcirculatory districts (arterioles) where viscosity begins to prevail and balance inertial forces, the oscillatory nature of blood flow is almost completely damped, thus the standard parabolic profile can be assumed here as the classic Poiseuille parabolic velocity profile. The problem becomes even more complicated when it comes to venous vessels, given the high deformability and irregular shape of those vessels for which the standard theory of pulsatile profiles in rigid tubes can no more be applied [236].

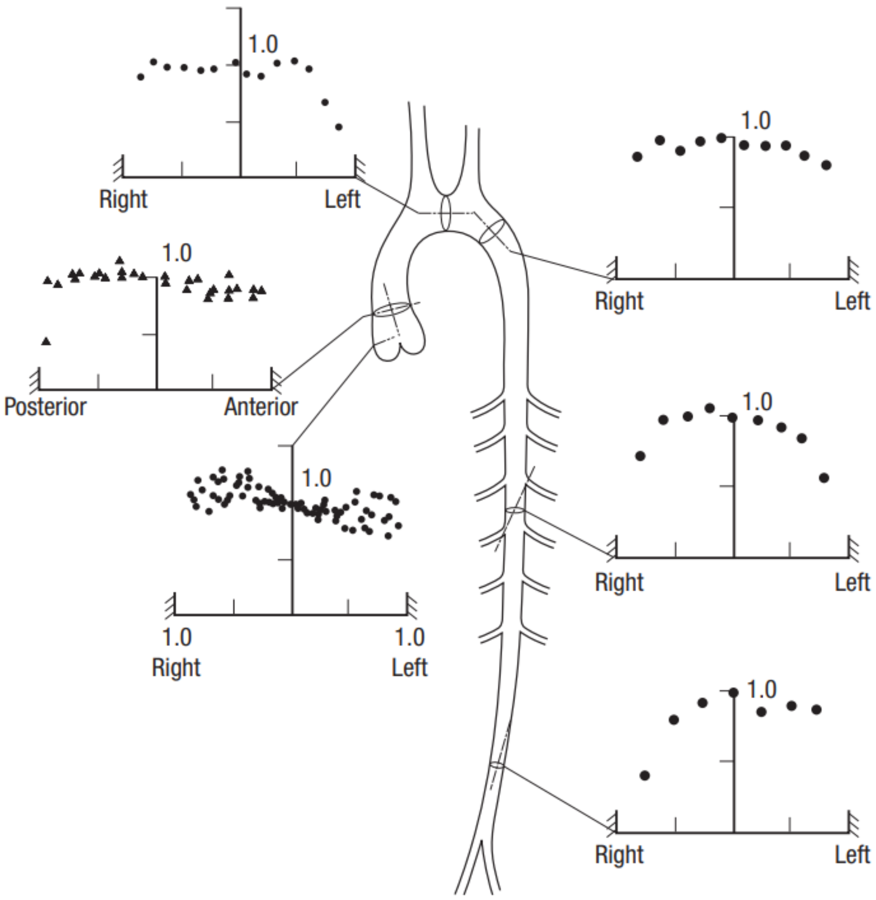

Figure 1.3: Blood velocity profile at various points along the canine aorta (data normalized by the mean centerline velocity). Image taken from [151].

Blood vessels vary largely their mechanical properties and behavior depending on their size, function, wall thickness and constitution (amount of different wall components) [117]. Figure 1.4 illustrates the most typical types of vessels according to the vascular district they represent, together with their average diameter, wall thickness, and wall constitutive components. From Figure 1.4 it is evident that the aorta, all large arteries and arterioles are those characterized by the highest elastic properties thank to their constitutional components, whereas veins are less elastic as they serve as blood reservoirs thank to their elevated blood compliance [278, 92] (Figure 1.5, vessels compliance can be quantified as the ratio between volume variation and the corresponding pressure variation). As also evidenced in Figure 1.4, microvascular vessels (terminal arterioles, capillaries and venules) are the least elastic vessels, as well as the narrowest of the whole vasculature. Their smaller radius is the main reason why they are considered to be the highest resistive vessels, where pressure drops from the high arterial level to a new level low enough to allow for a correct gas exchange process with extra-vascular tissues [278, 92, 117]. The steep pressure reduction occurring at microvascular level is displayed in Figure 1.2, top diagram, where it is visible how high and oscillating arterial pressure is dumped down to low pressure level. The bottom diagram of Figure 1.2 highlights that, despite their high resistance, vessels total cross-section area reaches its highest values at microvascular levels, thank to the incredibly numerous microvessels composing this vascular level. As a consequence, because of mass conservation, the overall blood velocity is the lowest possible across the microcirculatory districts, further enhancing a correct gas exchange process [278, 117].

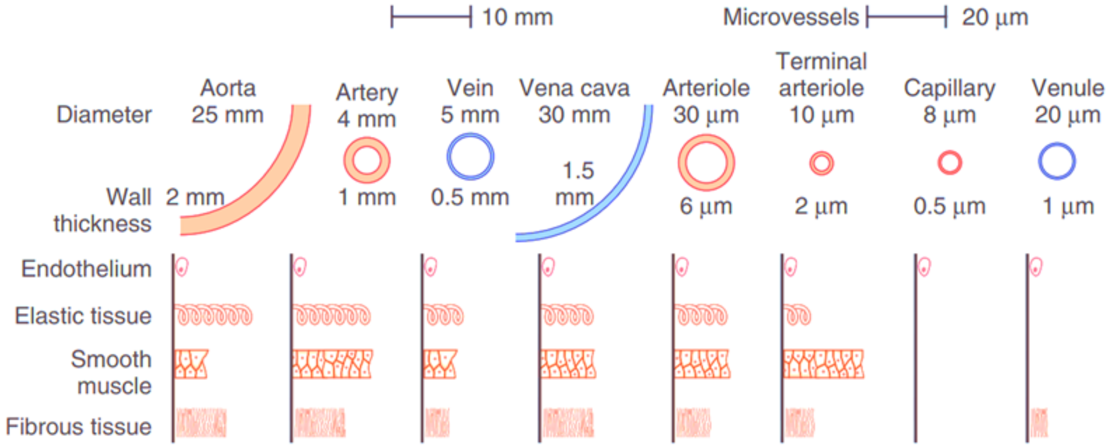

Figure 1.4: Characteristics of blood vessels organized by vascular districts: diameter, wall thickness and amount of wall constitutive components. Image taken and adapted from [117].

1.2 The heart

The heart is the pump mainly responsible for blood motion throughout the entire CVS [92]. The human heart - illustrated in Figure 1.6 - is divided into two halves, that is right and left heart, each including an atrium and a ventricle chamber for a total of four heart chambers. These heart chambers beat alternatively and are governed by the same heart pacing electrical stimulus originated at the apex of the right atrium, at the sinoatrial node, transmitted to the other chambers with a certain degree of phase shifting occurring at the atrioventricular node. Between the corresponding atrium and ventricle there are cardiac atrioventricular valves allowing for unidirectional flow from atria to ventricles only, and to prevent from reverse flow into both atria. In addition, specific semilunar valves are enclosed at the interface between each ventricle and the subsequent arterial vessel. The left part of the heart, including left atrium and ventricle separated by the mitral valve,

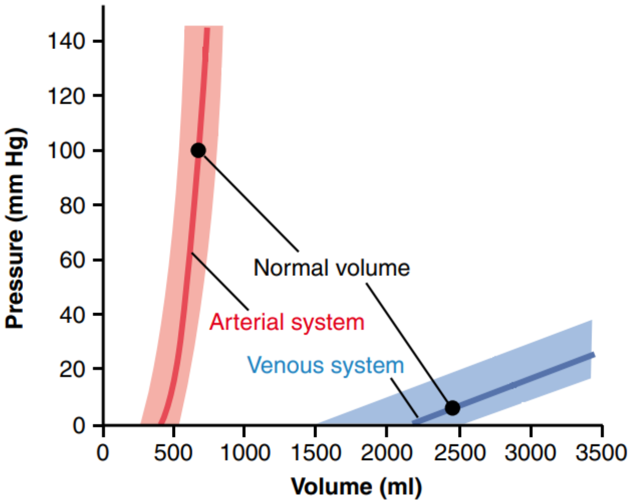

Figure 1.5: Arterial and venous walls elastic/compliant mechanical behavior. Image taken and adapted from [92].

pumps blood into the aorta through the aortic valve, and thus towards the systemic circulation. For this reason, pressure generated into and out from the left ventricle is high (Figure 1.2, top diagram) to allow for a proper amount of blood flow to be ejected and delivered to all body districts. The right part of the heart, instead, is composed of the right atrium and ventricle separated by the tricuspid valve, pumps blood towards the pulmonary circulation through the pulmonary valve and into the main pulmonary artery, at a pressure typically lower than within the aorta.

1.2.1 Heart fluid mechanics

Each part of the heart follows a specific fluid mechanics pattern that is repeated at each heartbeat, called cardiac cycle [92, 278]. Each cardiac cycle is subdivided into a phase named systole and a subsequent phase named diastole, whose mutual weight with respect to the entire cardiac cycle length depends on the current heart beating rhythm (i.e., the heart rate, HR). Cardiac systole of both ventricles begins with a first, rapid isovolumic contraction followed by a second stage of ejection, whereas cardiac diastole is composed of an initial isovolumic relaxation followed by a second, slower filling stage. Figure 1.7 shows the so-called Wiggers diagram for the left heart throughout two consecutive heartbeats. The thick, red curve is left atrial pressure, oscillating between the lower left atrial pressure and aortic pressure (both in black, dashed lines), whereas left ventricle volume is represented by the thick, blue curve below. When left ventricle systole starts, at closure of the mitral valve when left ventricle pressure exceeds left atrial pressure, left ventricle pressure rises rapidly during isovolumic contraction (aortic valve still closed). Afterwards,

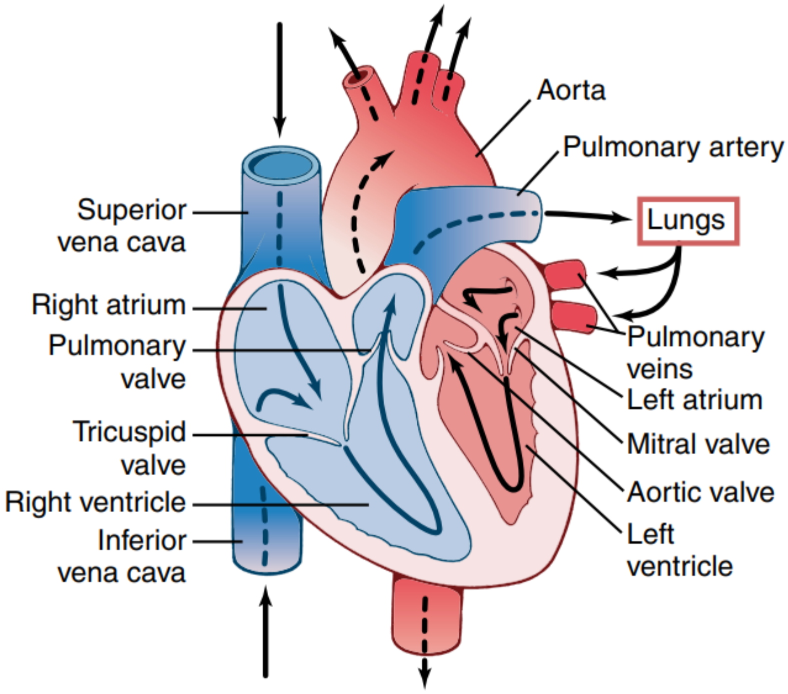

Figure 1.6: Illustration of the human heart composition. Image taken from [92].

when left ventricle pressure exceeds aortic pressure, the aortic valve opens allowing for blood volume to flow out from the heart during the systolic ejection phase. Systolic ejection continues until aortic pressure falls below left ventricle pressure, with consequent end of systole and closure of the aortic valve. Here, the initial isovolumic relaxation of left ventricle diastole starts, with left ventricle pressure falling rapidly below left atrial pressure. Then, when left atrial pressure is higher than left ventricle pressure, the mitral valve opens again and blood starts flowing from the atrium to the ventricle, during left ventricle diastolic filling. This phase is ended with the typical atrial kick, that is a rapid atrial contraction impulse that achieve complete emptying of the left atrium just before closure of the mitral valve and the beginning of a new cardiac cycle.

1.2.2 Coronary circulation

The coronary circulation is the portion of the systemic circulation aimed at providing the needed nutriments and oxygen supply to the heart and its contractile muscle fibers, that is the myocardium [92, 278, 117]. Figure 1.8 displays a sketch of the main superficial coronary arteries and veins wrapping the heart most external layer of the myocardium. The coronary circulation originates at the aortic sinus with the left and right main coronary arteries. The left main coronary artery is further branched into the left anterior descending coronary artery and the left

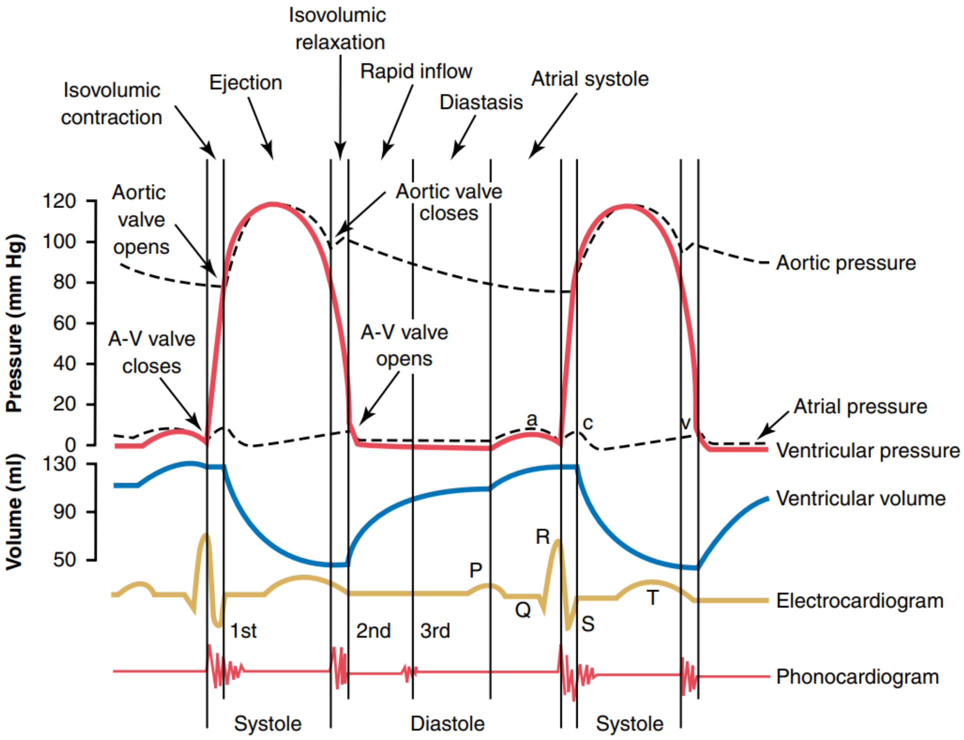

Figure 1.7: Wiggers diagram of the left heart. Image taken from [92].

circumflex artery, together perfusing the left heart and part of the interventricle septum. The right main coronary artery also reaches the interventricle septum and feeds the right part of the heart. At multiple sites along the large superficial coronary arteries, a series of perforating arteries depart and penetrate into the myocardium reaching and feeding all myocardial layers. Eventually, perforating veins and subsequent large coronary veins collect deoxygenated blood and flow back to the vena cava.

Due to its development onto, within and all around the cardiac muscle, the coronary circulation is peculiar since it behaves differently from the rest of systemic circulation. In spite of most of blood flow in the aorta and all across depending vasculature takes place during systole, with blood flow slowing down during cardiac diastole, the coronary circulation shows the opposite behavior with the majority of coronary blood flow occurring during ventricles diastole (Figure 1.9, middle and bottom diagrams). The reason for this peculiar behavior is the contraction of the ventricles during systole, increasing aortic and intra-ventricle pressures (Figure 1.9, top diagram) and in turn also intramyocardial pressure (*i.e.*, the pressure inside the myocardium and exerted directly onto the coronary vasculature). High ventricle and intra-myocardial pressure during systole therefore obstruct coronary blood flow through coronary arteries. By contrast, during subsequent diastole the myocardium

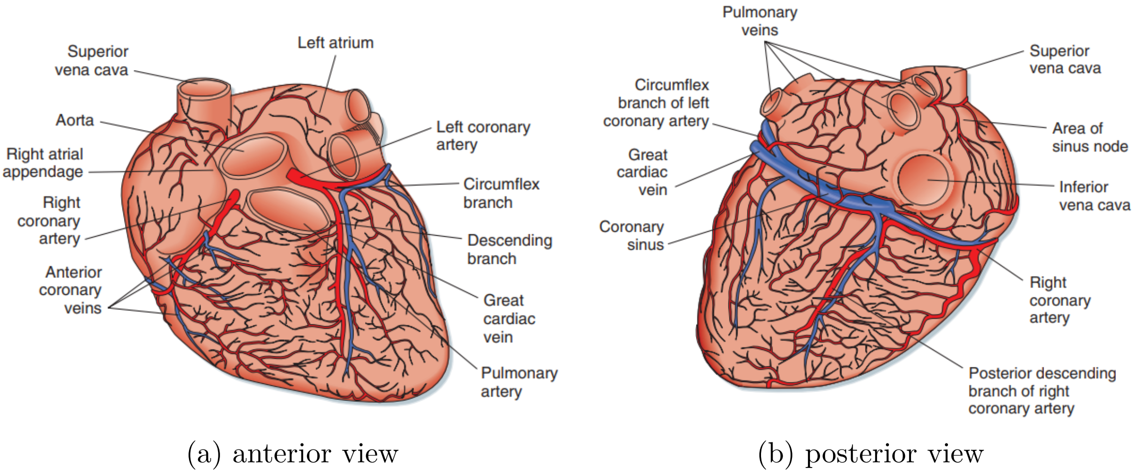

(a) anterior view (b) posterior view

Figure 1.8: Illustration of the coronary circulation. Images taken from [117].

relaxes letting blood flow again through the coronary vasculature. As displayed in Figure 1.9, this phenomenon is much more evident in left coronary arteries than in right coronary arteries, because of the much higher ventricular pressure coming from the corresponding adjacent ventricle.

Circulation of blood in the coronary vasculature is matter of profound interest due to the importance of preserving a correct level of feeding to the cardiac muscle. In particular, the impact of several conditions onto coronary and myocardial perfusion is object of investigation in many research field. Among the most widely known and common cardiac arrhythmias, atrial fibrillation is certainly one of the most widespread, and thus one scope of the present thesis is to assess the coronary hemodynamics under this detrimental condition (see chapter 4). In addition, we also aim at exploring how the coronary circulation is affected by gravity alterations and posture changes (chapter 5), which is also another context that has received poor consideration so far.

1.3 Principles of hemodynamics

Hemodynamics is the branch of fluid mechanics studying blood motion in vessels and through the heart. Blood is considered a non-Newtonian fluid with lots of suspended particles (hematocrit), although - especially if large vessels are concerned - it is often considered as Newtonian for simplicity. In this section, we will present the basic concepts of cardiac and vascular hemodynamics, introducing the most important parameters used to characterize blood motion, cardiac performance, and propagation of waves throughout the vasculature.

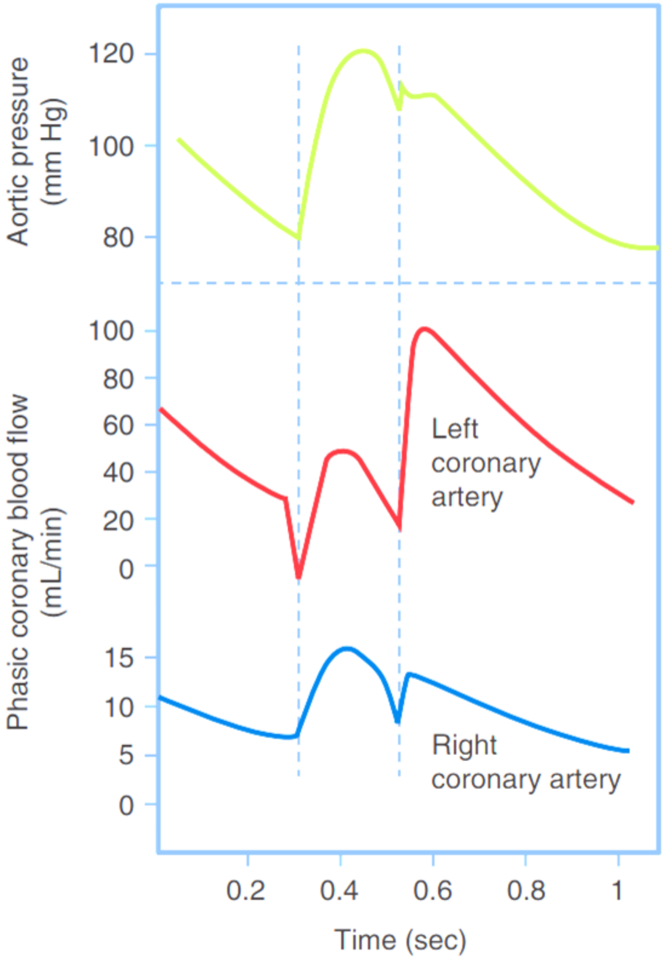

Figure 1.9: Aortic pressure vs. left and right coronary blood flow. Image taken and adapted from [117].

1.3.1 Cardiac loop and basic hemodynamic parameters

Following the description of the cardiac loop presented in section 1.2 and the Wiggers diagram of the left heart displayed in Figure 1.7, it is possible to map the pressure-volume relationship of the left ventricle (as well as of all cardiac chambers) during one single heartbeat, obtaining the so-called PV-loop reported in Figure 1.10 [92, 278]. The left ventricle PV-loop shows both phases of the cardiac cycle, that is systole and diastole, together with systolic isovolumic contraction, ejection, diastolic isovolumic relaxation and eventual filling. In addition, it is possible to clearly identify the points where the mitral and aortic valves open and close, at the beginning/end of each cardiac phase. The maximum and minimum volumes reached by the left ventricle during the cardiac cycle are called end-diastolic volume (V_{LVED}) and end-systolic volume, respectively (V_{LVES}). The difference between

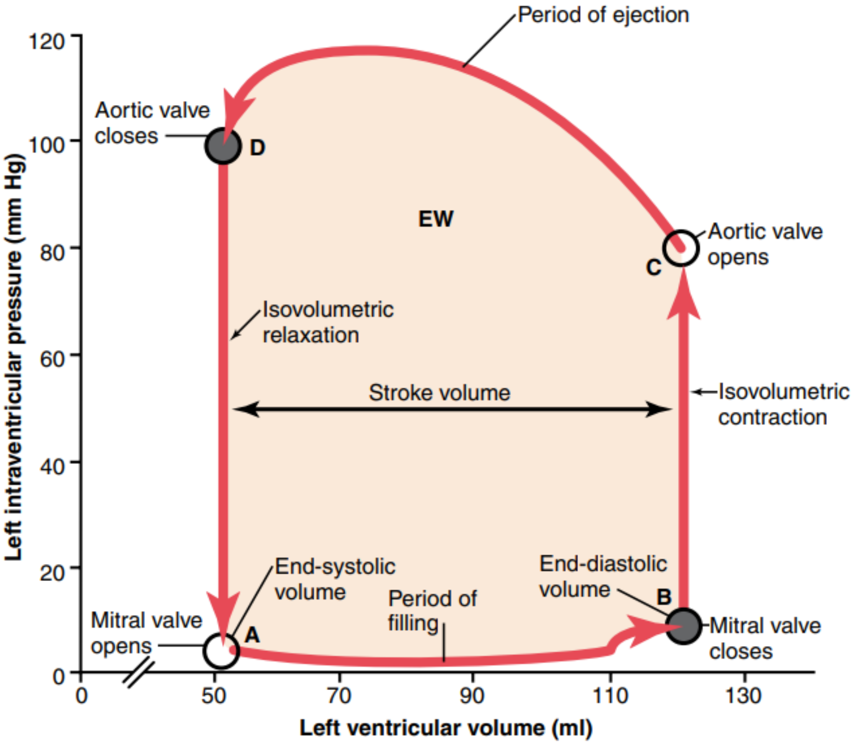

Figure 1.10: Left ventricle PV-loop. Image taken from [92].

these values (*i.e.*, the amount of volume entering the left ventricle during diastole and in turn being ejected through the aortic valve at each heartbeat during systole) is called stroke volume (SV), that is

$$SV = V_{LVED} - V_{LVES}.$$

The area of the PV-loop is cardiac work, stroke work (SW) or external work (EW), that is the energy produced by the heart during one cardiac cycle, obtained as

$$EW = \int_{PV-loop} p_{LV}\, dV_{LV},$$

where p_{LV} is left ventricular pressure and V_{LV} is left ventricular volume. To quantify the overall flow rate ejected from the heart through the systemic vasculature, another parameter named cardiac output (CO) is often adopted, defined as

$$CO = HR \cdot SV,$$

where HR indicates the heart rate and SV is stroke volume defined above. If stroke volume is measured in liters and HR in beats per minute (bpm), CO units are l/min. Usually, a healthy human with resting $HR \approxeq 70$ bpm and $SV \approxeq 70$ ml has typical values of CO of around 5/5.5 l/min and $EW \approxeq 0.5/1.5$ J [92, 278]. CO is also linked to arterial and venous blood pressure through Ohm's law, by linking the overall amount of blood flowing through a given conduit to upstream and downstream pressure difference and to internal hydraulic resistance. Considering mean arterial pressure (MAP) and central venous pressure (CVP) as the pressure at inlet and outlet of systemic circulation, and considering total peripheral resistance (TPR, mostly arteriolar and capillary resistance) as the overall hydraulic resistance of the whole systemic vasculature (as large main arteries and veins do not retain high resistive characteristics, see Figure 1.2), then according to Ohm's law:

$$CO = \frac{MAP - CVP}{TPR} \approx \frac{MAP}{TPR},$$

assuming that generally $CVP \ll MAP$.

Besides the concept of hydraulic resistance, linked to vessels geometry and blood viscosity according to Poiseuille's law ($R = 8\mu l/(\pi r^4)$, with μ blood dynamic viscosity, l vessel length and r vessel internal radius), other useful hemodynamic parameters are also [278]:

- vasculature capacity/compliance (C, as opposed to vessels elastance, E), depending on the local vessels wall characteristics and defined as $C = \Delta V/\Delta p$ (units ml/mmHg). Vascular compliance quantifies the variation of blood volume in response to a variation of blood pressure in a given vascular district, see section 1.1;
- vessels inertance (L) related to blood inertia and vessels geometry and thus defined as $L = \rho l/A$ (units mmHg s^2/ml, ρ is blood density, A is vessel cross-section area). Inertance determines an additional blood acceleration/deceleration especially during cardiac systole and within large arterial vessels (since $L \propto r^{-2}$, while $R \propto r^{-4}$ dominates small vessels).

While for two or more vessels organized 'in series' resistances and inertances can be summed up (as for consecutive tracts of the aorta), the inverse of total resistance should be computed as the sum of the inverse of single vessels resistance/inertance (*i.e.*, $1/R_{tot} = 1/R_1 + 1/R_2 + \dots$) for vessels organized 'in parallel' (such as for vessels belonging to different vascular districts). The contrary holds for vessels compliance [278].

Additional indices of cardiac performance are left ventricle ejection fraction (EF) and oxygen consumption indices, such as rate pressure product (RPP), tension time index (TTI), left ventricle pressure-volume area (PVA), as well as also cardiac efficiency. For the definition of these indices the interested reader is referred to [278], or to chapters 5 and 6 of the present thesis, where we will address the impact of posture changes and varying gravity, respectively, on the human circulation and cardiac performance. This topic is indeed fundamental to the enable thorough understanding of human CVS physiology on Earth and upon altered gravity, such as during human spaceflight, in microgravity.

1.3.2 Wave dynamics

As in any fluid system, blood motion across the CVS is accompanied by the propagation of waves traveling throughout the entire vasculature [278, 151, 163]. Waves are originated at the level of the aortic valve by heart contraction, pumping, valve opening and closure, etc., and they propagate all over the CVS down to the vascular periphery and back through the various venous paths. In addition, waves are continuously reflected so that part of their energy is sent back upstream towards the originating points, while the remaining is transmitted further downstream. As a results, at any point of the CVS, the local measured pressure or flow signals can be thought as the composition (summation) of a forward running wave and a backward running wave, in a 1D framework. This situation is clearly illustrated in Figure 1.11, showing how the composition of forward and backward running waves at a given arterial site leads to the more familiar pressure and flow waveforms obtained from direct measurement.

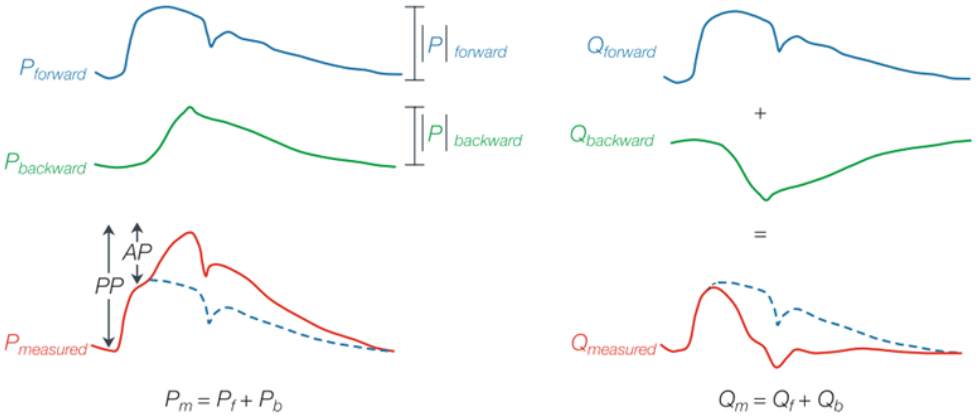

Figure 1.11: Arterial waves decomposition: P_m and Q_m indicate total (measured) pressure and flow waves, respectively; P_f, P_b, Q_f and Q_b are forward and backward components of pressure and flow waves PP is pulse pressure, and AP is augmented pressure. Image taken from [278].

Waves travel along the CVS at a specific (and finite) wave speed c, depending on the local mechanical characteristics of blood vessels. One widely adopted formulation for arterial wave speed comes from the Moens-Korteweg equation, such that $c = \sqrt{A/(\rho C_A)}$, thus depending on the local vessel cross section area A, blood density ρ, and local area compliance $C_A = \Delta A/\Delta p$ - similarly to the definition of standard (volume) compliance C.

Dynamics of waves traveling along the human vasculature is object of continuous investigation, due to the complex interplay between direct and reflected waves, their variation upon global cardiovascular changes and their relationship with all other cardiovascular protagonists (valves, stenoses, atherosclerotic plaques, etc.). Thus, another goal of the present thesis is that of investigating the so far unexplored mechanisms at the basis of wave dynamics changes elicited by postural changes, trying to elucidate the causes for the observed variations of wave reflection indices and their association with global posture-induced cardiovascular changes. Refer to chapter 5 for more detail on this topic.

1.4 Regulatory mechanisms of homeostatic control

Our organism employs a series of control mechanisms such to preserve global homeostasis. Among the aims of these regulatory actions, we focus on the proper maintenance of arterial and venous mean blood pressure and adequate level of blood perfusion to specific districts of the body. Short-term control of high (arterial) and low (venous) blood pressure level is operated by beroreflex and cardiopulmonary reflex controls, while one of the most important blood flow regulatory mechanism is cerebral autoregulation, preserving correct amount of cerebral blood flow. Such control mechanisms are addressed in further detail in the following.

1.4.1 Baroreflex and cardiopulmonary reflex

Baroreflex are high pressure sensors of arterial blood pressure [177, 92, 172, 93]. They are located in the aortic arch and at both carotid bifurcations sinus, and communicate with the central nervous system (CNS) to promote sympathetic or parasympathetic activities such to control arterial blood pressure level. A sketch of the control mechanism principle operated by arterial baroreflex is depicted in Figure 1.12a. Via sensing of high/low arterial pressure at baroreceptor sites, a series of afferent signals are delivered to the medulla oblongata of the CNS where subsequent signals of sympathetic/parasympathetic activity efferent signals are produced. These signals of efferent control are transmitted to te various efferent organs controlled by the baroreflex control loop, including heart rate (chronotropic control), cardiac chambers contractile state (inotropic control), arterial and arteriolar vasodilation/constriction, and regulation of large veins and venae cavae tone (volume, compliance).

Cardiopulmonary reflex - and corresponding cardiopulmonary receptors - are low pressure sensors situated at the low pressure side of the circulation, that is in the right atrium, sensing CVP and actual heart filling (cardiac preload) [93]. Cardiopulmonary reflex works similarly to arterial baroreflex, controlling mainly arterial and arteriolar vasodilation/constriction and venous/venae cavae tone.

Both baroreflex and cardiopulmonary reflex play a fundamental role in controlling the CVS state and preserving correct functioning and homeostasis of the

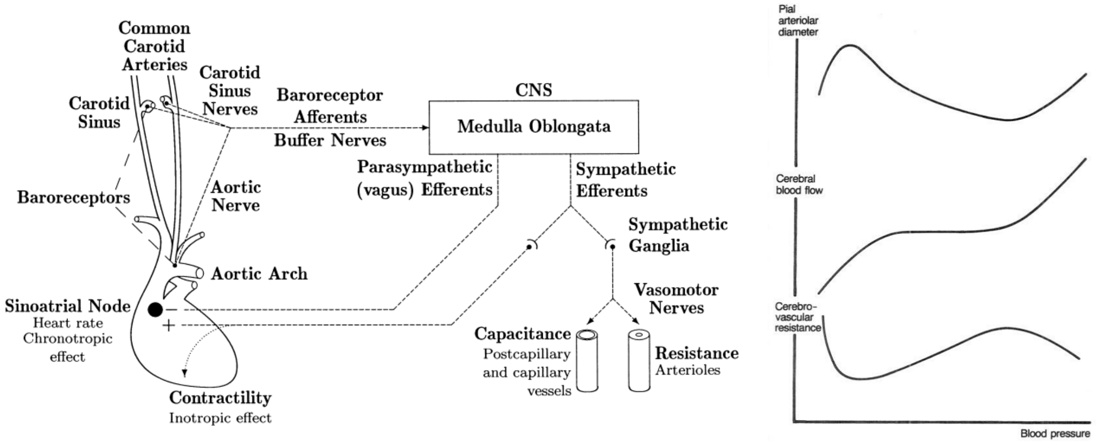

(a) (b)

Figure 1.12: (a) mechanism of baroreflex control (sensed arterial and venous central pressures are trasmitted to the CNS which, then, regulates the response of efferent controlled organs), image taken from [177]; (b) cerebral autoregulation functioning (cerebral blood flow is kept nearly constant by decreasing cerebral pial arteriolar diameter while increasing cerebrovascular resistance, at increasingly higher blood pressure), image taken from [187].

human organism especially during acute posture and gravity changes. Therefore, since in the present thesis we will deal with posture and altered gravity-induced cardiovascular alterations, baroreflex and cardiopulmonary reflex action are crucial aspects shaping the observed CVS responses to the different investigated scenarios (see chapters 5-6 for further details).

1.4.2 Cerebral autoregulation

As a mechanism to protect the brain from acute hypo- and hyperperfusion events that may lead to brain injury and severe ischemic damages or to cerebral hemorrhage, cerebral autoregulation acts such to preserve almost constant levels of cerebral perfusion (controlling cerebral blood flow) over a wide range of cerebral perfusion pressure (*i.e.*, in turn, of central MAP) [187, 122, 172, 258]. Cerebral autoregulation operates by acting on the active control of deep cerebro-vascular state, especially of pial cerebral arteries, through modification of their vasodilation/constriction and compliance state in order to allow for recruitment of more blood flow in case of low perfusion pressure, or, conversely, obstruct cerebral blood flow in case of high cerebral perfusion pressure (Figure 1.12b).

As already acknowledged for baroreflex and cardiopulmonary reflex control, also cerebral autoregulation becomes essential in the framework of cardiovascular physiology, especially when posture and gravity changes are concerned (refer to chapters 5-6). Cerebral autoregulation is not the only autoregulatory system present in the human CVS, even though it is crucial to understand the mechanisms of cerebral blood flow preservation needed during posture and gravity changes, as well as to comprehend the arising of complications deriving from malfunctioning or disorders of the autonomic control and autoregulation efficiency.

Chapter 2

Effects of gravity on the human cardiovascular physiology

As anticipated in Chapter 1, the motion of blood throughout the human vasculature is dictated by several factors [151, 278] including pressure, viscous and external forces. Among these latter, gravity plays a relevant role determining blood pressure, flow and volume distributions across the vasculature [73, 96]. On the Earth's surface, the gravity acceleration vector ($\boldsymbol{g}$) is constant and uniformly directed along the head-to-feet direction on a standing subject. On and close to the ground, the gravity acceleration magnitude (g_0) is taken as about 9.81 $\mathrm{m/s^2}$ (hereinafter referred to as 1g). However, the effects of gravity on the circulation may vary whenever the relative orientation between the gravity vector $\boldsymbol{g}$ and the body is changed [24, 43]. That is, when posture is changed, for example, sitting or standing from supine, or laying horizontally from upright. A different situation is encountered wherever actual altered gravity comes into play. This could be the case, for instance, of space travels to different planets, or very far from the Earth. Yet, even situations where the gravity attraction is balanced by a different force (such as an inertial force, *e.g.*, centrifugal) result in a condition of altered gravity on the subject. This is the case of parabolic flights, where the subjects onboard of the plane experience different levels of hyper- and microgravity depending on the acceleration and trajectory of the aircraft; or weightlessness experienced by astronauts on the International Space Station (ISS). Indeed, people and objects flying onboard of the ISS are only virtually weightless (at the ISS altitude of 400 km the magnitude of the gravity acceleration is only about 10% less than on the Earth's surface), since they are in a particular state of continuous free falling thanks to their high orbital velocity [169]. Hereinafter, the terms microgravity, weightlessness, and 0g will be used as synonyms and referred to the free falling condition described above and in [169].

In this chapter, the effects of gravity on the human cardiovascular physiology are introduced and discussed by reviewing the currently available literature. The contents are subdivided in two sections, the first of which illustrates the cardio-circulatory changes occurring at normal Earth's gravity (1g), in response to change of posture and to different treatments (*e.g.* lower body negative pressure, immersions, centrifugation and gravity suits). Successively, the second section reports the current knowledge of cardiovascular alterations resulting from exposure to the space environment, that is during short and long-term spaceflight. Additional insights on the use of ground analogs to reproduce (simulate) spaceflight are also discussed, as well as the usefulness of computer simulations (modeling) to further explore and bridge the existing gaps in the field.

2.1 Gravity-driven cardiovascular alterations on Earth (1g)

2.1.1 Cardio-circulatory response to posture changes

Postural changes elicit remarkable responses in terms of cardiovascular physiology [24, 43], especially according to the way the change of posture is achieved. Basic posture changes on Earth - from supine to seated or upright standing and *vice versa* - may be separated into passive posture changes (*e.g.* by means of a tilt table facility, performing what is usually known as head-up or head-down tilt test, respectively HUT and HDT), and active posture changes, that is by using the human musculature of legs, calves, abdomen etc. to stand up and sustain the new position. In addition, the mere change of posture triggers a number of specific, subsidiary mechanisms determining the overall physiological response. The duration and maintenance of a particular posture should also be considered. In the following paragraphs, the cardiovascular physiology of posture changes under Earth's gravity is summarized and discussed in detail.

Passive posture change

Passive changes of posture are usually performed by means of a tilt table facility, as illustrated in Figure 2.1. The subject is strapped to the tilt table or to the tilt bed in such a way that no active movement is permitted or required to change the body position. Therefore, the body musculature is not activated as the subject is tilted from one position to another (*e.g.*, from supine to upright standing) and the physiological response of the cardiovascular system is completely passive (*i.e.*, not influenced by extra-vascular compressive forces). HUT tests on the tilt table facility are often adopted in autonomic medicine [81] to study some autonomic disorders reported by subjects experiencing difficulties in sustaining the standing position.

Among these disorders, we recall orthostatic hypotension (OH), chronic orthostatic intolerance (COI), and unexplained syncope [36].

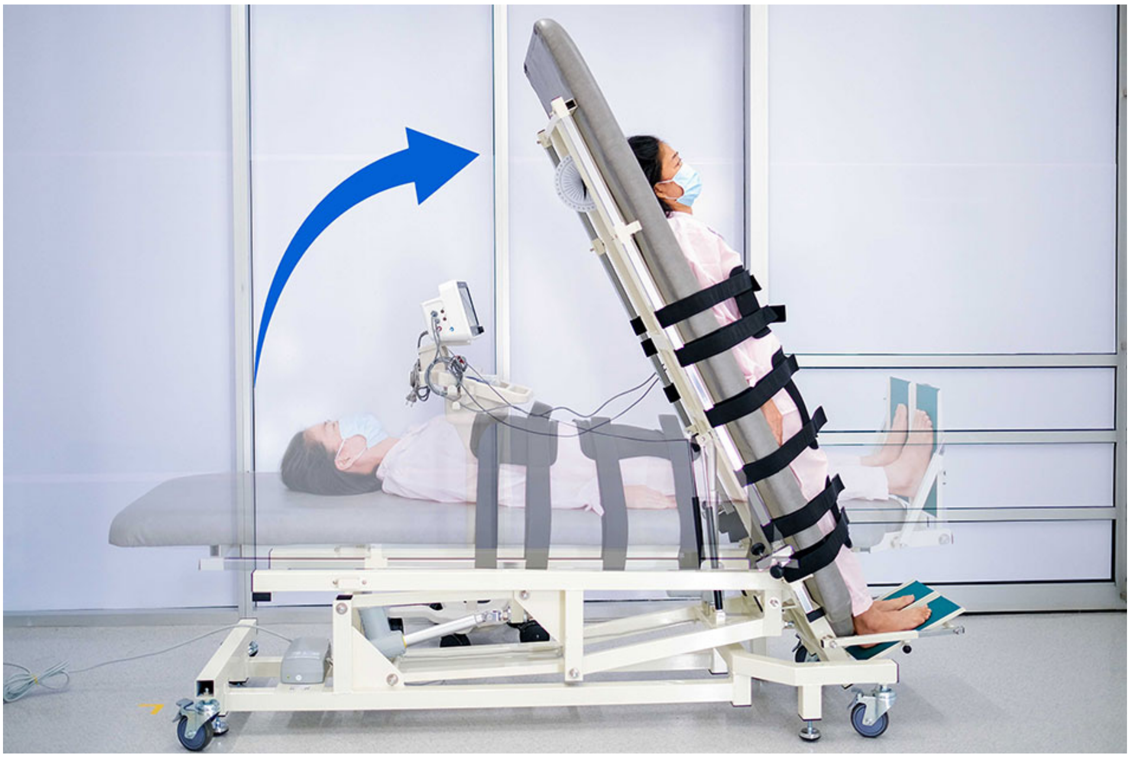

Figure 2.1: Tilt table bed facility to perform HUT and HDT experiments. Image taken from `https://www.fvhospital.com/`.

The first physiological reaction of the cardiovascular system to acute passive posture change from supine to standing is a progressive and massive blood volume migration - called blood shift - from the upper to the lower parts of the vasculature. That is, blood is transferred from the vascular pools of the thoracic (cardio-pulmonary) and abdominal regions [31, 155] to those of the pelvic, legs and calves (about 500 ml) [83, 257], as shown in Figure 2.2. This blood shift involves mostly the venous side of the circulation, being characterized by the highest compliance with respect to the arterial and microcirculatory districts [23]. According to several authors, the remarkable amount of blood accommodated in the lower extremities of the body during passive standing determines the so-called venous pooling [253, 83]. Therefore, the withdrawal of blood volume from the cardio-pulmonary and upper body compartments may result in a condition of central hypovolemia [96, 23] eventually leading to fainting, dizziness, loss of consciousness and other potentially severe orthostatic complications investigated by autonomic medicine [81, 36].

Beside blood volume shift, the second immediate hemodynamic response to change of posture is related to blood pressure. The main determinants of arterial and venous intravascular blood pressure are (i) the dynamic pressure generated by the heart acting as a pump on a closed fluid system (*i.e.*, the CVS); (ii) the visco-elastic component linked to the local mechanical properties and behavior of the vessels wall; and (iii) the hydrostatic pressure component [23]. Among these components, the hydrostatic pressure is the most affected by body position changes, according to Stevino's law [43, 92, 278, 73] (see Figure 2.2), at least as long as blood vessels can be treated as a unique fluid system with a given anatomical extension aligned with the gravity vector $\boldsymbol{g}$ (in fact, this is not always the case for the venous system due to venous collapse and venous valves closure [253, 96, 92]). Concerning components (i) - dynamic - and (ii) - elastic - of blood pressure, it is not clear and not trivial at all what their role and contribution are in shaping the hemodynamic response to posture changes, to date. By comparing Figures 2.2a and 2.2b it is evident how blood pressure changes depending on the considered body region (from head to feet), going from supine to standing position. Both arterial and venous mean pressure tend to remain constant close to the heart level. This fact sets the base for the definition of a hydrostatic indifference point (HIP), *i.e.*, the point along the longitudinal body axis where blood pressure remains constant regardless of the body tilting position [96], with arterial and venous HIPs generally not coinciding. While both arterial and venous mean pressure increase by some $\sim$90 mmHg proceeding from central to feet level at passive standing posture, they decrease by about $\sim$45 mmHg towards the head, with venous pressure levels approaching negative values in the veins at the apex of the cranium.

The steady-state (acute) responses of the most common hemodynamic parameters following various degrees of tilt (30°, 70° and 90°) from supine are reported in Tables 2.1a-2.1b. As evidenced by Tables 2.1a-2.1b, central mean arterial pressure (MAP) is maintained to almost constant levels with progressive increasing tilt angle, from supine to upright, although in some cases it might be found as slightly increased compared to supine values due to the more pronounced increase in central diastolic arterial pressure (DAP) revealed at all tilt angles. By contrast, central systolic arterial pressure (SAP) does not show specific trends of variation upon HUT. Such arterial pressure changes revealed at steady-state (typically within few minutes of tilt to the desired position) are approached after an initial transient dynamics, with all pressure dropping following the sudden blood volume downshift associated with assumption of the tilted position. All pressure levels eventually recover to the reported steady-state values thank to the prompt intervention of the arterial and venous pressure control mechanisms (arterial baroreflex and cardiopulmonary reflex), promoting peripheral vasoconstriction (augmented total peripheral resistance, TPR) and accelerated heart beating (augmented heart rate, HR, ranges reported in Tables 2.1a-2.1b) to counteract central hypovolemia and hypotension [73, 45, 141, 281, 93]. Brachial MAP mirrors the same response of central MAP, whereas cerebral and legs MAP align with mean arterial pressure

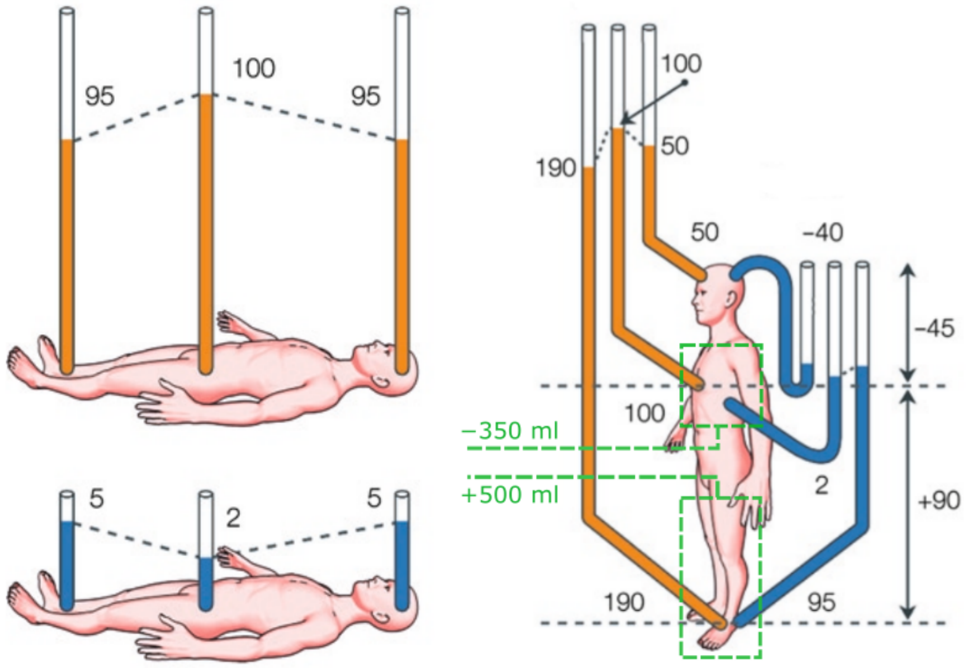

(a) Supine (b) Standing

Figure 2.2: Pressure distributions (black numbers, mmHg units) in a supine (a) and standing (b) subject. Red columns indicate arterial pressure whereas blue columns indicate venous pressure. Green numbers denote the total blood volume being transferred out (minus sign) or to (plus sign) the corresponding body region (thorax and legs) when passing from supine to upright position. Image taken and modified from [278].

levels reported in Figure 2.2.

As an additional consequence of the downward blood shift, also cardiac filling and thus cardiac end-diastolic volume are remarkably discouraged after tilting to the upright position. This in turn translates into a reduced central venous pressure (CVP) [248], taken as corresponding to right atrial pressure, that is responsible for right heart filling (cardiac preload) during the cardiac cycle. Through the Frank-Starling mechanism [106, 278], the reduction of cardiac preload causes a subsequent reduction of left ventricle stroke volume (SV). This results in a consequent drop of the cardiac output (CO) pumped by the heart into the aorta (after a first initial rise due to the augmented HR driven by the baroreflex and cardio-pulmonary reflex response), further exacerbated in concert with peripheral vasoconstriction (increasing cardiac afterload). As a result, the total circulating blood volume is diminished and venous return is considerably reduced after assumption of the passive tilted posture. Despite the overall reduction of circulating blood volume (proportional to CO), sufficient blood flow and thus life-essential nutrients supply is guaranteed within adequate levels throughout all the body districts [23]. Furthermore, while most regions show blood flow rate reductions linked to the CO drop registered at central level (renal, spanchnic), specific regions exhibit a certain degree of blood flow control thank to their peculiar autoregulation mechanisms. For instance, cerebral autoregulation ensures a suitable level of brain perfusion within a wide range of perfusion pressure and stimuli (such as during posture changes) [23, 156, 34, 78, 187, 172], similarly to myocardial blood flow regulation [23, 82, 268] (although the coronary perfusion specifically under HUT has not been thoroughly explored yet).

As anticipated, a number of autonomic responses are activated to counteract the abrupt central pressure drop following blood shift during upright tilt. On top of the chronotropic and vasomotor control on HR and TPR as efferent organs, respectively, acting on faster time scales, the short-term control mechanisms are also able to govern the cardiac inotropic state (through control of the contractility of both cardiac ventricles, Tables 2.1a-2.1b) and venous tone [48]. In this context, the degree of autonomic response and effectiveness dictated by the efficient control of the efferent organs and maintenance of the system homeostasis, appears to vary widely among individuals [249]. A first classifications (clustering) into phenotypes has been proposed in [249], based upon the extent of TPR and CO response of the subjects involved in the study to acute passive tilt (Figure 2.3a). The clustering has identified three main phenotypes denominated as 'constrictor', 'intermediate' and 'sustainers', going from the subjects showing the highest rise in TPR and CO drop, to those reporting the weakest response. Interestingly, the study highlighted that sustainers were the group characterized by the highest values of pulse wave velocity (PWV, an indicator of arterial stiffness, and thus often associated with hypertension [124, 214]), while intermediates and constrictors showed progressively lower values of PWV. Thus, according to the authors, the degree of the autonomic and hemodynamic response to upright posture changes is associated with arterial stiffness and thus, in turn, with the level of cardiovascular risk.

PWV is not the only parameter of interest when it comes to grasp the wave dynamics of the arterial tree, especially when changes of posture are considered. The exact mechanisms underlying propagation and reflection of traveling waves have not been fully understood so far, and the influence of orthostatic stress on the cardiovascular wave dynamics has still to be fully explored. A few seminal studies have revealed how PWV seems to be increased with HUT from supine [102, 101, 200, 287], confirming the overall stiffening of the arterial tree. Yet, central level augmentation index (AI) and reflection magnitude (RM) values have been found to decrease [102, 101, 14, 13] indicating a lower or weaker amount of wave reflected from the periphery to central regions. Further elucidation on these aspects needs to be addressed.

The same tilting table facility displayed in Figure 2.1 is used also to test the

Table 2.1a: Literature data (≊: no significant variation, - : no data available) for supine, HUT 30°, 70° and 90°. Asterisked superscripts *: transient information available, **: peripheral measure, not catheterized, ***: active standing, ****: subject seated, *****: typically surrogating the upright posture. Table taken from [68].

Variable	Supine	HUT 30°
Mean central arterial pressure [mmHg]	75÷110, [23], [96], [23], [141]	≊, [267]**,[256]*,**
Systolic central arterial pressure [mmHg]	100÷150, [23], [23], [141], [290]**	-1%÷-5%, [267]**
Diastolic central arterial pressure [mmHg]	60÷90, [23], [141], [290]**	+1%÷+7%, [267]**
Mean brachial arterial pressure [mmHg]	66÷105, [108], [45], [155]	-5%÷+23%, [292](45°)**, [45]*,**
Mean cerebral arterial pressure [mmHg]	75÷110, [23],[96]	-
Mean legs arterial pressure [mmHg]	75÷110, [23], [96]	110 (dia)÷175 (sys), [23],[246](35°)
Central venous pressure (right atrium) [mmHg]	0÷8, [253], [248],[23], [27]	-27%÷-36%, [248] (from transitory), [23]
Legs venous pressure [mmHg]	8÷10, [253],[142], [184]	27÷33, [246](35°)
Cerebral venous pressure [mmHg]	7÷10, [253]	-
Intraocular pressure [mmHg]	10.7÷21.6, [189],[4],[240], [150],[165],[125]	17.3÷18.5, [189]
Intracranial pressure [mmHg]	8.9÷17, [98],[125]**,[128],[150]**,[138]	-0.6÷4.0, [98],[138]
Heart rate [bpm]	69÷77, [108], [292], [23], [23], [45], [141], [155], [93]	≊÷+13%, [196], [256]*, [292](45°), [267], [45]*
Stroke volume [ml]	59÷119, [23], [23], [292], [156], [45], [141], [155], [27]	-13%÷-25%, [256]*, [292](45°), [156], [45]*
Cardiac output [l/min]	3.9÷8.7, [23], [23], [292], [108], [156], [141], [155], [27]	-13%÷-17%, [256]*, [292](45°), [45], [156]
Cardio-pulmonary blood volume [ml]	800÷1170, [131], [141], [23]	-90÷-150, [246](35°)
Lower limbs blood volume [ml] (% of total blood volume)	680÷1197, [109], [11]	+4%÷+5%, [246](35°)
Cerebral blood flow [ml/s]	9.5÷15, [23], [104]	≊, [156]*
Total peripheral resistance [mmHg s/ml]	0.79÷1.32, [23], [45], [155], [156], [141],[93]	+17%÷+28%, [256]*, [156], [45]*
Left max cardiac elastance [mmHg/ml]	1.8÷3.6, [235]	up to +25%, [215]
Right max cardiac elastance [mmHg/ml]	0.5÷2.1, [53]	up to +25%, [215]

hemodynamic response to HDT. It has been observed that tilting subjects head-down to a given position elicits almost the exact symmetric response mechanisms as during tilt-up for a number of hemodynamic parameters (HR, DAP, SV, CO, TPR, rate pressure product, RPP [23, 281, 279], and CVP [263]). The primary

Table 2.1b: (continue Table 2.1a) literature data (≊: no significant variation, -: no data available) for supine, HUT 30°, 70° and 90°. Asterisked superscripts *: transient information available, **: peripheral measure, not catheterized, ***: active standing, ****: subject seated, *****: typically surrogating the upright posture. Table taken from [68].

Variable	**HUT 70°,*******	**HUT 90°**
Mean central arterial pressure [mmHg]	≊, [263], [141](50°), [267](60°)**, [249](60°)**, [176]**	≊, [43]****, [241]*,***, [267](80°)**, [23]****, [268]***
Systolic central arterial pressure [mmHg]	105÷139, [241]*, [290]*,**, [267](60°)**, [249](60°)**, [141](50°)	97÷148, [43]****, [267](80°)**, [23]****, [268]***
Diastolic central arterial pressure [mmHg]	70÷88, [241]*, [290]*,**, [267](60°)**, [249](60°)**, [141](50°)	70÷109, [43]****, [267](80°)**, [23]****, [268]***
Mean brachial arterial pressure [mmHg]	-3%÷+33%, [292](60°,75°)**, [45](55°)*,**, [155](60°), [239](65°)**	97÷125, [242]*,***, [292]**, [268]***, [252]**,***, [61]**,***
Mean cerebral arterial pressure [mmHg]	-	65÷90, [96],[43]****, [61]***
Mean legs arterial pressure [mmHg]	150 (dia)÷200 (sys), [23](75°)	140÷230, [146],[9]
Central venous pressure (right atrium) [mmHg]	0.4÷6.2, [23](75°), [263],[141](50°),[155](60°), [248](80°)	0÷2 (-50%÷-100%), [241]****
Legs venous pressure [mmHg]	75÷100 (feet), [23](75°)	40÷100, [23],[96]
Cerebral venous pressure [mmHg]	-	-10÷0, [23],[96]
Intraocular pressure [mmHg]	13.3÷13.9, [165] (50°),[35](50°)	9.5÷16.5, [189],[4]****,[240]****,[165],[125]****
Intracranial pressure [mmHg]	-4.4÷2.6, [98],[138]	-2÷5 [125]**,****, [128],[294]
Heart rate [bpm]	+7%÷+34%, [257]*, [242]*, [263], [241]*, [155](60°), [45](55°)*, [239](65°), [141](50°)	+15%÷+45%, [23]****, [242]*,***, [43], [292], [61]***, [252]***, [241]***
Stroke volume [ml]	-20%÷+40%, [257]*, [242]*, [263], [241]*, [155](60°), [45](55°)*, [141](50°)	-25%÷-50%, [253], [292], [242]*,***, [23]****, [43]****, [61]***, [252]***, [241]*,***
Cardiac output [l/min]	-4%÷-21%, [257]*, [242], [155](60°), [263], [241]*, [141](50°), [249](60°)	-15%÷-40%, [253], [292], [242]*,***, [23]****, [43]****, [61]***, [252]***, [241]*,***
Cardio-pulmonary blood volume [ml]	-78÷-360, [141](50°)	-200÷-500 (-2%÷-9%), [43]****, [241]*,***
Lower limbs blood volume [ml] (% of total blood volume)	+6%÷+9%, [257]*, [11](60°)	+300÷+800 (+5%÷+15%), [257], [23],[83]*,[9]
Cerebral blood flow [ml/s]	-2.6%÷-9.4%, [34]	up to -10%÷-20%, [43]****,[241]
Total peripheral resistance [mmHg s/ml]	+3%÷+44%, [257], [242]*, [141](50°), [61], [155](60°),[241]*, [45](55°)*, [249](60°)	+20%÷+60%, [43]****, [61]***, [242]*,***, [252]***, [241]*,***
Left max cardiac elastance [mmHg/ml]	up to +25%, [215]	up to +25%, [215]
Right max cardiac elastance [mmHg/ml]	up to +25%, [215]	up to +25%, [215]

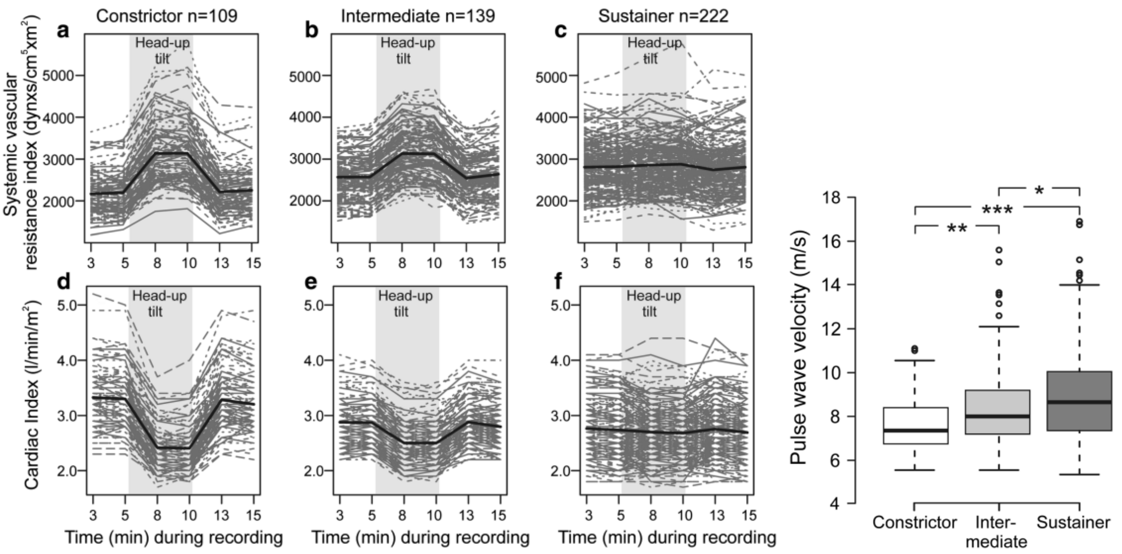

(a) (b)

Figure 2.3: Classification (clustering) of individuals phenotypes according to the degree of autonomic response (assessed on the basis of TPR and CO). (a): systemic vascular resistance (SVR, analogue to TPR) and cardiac index (CI, that is CO normalized by subjects' body surface area) response to HUT; (b): pulse wave velocity (PWV) response to HUT (asterisks denote statistical significance). Images taken from [249].

driver is again the initial blood shift - directed headwards, from feet to the central-thoracic area -, causing an increased cardiac filling (preload) and the subsequent promotion of a bradycardic and peripheral vasodilation response mediated by short-term controls. Due to blood accumulation in the cardio-pulmonary district, also pulmonary arterial pressure results as increased during HDT [263]. The symmetric behavior of HDT with respect to corresponding HUT positions holds at least within -75°, beyond which blood volume accumulation and pooling in the cephalic region starts to decrease cardiac filling, and, thus, also blood pumping from the heart in a way similar to the upright position [43]. However, adequate levels of brain perfusion in terms of cerebral blood flow are still guaranteed by cerebral autoregulation during tilt down [42].

In light of the profound hemodynamic changes following posture variations seen above, and given the consequent mechanisms activated to sustain and control the organism homeostasis discussed so far, the fact that human beings spend a considerable amount of their day-life in the erect position may sound poorly efficient and extremely energy consuming [43]. However, it should be considered that, in fact, the net increase in energy expenditure linked to assumption and sustaining of the upright position comes with a limited increase of oxygen consumption of only

7% [73]. Further investigations need to be conducted to confirm these data, especially when passive vs. active standing or sitting are compared, and when long-term assumption of the erect posture is the case. The latter situations will be covered more in detail in the following paragraphs.

Active change of posture

Beside passive posture changes achieved by means of the tilt table facility, active posture changes elicit a set of similar hemodynamic responses that should be considered in detail. Active standing is by far considered as men's normal or physiological state [43, 73], and the maintenance of homeostasis should therefore be guaranteed also in this position without excessive physiological effort. The active standing position is reached when a subject stands from sitting or supine without the need for external assistance or intervention (such as, for instance, the tilt bed), but only using their muscle strength of the legs and abdomen.

The first reaction observed after active assumption of the standing position is a sudden and marked drop of MAP accompanied by a fast rise of HR (both more pronounced than after passive upright tilting, as displayed in Figure 2.4) [242, 243]. The same holds also for SV and CO (Figure 2.4), with this latter usually showing a first initial positive peak following the rapid HR increase after stand up. The reason for these exacerbated responses with respect to passive tilt is mostly the peripheral (especially lower limbs) vasodilation promoted in order to recruit more blood towards the muscle districts involved in performing the task. That is, abdominal, calves and thighs muscles needs to receive more oxygenated blood to correctly sustain the effort [252, 61]. In light of this, active standing can thus be considered a sort of exercise condition for which peripheral vasodilation is required, as opposed to vasoconstriction promptly promoted during passive upright tilting. After first activation to reach the erect position, TPR is raised also after active standing to counteract blood pooling in the legs.

Both during standing and after assuming the upright position, if muscles continue to be activated such as during walking, cycling or other kinds of exercise, the contraction of muscle fibers against blood vessels (mostly veins) acts as a pumping effect facilitating blood return (*i.e.*, venous return) to the heart [73]. Venous pumping performed by legs muscles operates in coordination with venous valves opening and closure so that no reverse venous flow is allowed during each vessel compression. Figure 2.5 illustrates the mechanism of venous pumping through calf muscle contraction: when the calf muscle is relaxed (left image), the lower valve opens letting blood advance upward; afterwards, as the calf contracts (right image), pressure rises in the compressed venous tract closing the lower venous valve meanwhile opening the successive upper one, letting blood escape from above towards the heart [142, 195]. Furthermore, through muscle compression and therefore venous

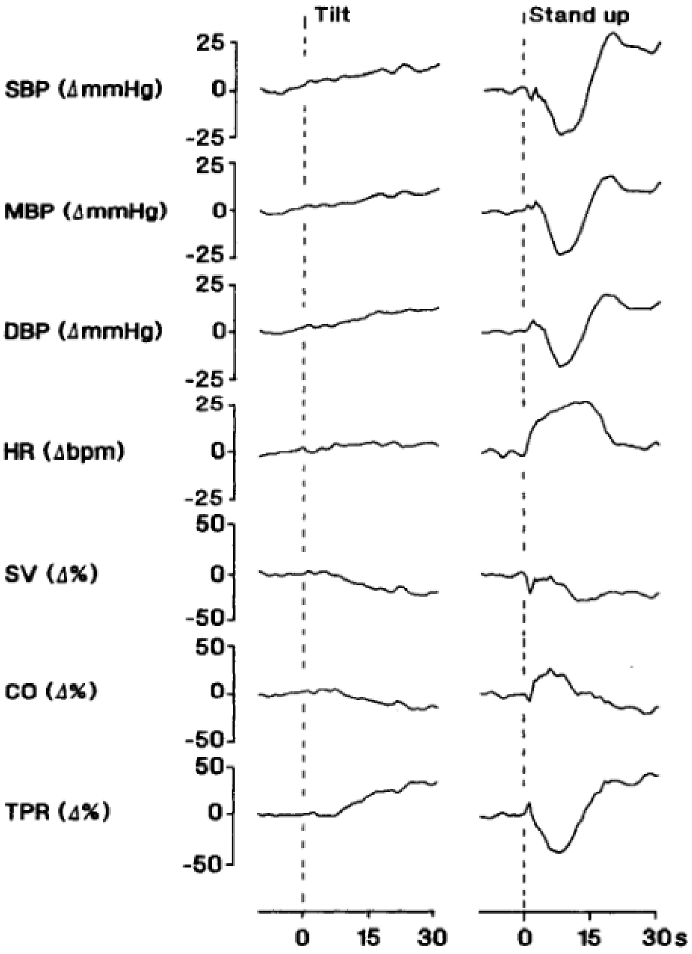

Figure 2.4: Passive tilt (70° HUT, on the left) vs. active standing (on the right) comparison for central hemodynamic parameters. Image taken from [242].

valves repeated closure, venous pressure in the veins of the legs is dramatically reduced since the hydrostatic column of blood is interrupted at multiple points. This aspect may likely be of help in preventing from valves incompetency occurrence, varicose veins and edema [92, 142, 72].

Specific physiological mechanisms in response to posture change

Posture changes from supine to head-up or head-down position imply a number of additional, concurrent physiological mechanisms inextricably linked to the cardiovascular functioning and that have thus an impact on the final hemodynamic response. In this paragraph, we will discuss the role of (i) intrathoracic pressure, (ii) veins collapsibility, (iii) venous valves, (iv) cerebrospinal fluid and intracranial

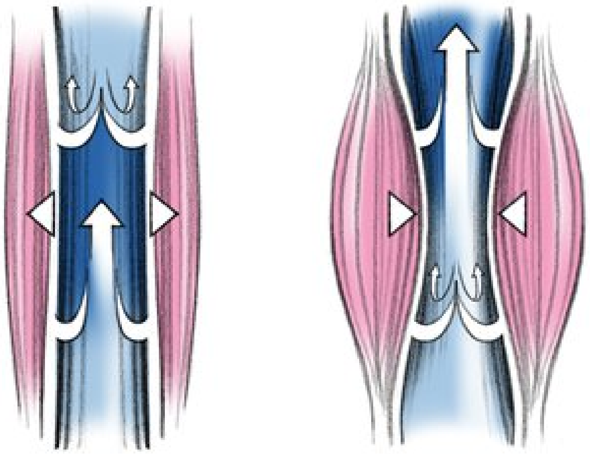

Figure 2.5: Calf muscle contraction and venous pumping. Image taken from [255].

pressure, and (v) intraocular pressure in contributing to shape the overall hemodynamic response to posture changes.

i. *Intrathoracic pressure.* Intrathoracic pressure (ITP) is the level of pressure inside the thoracic cavity, and it is often considered to be an analogue of intrapleural pressure, the pressure within the pleural cavity, where both the heart and lungs are located [92]. Therefore, ITP is considered to be the pressure surrounding all cardiac chambers, and influencing the behavior of myocardial walls in concert with intrachamber pressures. For this reason, ITP and cardiovascular functioning are tightly linked and understanding of their mutual interaction in combination with changes of posture is crucial to fully grasp the nature of the observed hemodynamic response [114, 288, 265, 199, 52, 30].

The least invasive way to measure ITP is by adopting esophageal pressure as its best surrogate [152, 186, 208]. ITP is typically below atmospheric pressure, to maintain the lungs always distended and inflated towards the thoracic cage. ITP ranges normally between -2 mmHg and -6 mmHg [92, 114, 289] at supine posture, relatively to the external atmospheric pressure. Furthermore, under normal respiration, ITP fluctuates between its maximum and minimum value as the thoracic cavity expands (ITP decreases) or contracts (ITP rises again). The ITP variation influences cardiac pressure inside the cardiac chambers, with intrachamber pressure values fluctuating at breathing rhythm. Indeed, during inspiration, as the thoracic cavity expands, ITP falls down and so do all cardiac intrachamber pressures. As a consequence, the pressure gradient driving venous return is augmented, venous return is promoted and therefore right atrial filling is also enhanced, increasing cardiac preload and, in turn, through the Frank-Starling mechanism, also cardiac ejection (SV and CO) [114, 288, 208, 265, 52]. The contrary occurs during the following expiration phase, with ITP rising again, together with right atrial pressure and diminished venous return, cardiac preload and blood pumping from the heart (*e.g.*, as during Valsalva's maneuver [199]).

Since the pleural cavity is basically composed of a fluid system, the action of gravity pull has noticeable effects on the ITP distribution within such cavity. Indeed, simply changing posture from supine to head-up, seated or standing induces a vertical gradient on ITP such that the organs suspended at the apex of the thoracic cavity experience lower level of ITP than at the bottom [289]. This is in fact the case for the right atrium. In addition, posture change from supine to standing causes a downward movement of the diaphragm at the base of the thoracic cavity being pulled down under its own weight. This effect produces an additional expansion of the intrapleural cavity and, therefore, a further decrease of ITP [192]. For all these reasons, while on the one hand assumption of the standing posture discourages venous return by inducing blood pooling in the lower extremities of the body and thus reducing cardiac preload, on the other hand the posture-induced ITP reduction is analogous to a deep inspiration, decreasing right atrial pressure and so partly contributing to enhance cardiac filling and venous return.

ii. *Veins collapsibility.* As veins are the low-pressure side of the circulation, venous blood flow occurs at a pressure little higher than the extra-vascular pressure (typically the atmospheric pressure). For this reason, and considering also the higher deformability of venous vessels compared to arteries due to their different walls mechanical properties, venous collapse may arise whenever blood pressure in veins should fall below the external pressure (*i.e.*, the atmospheric pressure or the surrounding tissue pressure) [278, 253]. The wall mechanics and fluid dynamics of deformable and collapsible tubes are peculiar and, as such, have been investigated for decades [56, 212, 236]. However, venous collapse plays a crucial role especially when it comes to change of posture. While all veins are usually in their distended state in a supine subject, HUT causes blood pressure to drop in vessels above heart level (Figure 2.6a), such as for the jugular veins, which are therefore subject to negative transmural pressure (relatively to the external pressure) even at modest tilt angles and, thus, tend to collapse [92, 253, 96, 279, 98, 97, 120]. Figure 2.6b shows also other points where veins might collapse due to an external higher pressure, although below heart level, such as for abdominal veins compressed by the intra-abdominal pressure [92]. The same applies to the veins of the legs during HDT, with venous collapse occurring when intravascular blood pressure in the legs veins falls below the external pressure as the subject's legs are raised above the level of the heart [24].

Venous collapse is crucial to the understanding of the cardiovascular physiology of posture changes. Stevino's law for hydrostatic pressure is no longer applicable to collapsed vessels, as the fluid column is interrupted subdividing the circulation into distinct branches [253, 96, 24]. Therefore, pressure inside and along a collapsed vessel stays constant and equal to the extra-vascular surrounding pressure (*i.e.*, zero relative pressure, Figure 2.6a). The veins inside the skull are in a particular non-collapsible state as they are attached to the cranial box keeping their shape almost unaltered even at negative transmural pressure [92, 24]. Therefore, negative venous blood pressure may occur in the veins of the head, according to their elevation with respect to the last point of collapse underneath the skull [92, 24].

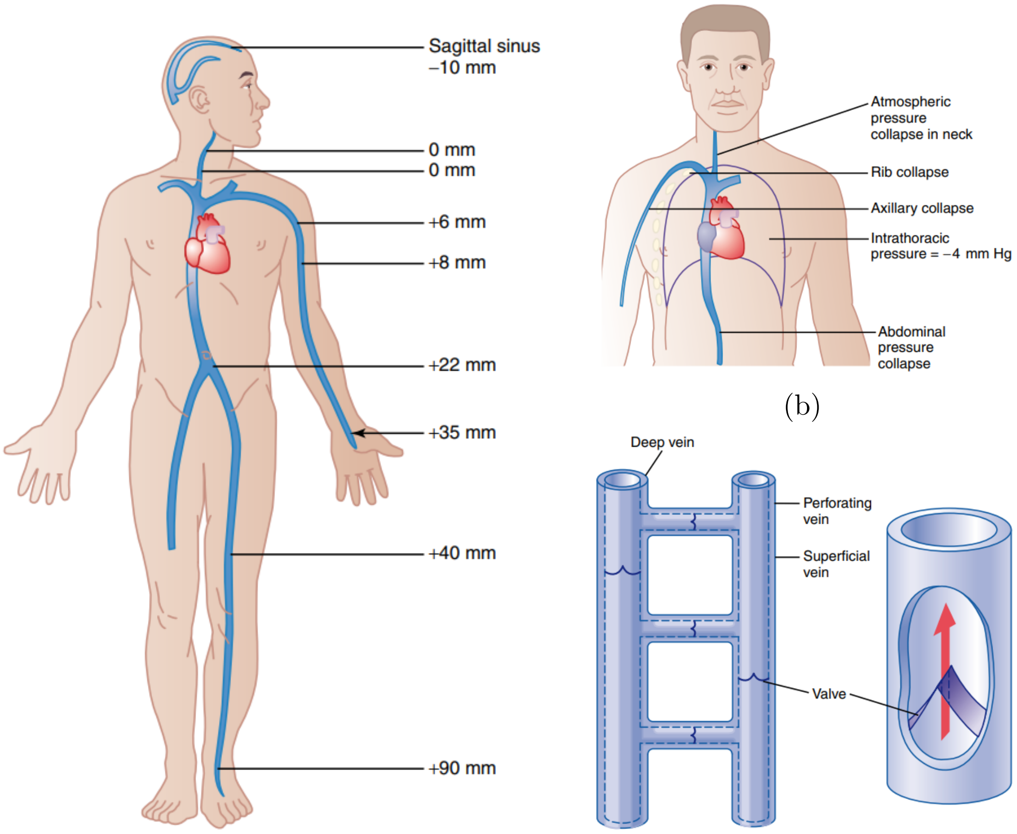

(a) (b) (c)

Figure 2.6: Mechanisms of veins functioning: (a) venous system pressure at upright posture, (b) venous collapse points, (c) venous valves. Images taken from [92].

iii. *Venous valves.* Veins have valves distributed all over the venous circulation to prevent from reverse flow to take place [92, 142, 72]. The mechanisms and functioning of venous valves between deep and perforating veins of the legs is sketched in Figure 2.6c: each valve operates such that unidirectional flow only is allowed, by opening their leaflets under favorable pressure gradient (leading to the desired flow direction), whereas by closing rapidly whenever a negative (*i.e.*, giving rise to backward flow) pressure gradient is encountered. Venous valves become fundamental when it comes to posture changes, as during assumption of the standing posture blood is shifted downward and pools in the feet due to the action of gravity. As such, closure of venous valve obstacles blood backflow from the upper venous districts to the veins of the legs, letting thus blood accumulate in the lower extremities only through arteries.

In addition, complete closure of venous valves interrupts the hydrostatic column of blood, helping thus reduce blood pressure in the dependent vasculature [253, 195]. Venous valves often operates in combination with muscle activation enabling venous pump: by altering the venous intravascular pressure with compression and release of muscle fibers against the veins wall, blood can be pumped in the desired direction favoring venous return to the heart [195] (refer to the next section on active standing for more detail on muscle pumping action). Incompetency or disfunctioning of venous valves leads therefore to abnormal and prolonged elevated venous pressure in the dependent vasculature. These problems often arise in subjects associated with long periods of sitting, standing still or prolonged immobility. Elevated venous pressure translates into excessive stretching and deformation of veins cross-section area, leading to further incomplete closure and incompetency of venous valves and failure of venous pump, setting the base for varicose veins development and edema formation [92, 142, 72].

iv. *Cerebrospinal fluid and intracranial pressure.* The cranial box contains the brain which is suspended in a state of buoyancy within the cranial cavity, immersed in the cerebrospinal fluid (CSF) [92]. This fluid media communicates directly with the brain walls and vessels, and extends along the spinal cord forming a unique fluid system. CSF pressure is referred to as intracranial pressure, (ICP), and is regulated by specific rates of formation and reabsorption of the CSF [47]. While the rate of formation of CSF secreted at the four cerebral ventricles is usually unchanged, CSF rate of reabsorption taking place at the arachnoidal villi is responsible for ICP regulation under various conditions [92, 221]. The arachnoidal villi protrude into the dural venous sinuses and thus communicate directly with dural venous pressure. For this reason, CSF reabsorption and, thus, ICP depends directly on the venous pressure at dural sinuses.

As such, ICP pressure may vary largely due to variation of dural venous pressure, such as during posture changes [98, 97, 206]. In fact, ICP is strongly affected by body posture, with the CSF system behaving like any other fluid system reflecting all hydrostatic pressure changes following change of the body position. This effect translates into almost symmetric posture-driven ICP changes with respect to cerebral venous pressure changes, contributing to keeping nearly constant levels of cerebral venous transmural pressure at all body positions[24]. Furthermore, it is also evident how venous collapse impacts on ICP by affecting venous pressure levels at the dural sinuses. It is therefore widely believed that jugular veins collapse helps regulate ICP during posture changes [98, 97, 206, 79], playing a crucial role when it comes to the interplay between ICP and the surrounding elements such as cerebral veins and the ocular bulbs.

Direct invasive measures of ICP through catheterized inspection are diffucult, harmful and thus hard to achieve. Several non-invasive solutions are available nowadays exploiting trans-cranial doppler, otic methods or other modeling approaches [297, 62]. Normally, in a supine subject, physiological levels of ICP range between 10 mmHg and 15 mmHg [92, 221]. ICP was then measured at various degree of HUT and HDT, reaching values as low as -4/-2 mmHg at 70°/90° HUT (Tables 2.1a-2.1b) [98, 97, 206, 125, 128, 294], whereas as high as 15 mmHg at 20° HDT [150].

v. *Intraocular pressure.* The eye is an additional fluid system of relevant importance because of its interaction with the CVS and the cerebrovascular circulation. Indeed, the eye is filled with intraocular fluid at a sufficiently high pressure such to preserve its spherical shape. The pressure of the intraocular fluid is referred to as intraocular pressure (IOP), and depends on several factors such as blood arterial (perfusion) and venous (episcleral) pressure reaching the eyeball, the pressure in the retrobulbar space (that is, ICP), and the regulatory mechanisms of production (inflow) and drainage (outflow) of the acqueous humor [92, 198]. An illustration of the ocular system and of the main contributors to IOP dynamics is provided in Figure 2.7.

Since it relies on blood arterial and venous pressure, posture-induced variations in the systemic circulation influence also IOP variation, although to a modest extent. That is, increase and descrease in ocular arterial perfusion pressure and episcleral venous pressure revealed during body tilting reflect onto IOP changing the pressure inside the eyeball, at least over a short-term scale [189, 198, 4, 165]. Similarly, also ICP in the retrobulbar subarachnoid space influences IOP variation during posture changes by communicating with the eyeball through the lamina cribrosa [189, 157].

The physiological range of IOP for a supine subject at rest is usually between 12 and 20 mmHg [92], but it fall down to ∼10 mmHg upon 70°/90° HUT (Tables 2.1a-2.1b) [189, 4, 240, 165, 125] or rise up to ∼30 mmHg during 90° HDT [150].

Long-term orthostatic stress

In spite of the remarkable acute posture-driven changes discussed in the previous sections following upright tilting, only humans are capable of maintaining the erect posture for prolonged period. Human life is conducted in the upright posture for most of the time during daylight, with no excessive or harmful conditions and at affordable energy expenditure. This is made possible thanks to the first acute and secondary long-term adaptations of the CVS to the erect posture. In fact, prolonged orthostatic stress triggers a number of additional longer scale effects and mechanisms that profoundly alter the final hemodynamic picture [241, 73].

To sustain prolonged orthostatic stress, proper level of cerebral blood flow is essential (promptly achieved and maintained by means of cerebral autoregulation [156]), as well as venous pumping from the lower extremities operated by

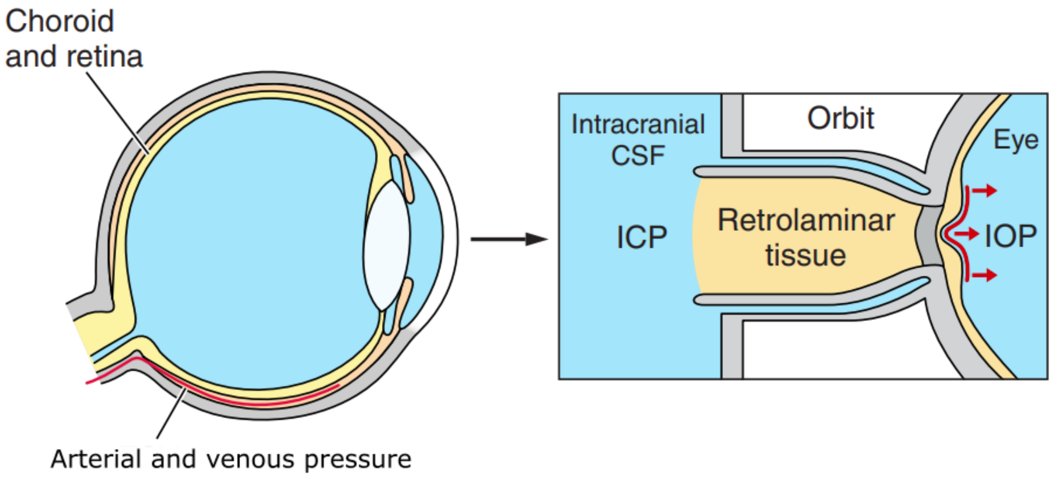

Figure 2.7: Illustration of the ocular system and related pressures players contributing in shaping the IOP dynamics (ICP intracranial pressure, CSF cerebrospinal fluid). Image taken and modified from [294].

Table 2.2: Central hemodynamic parameters time course during various instants of passive HUT to 70° ($pulMAP$ is pulmonary MAP, TA is thoracic admittance). Taken from [263].

Parameter	**Supine start**	**HUT 20 min**	**HUT 50 min**	**Supine end**
HR [BPM]	53 ± 10	86 ± 18	92 ± 12	62 ± 17
MAP [mmHg]	93 ± 9	93 ± 10	91 ± 19	92 ± 17
CVP [mmHg]	3.6 ± 0.9	0.9 ± 1.4	0.9 ± 1.7	3.9 ± 1.4
$pulMAP$ [mmHg]	13.9 ± 2.7	9.3 ± 3.8	9 ± 3	14.3 ± 2.8
SV [ml]	112 ± 18	65 ± 25	48 ± 22	113 ± 22
CO [l/min]	6.4 ± 1.3	4.9 ± 0.6	4.4 ± 1.0	6.4 ± 1.0
TA [mS]	30.8 ± 7.1	26.7 ± 6.8	26.4 ± 6.7	28.7 ± 7.2

the combined action of venous valves and muscle contraction. In the absence of these mechanisms, such as during passive standing, blood pressure remains high in the dependent vasculature of the legs and feet, leading to excessively high transmural venous pressure and marked decrease of venous compliance [43]. As a consequence, blood filtration from the vessels to the surrounding interstitium becomes more pronounced, acting as a second, slower flow shift as opposed to the first, initial and faster downward fluid shift from the central-thoracic compartment [241, 83]. The interstitial fluid is eventually carried away and drained by the lymphatic system, leading to dramatic reduction of circulating blood volume and consequent conditions of hypovolemia [43, 43, 241, 83]. Prolonged orthostatic stress of 40 minutes or beyond, often leads to decreases in systolic and pulse pressure, decrease of cardiac filling and increasing incidence of dizziness, faint, collapse and vasovagal syncope [241, 43]. Table 2.2 taken from [263] reports the time course of some central hemodynamics parameters during HUT up to 50 minutes. Results shown in Table 2.2 highlight how much the CVS tends to a more and more inefficient and disadvantageous functioning upon passive standing, with progressively decreasing SV and CO as the circulating blood volume is reduced by fluid being transferred from the lower pools to the interstitial space. Besides, HR rises and strives to maintain a normal level of MAP. Increased HR accompanied by blood pressure drop are clear evidences of pre-syncopal conditions.

Additional hormonal regulation mechanisms come into play and act to regulate blood pressure over long time scales [73]. Some of these adjustments are schematized in Figure 2.8, involving mainly the total body water content by controlling renal activity and fluid excretion.

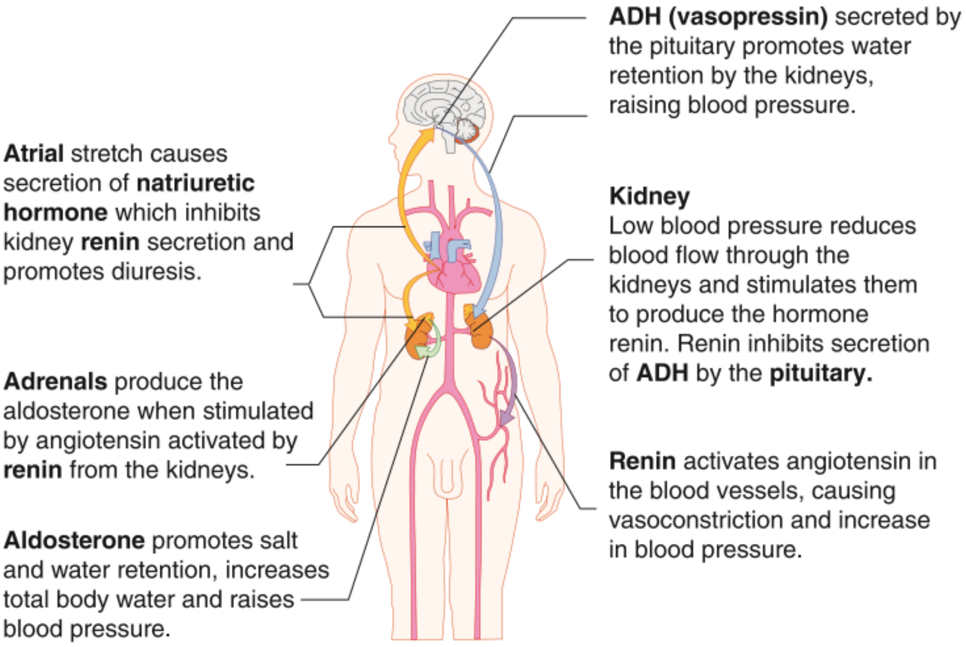

ADH (vasopressin) secreted by the pituitary promotes water retention by the kidneys, raising blood pressure.

Atrial stretch causes secretion of **natriuretic hormone** which inhibits kidney **renin** secretion and promotes diuresis.

Kidney
Low blood pressure reduces blood flow through the kidneys and stimulates them to produce the hormone renin. Renin inhibits secretion of **ADH** by the **pituitary.**

Adrenals produce the aldosterone when stimulated by angiotensin activated by **renin** from the kidneys.

Renin activates angiotensin in the blood vessels, causing vasoconstriction and increase in blood pressure.

Aldosterone promotes salt and water retention, increases total body water and raises blood pressure.

Figure 2.8: Mechanisms of hormonal regulation and other long-term adjustments to control the total body fluid content after prolonged orthostatic stress. Image taken from [73].

2.1.2 Different methods to trigger posture- and gravity-driven effects at 1g

Beside actual change of posture under normal Earth gravity (1g), a number of different alternatives are possible to simulate or reproduce similar cardiovascular alterations without directly changing the body position. Not all of these methods align completely with actual change of posture, although several hemodynamic responses are analogue and accurately mimic the cardiovascular acute response and mid-term adaptation. In the following overview, we will briefly cover (i) Lower Body Negative Pressure (LBNP), (ii) gravity (or anti-gravity) suits, (iii) centrifugation, and (iv) partial/total water immersion (WI) [60, 41, 91].

i. *Lower Body Negative Pressure.* The LBNP is a system conceptualized to create a region of partial vacuum (typically from ambient pressure up to -100 mmHg) inside a closed chamber. The most typical configurations consist of either a larger chamber hosting the lower limbs of the subject (Figure 2.9a), or a smaller, foldable device that can be worn directly by the subject. When the negative pressure is created inside the chamber, the legs of the subject are exposed to a reduced ambient pressure and all vessels of the lower body experience thus cross-section area distention and increased transmural pressure [84]. This condition is almost analogue to assumption of the standing posture, with blood recruiting from the upper to the lower body compartments, increase of veins size and pressure, and central hypovolemia. Beside legs volume increase, LBNP resembles passive standing also for CVP decrease, TPR increase, drop of heart filling, SV and CO, HR increase and stimulation of the autonomic response (baro and cardiopulmonary reflex) to maintain constant central MAP [23].

Subjects undergoing LBNP at a chamber pressure of -50/-60 mmHg in the supine position report that even their perception of posture is altered, as they have the feeling of standing upright [213, 260]. However, the pressure gradient along the body longitudinal gradient is discontinuous (pressure is stepwise constant, with a sudden increment entering the LBNP chamber), and pressure does not increase linearly as according to Stevino's law [23]. The usefulness of this device though, from a clinical point of view, is obviously that of triggering hemodynamic responses similar to free (passive) standing without moving the patient from the supine position, taking measurements directly from the clinical bed, furthermore excluding any sort of muscle activation and resulting venous pumping likely to influence the observations [23]. LBNP, because of its versatility, is used in the clinical context also to study the effects of hypovolemia during (simulated) orthostatic challenges [83].

ii. *Gravity suits.* Also abbreviated as G-suits, the gravity suits (or anti-gravity suits) are wearable devices used to counteract the force of gravity by increasing peripheral constriction of the dependent vasculature and preventing lower body blood pooling [41, 23]. For this reason, they are mostly used to resemble the cardiovascular functioning at supine posture rather than to simulate the upright position (as opposed to LBNP). An example of gravity suit design is illustrated in Figure 2.9b. To date, at least two different types of G-suits have been proposed:

- anti-gravity-suits type: these suits contain balloon-like pressure bladders in the pants, which can be inflated with air. When inflated, the bladder presses against the legs, forcing body fluid into the upper body [41];
- elastic straps type: composed of several elastic rubber bands used to wrap the lower body limbs tightly to achieve the same effect as the anti-gravity suit (tissue compression and blood flow promotion towards the upper body) [41]. Also known as penguin suits.

Therefore, both G-suit types work pretty much in the same way, inducing a first mechanical increase in TPR (in the lower limbs) by external compression to encourage venous return to the heart, and preventing venous pooling in the feet. Eventually, and only as a subsequent effect, cardiac filling is increased and thus SV and CO are raised [23], mimicking the cardiovascular response to a change of posture from standing to supine (with registered increase in arterial pressure and CVP [26]).

The gravity suits have been proved to be very useful also in clinical and medical applications [77, 23, 43], such as on seated neurosurgical patients [26] or to assess the different response elicited during immersion-induced ophthalmological changes [112].

iii. *Short-arm centrifugation.* Among the most intuitive ways to induce different accelerations on the human body one is short-arm human centrifugation. With the subject placed on a rotating platform in a seated or supine posture, as shown in Figure 2.10a, the centrifuge can provide different levels of centrifugal acceleration that therefore influence the motion of blood and of the other body fluids [41, 91]. The subject can be placed in a head-to-feet acceleration direction or in the opposite configuration, to reproduce different centrifugation scenarios. The first case is mostly used to re-create the gravity loading on a supine (rotating) subject, resembling partly the cardiovascular response to orthostatic stress [85]. Subjects undergoing this kind of experiment report experiences of altered graviception, such as if they were standing upright [260]. The effect of supine head-to-feet centrifugation indeed is similar to the gravity pulling at standing posture, with blood being shifted from central compartments to the lower limbs, decreased heart filling, SV and CO and the consequent autonomic responses already discussed for posture changes from supine to standing. However, the centrifugal acceleration is not uniform throughout the body as it depends on the distance from the center of rotation of the centrifuge, leaving therefore the possibility for many different centrifuge layouts and configurations.

Short-arm centrifugation is also used in combination with LBNP, to balance their mutual effects onto the CVS response and therefore to quantify and compare their effectiveness [260]. Further interesting usages of centrifugation involve the

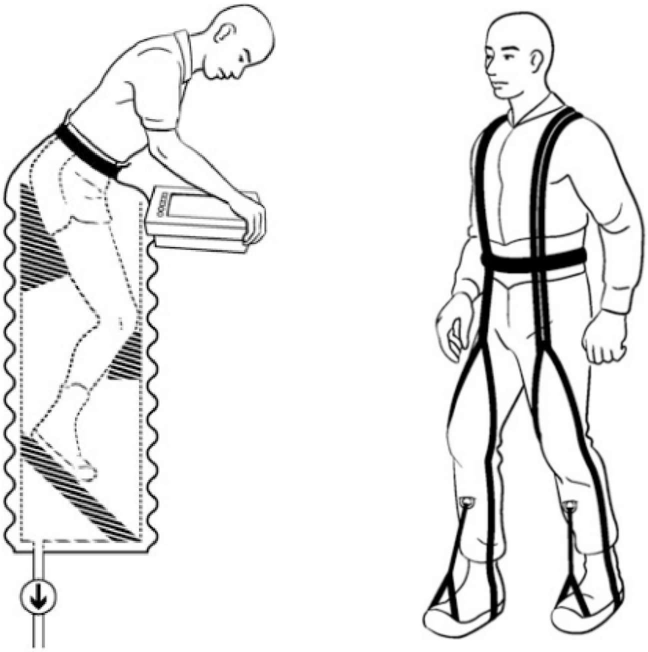

(a) (b)

Figure 2.9: Different methods to trigger posture and gravity-driven effects (I): (a) lower body negative pressure; (b) gravity suit. Images taken from [41].

study of cerebral hemodynamics and perfusion under different acceleration stress (gravity stress) and physiological g-tolerance assessment [121, 105].

iv. *(Dry) Water immersions.* Partial (head-out) and total (head-in) immersions are another technique to reproduce gravity and posture-like effects onto the circulation. The subject is immersed partially or completely in a water tank, while in a seated or standing posture, as shown in Figure 2.10b [91]. The observed response in terms of cardiovascular dynamics is similar to what is found in the supine posture, and thus reverses the observed hemodynamic changes registered at standing posture. Blood is shifted from the extremities to the central region, increasing cardiac filling, CVP, SV and CO, and reducing HR [23, 43, 91]. The mechanism is similar to the gravity suits, with external compression of peripheral tissues exerted by the hydrostatic pressure of water onto the whole body surface. This vessels squeezing increases peripheral constriction and induces blood to move towards the central-thoracic region.

WIs are usually adopted in combination with vasoconstriction cuffs/straps [112] or head-down tilt to compare the two hemodynamic responses in terms of blood shift to and out from the central regions, increase in cardiac parameters (SV and CO), and HR reduction [238, 269]. Indeed, WIs provokes heamodynamic changes that are somewhat more exacerbated than those observed in simple posture change from standing to supine. HDT to a little extent is thus more accurate as analogue of WIs [238].

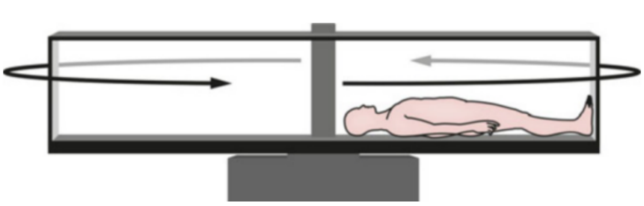

(a) (b)

Figure 2.10: Different methods to trigger posture and gravity-driven effects (II): (a) short-arm centrifugation; (b) water immersion. Images taken from [91].

2.2 Cardiovascular changes related to the space environment

Understanding of human physiology and human life adaptation to the space environment is of crucial importance for the success of future manned missions to the Moon and Mars. Therefore, the newborn disciplines of space medicine and bioastronautics have been created to investigate the causes and effects of the space environment and related hazards for the human systems, as well as to explore possible solutions to improve healthiness of astronauts undergoing long-term missions in space [41, 291, 21].

In this section, we will first present the current knowledge of cardiovascular responses and coping to human spaceflight, from the early access to microgravity to long-term adaptation, covering the available literature of short and long duration missions onboard of the ISS and other related studies (*e.g.*, Skylab missions, etc.). Secondly, we will review the most diffused ground analogues of human spaceflight used as alternatives to conduct cardiovascular observations and measurements without directly accessing the space environment.

2.2.1 Short and long duration spaceflight

A huge amount of research studies and experiments have been carried out in space over recent years. Concerning the cardiovascular system, the observed responses and results evidenced in space subdivides into short-term changes (from immediate response to a week in space) and long-term changes (from a week to several months). Following this subdivision, the present section will present the most important hemodynamic changes and eventual adaptation to the 0g environment, with respect to 1g conditions on Earth [171, 169, 170, 41, 91].

Initial access to microgravity

Entering weightlessness - or free falling (0g) - induces a number of cardiovascular alterations that ranges from the initial fluid shifts to the following redistribution and adjustment of blood pressure, flow and related hemodynamic parameter throughout the body. The acute response to early stage microgravity from 1g is similar to changing posture from standing to supine on Earth [169], although to a somewhat higher extent. Indeed, it should be always distinguished between subjects entering 0g from 1g supine, seated or standing posture, as the amplitude of the associated response depends strongly on the initial condition on Earth [169]. Missing or not reported data concerning reference 1g posture of astronauts undertaking cardiovascular monitoring in space have led to parameter mismatches, discordance and misinterpretations.

In the framework of space missions, the early cardiovascular alterations start occurring even before launch, when astronauts are placed in the capsule assuming the so-called pre-launch position (Figure 2.11a) [91, 41]. During this preliminary phase - lasting even up to a few hours - astronauts have to lie supine with their legs raised and their hips and knees flexed by 90°. This position not only prevents blood from excessive pooling in the feet during the highly stressing and accelerated launch phase (protecting thus from syncope, cerebral hypoperfusion and black vision), but it also allows for blood volume to start being accommodated in the central-thoracic area. In fact, blood shifting from the lower extremities to central and cephalic regions is the first immediate consequence of entering 0g, with about one liter of blood being transferred upward from each leg ($\sim$2 l upward blood shift, with respect to 1g standing posture on Earth) as illustrated in Figure 2.11b. During the first days of flight, astronauts commonly reported feeling of fullness in the head and puffy faces, as well as decreased thirst, loss of smell sensation, nasal stuffiness and pressure felt in upper sinuses and eyeballs [169, 91, 41, 291]. By contrast, the lower limbs result as markedly decreased in size and leg/thigh circumference (-10%/-30%) upon fluid shift completion, leading to the so-called ‘chicken legs syndrome’ [91, 41, 291]. In addition to this first rapid fluid shift from the lower to the upper body, taking place in the first few seconds after entering 0g, a second slower fluid transfer is operated throughout the various compartments and across tissues, completely extinguishing in about 6-10 hours after approaching 0g [91].

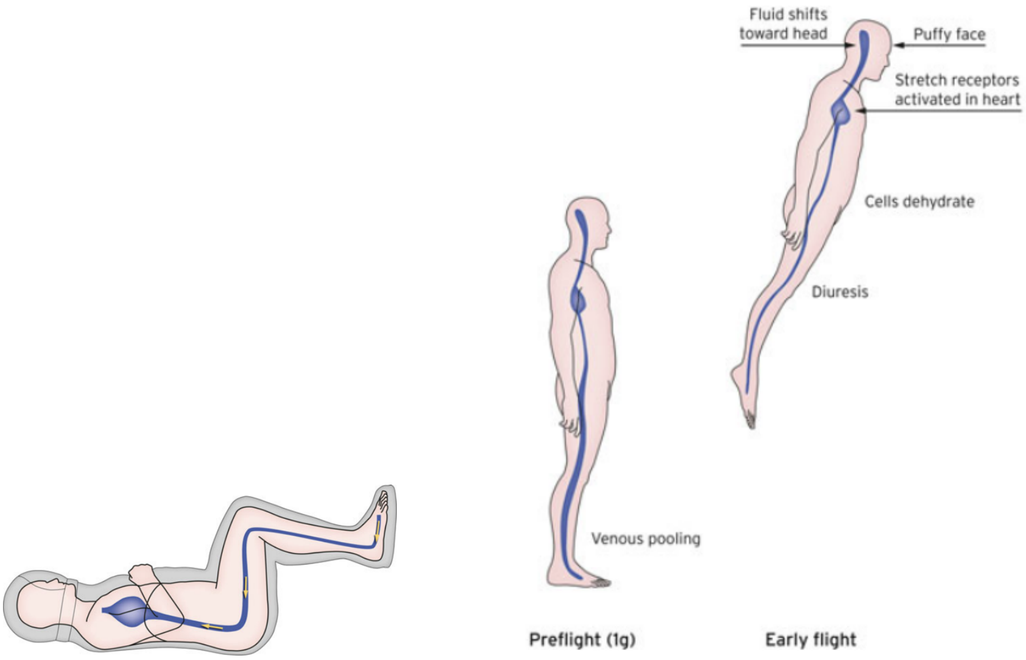

(a) (b)

Figure 2.11: Blood volume distribution and blood shift at pre-launch position (a), at 1g pre-flight on Earth (b, left) and during the first acute phase of flight (b, right). Images taken from [91].

As a consequence of blood shift towards the central (cardio-pulmonary) and cephalic regions, cardiac filling is enhanced at initial 0g, with subsequent increased heart size, SV and CO [171, 91]. Figure 2.12a displays the percentage increase registered for the heart volume of astronauts in the first day of flight (FD1), while Figure 2.12b reports CO and SVR at initial 0g compared to pre-flight 1g supine and seated states. Besides, mechanisms of orthostatic control (baroreflex, cardiopulmonary reflex) sensing increased blood filling activates parasympathetic response, decelerating HR sensibly and promoting peripheral vasodilation (Figure 2.12b) to accommodate blood flow back to the body periphery. The CVS results thus as more vaso-relaxed and less stressed during acute exposure to 0g than it is on Earth at 1g seated or standing posture [171].

Parallel to blood shift recorded in the first phases of flight, blood pressure equalizes throughout the body when entering 0g because of removal of all hydrostatic forces (similarly to what is observed on Earth at supine position) [91, 41]. In particular, SAP and MAP are not very consistent among studies, as they have been found to grow or lower slightly upon entering 0g according to the degree of

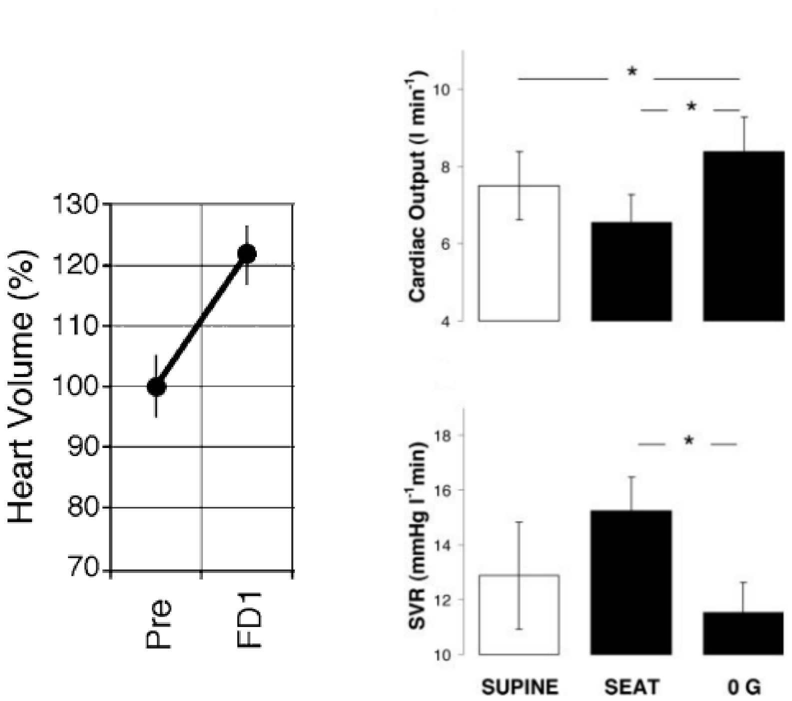

(a) (b)

Figure 2.12: (a): percentage variation of heart volume during the first phase of spaceflight (pre: pre-flight, FD1: flight day 1), image taken and modified from [41]; (b): cardiac output (CO) and systemic vascular resistance (SVR) at acute 0g compared to 1g supine and standing (data reported as mean±SE, asterisks denote statistical significance), image taken from [171].

autonomic response mediated by baroreflex and other homeostatic controls. On the other hand, DAP seems to be decreased consistently in acute microgravity compared to 1g standing on Earth [91], with consequent augmented pulse pressure ($SAP-DAP$), in line with increased SV and CO pumped by the heart.

However, not all cardiovascular responses to acute 0g are analogue to passing from standing to supine on Earth. The most evident discordance is represented by CVP, which is found to increase on Earth, at 1g, going from standing to supine posture and further head-down to negative tilt angles. This behavior is in agreement with blood shift from the lower to the upper body compartments, as described earlier in section 2.1. While CVP goes up as the heart and veins of the head and neck are filled with blood volume during tilt down at 1g on Earth, it is seen to decrease when entering 0g to values lower than 1g supine (though still higher than at 1g standing) [91, 41]. This surprising result was at first seen as paradoxical given the same mechanisms triggered by blood shifting headwards as registered on Earth atb 1g, and was initially believed to be caused by the somehow increased thoracic venous compliance experienced at 0g [91, 41]. Successively, further experiments onboard of parabolic flights reproducing short-duration free falling conditions allowed to understand better this phenomenon leading to the CVP reduction observed at 0g [266, 29, 237, 169, 171]. According to [266], the machanism explaining the observed CVP reduction is linked to the expansion of the thoracic cavity experienced at removal of the gravity load, at 0g, with respect to 1g. In particular, ITP (or intrapleural pressure, IPP, see section 2.1.1) has been seen to decrease upon entering 0g compared to 1g supine due to removal of the diaphragm weight. This behavior reduces transchamber and intrachamber cardiac pressure, and, thus, also CVP, as illustrated in Figure 2.13. In fact, the augmented cardiac and central venous filling contributes to increase pressure in the jugular veins communicating directly with the right atrium, such that transmural CVP ($CVP - IPP$) is actually decreased at 0g, with respect to 1g supine (Figure 2.13) [169]. In [29] the authors underline a different mechanism likely leading to the observed CVP reduction, focusing on the removal of all tissue weights and related extravascular pressure onto venous vessels. However, the two mechanisms might in fact be interconnected or even coincident, resulting in the eventual further enhancement of venous return, cardiac preload and heart filling by means of reduced ITP, similarly to what is observed going from supine to standing on Earth [91, 41, 169, 171] (section 2.1.1). As a result, SV and CO are therefore increased in 0g with respect to supine 1g, and cannot be explained only by simple removal of all hydrostatic pressures throughout the body [169, 171].

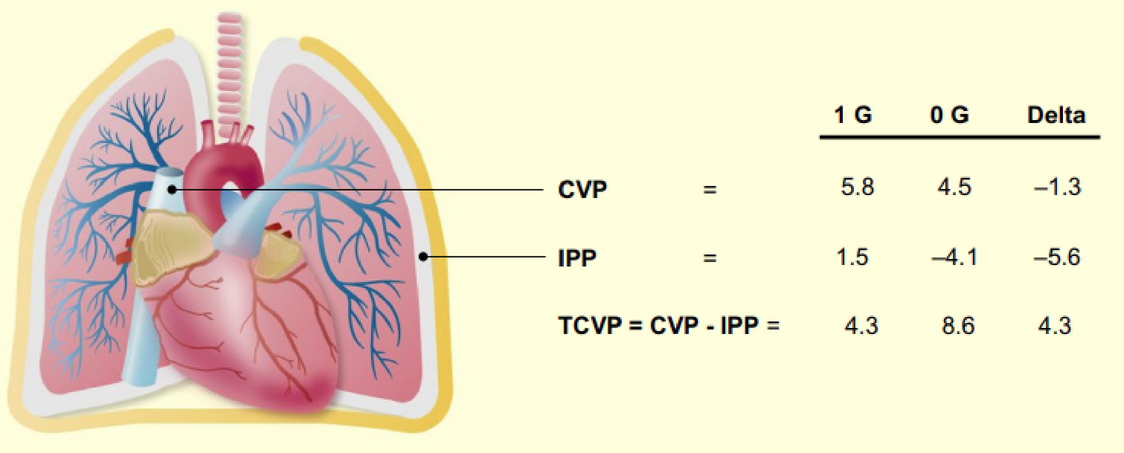

	1 G	0 G	Delta
CVP =	5.8	4.5	–1.3
IPP =	1.5	–4.1	–5.6
TCVP = CVP - IPP =	4.3	8.6	4.3

Figure 2.13: Mechanism of CVP reduction at 0g compared to 1g supine (IPP: intrapleural pressure; $TCVP$: transmural CVP; values in mmHg). Image taken from [169].

Also IOP and ICP are influenced by early access to microgravity. Indeed, removal of the gravity load results in rapid alteration of blood pressure at eye level, as well as in a marked cephalad congestion due to upward blood shift, with both factors shaping the associated ocular pressure response. As a result, IOP is found to increase at acute 0g at least by some 3/5 mmHg with respect to 1g supine/standing position, respectively, stabilizing at a level even above 1g supine in the first hours of flight [4, 39, 55, 144, 143]. Besides, the cerebrovascular system also adapts to the new gravitational environment, with CSF pressure being influenced by removal of all CSF hydrostatic gradients as well as the CVP reduction described above. Therefore, it is reasonable to expect ICP to behave similarly to IOP at 0g, increasing to values about those registered at 1g supine on Earth. Yet, unfortunately, no data is currently available concerning ICP direct measurement during actual spaceflight, underlining thus the necessity to conduct further experiments to bridge the existing gaps.

Long-term permanence in space

Long-term space travel and permanence at 0g elicit a number of cardiovascular remodeling and alterations beyond the observed acute responses. The behavior and adaptation of the human CVS to long duration spaceflight is currently object of study of bioastronautics and space medicine, especially in view of future long-term missions to deep space [41, 291, 21].

Already after the first few hours of spaceflight, upon completion of all acute responses to 0g described in the previous paragraph, the CVS starts to adapt to the new gravitational environment by re-organizing a series of mechanisms aimed at restoring the system equilibrium (*i.e.*, homeostasis) [41, 91]. At first, as the excess of fluid (blood) in the central-thoracic and cephalic compartment is sensed by the baroreflex control, a slow trans-capillary drainage of fluid (mostly plasma) starts occurring from intravascular to extravascular interstitial space. This plasma reduction, in concert with reduced thirst and - although debated - increased water excretion, acts over a period lasting 3-5 days, adjusting the total level of liquid content of the body until the intravascular plasma volume is reduced overall by 1-2 l (up to 22% of pre-flight total plasma volume). This new configuration is then maintained throughout the entire flight duration, with a total blood volume content that would be considered as moderately hypovolemic under normal 1g conditions on Earth [41, 91, 291, 169, 87, 76]. Figure 2.14, left image, shows the decreased total blood volume at midflight (hypovolemia). As the most relevant consequence, upon re-entry to normal Earth gravity, astronauts standing up after exiting the re-entry capsule immediately experience marked venous pooling and resulting orthostatic hypotension caused by the severe hypovolemic state of upper thoracic and brain regions (2.14) [41, 91].

Additional effects arise after few days of spaceflight. The reduced total (and circulating) blood volume causes a progressive decrease of the heart size(2.15a) and thus of SV and CO (-14/-23 % and -11/-18 % over a 6-week time, Figure2.15b) [41,

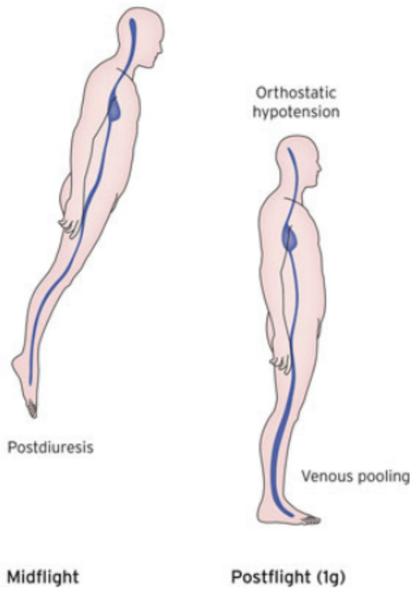

Figure 2.14: Blood volume distribution and blood shift shift at late on-orbit flight phase (several weeks of spaceflight, left) and after re-entry on Earth (right). Images taken from [91].

171, 76]. Furthermore, similarly to muscle atrophy occurring to the most of body muscle mass because of on-orbit sedentary lifestyle, absence of external loads and inactivity, also cardiac muscles lose their size and strength over time, further reducing cardiac volume 2.15a, efficiency and contractility [76]. The resulting condition of cardiac atrophy forces the heart to beat faster to sustain adequate levels of blood pressure, with consequent elevated HR in astronauts undergoing long space journeys [41]. Cardiac atrophy and hypovolemia affect also the overall astronauts exercise capacity [41] - evaluated by the maximum VCO_2 consumption reached during exercise -, with subsequent compromising consequences on occasional space maintenance tasks (*e.g.*, as during extra-vehicular activities), landing on different planets and upon re-entry.

To help keep elevated level of central blood pressure, the initially vasodilated peripheral circulation 2.12b is then adjusted such to slowly recover normal (or subnormal) levels of SVR throughout the first week of weightlessness in space 2.12b [171, 87], although arterial and venous vessels of the lower limbs, not being stimulated to bear high blood pressure such as during standing at 1g, tend to progressively lose their muscular tone. Consequently, venous compliance and cross-section area of leg veins are found to slowly increase with respect to early- and pre-flight levels [87]. It is also believed that during long-term permanence at 0g even the efficiency of

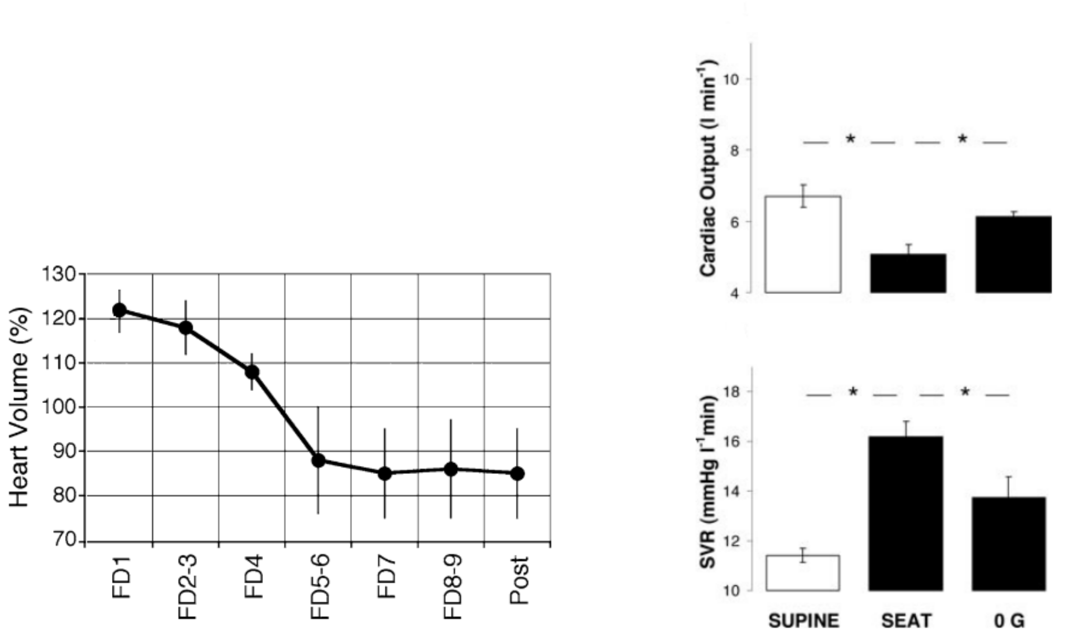

(a) (b)

Figure 2.15: (a): percentage variation of heart volume during spaceflight relative to pre-flight (FD1…FD8-9: from flight day 1 to flight days 8-9), image taken and modified from [41]; (b): cardiac output (CO) and systemic vascular resistance (SVR) after 6-7 days at 0g compared to pre-flight 1g supine and standing (data reported as mean±SE, asterisks denote statistical significance), image taken from [171].

response of baroreflex control is somewhat impaired [41]. The hyphothesis is that baroreflex mechanisms become attenuated and less efficient over prolonged exposure to weightlessness, as they are not stimulated by the constant body posture changes under the normal gravity load on Earth [169].

The combination of all these mechanisms leads to the so-called ‘cardiovascular deconditioning’ following long-term spaceflight (lasting from some weeks up to a few months) [41, 91, 87]. This undesirable cardiovascular state consists of marked hypovolemia, blood pooling in the feet, accelerated HR to sustain adequate blood pressure levels, medium to severe cardiac atrophy, reduced cardiac contractility, reduced vessels tone and slow or absent autonomic response. Upon re-entry on Earth, especially without assumption of appropriate countermeasures, severe cardiovascular deconditioning in most cases (2/3 of astronauts) entails ‘orthostatic intolerance’ [41, 291, 91, 169]. This condition refers to the impossibility for astronauts returning from long missions in space to stand up autonomously, get out of their re-entry capsule, walk and perform tasks upon landing (Figure 2.14, right image), including common symptoms of autonomic insufficiency such as orthostatic hypotension, accelerated heart beating, dizziness, sweating and eventual syncope. This is obviously a very limiting condition for astronauts involved in long-term missions, such as onboard of future missions to the Moon and Mars, highlighting the need of addressing this problem and to find effective solutions to counteract, mitigate, or abolish deconditioning of the CVS while on orbit, in order to make individuals capable of withstanding gravity of the celestial bodies on which they are supposed to land.

Another harmful and potentially hazardous condition which has recently been identified by NASA on astronauts returning from long-term spaceflight is 'spaceflight associated neuro-ocular syndrome', or SANS [127, 130, 128, 294, 245, 16, 291, 169, 125, 150]. The syndrome consists of a number of ophthalmic anomalies and neuro-ocular changes (including optic disc edema, optic nerve sheath distension, choroidal folds, globe flattening, hyperopic shift, and cotton wool spots) detected in astronauts returning from the (ISS) that may even persist permanently after re-entry [145, 148]. Among researchers, it is widely hypothesized that cephalic fluid congestion caused by microgravity-induced headward fluid shift, chronically ICP, and reduced or even reversed translaminar pressure (*i.e.*, $TLP{=}IOP{-}ICP$) may play a critical role in the development of the above mentioned symptoms. In spite of IOP seems to stabilize to normal pre-flight (1g seated) values after few days of flight [99, 250, 178, 38], ICP in principle should continue to remain high, thus setting the basis for TLP reduction/inversion and possible ocular remodeling. Thus, the etiology and pathophysiology of SANS is still largely under debate, although its connection with the CVS and the implication of related gravity-induced cardiovascular alterations are clearly of great importance in this picture. These hypotheses still need elucidation and more evidences shall be collected to draw reasonable conclusions. Therefore, future scientific experiments aimed at obtaining on-orbit clinical measures of IOP and ICP during long-term space missions are of crucial importance.

2.2.2 Alternative access to microgravity

Due to the high cost and hard accessibility of space experiments in actual microgravity - such as onboard of the ISS or different missions(Skylab, Spacelab) - a number of alternative ways of reproducing microgravity effects on the human body have been devised in recent years [41, 91, 180, 269, 238, 23]. Different approaches are adopted according to the human system we want to investigate (cardiovascular system, musculo-skeletal system, . . .). Moreover, the duration of the experiment is also of crucial importance, as different approaches give actual or simulated access to microgravity of different time extension. Table 2.3 reporting information from [41] and [180] present the most diffused methods to access actual or simulated microgravity, from ground to flying and in-space experiments. All cases are indicated together with their typical duration, magnitude/type of microgravity reproduced, and the degree of comparability to the actual CVS changes observed during spaceflight.

Table 2.3: Different ways to access actual or simulated microgravity. The degree of comparability (takes into account the nature and extent of the CVS response, as well as the time duration) to the actual CVS changes occurring in space is expressed through asterisks: *: weak comparability, **: moderate comparability, ***: strong comparability. Taken and adapted from [41, 180].

Method	**Magnitude/Type**	**Duration**	**Comparability**
6° Head-down tilt	simulated	3/12 months	***
Unilateral lower limb suspension	simulated	$\sim$ 30 days	*
Wet immersion	simulated	$\sim$ 4 h	**
Dry immersion	simulated	3/7 days	***
Drop tower	$< 10^{-4}$g	2/5 s	**
Parabolic flight	$10^{-1}/10^{-2}$g	$\sim$ 20 s	**
Sounding Rocket	10^{-5}g	6/15 min	**
ISS (or other on-orbit)	10^{-4}g	1/6 months	n.a.

In this section, we will briefly review some of the popular ground analogues of spaceflight reported in Table 2.3. Ultimately, we will give additional hints on the surprising usefulness and versatility of numerical tools and mathematical modeling to enable the study of the gravity-induced effects on the human CVS at a very modest cost.

Ground analogues of spaceflight

By ground analogue of human spaceflight we specifically refer to experimental frameworks that can be used on Earth, under normal 1g gravity, to resemble - completely or at least partially - the presence of one or more typical features of the space environment, such as isolation, radiation or weightlessness encountered by astronauts flying in space. The focus of this overview is on the cardiovascular system, thus we will discuss here only those ground analogues of spaceflight that are used to reproduce microgravity-induced effects on the human CVS. Among the ground analogues listed in Table 2.3, there are some the have been particularly leveraged in recent years to explore the effects of short- and mid-term weightlessness on the CVS. In particular, in the following paragraphs we will describe the adoption of (i) 6° head-down tilt, (ii) water immersions, and (iii) parabolic flights to reproduce the hemodynamic response to simulated or actual (although for a few seconds only) free falling.

i. *6° Head-down tilt.* The use of HDT to a modest extent - typically around 6° head-down - constitutes probably the majority of human subjects research related to the microgravity effects on the human CVS, and on human physiology in general [46, 188]. This is particularly true because of the limited costs and ease of operability associated with this kind of experiments. The experimental layout includes the tilting bed facility described in section 2.1.1, with the subject tilted head-down to enable blood shift from the lower limbs to the upper thoracic and cephalic compartment, as it is observed when entering microgravity (Figure 2.16). The subject is instrumented so that a set of hemodynamic variables can be collected while resting head-down. 6° HDT is often employed when long-term effects are targeted in particular, as the subject can be left resting head-down from a few hours to several weeks or months, with the longest study to date lasting one year (2.3) [24, 46, 86, 38, 210, 194]. 6° HDT to resemble microgravity effects on the human body is often referred to also as head-down bed rest (HDBR) or stress (HDBS).

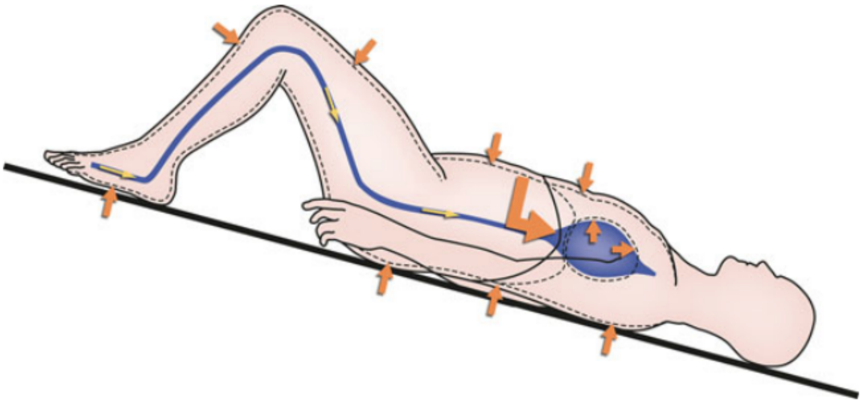

Figure 2.16: 6° head-down tilt as analogue of spaceflight and associated blood volume shift. Image taken from [91].

In 6° HDT experiments, weightlessness is only simulated (2.3) as the component of the gravity vector $\boldsymbol{g}$ parallel to the longitudinal body axis is null or minimized. The little head-down angle is used to reproduce the cephalic blood shift registered at 0g to a more accurate extent [23]. In other terms, the little negative tilt angle mimics the increase in venous return operated by thoracic expansion seen in true microgravity and that cannot be achieved under normal 1g gravity on Earth. As head-down tilt is initiated, blood volume is transferred from the subject's legs to the upper compartments, leading to increased cardiac filling, SV, CO and CVP already described in section 2.1.1 and upon entering 0g [24] (apart from CVP, which decreases in microgravity, section 2.2.1). These changes are accompanied by a decrease in HR, which is then recovered throughout the first 24h of HDBR [24]. Also, additional data regarding height, body mass, aerobic capacity, plasma volume, bone density, muscle mass and strength, and their agreement with actual spaceflight changes are reported in the review article on HDBR by [188]. Prolonged bed rest leads to volume losses by capillary plasma filtration and subsequent excretion halfway between supine and upright postures (-10/-15%) [188, 73], and is therefore used to investigate the occurrence and implications of orthostatic intolerance [86, 194, 295]

6° HDT is also adopted to study SANS onset and development [175, 99, 150, 198, 125, 126, 210, 279, 281, 189, 128]. In particular, ICP is seen to rise in response to tilt down [125, 150, 128], which should resemble what happens to astronauts entering 0g at least during the first phases of flight. The ICP increase is driven by the cephalic volume congestion, as well as by the augmented dural venous pressure in the head. Also IOP increases during acute 6° HDT with respect to standing/sitting and supine [139, 144, 125, 150], although it decreases again by a few mmHg after some days of HDT, restoring almost the same pre-tilt normal values [38]. The secondary IOP recover taking place in the next hours after tilt down is possibly caused by total volume losses, ocular dehydration and systemic cardiovascular or hormonal adjustments coming into play over longer time scales.

ii. *Water immersions.* As introduced in section 2.1.2, WIs trigger cardiovascular responses very similar to changing posture from standing to supine, with blood volume being shifted from the extremities (in particular from lower limbs) to central regions. Actually, the amount of blood transferred to the central compartments by external compression of water hydrostatic pressure is somewhat greater than during simple change of posture to supine, making this type of experiment a good ground based analogue of spaceflight and microgravity. Also in WIs, microgravity is only simulated by virtual removal of the gravitational load thank to the buoyancy forces exerted on the immersed body [238, 23, 91, 180]. Beside distinguishing between partial or total immersions (section 2.1.2), WIs can be also performed as 'wet' (Figure 2.10b) - that is without the need for a specific dry suit, and thus lasting no more than a few hours (Table 2.3) - or as 'dry', by adopting specific dry suits to limit the contact with water (thus referred to as dry immersions), and lasting even several days (Table2.3) [180]. For this reason, wet WIs are often used to study long-term effects of simulated weightlessness onto the CVS. Concerning the hemodynamic response observed during both wet and dry WI studies, through comparisons with 6° HDBR [238] it has emerged that WIs produce cardiovascular changes slightly larger than those detected during HDBR. Thus, SV and CO are found to be increased by a little more during WI than in HDBR, and HR is decreased a little less due to the lower baroreflex stimulation compared to head-down tilt.

This type of ground experiments are usually adopted when it comes to astronauts extra vehicular activity (EVA) trainings, or to test for the functionality of real or nearly-real scale space modules mockup [167].

iii. *Parabolic flight.* Among ground analogues of spaceflight, parabolic flights are by far those providing the closest condition possible to true microgravity encountered in space, and therefore this is the reason why their use is so widespread in the literature to explore human physiology under free falling [12, 91, 20, 237]. Parabolic flights are special maneuvers operated by specific aircrafts flying along multiple, successive parabolic trajectories such as the one shown in Figure 2.17. Along each parabola, the aircraft undergoes an initial phase of hypergravity (pull-up, usually between 1.5g and 2g of acceleration) lasting about 20 s, followed by a phase of almost complete free falling (0g, typically as accurate as 10^{-2}g) at the apex of the parabola and lasting about another 20 s. Finally, the parabola is completed with last hypergravity phase at pull-out. During each parabolic flight session, the aircraft performs up to 20/30 parabolas, such that a series of short-term exposures to 0g are reproduced, one for each parabola. Thus, parabolic flight can accurately reproduce true free falling, despite of very short duration. However, this type of experiments are used not only to evaluate the acute cardiovascular coping to 0g [140, 20, 190, 159, 201, 33, 137, 173, 234, 18, 282, 17, 229, 228], but also for a number of different medical purposes [222].

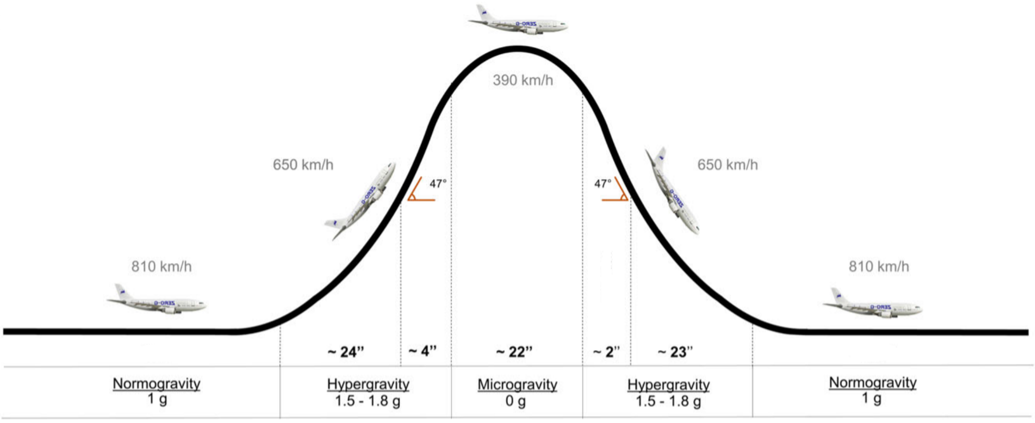

Figure 2.17: Parabolic flight maneuver: trajectory, phases and duration. Image taken and adapted from [222].

Despite the short 0g phase duration, parabolic flights are useful to accurately capture acute cardiovascular changes observed upon initial exposure to 0g (section 2.2.1), such as upward blood shift to central-cephalic regions, increased venous return, heart filling and size, augmented SV, CO as well as decreased HR and TPR [237, 33]. Table 2.4 reports the variation registered for the most common central hemodynamic parameters during the various phase of the parabolic flight maneuvers, at three different postures (*i.e.*, supine, seated and standing). Indeed, posture is essential when reflecting on the cardiovascular alterations elicited by varying gravity, as the response of the given parameters depends strongly on the body position [159, 20, 18]. Data reported in Table 2.4 evidence how the widest parameter variations are observed at standing and seated postures, due to the alignment of the varying gravity vector with the longitudinal body axis and thus

Table 2.4: Central hemodynamic parameters variation during parabolic flight divided by posture and flight phase. MAP mean arterial pressure, SAP systolic arterial pressure, DAP diastolic arterial pressure (blood pressures always referred to finger arterial pressure corrected at heart level), HR heart rate, SV stroke volume, CO cardiac output, TPR total peripheral resistance. Percentage values referred to 1g pre-flight standing cases. Values taken from [140, 20, 190, 159, 201, 33, 137, 173, 234, 18, 282, 17, 229, 228], table taken from [66]. Symbols identify trends for the corresponding variables, with respect to their 1g pre-flight state (≊: not clear trend, ↑: parameter increase, ↓: parameter decrease).

Posture	**Parameter**	**1g**	**1.8g**	**0g**	**1.8g**	**1g**
Supine	MAP [mmHg]	73÷101	68÷98 ≊	78÷96 ≊	68÷95 ≊	75÷95
	SAP [mmHg]	112÷144	13÷139 ≊	120÷144 ≊	111÷139 ≊	114÷144
	DAP [mmHg]	55÷83	53÷81 ≊	60÷80 ≊	53÷75 ≊	57÷79
	HR [bpm]	60÷89	60÷88 ≊	61÷91 ≊	61÷84 ≊	60÷88
	SV [ml]	132%÷134%	126%÷142% ≊	125%÷151% ≊↑	124%÷138% ≊	130%÷136%
	CO [l/min]	106%÷108%	97%÷121% ≊	98%÷122% ≊↑	91%÷115% ≊	103%÷109%
	TPR [mmHg·min/l]	80%÷82%	70%÷90% ≊	71%÷89% ≊	77%÷87% ≊	77%÷87%
Seated	MAP [mmHg]	85÷105	90÷110 ≊↓	70÷101 ↓	80÷105 ≊↓	80÷110
	SAP [mmHg]	109÷153	110÷155 ≊↑	102÷133 ≊↓	110÷156 ≊	125÷163
	DAP [mmHg]	69÷89	73÷99 ↑	57÷79 ↓	68÷92 ≊	71÷89
	HR [bpm]	63÷86	74÷113 ↑	62÷90 ↓	74÷109 ↑	67÷93
	SV [ml]	50÷111	40÷90 ↓	70÷125 ↑	50÷100 ↓	50÷100
	CO [l/min]	4.0÷8.5	4.0÷8.9 ↓	5.0÷9.9 ↑	4.5÷8.9 ↓	4.0÷8.0
	TPR [mmHg·min/l]	11.8÷22.2	12.5÷25.0 ≊↑	9.1÷16.7 ↓	10.0÷22.2 ≊	11.8÷22.2
Standing	MAP [mmHg]	90÷102	95÷105 ≊↑	75÷97 ↓	90÷94 ≊↓	88÷98
	SAP [mmHg]	136÷154	131÷151 ≊↓	127÷151 ≊↓	127÷139 ≊↓	139÷149
	DAP [mmHg]	72÷86	80÷90 ≊↑	57÷75 ↓	73÷79 ≊↓	70÷82
	HR [bpm]	69÷104	82÷117 ↑	60÷90 ↓	80÷119 ↑	73÷102
	SV [ml]	39÷77	28÷70 ↓	41÷117 ↑	85%÷109% ↓	97%÷105%
	CO [l/min]	4.3÷5.7	83%÷99% ↓	7.9÷15.1 ↑	92%÷124% ↓	99%÷103%
	TPR [mmHg·min/l]	100%	102%÷130% ≊↑	63%÷83% ↓	79%÷107% ≊	94%÷98%

allowing for the largest blood volume shifts to occur. On the other hand, also at supine posture some hemodynamic changes are evidenced in the same direction, with slightly increased SV and CO and reduced HR and TPR at 0g flight phase with respect to 1g pre-flight. Interestingly, parabolic flight experiments have helped grasp the underlying mechanism of reduced CVP observed immediately upon entering 0g (with respect to supine at 1g) [266, 237, 190], identifying the thoracic expansion and removal of all tissue weights as responsible for this phenomenon, explaining the improved venous return and augmented SV and CO with respect to 1g supine (section 2.2.1).

Because of the possibility of accessing true microgravity - although of very limited duration - parabolic flights have also been exploited to study IOP and ICP behavior under acute 0g, trying to make inferences and speculations onto SANS onset and development in astronauts exposed to weightlessness for longer duration [4, 143, 128, 294]. In [128] the authors found ICP to decrease slightly when entering 0g with respect to 1g supine (while remaining much higher than at 1g standing or seated), similarly to the CVP reduction observed because of thoracic expansion. The cause of reduced ICP compared to 1g is likely to be linked directly to venous pressure, and thus to CVP reduction, since the cerebrospinal fluid dynamics is strictly related to the dural venous pressure in the brain (section 2.1). However, parabolic flights cannot extend these findings to longer time frames, and extrapolation of data is not straightforward. Further in-flight ICP measurements should be conducted during long duration spaceflight to help clear the picture. Besides, results presented in [4] underline how IOP is increased upon entering 0g during parabolic flight from 1g supine, and even more so from 1g standing/seated. Therefore, the relationship between IOP and ICP during the acute 0g phase of parabolic flight suggests that TLP ($IOP - ICP$) could be reduced in acute weightlessness with respect to 1g standing or seated, whereas it may result to be slightly increased with respect to 1g supine - which should represent a favorable condition discouraging SANS development.

Mathematical modeling

Given the so far unclear and incomplete picture of the cardiovascular changes elicited by short- and long-term spaceflight, including comprehension of the CVS responses to varying gravity at different postures across the various mission phases, how to deal with cardiovascular deconditioning, post-flight orthostatic intolerance and design of possible countermeasures, further investigation is strongly encouraged. Moreover, increasing efforts are advisable to understand the underlying mechanisms at the onset of SANS and determining its future development. In this context, mathematical modeling can represent a powerful, versatile and cheap alternative to shed light on the hidden mechanisms, identify cause-effect links and come to innovative solutions to help improve healthiness of astronauts in space.

Cardiovascular models combine flexibility easy accessibility, offering numerous solutions depending on the level of spatial detail assigned to each represented vascular region (from 0D to 3D models reconstructed from clinical x-ray or magnetic resonance images) [22, 209, 162, 203, 205]. The computational cost increases accordingly, and validation is essential especially when patient-specific models are involved, but the enormous advantages from the diagnostic and prognostic point of view certainly overcome these drawbacks. Mathematical modeling of the human CVS has been proved to be successful and of great help in numerous applications, ranging from clinical and pathological scenarios [225, 226, 135] to physiological cases of interest such as the response to aerobic exercise [54], centrifugation [10], LBNP [153] or to posture changes on Earth [94, 93, 280, 103, 123, 296]. However, few attempts to use mathematical modeling to grasp the hemodynamic coping to spaceflight have been conducted so far [154], especially concerning long-term adaptation and deconditioning at 0g [76].

In the next chapters, we will thus present a novel 1D-0D multiscale model of the CVS, which has been validated *in vivo* under several conditions (change of posture at 1g) and used to study the cardiovascular and hemodynamic acute response to posture changes from supine to seated or standing, to simulated parabolic flight, and to short-term 6° HDT as ground analogue of spaceflight.

Concluding remarks

In summary, the human cardiovascular physiology results to be strongly affected by gravity, either due to variation of the gravity vector orientation with respect to the reference body axis (*i.e.*, posture changes) or to actual variations of the gravity vector magnitude. In either cases, blood volume distribution across the human vasculature is markedly modified, with resulting physiological responses triggered to preserve homeostasis, including control of chronotrropic and inotropic cardiac state, vascular tone and local vascular autoregulation. The extent to which such mechanisms are activated relies strongly on the way gravity effects are applied to the cardiovascular system, on the presence of external inputs forcing the overall cardiovascular response (*e.g.*, muscle activation during active standing, LBNP applications) as also on the duration of the effects (short-term versus long-term effects). A number of open topics remain totally or partly unexplained - such as SANS manifestation in astronauts returning from long space travels -, part of which have been addressed in the following of the present thesis.

Chapter 3

Mathematical modeling of the cardiovascular system

In this chapter we introduce the multiscale (1D-0D) mathematical model of the human CVS which has been developed and used to conduct the numerical investigations described in the present thesis. The original 1D-0D multiscale CVS model is taken from previous works by Guala *et al.* [89] and Gallo *et al.* [74, 76, 75], which has then been further expanded as the main objective of the present PhD activity, throughout the last three years, by accounting for the effects of gravity on the whole circulation, including also all the different related mechanisms described in the following and additional lumped compartments such as the cerebrovascular and ocular ones. The reduced order (1D-0D) modeling architecture has been preferred to more detailed mathematical approaches (*i.e.*, 3D representation) mainly for computational costs reduction and simplicity of description of a large network including all main arteries and surrounding vasculature. 3D models are generally preferred when detailed hemodynamics related to specific 3-dimensional geometries and flow patters have to be investigated, such as the aortic bifurcation, atherosclerotic accretion, heart chambers etc. [203, 205].

The model is composed of a 1-dimensional description of the arterial tree (including all main large arteries), connected to lumped parameter representations of the remaining systemic circulation (arterioles, capillaries, venules, veins and venae cavae). The model is arranged in a closed-loop layout, including 0D representations of the cardiac chambers and pulmonary circulation, of the coronary microvasculature of the myocardium, and of the cerebrovascular circulation from the circle of Willis to deep cerebral arteries and cerebral capillary-venous circulation. In addition, a lumped parameter model of the ocular compartment is also attached to the global architecture. The overall model layout is schematized in Figure 3.1, highlighting the 1D and 0D counterparts, the global circulation pathways, and all the different lumped components and districts mentioned above.

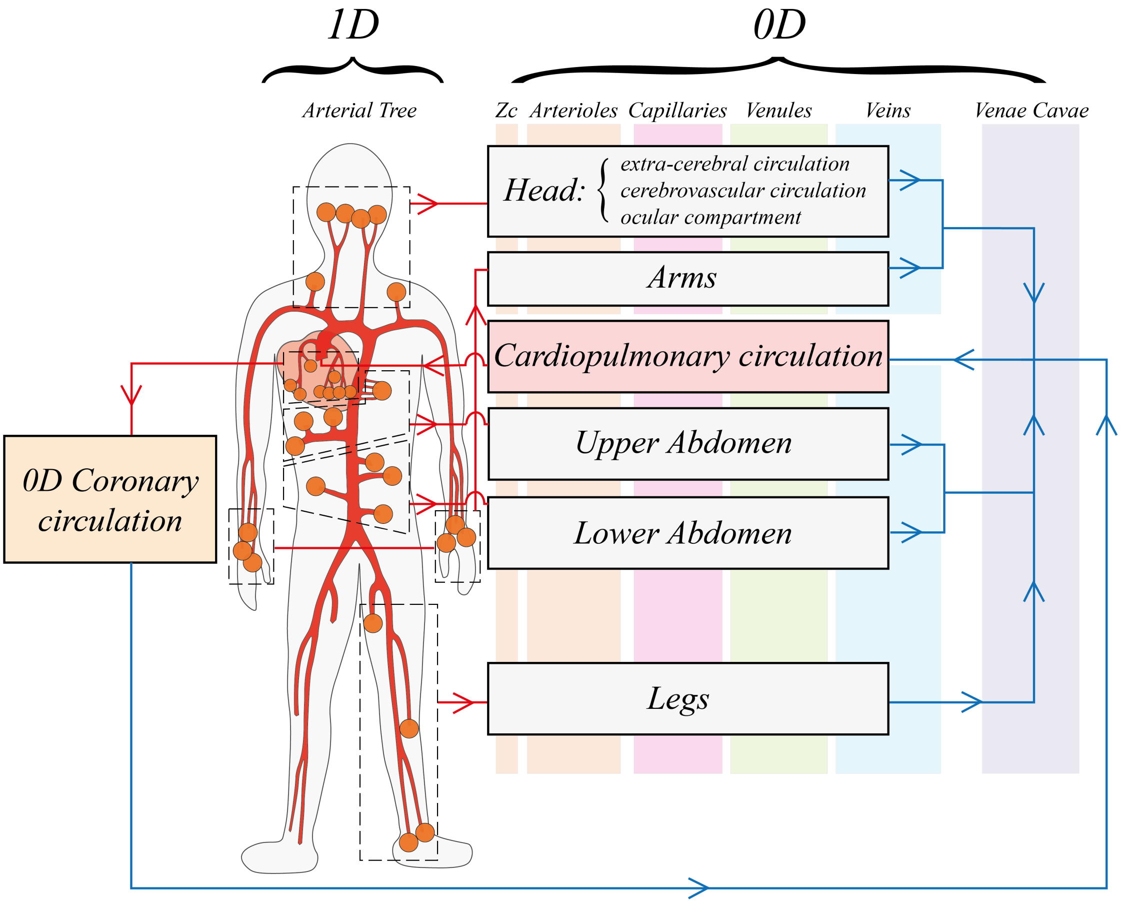

Figure 3.1: Illustration of the global multiscale cardiovascular model. The 1D arterial tree is sketched in red, red arrow indicate the arterial blood pathway, whereas blue arrows denote venous return blood pathway. Orange circles denote 1D terminal arteries linked to the downstream 0D compartments, grouped into regions from head to legs. Vertical rectangles (orange, pink, green and blue, from left to right) divide the 0D peripheral circulation into arteriolar, capillary, venular, venous and venae cavae compartments. Z_c are arteriolar characteristic impedances.

The present chapter is organized by first introducing - in section 3.1 - the 1D arterial network and related equations governing blood motion in arteries, 1D vessels wall mechanics and boundary condition imposition. Then, in section 3.2 the remaining 0D counterpart of systemic circulation is presented, while the 0D cardiopulmonary compartments are described in section 3.3. Following sections 3.4, 3.5, and 3.6 present the descriptions of the coronary, cerebrovascular, and ocular compartment models, respectively, while in section 3.7 the short-term control mechanisms (arterial baroreflex, cardiopulmonary reflex, and cerebral autoregulation) implemented to regulate the CVS model functioning are described. Ultimately, details about the adopted numerical methods and discretization schemes, as well as spatial and time resolution algorithms are provided in section 3.8.

3.1 1D arterial network

The 1D description of the arterial tree is taken directly from [89] and [74]. The arterial network is composed of 63 large arteries (49 systemic plus 14 coronary arteries), starting from the aorta and extending towards all the body periphery via successive bifurcations, branching and gradual cross-section tapering. The arterial tree geometry composed of the 63 represented large arteries is shown in Figure 3.2, whereas specific arteries nomenclature and 1D geometrical features are reported in appendix A, Table A.1.

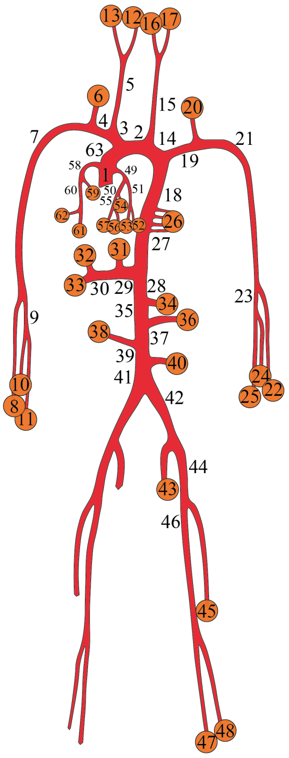

Figure 3.2: Illustration of the 1D arterial tree, with black numbers identifying each of the 63 large arteries (see appendix A, Table A.1 for more details on arteries nomenclature and characteristics). Orange circles denote 1D terminal arteries at 1D-0D arteriolar interfaces.

In this section, we will first derive the set of governing equation describing blood motion in 1D arteries, together with the algebraic constitutive equation linking blood pressure and vessels wall mechanics (*i.e.*, local cross-section area). Finally, derivation of suitable boundary equations will be discussed to deal with 1D-0D coupling.

3.1.1 1D axisymmetric governing equations

Blood is treated as an incompressible fluid. Therefore, the incompressible form of Navier-Stokes equation for mass and momentum balance can be applied to describe blood motion [202]:

$$\begin{cases} \nabla \cdot \mathbf{u} = 0, \\ \rho \dfrac{\partial \mathbf{u}}{\partial t} + \rho \mathbf{u} \cdot \nabla \mathbf{u} = -\nabla p + \mu \nabla^2 \mathbf{u} + \rho \mathbf{g}, \end{cases} \tag{3.1}$$

where independent variable t denotes time, $\mathbf{u} = (u_x,\, u_y,\, u_z)^T$ is the velocity vector with its cartesian components $u_x = u_x(x,\, y,\, z)$, $u_y = u_y(x,\, y,\, z)$, $u_z = u_z(x,\, y,\, z)$, along the three cartesian spatial coordinates x, y, and z; $p = p(x,\, y,\, z)$ is pressure, $\mathbf{g} = (0,\, 0,\, -g)$ is gravity acceleration vector (directed along the z axis, with $g \approxeq 9.81$ m/s^2). Symbol ∇ denotes the nabla operator, defined as the vector of spatial derivative in cartesian coordinates, that is $(\frac{\partial}{\partial x},\, \frac{\partial}{\partial y},\, \frac{\partial}{\partial z})$.

By assuming that arterial vessels can be approximated as straight cylinders, it is reasonable to re-write equations (3.1) in a cylindrical coordinate system, that is applying the coordinate transformation $(x,\, y,\, z) \to (x,\, r,\, \theta)$, where $x = x$, $r = \sqrt{y^2 + z^2}$, and $\theta = \arctan(\frac{z}{y})$, so that $(u_x,\, u_y,\, u_z) \to (u_x,\, u_r,\, u_\theta)$. Furthermore, additional assumptions apply [70, 71, 203] such as (i) flow is 1D along x ($u_\theta = u_r = 0$ everywhere, thus flow velocity is simply $u_x = u$) and axisymmetric in the cylindrical framework, that is all $\frac{\partial}{\partial \theta} = 0$; (ii) vessels are deformable in the radial direction only, with local cross-section area keeping always a circular shape perpendicular to the vessel axis; (iii) vessels are inextensible in the longitudinal direction (vessels length fixed); (iv) vessels wall do not allow fluid filtration (*i.e.*, impermeable walls; (v) viscus stress are present next to vessels wall, and no-slip condition applies (*i.e.*, $u_x = 0$ at vessels wall); (vi) flow is laminar everywhere and blood is treated as an incompressible and Newtonian fluid with constant density $\rho = 1050$ kg/m^3 and (dynamic) viscosity $\mu = 0.04$ Pa s. Thus, the following 1D axisymmetric formulation of (3.1) is obtained

$$\begin{cases} \dfrac{\partial \rho}{\partial t} + \dfrac{\partial (\rho u)}{\partial x} = 0, \\ \rho\left(\dfrac{\partial u}{\partial t} + u \dfrac{\partial u}{\partial x}\right) = -\dfrac{\partial p}{\partial x} + \mu\left(\dfrac{1}{r}\dfrac{\partial}{\partial r}\left(r \dfrac{\partial u}{\partial r}\right)\right) + \rho g_x. \end{cases} \tag{3.2}$$

Here, x represents the single vessel axial coordinate and g_x is the projection of the gravity acceleration vector $\mathbf{g}$ on it. Specifically, given a single arterial vessel randomly oriented in the 3D space representing a single branch of the human arterial tree, Figure 3.3 illustrates its orientation with respect to the horizontal reference and the transverse and longitudinal body axes y_b and z_b. In Figure 3.3, the local vessels axial coordinate x is named as x_{ves}, and the projection of the gravity acceleration vector $\mathbf{g}$ on x_{ves} is therefore

$$g_x = g \sin\gamma \sin\alpha,$$

where γ is the angle between $\mathrm{x_{ves}}$ and y_b in the y_b - z_b, and α is the angle between z_b and the horizontal reference (tilt angle). Values of γ adopted in the present work are reported for each artery of the arterial network in Table A.1.

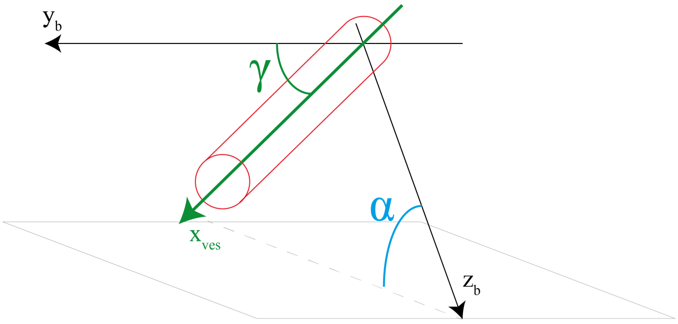

Figure 3.3: Schematic illustration of the generic 1D arterial vessel (in red) orientation with respect to the horizontal reference (grey plane). y_b and z_b are transverse and longitudinal body axis, respectively, while $\mathrm{x_{ves}}$ is the single vessel local longitudinal coordinate in the y_b - z_b plane. γ is the angle between $\mathrm{x_{ves}}$ and y_b in the y_b - z_b, and α is the angle between z_b and the horizontal reference.

By integrating (3.5) over vessels local cross-section area A - recalling that $\int dA = \int_0^{r_v} 2\pi r\, dr = \pi r_v^2 = A$ (r_v local vessel radius), $\int u\, dA = Q$ (blood flow rate), and $\frac{\mu}{\rho} = \nu$, blood kinematic viscosity - one obtains the integral form of equations (3.5), that is

$$\frac{\partial A}{\partial t} + \frac{\partial Q}{\partial x} = 0, \tag{3.3}$$

and

$$\frac{\partial Q}{\partial t} + \frac{\partial}{\partial x}\int_0^{r_v} 2\pi r u^2\, dr = -\frac{A}{\rho}\frac{\partial p}{\partial x} + 2\pi\nu\left[r\frac{\partial u}{\partial r}\right]_{r=r_v} + Ag\sin\gamma\sin\alpha. \tag{3.4}$$

Adopting a conventional flat-parabolic velocity profile $u(r)$ defined as

$$u(r) = \begin{cases} \bar{u}, & \text{if} \quad 0 \le r < r_v - \delta \\ \bar{u}\dfrac{r_v^2 - r^2}{2r_v\delta - \delta^2}, & \text{if} \quad r_v - \delta \le r \le r_v \end{cases}, \tag{3.5}$$

where $\bar{u} = \frac{Q}{A}$ is mean blood velocity, while the boundary layer thickness δ can be estimated as [74] $\delta = \min(r_v, \sqrt{\frac{\nu}{\omega}})$, where ω denotes cardiac pulsation (*i.e.*, $\omega = 2/pi\frac{HR}{60}$). By plugging definitions of $u(r)$ and δ to equation (3.4), the convective and diffusive (viscous) terms can be computed and the following final form of 1D momentum balance equation is reached:

$$\frac{\partial Q}{\partial t} + \beta \frac{Q^2}{A} = -\frac{A}{\rho}\frac{\partial p}{\partial x} + N_4 \frac{Q}{A} + Ag \sin\gamma \sin\alpha, \tag{3.6}$$

with β the Coriolis coefficient and N_4 the viscous coefficient (detailed definitions of β and N_4 are provided in appendix A, equations (A.1)-(A.2)). These coefficients are dependent on the local vessel cross-section area A and δ, and thus are functions of vessels geometry, position and time. However, in the present work, for the sake of simplicity, coefficients β and N_4 are determined once for all at each point of the arterial tree at a given reference pressure ($p_0 = 100$ mmHg [74], for which the arterial network geometry is that reported in Table A.1), and thus no longer vary with time.

3.1.2 Pressure constitutive law

Mass and momentum balance equations (3.3)-(3.6) involve three dependent variable describing blood hemodynamic, that is local vessel cross-section area $A(x, t)$, blood flow rate $Q(x, t)$, and blood pressure $p(x, t)$. Therefore, an additional equation is needed to close the mathematical system, namely, a constitutive equation - also named as tube law - describing blood-walls interaction through local vessels mechanical properties. This equation is an algebraic relationship linking blood pressure $p(x, t)$ (notice that, here, intraluminal pressure coincides with transmural pressure, although to the end of the present thesis all pressures external to the arterial tree are considered as null, *i.e.*, equal to the external environmental pressure) and local area $A(x, t)$ taking into account the elastic and visco-elastic properties of arterial walls [89, 74]. Furthermore, in the present work an additional component has been introduced to model arterial vessels mechanical behavior at very low transmural pressure, such as during the hypergravity phases of parabolic flight at seated or standing posture [66].

The pressure constitutive law can thus be expressed in the form $p = p_e + p_v + p_h$, where p_e and p_v are elastic and viscoelastic components taken by Guala's original model [89, 74], while p_h denotes the hyperbolic partial collapse model from Drzewiecki *et al.* [56]. At a given point of the arterial network, the local p - A relationship thus reads

$$p = B_1 + B_2 A + B_3 A^2 + B_4 A^3 - B_5 \frac{1}{\sqrt{A}}\frac{\partial Q}{\partial x} - \widehat{EI}\left(\left(\frac{A_b}{A}\right)^m - 1\right) + p_b, \tag{3.7}$$

where terms $B_1 \dots B_4 A^3$ represent the elastic pressure component p_e, while term $B_5 \frac{1}{\sqrt{A}} \frac{\partial Q}{\partial x}$ is the viscoelastic pressure component p_v of the original Guala model. Coefficients B_i $(i = 1 \dots 5)$ are function of vessels geometry and mechanical properties, through the local wave velocity at time $t = 0$ (c_0), and are defined as:

$$B_1 = -\frac{1}{a_3^3}\left(a_5^3 + c_0^6\rho^3 + 3c_0^4\rho^2 a_5 + 3a_5^2 c_0^2 \rho\right),$$

$$B_2 = \frac{3\rho c_0^2}{A_0 a_3^3}\left(\rho^2 c_0^4 + 2\rho a_5 c_0^2 + a_5^2\right),$$

$$B_3 = -\frac{3\rho^2 c_0^4}{A_0^2 a_3^3}\left(a_5 + \rho c_0^2\right),$$

$$B_4 = \left(\frac{\rho c_0^2}{a_3 A_0}\right)^3,$$

$$B_5 = \frac{K_v h_w}{2\sqrt{A_0} r_0},$$

where $a_3 = 1914$ $\mathrm{N}^{2/3}/\mathrm{m}^{4/3}$, $a_5 = -45348$ $\mathrm{N/m}^2$, K_v is the effective viscosity of the wall, h_w is the wall thickness while A_0 and r_0 are the vessels cross-section area and radius at time $t = 0$, respectively (1D arteries geometrical data reported in table A.1). Local wave velocity is estimated as $c_0 = a_2/(2r_0)^{b_2}$ [89], where $a_2 = 13.3$ $\mathrm{m}^{1.3}/\mathrm{s}$ and $b_2 = 0.3$.

The remaining terms of equation (3.7) represent Drzewiecki's partial collapse model [56], where $\widehat{EI} = 4.14$ mmHg is the vessel flexural rigidity normalized by the lumen radius cubed, $A_b = 10$ mm^2 and $p_b = -0.64$ mmHg are buckling cross-section area and pressure (at maximum compliance), respectively, while $m = 2$ is a constant defining the degree of curvature of the p-A hyperbola. Equation (3.7), that is Guala original model modified by introducing Drzewiecki partial collapse model applies to carotid and vertebral arteries numbered as 6, 12, 13, 16, 17 and 20 in Figure 3.2, while the original model version is employed for all the remaining branches of the arterial tree. By plugging equation (3.7) to equation (3.6), the final form of the momentum balance equation reads

$$\begin{aligned}\frac{\partial Q}{\partial t} + \beta\frac{Q^2}{A} + \frac{A}{\rho}\frac{\partial}{\partial x}\Bigg(B_1 + B_2 A + B_3 A^2 + B_4 A^3 - B_5 \frac{1}{\sqrt{A}}\frac{\partial Q}{\partial x} + \\ + \widehat{EI}\left(\frac{A_b^m}{A^m} - 1\right) + p_b\Bigg) - N_4 \frac{Q}{A} - Ag\sin\gamma\sin\alpha = 0,\end{aligned} \tag{3.8}$$

Figure 3.4 shows the comparison between the original versions of Guala and Drzewiecki models as well as their integration (Guala modified model). While the original version proposed by Guala is calibrated and thus valid within an arterial pressure range of 50 - 150 mmHg, and thus cannot mimic the correct arterial mechanical behavior at very low transmural pressure (Figure 3.4, orange curve), Drzewiecki model accounts for the partial collapse of arterial vessel. Indeed, Drzewiecki model prevents arterial cross-section area to fall below zero at near-zero or negative transmural pressure, by imposing a hyperbolic transition towards an asymptotic lower bound (Figure 3.4, blue curve). The results of the integration of the two models is thus depicted as the yellow curve in Figure 3.4, with smooth transition between the original behavior at high/normal transmural pressure range and low transmural pressure levels.

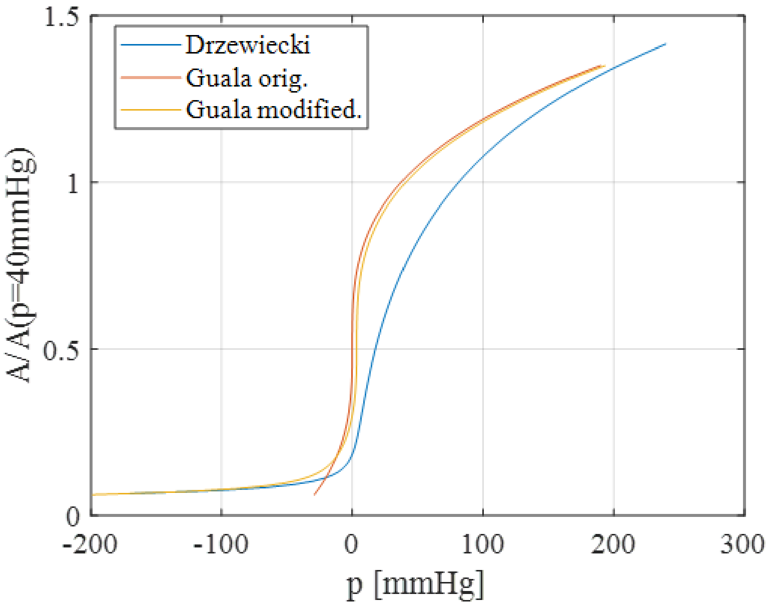

Figure 3.4: Behavior of different p - A relationships: from the original Guala model [89, 74] to the Guala modified model through integration with Drzewiecki partial-collapse model [56]. Example referred to carotid arteries outlet section, area A normalized by reference area value at 40 mmHg.

3.1.3 Boundary conditions

Suitable boundary conditions need to be identified and applied to all 63 arterial vessels composing the 1D arterial domain, including both at inlet/outlet sections of the arterial tree (*i.e.*, at the 1D-0D interfaces) and between adjacent arterial vessel branches, that is, at arterial bifurcations. In fact, at the inlet section of the 1D aorta, the 1D domain connects with the 0D model of the aortic valve and thus with the cardiopulmonary circulation (Figure 3.1). Conversely, all downstream terminal branches of the arterial tree denoted by orange circles in Figure 3.2 are linked to the following 0D arterial and systemic microcirculation through a set of lumped characteristic impedances Z_c. At arterial bifurcations, instead, typically one arterial vessel coming from upstream (hereinafter named as ‘parent vessel’) separates into two or more branches (named ‘daughter vessels) that proceed downstream with successive bifurcations. Therefore, at each arterial bifurcation each 1D parent vessel communicates with the related 1D daughter vessels.

Since the system of partial differential equations (3.3)-(3.8) involves two dependent variables, that is arterial cross-section area $A(x,t)$ and blood flow rate $Q(x,t)$, an equal number of conditions must be established at each boundary, that is one for each dependent variable ($A_\Gamma = A(x_\Gamma, t)$ and $Q_\Gamma = Q(x_\Gamma, t)$, with x_Γ indicating the boundary of each 1D arterial vessel). Boundary conditions for the 1D arterial problem should also respect a two-fold nature [89, 74]: (i) physical boundary conditions must be imposed and respected, accounting for the effect of adjacent CVS components (being these 0D districts communicating through the corresponding 1D-0D interface, or the remaining 1D arterial vessels of a given bifurcation) from which they are determined; (ii) compatibility conditions, extracted from the current vessel 1D internal domain through the method of characteristics. Indeed, at each arterial 1D boundary, one physical condition (i) coming from the external domain should be imposed in combination with one compatibility condition (ii) coming from the internal domain of the considered 1D vessel. An illustration of all types of boundary conditions implemented in the present model is provided in Figure 3.5. In the following, suitable physical and compatibility conditions are derived and presented for each type of boundary described above, that is at the entrance of the aorta, at terminal branches, and at arterial bifurcations.

Physical boundary conditions

- **Aortic entrance**: the first arterial vessel of the arterial tree, namely the aortic root (vessel No. 1 in Figure 3.2), is connected from upstream to the 0D model of the aortic valve. For the detailed description of the aortic valve model, refer to section 3.3, where cardiac valve lumped parameterization are introduced. The 0D aortic valve model provides a certain level of aortic blood flow (*i.e.*, Q_{ao}) which in turn enters the aorta through the aortic root. Thus, time variant $Q_{ao}(t)$ is imposed as external physical boundary condition onto the aortic entrance (Figure 3.5a).

- **Terminal branches**: at each outlet section of distal 1D arteries (orange circles in Figure 3.2), an external physical boundary condition is applied through connection with subsequent 0D arteriolar and systemic peripheral circulation. The coupling between 1D distal branches and following 0D arteriolar compartments (described in section 3.2) is achieved by means of a set of characteristic impedances Z_c plugged to each 1D aortic terminal branches (Figure 3.5b). Local characteristic impedances are defined such to minimize wave reflections at terminal 1D boundaries [278, 163, 2], and their expression takes thus the form

$$Z_c = \frac{\rho c}{A},$$

according to terminal arteries outlet section geometry and local wave velocity c (refer to table A.1 for details on 1D arterial geometry). Notice that, in order to match reported upright arterial pressure levels [292, 45, 155, 239, 242, 292, 268, 252, 61], values of Z_c belonging to arms (arteries No. 8, 10, 11, 22, 24, 25) have been reduced by 30%, while those belonging to legs (No. 43, 45, 47, 48) have been augmented by 70%, respectively, with respect to calibration reported in [74]. In addition, values of Z_c pertaining to the cerebral circulation (arteries No. 6, 12, 16, 20) have been decreased by 50% with respect to [74] (refer to section 3.5) balancing a suitable level of cerebral blood flow with a stable 1D-0D model coupling. 1D-0D coupling through characteristic impedance is achieved also between 1D coronary arteries (vessels No. 49. . . 62) and following 0D coronary miscovasculature, although for detailed definition of coronary arterial input Z_c refer to section 3.4.

Given the generic terminal branch, blood flow drained from the 1D terminal artery can be determined as

$$Q_{art1D} = Q_{art0D} = \frac{p_{out1D} - p_{art0D}}{Z_c}, \tag{3.9}$$

where p_{art0D} is 0D arteriolar compartment pressure (section 3.2), while p_{out1D} is obtained from A_{out1D} through the corresponding compatibility boundary condition.

- **Arterial bifurcations**: at junctions between arterial parent (subscript p) e subsequent daughter vessels (subscripts $d1$, $d2$, etc., Figure 3.5c), physical boundary conditions are determined via mass and total pressure conservation across the single bifurcation. To this end, the bifurcation is treated as a single point and all higher-dimensional effects - such as vessels bifurcation angles - are neglected. Thus, At a given bifurcation, the following system of equations holds

$$\begin{cases} Q_p = Q_{d1} + Q_{d2} + \dots \\ p_p + \frac{1}{2}\rho\left(\frac{Q_p}{A_p}\right)^2 = p_{d1} + \frac{1}{2}\rho\left(\frac{Q_{d1}}{A_{d1}}\right)^2 = p_{d2} + \frac{1}{2}\rho\left(\frac{Q_{d2}}{A_{d2}}\right)^2 = \dots \end{cases} . \tag{3.10}$$

Therefore, for a standard bifurcation with two daughter vessels, out of six total unknown involved in the boundary value problem of a given arterial bifurcation (A_p, A_{d1}, A_{d2}, Q_p, Q_{d1}, Q_{d2}) three equations are represented by the system of physical boundary conditions (3.10), while the remaining three equations are derived from the corresponding compatibility equations. The CVS model presented in this work includes also one atypical bifurcation, that is coronary bifurcation with the aortic root (vessel No. 1) branching into a first segment of the ascending aorta (vessel No. 63) plus left and right main coronary arteries (vessels No. 49, 58). An additional atypical bifurcation is the iliac bifurcation, with two identical daughter vessels (No. 42) branching from the same common parent vessel (No. 41), in order to save some computational efforts exploiting the symmetry of the lower portion of the human arterial tree [74].

Compatibility boundary conditions

A set of compatibility boundary conditions needs to be derived in order to completely define the boundary value problems at 1D boundaries. To this aim, the method of characteristics is applied to determine directions along which signals propagate within arterial vessels, along with conservation of the corresponding characteristic variables [44, 204]. From the quasi-linear form of the mass and momentum balance equations (3.3)-(3.8) (reported in appendix A, equations (A.3); notice that the pressure viscoelastic term is omitted for simplicity), one can compute the eigenvalues of the advection matrix, corresponding to the slope of left (subscript 1) and right (subscript 2) characteristic lines $\lambda_{1,2} = \frac{dx}{dt}$, that is

$$\lambda_{1,2} = \beta \frac{Q}{A} \pm c_\lambda, \tag{3.11}$$

with c_λ being the local wave celerity (wave speed), defined as

$$c_\lambda = \sqrt{\beta(\beta - 1)\frac{Q^2}{A^2} + \sum_{j=1}^{3} \frac{jA^j B_{j+1}}{\rho} + \frac{\widehat{EI}}{\rho}\frac{mA_b^m}{A^m}}.$$

Then, the characteristic variables are obtained as corresponding to the eigenvectors of system (A.3), although referred to as pseudo-characteristic variables due to the presence of source terms that do not allow for complete conservation along the characteristic lines. From time marching of the characteristic variables one eventually obtains the compatibility equations corresponding to eigenvalues (λ_1, λ_2), as

$$\lambda_1 : \quad Q^{n+1} = \lambda_2^n A^{n+1} + K_1, \tag{3.12}$$

and

$$\lambda_2 : \quad Q^{n+1} = \lambda_1^n A^{n+1} + K_2, \tag{3.13}$$

respectively, linking dependent variables A and Q values on the corresponding boundary (left: subscript 1; right: subscript 2) at time t^{n+1} to their respective values at time t^n and at the wavefoot situated at distance $\lambda \Delta t$ from the corresponding

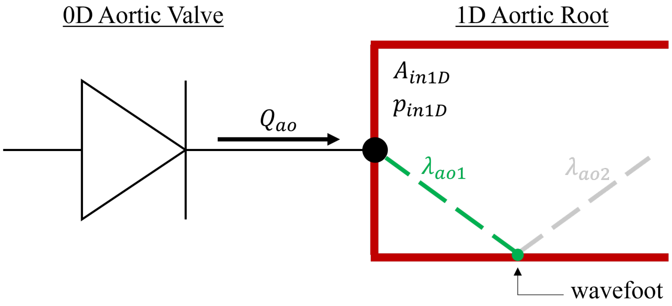

(a) Aortic entrance

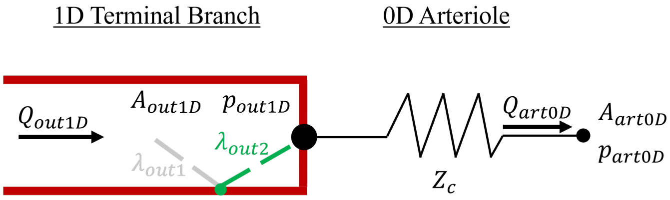

(b) Terminal branch

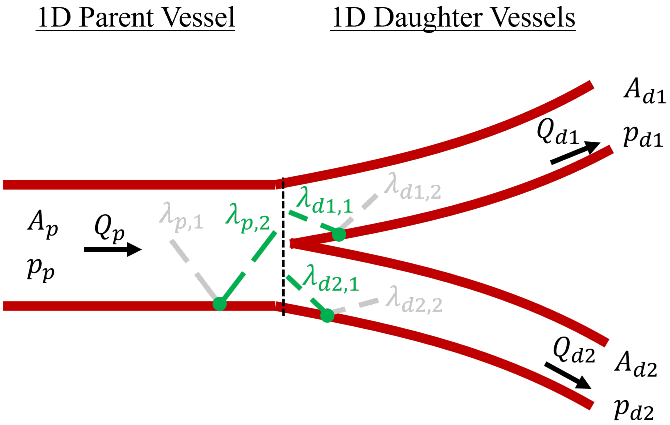

(c) Bifurcation

Figure 3.5: Physical and compatibility boundary conditions.

boundary (where $\Delta t = t^{n+1} - t^n$), through terms K_1 and K_2. K_1 and K_2 are defined as

$$\begin{aligned}K_1 = Q_*^n - \lambda_2^n A^0 - \lambda_{2,*}^n(A_*^n - A_*^0) + \Delta t\Bigg(- \lambda_{1,*}^n \frac{\partial \lambda_{2,*}^n}{\partial x}(A_*^n - A_*^0) + \\ - \Bigg(\sum_{j=1}^{4} \frac{A_*^{j,n}}{\rho}\frac{dB_{j,*}}{dx} - N_{4,*}\frac{Q_*^n}{A_*^n} - A_*^n g^n \sin\gamma \sin\alpha^n - \sum_{j=1}^{4} \frac{A_*^{j,0}}{\rho}\frac{dB_{j,*}}{dx} + \\ + N_{4,*}\frac{Q_*^0}{A_*^0} + A_*^0 g^0 \sin\gamma \sin\alpha^0\Bigg)\Bigg),\end{aligned} \tag{3.14}$$

and

$$\begin{aligned}K_2 = Q_*^n - \lambda_1^n A^0 - \lambda_{1,*}^n(A_*^n - A_*^0) + \Delta t\Bigg(- \lambda_{2,*}^n \frac{\partial \lambda_{1,*}^n}{\partial x}(A_*^n - A_*^0) + \\ - \Bigg(\sum_{j=1}^{4} \frac{A_*^{j,n}}{\rho}\frac{dB_{j,*}}{dx} - N_{4,*}\frac{Q_*^n}{A_*^n} - A_*^n g^n \sin\gamma \sin\alpha^n - \sum_{j=1}^{4} \frac{A_*^{j,0}}{\rho}\frac{dB_{j,*}}{dx} + \\ + N_{4,*}\frac{Q_*^0}{A_*^0} + A_*^0 g^0 \sin\gamma \sin\alpha^0\Bigg)\Bigg),\end{aligned} \tag{3.15}$$

where asterisks denote variables taken at the foot of the wave (that is at distance $\lambda\Delta t$ from the considered boundary) at a given time, while superscript 0 refers to the initial condition. Full derivation of derivative terms $\frac{\partial \lambda_2}{\partial x}$ and $\frac{\partial \lambda_1}{\partial x}$ are reported in appendix A, equations (A.4).

- **Aortic entrance**: the second boundary condition applied to fully characterize the aortic inlet section is the compatibility condition coming from the internal domain of the 1D aortic root vessel. As shown in Figure 3.5a, while aortic root blood flow rate (Q_{ao}) is provided by the 0D aortic valve model, aortic root cross-section area (A_{in1D}) and blood pressure (p_{in1D}) are obtained from the internal 1D domain by projecting the corresponding left characteristic line (λ_{ao1}) from the foot of the wave onto the corresponding boundary. Therefore, A_{in1D} and p_{in1D} are computed through equations (3.12) and (3.7).

- **Terminal branches**: at various terminal branches, exploiting the right characteristic line (λ_{out2}) reaching each 1D outlet section boundary from upstream (Figure 3.5b), equation (3.9) now becomes

  $$\lambda_{out1}A_{out1D} + K_{2,out1D} = \frac{p_{out1D} - p_{art0D}}{Z_c},$$

  and by writing p_{out1D} as a function of A_{out1D} through equation (3.7), one obtains a non-linear problem which can be solved through Newton-Raphson method to finally determine A_{out1D}, p_{out1D} and Q_{out1D} (details in [74]).

- **Arterial bifurcations**: to fully characterize each boundary value problem at a given arterial bifurcation, system (3.10) is re-arranged by employing all compatibility equations related to characteristic lines reaching the corresponding boundaries (*i.e.*, right characteristic line $\lambda_{p,2}$ for the parent vessel, and left characteristic lines $\lambda_{d1,1}$, $\lambda_{d2,1}$, ... for all daughter vessels, Figure 3.5c). Thus, system (3.10) takes the form

$$\begin{cases} \lambda_{p,1} A_p + K_{2,p} = \lambda_{d1,2} A_{d1} + K_{1,d1} + \lambda_{d2,2} A_{d2} + K_{1,d2} + \dots \\ p_p + \dfrac{1}{2}\rho\left(\dfrac{\lambda_{p,1} A_p + K_{2,p}}{A_p}\right)^2 = p_{d1} + \dfrac{1}{2}\rho\left(\dfrac{\lambda_{d1,2} A_{d1} + K_{1,d1}}{A_{d1}}\right)^2 \\ p_p + \dfrac{1}{2}\rho\left(\dfrac{\lambda_{p,1} A_p + K_{2,p}}{A_p}\right)^2 = p_{d2} + \dfrac{1}{2}\rho\left(\dfrac{\lambda_{d2,2} A_{d2} + K_{1,d2}}{A_{d2}}\right)^2 \\ p_p + \dfrac{1}{2}\rho\left(\dfrac{\lambda_{p,1} A_p + K_{2,p}}{A_p}\right)^2 = \dots \end{cases},$$

and by applying again equation (3.7) to write terms p_p, p_{d1}, p_{d3}, ... as functions of the corresponding area A_p, A_{d1}, A_{d2}, ..., one obtain a non-linear system of equations which can be solved through Newton-Raphson method to determine all cross-section areas, pressures and flow rates of the selected bifurcation (details in [74]).

3.2 0D systemic microcirculation and venous return

The global CVS model encompasses a wide 0D counterpart representing systemic microcirculation and venous return, departing from terminal 1D distal arteries and eventually connecting to the cardiopulmonary circulation, at the level of the right atrium. Figure 3.1 shows the overall CVS layout with the 0D systemic circulation on the right side, linked to the 1D counterpart through red and blue arrows representing arterial and venous blood pathways.

In the following, the model of 0D systemic circulation is presented starting from the general architecture of the various lumped parameter districts and compartments, while introducing then a number of peculiar elements such as non-linear constitutive laws and venous valves. Finally, details on the parameters calibration are provided.

3.2.1 Topology of the 0D model counterpart

The model of 0D systemic circulation is multifaceted and topologically intricated. Starting from the 1D-0D interface at multiple distal arterial branches (orange circles in Figures 3.1 and 3.2), a distinct arteriolar 0D circuital model is included for each 1D terminal artery. As illustrated in Figure 3.1, arteriolar compartments are then grouped into five body macro-regions: head, arms, upper abdomen, lower abdomen and legs (grey boxes in Figure 3.1). For each region, one capillary, one venular and one venous compartment are introduced, as shown in Figure 3.6. As also show in the same figure, three additional districts are included to represent superior, inferior and abdominal venae cavae, collecting blood from prior venous compartments (also belonging to different regions) and directly connected to the subsequent downstream cardiopulmonary circulation (section 3.3). The subdivision of the 0D systemic circulation into five distinct regions allows for evident distinction of the gravitational effects onto different body compartments, from head to feet, especially at postures different from supine and devoting special attention to the head and legs compartments in particular, where the largest gravity impact occurs.

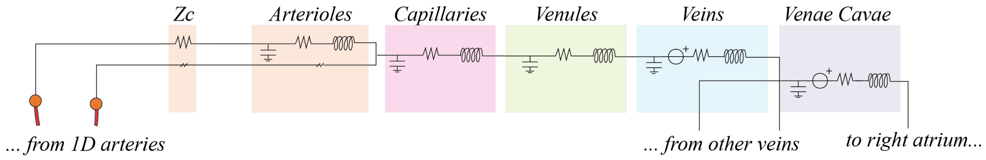

Figure 3.6: Generic branch (*i.e.*, region) of the 0D systemic circulation. From left to right, past the characteristic impedance(s) connecting to the 1D counterpart, arteriolar, capillary, venular, venous and venae cavae compartments are represented.

3.2.2 The generic RLC compartment

Systemic distal circulation (arteriolar), microcirculation and venous return are represented as lumped parameter compartments according to an electric analogy [278] and following the 3-element Windkessel approach [275, 233, 261]. Each vascular district (or compartment, that is arterioles, capillaries, veins or venae cavae) belonging to a given body region is composed of a 3-element RLC electrical circuit accounting for vessels hydraulic resistance (R), compliance (C) and blood inertia (L), respectively, as illustrated in Figure 3.6.

In the following, the 5 body macro-regions corresponding to separate body portions grouping 0D compartments are indicated as H, A, UA, LA and L, denoting head, arms, upper abdomen, lower abdomen and legs, respectively. Furthermore, arteriolar, capillary, venular, venous and venae cavae (superior, inferior, and abdominal venae cavae) districts are referred to as art, cap, ven, v, svc, ivc and avc, respectively.

Equations governing blood motion in the (i, j)-th 0D compartment are

$$\frac{dV_{i,j}}{dt} = Q_{i,j-1} - Q_{i,j}, \tag{3.16}$$

for mass balance, and

$$\frac{dQ_{i,j}}{dt} = \begin{cases} \dfrac{p_{i,j} + \Delta p^h_{i,j} - R_{i,j}Q_{i,j} - p_{i,j+1}}{L_{i,j}}, & \text{if } j \in \{v, svc, ivc, avc\} \\ \dfrac{p_{i,j} - R_{i,j}Q_{i,j} - p_{i,j+1}}{L_{i,j}}, & \text{if } j \in \{art, cap, ven\} \end{cases}, \tag{3.17}$$

for momentum balance, where subscript i corresponds to the belonging body region (H, A, UA, LA, L)[1], whereas j denotes the compartment (art, gathering all arterioles connected to the considered body region, cap, ven, v, svc, ivc, and avc). Intraluminal pressure of the (i, j)-th compartment is indicated with $p_{i,j}$, blood flow rate is denoted as $Q_{i,j}$, with $p_{i,j+1}$ and $Q_{i,j-1}$ being blood pressure and flow rate of the following and previous 0D compartments, respectively. $V_{i,j}$ is the compartmental total blood volume, obtained as the summation of the corresponding unstressed blood volume $V^{un}_{i,j}$ and the stressed blood volume. This latter depends on the compartmental transmural pressure $p^t_{i,j} = p_{i,j} - p^{ext}_{i,j}$ and on the associated compliance $C_{i,j}$ according to the following constitutive law

$$V_{i,j} = V^{un}_{i,j} + p^t_{i,j}C_{i,j} = V^{un}_{i,j} + \left(p_{i,j} - p^{ext}_{i,j}\right)C_{i,j}, \tag{3.18}$$

where symbol $p^{ext}_{i,j}$ is extravascular pressure, corresponding to either intrathoracic, intracranial or intramyocardial pressure according to the specific compartment (where no external pressure is specified, an external environmental relative pressure of 0 Pa is assumed). An additional relation can be derived for blood pressure $p(t)$ by combining equations (3.18) and (3.16):

$$\frac{dp_{i,j}}{dt} = \frac{Q_{i,j-1} - Q_{i,j}}{C_{i,j}}. \tag{3.19}$$

Tuning values of 0D systemic circulation parameters are reported in appendix B, Tables B.1 and B.2, while details on the calibration strategy are reported later in this section.

Gravity contribution is accounted for by including gravity source terms in 0D compartments (represented as a lumped pressure generators within pertaining compartments, as reported in Figure 3.6) depending on hydrostatic pressure gradients

---

[1] notice that venae cavae compartments do not pertain to any of these body regions, *i.e.* no index i is assigned

through Stevino's law, as widely proposed in the literature [94, 93, 136, 10]. However, such previous models did not encompass arteriolar and venular compartments beside arterial and venous ones. In our model, instead, arteriolar, capillary and venular compartments are present and describe very confined and localized vascular districts, which are therefore not affected by gravitational stress when undergoing posture variations due to their limited anatomical extension. Thus, hydrostatic pressure terms are included within venous and venae cavae compartments only, being those with marked intrinsic anatomical extension with respect to the longitudinal body axis.

Hydrostatic pressure terms $\Delta p^h_{i,j}$ appearing in equation. (3.17) are thus expressed according to Stevino's law as:

$$\Delta p^h_{i,j} = \rho g \Delta h_{i,j} \sin \alpha, \tag{3.20}$$

where ρg is blood specific weight, $\Delta h_{i,j}$ is the hydrostatic height of the corresponding fluid column, and α is the compartment orientation with respect to the horizontal reference (tilt angle). Due to the feetwards orientation of the body axis, compartments hydrostatic heights are taken as positive when moving accordingly to a head-feet direction (head veins, superior vena cava) whereas negative when oriented in the opposite direction (leg and arm veins, abdominal and inferior venae cavae). Blood column hydrostatic heights are associated with the anatomical length of the corresponding compartments projected along the longitudinal body axis. They are determined as the summation/subtraction of half the characteristic lengths of two adjacent compartments, representing the vertical anatomical distance separating their compartmental midpoints, as shown in Figure 3.7. Assumed hydrostatic column heights are reported in Table B.3.

3.2.3 Non-linear p - V equation

For the legs venous compartment, a different constitutive law is introduced to resemble non-linear effects of distending veins volume, when subject to high pressure level caused by gravitational stress, as suggested by several authors [153, 94, 93, 136]. The different constitutive law adopted to resemble non-linear effects of legs veins pressure-volume relation reads

$$V_{L,v} = V^{un}_{L,v} + \frac{2\Delta V_{max}}{\pi} \arctan\left(\frac{\pi C_{L,v}}{2\Delta V_{max}} p^t_{L,v}\right), \tag{3.21}$$

in which ΔV_{max} is the maximum distending volume of leg veins, assumed as high as 1200 ml [94, 93], $C_{L,v}$ is the leg venous compliance at zero transmural pressure (taken equal to venous compliance in supine position), and $p^t_{L,v} = p_{L,v}$ for leg venous transmural pressure.

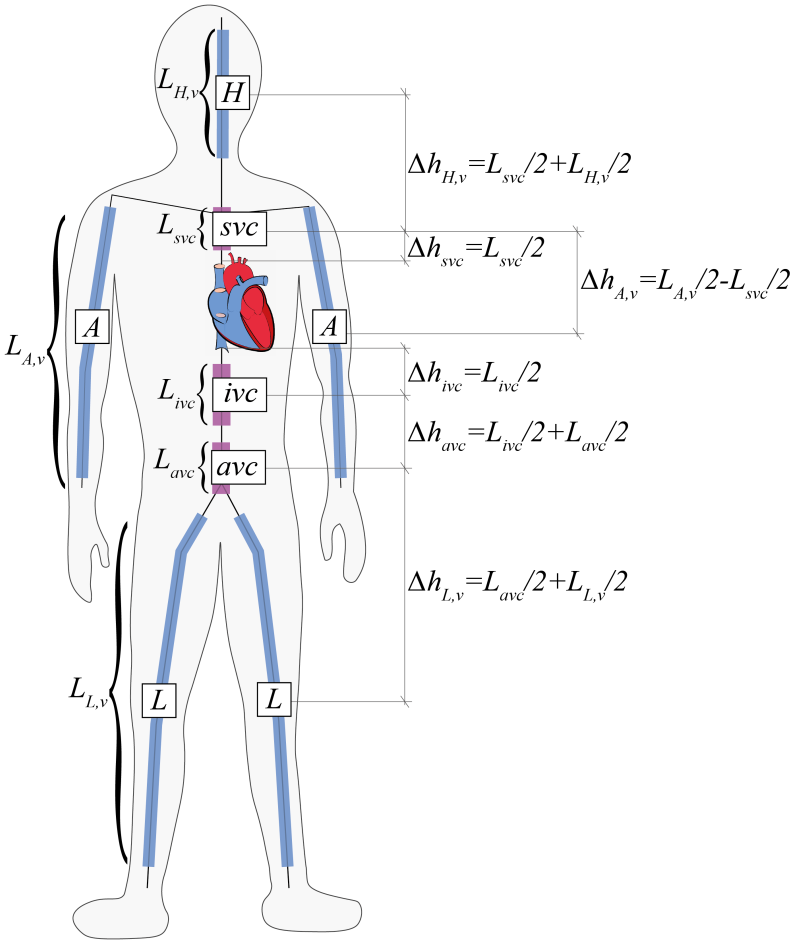

Figure 3.7: Venous and venae cavae vertical anatomical lengths. $L_{H,v}$, $L_{A,v}$, $L_{L,v}$, L_{svc}, L_{ivc} and L_{avc} are characteristic vertical anatomical lengths of the head, arms and legs veins, superior vena cava, inferior vena cava and abdominal vena cava compartments (reported in Table B.3), $\Delta h_{H,v}$, $\Delta h_{A,v}$, $\Delta h_{L,v}$, Δh_{svc}, Δh_{ivc} and Δh_{avc} are vertical hydrostatic columns heights corresponding to the same compartments midpoint distances. Image taken from [68].

3.2.4 Venous valves

Venous valves ensuring unidirectional flow in human veins, and thus preventing from venous blood backflow or reverse flow, are introduced in the global CVS model presented in this work as non-ideal diodes, as proposed in [164] and also adopted by [110, 111, 296]. The venous valve model is integrated within legs and arms venous compartments, and valves intervention is achieved by non-linear resistances and inertances associated with those compartments. Each venous valve is virtually placed in between the end of the corresponding venous compartment (arms or legs) and the following vena cava (superior or abdominal, respectively).

Venous valves are represented by adding a non-linear behavior to hydraulic resistances and inertances within the arms and legs venous compartments, that is $R_{A,v}$, $R_{L,v}$, $L_{A,v}$ and $L_{L,v}$. Equation (3.17) for the arms/legs venous compartments (subscript $A/L,v$) thus modifies as

$$\begin{aligned}\frac{dQ_{A/L,v}}{dt} &= \\ &= \frac{\xi_{A/L,v}(p_{A/L,v} + \Delta p^h_{A/L,v} - p_{svc/avc}) - R_{A/L,v}Q_{A/L,v} - B_{A/L,v}|Q_{A/L,v}|Q_{A/L,v}}{L_{A/L,v}}\,,\end{aligned} \tag{3.22}$$

where $p_{A/L,v} + \Delta p^h_{A/L,v}$ and $p_{A/L,vc}$ are pressures immediately upstream and downstream the venous valve, while the function of the valve opening state $\xi_{A/L,v}$ is expressed as

$$\xi_{A/L,v} = \begin{cases}(1-\xi_{A/L,v})k_{vo}(p_{A/L,v} + \Delta p^h_{A/L,v} - p_{svc/avc})\,, & \text{if} \quad \Delta p_{A/L,v} \geq 0 \\ \xi_{A/L,v}k_{vc}(p_{A/L,v} + \Delta p^h_{A/L,v} - p_{svc/avc})\,, & \text{if} \quad \Delta p_{A/L,v} < 0\end{cases}\,. \tag{3.23}$$

Parameters $k_{vo} = k_{vc} = 40$ 1/(mmHg s) are valve's opening and closing rate, respectively. $B_{A/L,v} = \rho/(2A^{eff}_{A/L,v})$ is the Bernoulli's coefficient, while $L_{A/L,v} = \rho(l^{eff}_{A/L,v}/A^{eff}_{A/L,v})$ and $R_{A/L,v} = 8\pi\mu/(A^{eff}_{A/L,v})^2$, with $l^{eff}_{A/L,v}$ assumed equal to the compartment radius, and the effective area $A^{eff}_{A/L,v}$ defined as

$$A^{eff}_{A/L,v} = \left(A^{eff,max}_{A/L,v} - A^{eff,min}_{A/L,v}\right)\xi_{A/L,v} + A^{eff,min}_{A/L,v}\,, \tag{3.24}$$

where $A^{eff,min}_{A/L,v} = 0$, $A^{eff,max}_{A/L,v} = A_{A/L,v}$, that is $V_{A/L,v}/L_{A/L}$ - ratio of the compartmental total blood volume and the characteristic length of the arms/legs venous compartments. Compartment radius can be determined from $A_{A/L,v}$ (assuming a circular compartment cross-section). Taking as reference the initial state of the system - for which $R_{A/L,v}(t=0) = R^0_{A/L,v}$ and $L_{A/L,v}(t=0) = L^0_{A/L,v}$, with venous valves completely open ($\xi_{A/L,v}(t=0) = 1$, $A^{eff}_{A/L,v}(t=0) = A^{eff,max}_{A/L,v}$) - the following expressions can be derived for the non-linear resistance $R_{A/L,v}$ and inertance $L_{A/L,v}$:

$$R_{A/L,v} = R^0_{A,L,v}\left(\frac{A^{eff,max}_{A/L,v}}{A^{eff}_{A/L,v}}\right)^2, \qquad L_{A/L,v} = L^0_{A/L,v}\frac{A^{eff,max}_{A/L,v}}{A^{eff}_{A/L,v}}. \tag{3.25}$$

3.2.5 Model calibration

Parameter setting was based on previous modeling works [76, 75, 93, 135, 136]. Specifically, nearly the same total peripheral resistance at the reference supine posture has been maintained with respect to [74], while resistance distribution across different regions (from head to legs) has been conducted following the same strategy reported in works by Liang *et al.* [135, 134]. The same approach has also been adopted for vascular compliance and inertances of various regions. Repartition of resistances, compliance and inertance across different compartments (from capillary to venae cavae) of a given body region has been conducted mostly by respecting proportions suggested in [74]. Whenever evident topological differences arose between the present CVS model and that from [135, 134], the procedure adopted consisted of splitting resistances, compliances and inertances in parallel when belonging to different body regions, or in series when associated with the same region, by resorting to circuital relations anticipated in chapter 1, section 1.3. Detailed model settings and parameter tuning are reported in appendix B, Table B.2.

Particular attention was devoted to total blood volume repartition over the global CVS system. A total blood volume of 5700 ml was assumed [74], and blood was distributed according to physiological proportions reported in [92, 131, 270, 109, 19]. Regional and compartmental levels of total and unstressed volume all over the 0D model side are reported in appendix B, Table B.2.

3.3 0D cardiopulmonary circulation

The 0D model of the cardiopulmonary circulation includes lumped models of the four cardiac chambers and the pulmonary circulation. The cardiopulmonary circulation completes the closed-loop CVS global model by draining blood collected from superior and inferior venae cavae to be then ejected again into the 1D aorta (Figure 3.1, central orange box). A schematic representation of the cardiopulmonary circulation including the four contractile cardiac chambers, pulmonary compartments and related analogue circuital components is displayed in Figure 3.8.

The present section is organized by first introducing the model of contractile cardiac chambers and related equations, as well as the models of cardiac valves. Subsequently, the pulmonary circulation compartments are described, to conclude with an introduction to intrathoracic pressure influencing the whole cardiopulmonary hemodynamics.

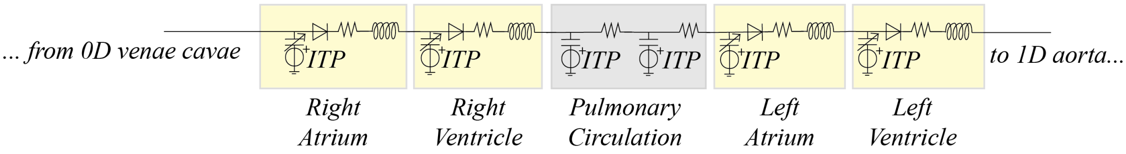

Figure 3.8: Cardiopulmonary circulation: from right atrium to left ventricle; cardiac valves are represented through non-ideal diodes, ITP denotes intrathoracic pressure.

3.3.1 Contractile heart chambers

Cardiac chambers are modeled as contractile compartments through a time-varying elastance model governed by the heart rate HR given as input (either externally provided or dictated by short-term regulation controls in a closed-loop arrangement).

Time-varying elastance functions $E_{ch}(t)$ (subscript ch stands for chamber, that is right atrium, right ventricle, left atrium, or left ventricle) are employed to mimic cardiac chambers mechanics, so that the equation linking cardiac transmural pressure $p^t_{ch} = p_{ch} - ITP$ (where ITP is intrathoracic pressure) and stressed volume $V_{ch} - V^{un}_{ch}$ (V^{un}_{ch} is chamber's unstressed volume) reads

$$p_{ch} = E_{ch}\Big(V_{ch} - V^{un}_{ch}\Big) + ITP, \tag{3.26}$$

where the single-chamber elastance function $E_{ch}(t)$ is governed by the relation

$$E_{ch} = E_{ch,A}e_{ch} + E_{ch,B}. \tag{3.27}$$

Here, parameters $E_{ch,A}$ and $E_{ch,B}$ are single-chamber's elastance amplitude and baseline value, respectively. Instead, the normalized shape-elastance function $e_{ch}(t)$ follows a different formulation depending on whether it is adopted for atria ($e_a(t)$)

$$e_a(t) = \begin{cases} \frac{1}{2}\left[1 + \cos\left(\pi \dfrac{t + RR - t_{ar}}{T_{ar}}\right)\right], \; 0 \leq t \leq t_{ar} + T_{ar} - RR \\ 0\,, \qquad t_{ar} + T_{ar} - RR < t \leq t_{ac} \\ \frac{1}{2}\left[1 - \cos\left(\pi \dfrac{t - t_{ac}}{T_{ac}}\right)\right], \; t_{ac} < t \leq t_{ac} + T_{ac} \\ \frac{1}{2}\left[1 + \cos\left(\pi \dfrac{t - t_{ar}}{T_{ar}}\right)\right], \; t_{ac} + T_{ac} < t \leq RR \end{cases}, \tag{3.28}$$

or for ventricles ($e_v(t)$):

$$e_v(t) = \begin{cases} \frac{1}{2}\left[1 - \cos\left(\pi \dfrac{t}{T_{vc}}\right)\right], \; 0 \leq t \leq T_{vc} \\ \frac{1}{2}\left[1 + \cos\left(\pi \dfrac{t - T_{vc}}{T_{vr}}\right)\right], \; T_{vc} < t \leq T_{vc} + T_{vr} \\ 0\,, \qquad T_{vc} + T_{vr} < t \leq RR \end{cases}, \tag{3.29}$$

where RR is the heart beat duration (*i.e.*, $60/HR$), parameters T_{ac}, T_{ar}, T_{vc} and T_{vr} correspond to atria and ventricles contraction and relaxation periods, respectively, and t_{ac} and t_{ar} denote atria contraction and relaxation starting time.

By differentiating equation (3.26), the single-chamber pressure differential equation is obtained:

$$\frac{dp_{ch}}{dt} = \frac{dE_{ch}}{dt}\Big(V_{ch} - V_{ch}^{un}\Big) + E_{ch}\Big(Q_{ch,in} - Q_{ch,out}\Big) + \frac{dITP}{dt}\,, \tag{3.30}$$

where $Q_{ch,in}$ and $Q_{ch,out}$ are injected and ejected blood flow rate into and out of each cardiac chamber. The latter equation (3.30) is employed to govern all intrachamber pressures, determining the overall cardiovascular functioning and blood ejection from the heart.

All cardiac chambers settings are summarized in appendix B, Table B.4.

3.3.2 Cardiac valves

Cardiac valves are modeled as non-ideal diodes accounting for several effects onto valve leaflets (*i.e.*, on each valve opening angle, θ_{va}), such as surrounding tissues friction, pressure across the valve and inertial forces, as well as the influence of downstream vortexes. Each 0D valve model includes the so-called Bernoulli's resistance of the valve - accounting for convective acceleration and dynamic pressure losses - as well as valve viscous resistance and inertance terms. The valve model governs blood flow rate across the valve (Q_{va}), reproduced according to the following model by Korakianitis *et al.* [118]:

$$\begin{aligned} L_{va}\frac{dQ_{va}}{dt} + R_{va}Q_{va} + B_{va}|Q_{va}|Q_{va} &= \\ &= \frac{\Big(1-\cos(\theta_{va})\Big)^4}{\Big(1-\cos(\theta_{va,max})\Big)^4}\Big(p_{va,u} - p_{va,d}\Big), \end{aligned} \tag{3.31}$$

$$\begin{aligned} I_{va}\frac{d^2\theta_{va}}{dt^2} =& K_{p,va}\Big(p_{va,u} - p_{va,d}\Big) + K_{q,va}Q_{va}\cos(\theta_{va}) \\ &- K_{f,va}\frac{d\theta_{va}}{dt} - K_{v,va}Q_{va}\sin(2\theta_{va}). \end{aligned} \tag{3.32}$$

In the previous relations, terms such as tissues friction ($K_{f,va}\frac{d\theta_{va}}{dt}$), pressure difference ($K_{p,va}(p_{va,u} - p_{va,d})$), inertial forces ($K_{q,va}Q_{va}\cos(\theta_{va})$), and the influence of downstream vortexes ($K_{v,va}Q_{va}\sin(2\theta_{va})$) are incorporated to control the valve opening state θ_{va} - with respect to the maximum valve opening state, $\theta_{va,max} = 75°$ - through valve's inertia (I_{va}, that is single-valve's momentum of inertia). B_{va} is Bernoulli's coefficient of the valve, R_{va} and L_{va} are valve resistance and inertance. $p_{va,u}$ and $p_{va,d}$ are upstream and downstream pressures acting onto valve leaflets. While $p_{va,u} - p_{va,d} \geq 0$, then vortexes action is taken into account, otherwise it is neglected. Valve model parameters are summarized in Table B.4, where k_p, k_q, k_f, k_v are coefficients K_{va} normalized by the valve's momentum of inertia I_{va}.

3.3.3 Pulmonary circulation

Arterial and venous pulmonary circulations are described simply as RC lumped compartments (Figure 3.8), that is by including a lumped viscous resistance and a vascular compliance each [75].

Equations governing pulmonary arterial and venous compartments read

$$\frac{dp_j}{dt} = \frac{Q_{j-1} - Q_j}{C_j} + \frac{d(ITP)}{dt}, \tag{3.33}$$

and

$$Q_j = \frac{p_j - p_{j+1}}{R_j}, \tag{3.34}$$

where $j - 1 = puv$ (pulmonary valve) and $j + 1 = pv$ (pulmonary veins) when $j = pa$ (pulmonary arteries), whereas $j - 1 = pa$ and $j + 1 = lv$ (left atrium) when $j = pv$. Values of pulmonary 0D parameters are reported in appendix B, Table B.2.

3.3.4 Intrathoracic pressure

As anticipated in chapter 2, intrathoracic pressure (ITP) can improve venous return by promoting cardiac preload, *i.e.*, right atrium filling [288, 114, 265, 52, 30, 199]. As intrinsically influenced by posture and gravity-induced alterations, intrathoracic pressure is integrated in the current model as additional mechanism shaping the overall cardiovascular response. As suggested by [93, 10], at fixed posture intrathoracic pressure is superimposed as external (extra-vascular or extra-chamber) constant pressure acting onto thoracic compartments (cardiac chambers and pulmonary circulation compartments). Specifically, ITP is believed to decrease by a few mmHg when assuming the upright posture at 1g, due to gravity pulling action onto thoracic cavity fluids and the diaphragm [28, 152, 289].

Moreover, Petersen *et al.* [192] explored further the role of ITP on the overall cardiovascular response under various conditions, evaluating the level of ITP reached at various gravity accelerations and different postures. Values of ITP proposed in [192] at supine, seated, and standing postures under 0g, 1g, and 1.8g gravity acceleration are reported in Table 3.1. Thus, the authors found that beside physiological ITP variation with body posture mentioned above, intrathoracic pressure is differently affected also by gravity acceleration depending on whether the subject lies supine or stands upright, due to the pushing action of the diaphragm against the thoracic cavity, as also confirmed by Norsk [169] and Videbaek & Norsk [266]. In the supine posture, the diaphragm is pushed headward by the compression of the abdominal cavity with increasing gravity, thus raising ITP inside the thoracic cavity. Conversely, at seated or standing posture, an augmented gravity results in a releasing effect onto the thoracic cavity (*i.e.*, lower ITP by pulling the diaphragm feetwards.

Table 3.1: assumed value of intrathoracic pressure (ITP) depending on body posture (supine or seated/standing) and gravity acceleration g/g_0 (values from [192, 169, 266]).

Intrathoracic pressure ITP [mmHg]			
	0g	1g	1.8g
supine	-4.1	-2.5	-2.2
seated	-4.1	-6.5	-7.2
standing	-4.1	-6.5	-7.2

To take into account both posture and gravity-drive effects onto the thoracic cavity state and ITP, in the present thesis we propose a model for ITP expressed as a function of posture (through the tilt angle α) and gravity acceleration (normalized as $\frac{g}{g_0}$, where g_0=9.81 m/s^2) by fitting data reported in Table 3.1 (Figure 3.9 shows the interpolating surface obtained with the data processing tool in Matlab). The ITP model thus reads

$$ITP(\alpha, g) = -4.014 + 1.127\frac{g}{g_0} + 0.895\left(\frac{g}{g_0}\right)^2 \sin\alpha - 4.508\frac{g}{g_0}\sin\alpha, \tag{3.35}$$

with standard squared error SSE $= 0.21$ mmHg^2 and coefficient of determination R$^2 = 0.99$.

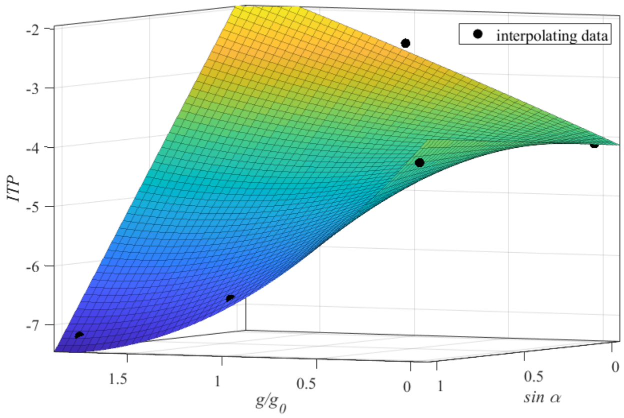

Figure 3.9: Interpolating surface for ITP based on $\sin\alpha$ and g data reported in [192]. Black dots are interpolating data taken from Table 3.1.

3.4 1D-0D coronary circulation

A multiscale description of the coronary circulation is adopted in the present model, as shown in Figure 3.10, distinguishing between a 1D representation of large coronary arteries (vessels No. 49-62 in Figure 3.2) and a 0D circuital model of the downstream coronary microcircirculation, perfusing the different layers of the cardiac muscle (*i.e.*, the myocardium). The same mathematical approach presented for the arterial tree in section 3.1 is applied here to the 1D portion of the coronary circulation, whereas to describe 0D coronary microvasculature the model introduced by [160, 162] is adopted and summarized in the following.

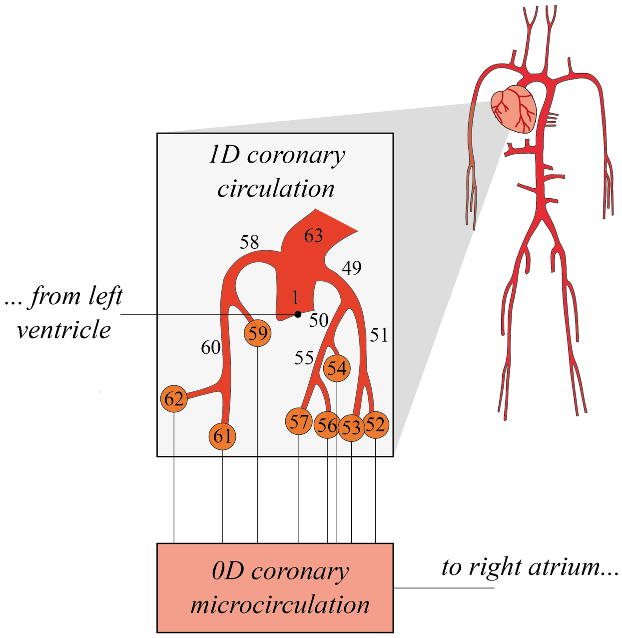

Figure 3.10: Illustration of 1D large coronary arteries, with black numbers identifying each of the 14 large coronary arteries (see appendix A, Table A.1 for more details on arteries nomenclature and characteristics). Thin, black lines departing from 1D coronary arteries terminal branches (orange circles) connects to the downstream 0D coronary microcirculation of the myocardium.

3.4.1 0D intramyocardial circulation layout

As depicted in Figure 3.10, each 1D coronary artery ends by connecting to a distinct 0D analogue of the downstream coronary microcirculation of the myocardial muscle [160, 162]. All 0D coronary miscovascular districts are topologically identical, and the generic architecture of a single coronary microvascular district is illustrated in Figure 3.11. Each 0D coronary microvascular district is subdivided into three perforating branches penetrating the cardiac muscle, representing the three layers of the myocardium (that is, subepicardium, midwall, and subendocardium). Each myocardial layer is further composed of an arterial, an intermediate and a venous compartment.

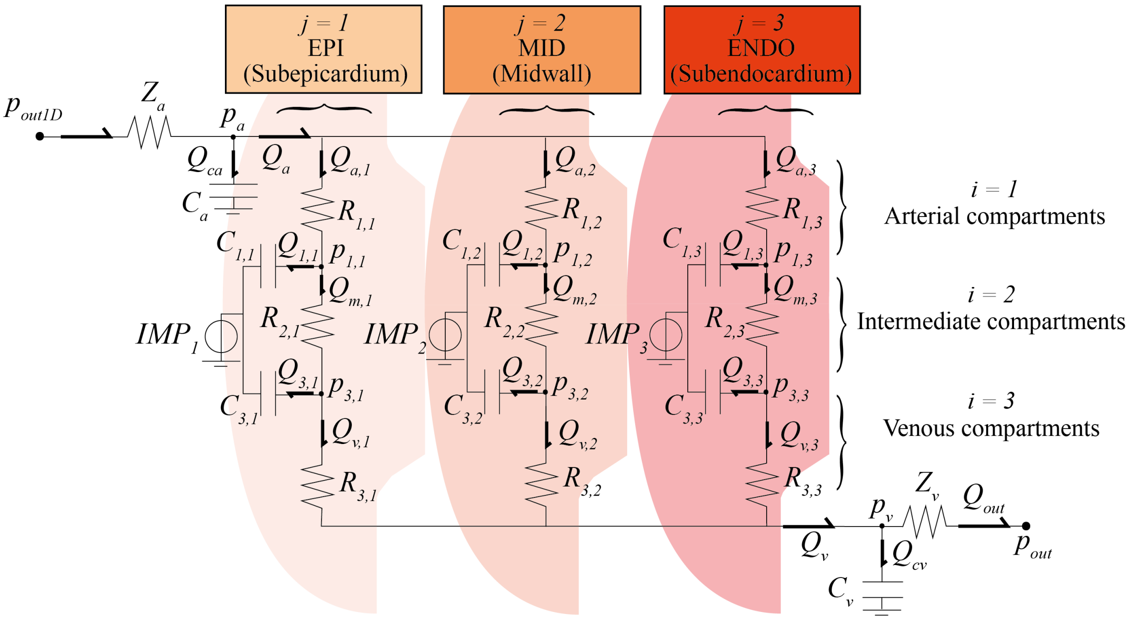

Figure 3.11: 0D lumped parameter circuital scheme of a generic coronary distal microvascular district. Different myocardial layers (index j, acronyms EPI, MID and ENDO stand for subepicardium, midwall and subendocardium, respectively) and compartments (index i, divided into arterial, intermediate and venous) of the myocardial circulation proposed by [160, 162] are displayed.

Therefore, blood flow reaching the 0D coronary microvasculature penetrates the myocardium and divides across the three myocardial layer of a given district according to their resistance and compliance. While going through myocardial layers, blood flow is also subject to the external compression exerted by the nearby cardiac chamber, determining the peculiar coronary hemodynamics as anticipated in chapter 1, section 1.2. Eventually, blood flows out from the venous side of the coronary vasculature and reaches the right atrium together with venae cavae blood flow (Figure 3.10).

3.4.2 Intramyocardial compliances, volumes and resistances

For each 0D coronary microvascular district (in the following referred to as the k-th district), intra-layer resistances are non-linear, and vary in time with the inverse of blood volume squared, according to Poiseuille's law. They are determined through Murray's law, on the basis of the total regional resistance (left ventricle, septum, right ventricle) pertaining to a given myocardial layer. Compliances and initial blood volumes are derived in a similar fashion, exploiting Murray's law with respect to the myocardial weight of each perfused region.

For the k-th 0D coronary microvascular district, arterial ($C_{1,j,k}$) and venous ($C_{3,j,k}$) compliances of the j-th layer ($j = 1$ subepicardium, $j = 2$ midwall, $j = 3$ subendocardium) are calculated exploiting Murray's law with respect to the myocardial weight of each perfused region (W_G, see Table B.5):

$$C_{1,j,k} = C_{1,T} \frac{W_G}{\sum_{k \in G} r_k^3} \gamma_j, \tag{3.36}$$

$$C_{3,j,k} = C_{3,T} \frac{W_G}{\sum_{k \in G} r_k^3} \gamma_j, \tag{3.37}$$

where $C_{1,T}$ and $C_{3,T}$ are the total arterial ($i = 1$) and venous ($i = 3$) coronary compliance, r_k is the outer radius of the upstream 1D coronary artery (see arterial geometry in Table A.1), W_G is the weight of the myocardial region G (left ventricle, septum or right ventricle) and γ_j is a vector allowing for the compliance repartition over the three layers (setting parameters reported in appendix B, Table B.5).

Similarly, initial (subscript 0) total blood volumes (arterial compartment $V_{0,1,j,k}$, and venous compartment $V_{0,3,j,k}$) of the k-th 0D coronary microvascular district are determined as

$$V_{0,1,j,k} = V_{0,1,T} \frac{W_G}{\sum_{k \in G} r_k^3} \gamma_j, \tag{3.38}$$

and

$$V_{0,3,j,k} = V_{0,3,T} \frac{W_G}{\sum_{k \in G} r_k^3} \gamma_j, \tag{3.39}$$

with $V_{0,1,T}$ and $V_{0,3,T}$ the total initial arterial ($i = 1$) and venous ($i = 3$) compartmental blood volumes (Table B.5).

The computation of input arterial ($C_{a,k}$) and output venous ($C_{v,k}$) compliances of the k-th 0D coronary microvascular district is carried out through equations

$$C_{a,k} = \frac{1}{10} C_{1,T} \frac{W_G}{\sum_{k \in G} r_k^3} \gamma_j, \tag{3.40}$$

and

$$C_{v,k} = \frac{1}{10} C_{3,T} \frac{W_G}{\sum_{k \in G} r_k^3} \gamma_j, \tag{3.41}$$

Lumped coronary initial (subscript 0) resistances of the k-th 0D cornonary microvascular district are determined as

$$R_{0,1,j,k} = 1.1 R_{0,s,j,k}, \tag{3.42}$$

$$R_{0,2,j,k} = \frac{R_{0,s,j,k}}{2.7}, \tag{3.43}$$

$$R_{0,3,j,k} = 0.9R_{0,s,j,k}, \tag{3.44}$$

where $R_{0,s,j,k}$ is the summation (subscript s) of the arterial ($R_{0,1,j,k}$), intermediate ($R_{0,2,j,k}$) and venous ($R_{0,3,j,k}$) resistances belonging to the j-th myocardial layer, given by

$$R_{0,s,j,k} = \frac{R_{0,j,T,G}}{r_k^3 \sum_{k \in G} r_k^{-3}},$$

and where $R_{0,j,T,G}$ is the total resistance of the j-th layer associated with the myocardial region G (Table B.5).

Non-linear behavior of time-varying coronary resistances ($R_{1,j,k}$, $R_{2,j,k}$, and $R_{3,j,k}$) is described through

$$R_{1,j,k} = R_{0,1,j,k}\left(\frac{V_{0,1,j,k}}{V_{1,j,k}}\right)^2, \tag{3.45}$$

$$R_{2,j,k} = R_{0,2,j,k}\left[0.75\left(\frac{V_{0,1,j,k}}{V_{1,j,k}}\right)^2 + 0.25\left(\frac{V_{0,1,j,k}}{V_{1,j,k}}\right)^2\right], \tag{3.46}$$

and

$$R_{3,j,k} = R_{0,3,j,k}\left(\frac{V_{0,3,j,k}}{V_{3,j,k}}\right)^2, \tag{3.47}$$

based on the corresponding time dependent total blood volume ($V_{1,j,k}$ and $V_{3,j,k}$). , that are determined as

$$V_{i,j,k} = V_{0,i,j,k} + C_{i,j,k}(p_{i,j,k} - IMP_{j,k}) \tag{3.48}$$

with $IMP_{j,k}$ being intramyocardial pressure acting on the j-th layer of the k-th 0D coronary microvascular district (see next paragraph).

Outlet venous impedance $Z_{v,k}$ of the k-th 0D coronary district is computed as

$$Z_{v,k} = \frac{Z_{a,k}}{1.4^2}, \tag{3.49}$$

depending on inlet arterial impedance $Z_{a,k}$, in turn obtained as described earlier for arterial characteristic impedances (section 3.1, that is $Z_a = Z_c = \frac{\rho c}{A}$).

3.4.3 Intramyocardial pressure

Intramyocardial pressure (IMP) accounts for the contribution of the cavity-induced extracellular pressure (CEP) - which is proportional to the intrachamber pressure of the adjacent ventricle and depends on the considered myocardial region G - and the shortening-induced intracellular pressure (SIP), directly related to the associated ventricle elastance function. IMP_j is assumed as the coronary microvasculature extravascular pressure, acting onto the j-th myocardial layer of each 0D microvascular district and representing external compression exerted by the heart onto coronary penetrating vessels. Each single-layer IMP_j is defined as

$$IMP_j(t) = CEP_j(t) + SIP(t) = \gamma_{CEP,j}(t) + \phi_{SIP} E_{ch}(t), \tag{3.50}$$

where CEP depends upon the adjacent ventricular pressure (right ventricle p_{rv}, left ventricle p_{lv}, or both) throughout the repartition vector $\gamma_{CEP,j}$ over the three layers, while SIP depends on the corresponding ventricular elastance function E_{ch}, through a constant parameter ϕ_{SIP}. All related parameters are enclosed in appendix B, Table B.5.

3.5 Cerebrovascular model

With respect to the previous version of the global CVS model reported in [74], in the present work we present a novel architecture of the upper body circulation, including a 0D lumped parameterization of the cerebrovascular circulation - taken from Ursino & Giannessi [259] - departing from internal carotid and vertebral arteries along with a parallel 0D circuital analogue of the extra-cerebral circulation attached instead to external carotids. Together, these two branches form the 0D circulation of the head macro-region, as schematized in Figure 3.1.

Figure 3.12 illustrates in more detail the architecture of the 0D head circulation, both encompassing cerebrovascular and extra-cerebral circulations and their circuital layout. The architecture of the extra-cerebral pathway is identical to those adopted to schematize the remaining 0D body macro-regions, from arms to legs, as described in section 3.2. The only difference with respect to the other 0D systemic compartments is that intracranial pressure ICP is appliead as extravascular pressure onto head veins (subscript H, v in equation (3.18)), so that the latter reads

$$V_{H,v} = V_{H,v}^{un} + \Big(p_{H,v} - ICP\Big) C_{H,v}, \tag{3.51}$$

The model of cerebrovascular circulation is a lumped representation of the main large cerebral arteries starting from the circle of Willis, and branching then into right and left pial circulation, intracerebral arterioles, further subdivided into anterior, middle and posterior distal compartments, and communicating with one another through cortical collateral vessels. The vessel compliances and hydraulic resistances of the pial circulation are controlled by the action of cerebral autoregulation (aimed at maintaining nearly-constant level of cerebral blood flow, CBF) and CO_2 reactivity. A unique capillary-venous branch closes the cerebrovascular network. The formation and outflow dynamics of the cerebrospinal fluid (CSF) and the hydrostatic contribution due to gravity regulate intracranial pressure (ICP) via a non-linear intracranial compliance. The outflow of the cerebrovascular model connects directly to the superior vena cava compartments, jointly with the arms region blood flow, the extra-cerebral head circulation, and the ocular model outflow (section 3.6).

The lumped cerebrovascular model has been validated and previously used as a self-standing lumped model to investigate the effects of cardiac arrhythmias on cerebral hemodynamics [8, 225, 217, 226], and more recently to explore the gravity-induced cerebrovascular dynamics during simulated parabolic flight [224].

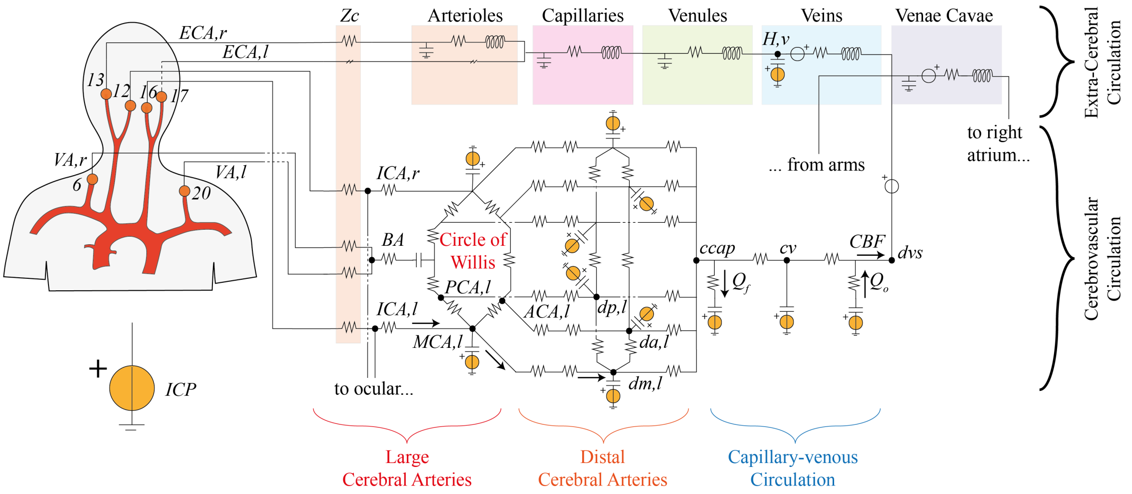

Figure 3.12: Illustrative scheme of the 0D cerebrovascular model architecture, connected from upstream to 1D internal carotid and vertebral arteries (No. 6, 12, 16, 20), while from downstream to 0D superior venae cavae, jointly with 0D extra-cerebral circulation.

3.5.1 Circle of Willis and large proximal arteries

The cerebrovascular model is attached to the internal carotid and vertebral arteries (No. 6, 12, 16 and 20) of the global CVS model, as shown in Figure 3.12. As anticipated in section 3.1 when dealing with boundary conditions of the 1D arterial model at terminal arterial branches, lumped characteristic impedance Z_c located at the end each 1D terminal internal carotid and vertebral arteries has been decreased by 50%, since the corresponding 0D large cerebral arteries entering the lumped cerebrovascular model should still describe arterial tracts, and not arteriolar (*i.e.*, at reasonably lower pressure) as done for the rest of the global model. Pressure downstream right and left internal carotid ($p_{ICA,r}$, $p_{ICA,l}$) and vertebral ($p_{VA,r}$, $p_{VA,l}$) arteries are used as input pressures for the right and left internal carotid and basilar ($p_{BA} = 0.5\,(p_{VA,r} + p_{VA,l})$) arteries of the cerebrovascular model, respectively. Blood flow rates through right and left internal carotid ($Q_{ICA,r}$, $Q_{ICA,l}$) and basilar (Q_{BA}) arteries are thus obtained as

$$\begin{cases} Q_{ICA,r} = \frac{p_{ICA,r} - p_{MCA,r}}{R_{ICA,r}} \\ Q_{ICA,l} = \frac{p_{ICA,l} - p_{MCA,l}}{R_{ICA,l}} \\ Q_{BA} = \frac{p_{BA} - p_{BA,w}}{R_{BA}} \end{cases}, \tag{3.52}$$

where $p_{MCA,r}$, $p_{MCA,l}$ and $p_{BA,w}$ are right and left middle cerebral artery and basilar pressures at the circle of Willis, determined from pressure constitutive equation combined with the conservation of mass:

$$\begin{cases} C_{ICA,l}\left(\frac{dp_{MCA,l}}{dt} - \frac{dICP}{dt}\right) = Q_{ICA,l} + Q_{PCoA,l} - Q_{MCA,l} - Q_{ACA1,l} \\ C_{ICA,r}\left(\frac{dp_{MCA,r}}{dt} - \frac{dICP}{dt}\right) = Q_{ICA,r} + Q_{PCoA,r} - Q_{MCA,r} - Q_{ACA1,r} \\ C_{BA}\frac{dp_{BA,w}}{dt} = Q_{BA} - Q_{PCA1,l} - Q_{PCA1,r} \end{cases}. \tag{3.53}$$

Here, C terms are compartments compliance, Q are blood flow rates entering and exiting each compartment, and ICP is intracranial pressure. $R_{ICA,r}$, $R_{ICA,r}$, and R_{BA} are right and left internal carotid and basilar arteries resistances. Furthermore, $Q_{ICA,r}$ and $Q_{ICA,l}$ upstream the specific Z_c and flowing out from the corresponding 1D vessels can be obtained as

$$\begin{cases} Q_{ICA,r,1D} = Q_{ICA,r} + Q_{eye,r} \\ Q_{ICA,l,1D} = Q_{ICA,l} + Q_{eye,l} \end{cases}, \tag{3.54}$$

where $Q_{eye,r} = Q_{eye,l} = 0.5\,Q_{a,eye}$ (half the arterial eye input blood flow, see section 3.6). Similarly, right and left vertebral arteries outflow flowing out from the 1D model can be determined as $Q_{VA,r,1D} = Q_{VA,l,1D} = 0.5\,Q_{BA}$.

Blood flow through remaining large and proximal cerebral arteries is computed through Kirchhoff's law at nodes as

$$\begin{cases} Q_{ACA2,l} = Q_{ACA1,l} + Q_{ACoA} \\ Q_{ACA2,r} = Q_{ACA1,r} - Q_{ACoA} \\ Q_{PCA2,l} = -Q_{PCoA,l} + Q_{PCA1,l} \\ Q_{PCA2,r} = -Q_{PCoA,r} + Q_{PCA1,r} \end{cases}, \tag{3.55}$$

and according to Ohm's law

$$\begin{cases} Q_{MCA,l} = \frac{p_{MCA,l}-p_{dm,l}}{R_{MCA,l}+R_{dm,l}/2} \\ Q_{MCA,r} = \frac{p_{MCA,r}-p_{dm,r}}{R_{MCA,r}+R_{dm,r}/2} \\ Q_{ACA1,l} = \frac{p_{ICA,l}-p_{ACA,l}}{R_{ACA1,l}} \\ Q_{ACA1,r} = \frac{p_{ICA,r}-p_{ACA,r}}{R_{ACA1,r}} \\ Q_{PCA1,l} = \frac{p_{BA,w}-p_{PCA,l}}{R_{PCA1,l}} \\ Q_{PCA1,r} = \frac{p_{BA,w}-p_{PCA,r}}{R_{PCA1,r}} \\ Q_{ACA2,l} = \frac{p_{ACA,l}-p_{da,l}}{R_{ACA2,l}+R_{da,l}/2} \\ Q_{ACA2,r} = \frac{p_{ACA,r}-p_{da,r}}{R_{ACA2,r}+R_{da,r}/2} \\ Q_{ACoA} = \frac{p_{ACA,r}-p_{ACA,l}}{R_{ACoA}} \\ Q_{PCA2,l} = \frac{p_{PCA,l}-p_{dp,l}}{R_{PCA2,l}+R_{dp,l}/2} \\ Q_{PCA2,r} = \frac{p_{PCA,r}-p_{dp,r}}{R_{PCA2,r}+R_{dp,r}/2} \\ Q_{PCoA,l} = \frac{p_{PCA,l}-p_{MCA,l}}{R_{PCoA,l}} \\ Q_{PCoA,r} = \frac{p_{PCA,r}-p_{MCA,r}}{R_{PCoA,r}} \end{cases}, \tag{3.56}$$

Refer to [259] for the complete nomenclature of large cerebral arteries. Large cerebral arteries setting parameters are reported in appendix B, Table B.6.

3.5.2 Distal pial circulation

Total blood volumes in cerebrovascular distal compartments of the pial circulation are obtained through mass conservation as

$$\begin{cases} \frac{dV_{dm,l}}{dt} = Q_{MCA,l} - Q_{dm,l} + Q_{cam,l} + Q_{cpm,l} \\ \frac{dV_{dm,r}}{dt} = Q_{MCA,r} - Q_{dm,r} + Q_{cam,r} + Q_{cpm,r} \\ \frac{dV_{da,l}}{dt} = Q_{ACA2,l} - Q_{da,l} - Q_{cam,l} + Q_{caa} \\ \frac{dV_{da,r}}{dt} = Q_{ACA2,r} - Q_{da,r} - Q_{cam,r} - Q_{caa} \\ \frac{dV_{dp,l}}{dt} = Q_{PCA2,l} - Q_{dp,l} - Q_{cpm,l} + Q_{cpp} \\ \frac{dV_{dp,r}}{dt} = Q_{PCA2,r} - Q_{dp,r} - Q_{cpm,r} - Q_{cpp} \end{cases}, \tag{3.57}$$

where subscripts da, dm, and dp representing distal anterior, middle and posterior pial arteries, respectively, while subscripts c denote cortical anterior-middle (am), posterior-middle (pm), anterior-anterior (left-right, aa), or posterior-posterior (left-right, pp) pial connections, and with all flow rates terms Q determined as

$$\begin{cases} Q_{dm,l} = \frac{p_{dm,l}-p_{ccap}}{R_{dm,l}/2} \\ Q_{dm,r} = \frac{p_{dm,r}-p_{ccap}}{R_{dm,r}/2} \\ Q_{da,l} = \frac{p_{da,l}-p_{ccap}}{R_{da,l}/2} \\ Q_{da,r} = \frac{p_{da,r}-p_{ccap}}{R_{da,r}/2} \\ Q_{dp,l} = \frac{p_{dp,l}-p_{ccap}}{R_{dp,l}/2} \\ Q_{dp,r} = \frac{p_{dp,r}-p_{ccap}}{R_{dp,r}/2} \\ Q_{cam,l} = \frac{p_{da,l}-p_{dm,l}}{R_{cam,l}} \\ Q_{cam,r} = \frac{p_{da,r}-p_{dm,r}}{R_{cam,r}} \\ Q_{cpm,l} = \frac{p_{dp,l}-p_{dm,l}}{R_{cpm,l}} \\ Q_{cpm,r} = \frac{p_{dp,r}-p_{dm,r}}{R_{cpm,r}} \\ Q_{caa} = \frac{p_{da,r}-p_{da,l}}{R_{caa}} \\ Q_{cpp} = \frac{p_{dp,r}-p_{dp,l}}{R_{cpp}} \end{cases}, \tag{3.58}$$

involving the subsequent cerebral capillary ($ccap$) compartment (see next paragraph). Distal blood volumes of pial arteries are used to compute distal compartmental blood pressures according to pressure constitutive law (equation (3.18)):

$$\begin{cases} p_{dm,l} = \frac{V_{dm,l}}{C_{dm,l}} + ICP \\ p_{dm,r} = \frac{V_{dm,r}}{C_{dm,r}} + ICP \\ p_{da,l} = \frac{V_{da,l}}{C_{da,l}} + ICP \\ p_{da,r} = \frac{V_{da,r}}{C_{da,r}} + ICP \\ p_{dp,l} = \frac{V_{dp,l}}{C_{dp,l}} + ICP \\ p_{dp,r} = \frac{V_{dp,r}}{C_{dp,r}} + ICP \end{cases}, \tag{3.59}$$

where p and V are the various pial compartment intravascular blood pressure and volume, while ICP is intracranial pressure. Settings of the cerebral distal circulation are reported in appendix B, Table B.7.

3.5.3 The capillary-venous circulation

The downstream capillary-venous circulation is connected at its end to the superior vena cava of the global CVS model (Figures 3.1 and 3.12). Dural venous sinus pressure (p_{dvs}) applied to the outflow branch of the cerebrovascular model is determined as

$$p_{dvs} = p_{svc} - \rho g \left(\frac{L_H}{2} + \frac{L_{svc}}{2} \right) \sin \alpha \,, \tag{3.60}$$

where p_{svc} is superior vena cava pressure, ρg is blood specific weight, α is the tilt angle and L_H and L_{svc} are the head and superior vena cava compartment anatomical extensions, respectively (see section 3.2 and refer to appendix B, Table B.3 for veins anatomical lengths). p_{dvs} is used to compute venous sinus blood flow (Q_{vs}) and cerebrospinal fluid outflow rate (Q_o) through Ohm's law, that is

$$\begin{cases} Q_{cv} = \frac{p_{ccap}-p_{cv}}{R_{pv}} \\ Q_{dvs} = \frac{p_{cv}-p_{dvs}}{R_{dvs}} \\ Q_f = \begin{cases} \dfrac{p_{ccap}-ICP}{R_f}, & \text{if } \; p_{ccap} \geq ICP \\ 0, \; \text{if } \; p_{ccap} < ICP \end{cases} \\ Q_o = \begin{cases} \dfrac{ICP-p_{dvs}}{R_o}, & \text{if } \; ICP \geq p_{dvs} \\ 0, \; \text{if } \; ICP < p_{dvs} \end{cases} \\ CBF = Q_{dvs} + Q_o \end{cases}, \tag{3.61}$$

where CBF is cerebral blood flow, *i.e.*, the overall blood flow drained from the brain. Cerebrospinal fluid rate of formation (Q_f) depends instead on the cerebral capillary pressure (p_{ccap}), whereas cerebral venous pressure (p_{cv}) is computed through pressure constitutive law combined with mass conservation (equation (3.19)):

$$C_{cv}\left(\frac{dp_{cv}}{dt} - \frac{dICP}{dt}\right) = Q_{cv} - Q_{dvs}, \tag{3.62}$$

with

$$\begin{cases} C_{ic} = \frac{1}{k_E ICP} \\ C_{cv} = \frac{1}{k_{ven}(p_{cv}-ICP-p_{v1})} \end{cases}, \tag{3.63}$$

$$R_{dvs} = \begin{cases} \dfrac{p_{cv}-p_{dvs}}{p_{cv}-ICP} R_{dvs1}, & \text{if } \; p_{dvs} < ICP \\ R_{dvs1}, \; \text{if } \; p_{dvs} \geq ICP, \end{cases}, \tag{3.64}$$

and

$$Q_{dm,l} + Q_{da,l} + Q_{dp,l} + Q_{dm,r} + Q_{da,r} + Q_{dp,r} = Q_f + Q_{cv}. \tag{3.65}$$

Parameter settings for the cerebral capillary-venous compartment are reported in appendix B, Table B.8.

3.5.4 CSF dynamics and intracranial pressure

Intracranial pressure (ICP) is the pressure of the cerebrospinal fluid (CSF), and is determined by pressure constitutive law combined with mass conservation (equation (3.19)), taking into account the action of gravity through the cerebrospinal fluid hydrostatic pressure according to Stevino's law, so that

$$\begin{aligned} C_{ic}\frac{dICP}{dt} &= Q_{MCA,left} - Q_{dm,l} + Q_{PCA2,l} - Q_{dp,l} + Q_{ACA2,l} - Q_{da,l} + \\ &+ Q_{MCA,r} - Q_{dm,r} + Q_{PCA2,r} - Q_{dp,r} + Q_{ACA2,r} - Q_{da,r} + \\ &+ Q_{cv} - Q_{dvs} + Q_f - Q_o - C_{ic}\frac{dICP^h}{dt}\,, \end{aligned} \tag{3.66}$$

where

$$ICP^h = \rho g\left(\frac{L_H}{2} + \frac{L_{svc}}{2}\right)\sin\alpha\,, \tag{3.67}$$

with C_{ic} being intracranial non-linear compliance, while various Q terms are blood flow rates entering and exiting the compartments communicating with the intracranial cavity, determine from the above-reported relations at all cerebrovascular levels.

3.6 Ocular model

The present model of the human CVS includes also a lumped parameter model of the eye and ocular circulation to account for ocular-vascular dynamics and interactions in view of potential ocular anomalies and disorders triggered by posture and gravity changes (check on SANS in chapter 2, section 2.2.1). The adopted model of the eye and ocular circulation is taken from [166, 189], and plugged to the global CVS model at the level of internal carotid arteries, as displayed in Figure 3.13. The outflow of the ocular model is then connected to the dural venous sinus, at the outlet section of the cerebrovascular model (section 3.5).

3.6.1 The six-compartment model of the eye

The lumped-parameter model of the eye is composed of six compartments governing intraocular pressure (IOP) and ocular globe volume (V_g), using arterial and venous blood pressure at the level of the eye (named $p_{a,eye}$ and $p_{v,eye}$, respectively) as well as the intracranial pressure (ICP) coming from the cerebrovascular model, as inputs. The original ocular model proposed by Nelson *et al.* [166] and later adopted by Petersen *et al.* [189] is composed of (i) an aqueous humor compartment, with inflow and outflow of aqueous humor fluid filling the eye globe and contributing in regulating IOP inside the eyeball; (ii-iv) 3 compartments representing ocular vasculature including lumped blood arteries, capillaries, and veins; (v) a passive and isovolumic compartment including the lens and vitreous humor; and (vi) the retrobulbar subarachnoid space (rSAS), communicating with the cerebrospinal fluid system (ICP, section 3.5) and not exchanging any fluid with the other compartments, although exerting an external influence through pressure difference (ICP vs. IOP and ocular blood pressures) acting via the rSAS-to-globe compliance.

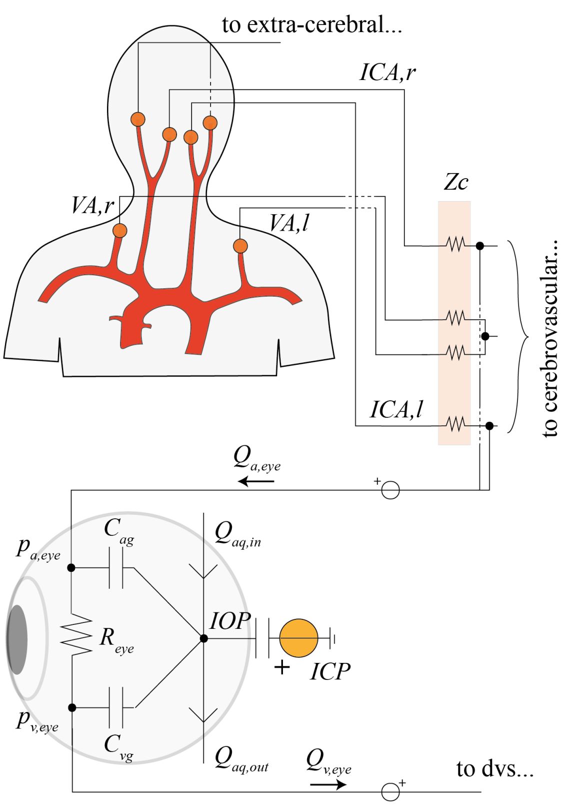

Figure 3.13: Illustration of the lumped ocular compartment, connected from upstream to internal carotid arteries (ICA,l and r, No. 12, 16 from the 1D arterial network, respectively) prior to entering the cerebrovascular circulation, while from downstream to dural venous sinus (dvs) at the outlet of the 0D cerebrovascular model.

3.6.2 IOP and V_g governing equations

IOP and V_g are modeled through the following governing equations:

$$\begin{aligned}\frac{dIOP}{dt} =& \frac{1}{C_g}\bigg(C_{rg}\frac{dICP}{dt} + C_{ag}\frac{dp_{a,eye}}{dt} + C_{vg}\frac{dp_{v,eye}}{dt} + \\ &+ Q_{aq,in} + C_{tm}EVP - Q_{uv} - C_{tm}IOP\bigg),\end{aligned} \tag{3.68}$$

and

$$\begin{aligned}\frac{dV_g}{dt} =& C_{ag}\frac{d}{dt}\Big(p_{a,eye} - IOP\Big) + C_{vg}\frac{d}{dt}\Big(p_{v,eye} - IOP\Big) + \\ &+ Q_{aq,in} + C_{tm}(EVP - IOP) - Q_{uv}\,,\end{aligned} \tag{3.69}$$

where involved parameters are the globe compliance, defined as:

$$C_g = V_g\left(\frac{C_1}{IOP} + C_2\right), \tag{3.70}$$

where constants $C_1 = 4.87e-3$, $C_2 = 3.90e-5$ 1/mmHg; the retrobulbar subarachnoid space-to-globe compliance $C_{rg} = 1.1e-9$ l/mmHg, the arterial blood-to-globe compliance defined as:

$$C_{ag} = 0.3\,V_g\left(\frac{C_1}{IOP} + C_2 - \frac{1}{k_g\,IOP}\right), \tag{3.71}$$

and venous blood-to-globe compliance:

$$C_{vg} = 0.7\,V_g\left(\frac{C_1}{IOP} + C_2 - \frac{1}{k_g\,IOP}\right), \tag{3.72}$$

with $k_g = 312$ being the non-dimensional globe stiffness. Then, the following terms in equations (3.68)-(3.69) are the aqueous humor formation rate $Q_{aq,in} = 0.048e-6$ l/s, the aqueous outflow facility $C_{tm} = 0.0035e-6$ l/(s mmHg) (as long as $EVP \leq IOP$, or 0 otherwise), the uveoscleral outflow rate $Q_{uv} = 0.0067e-6$ l/s (parameters adjusted according to physiological values [240]).

$p_{a,eye}$ and $p_{v,eye}$ are arterial and venous pressure at the level of the eye and episcleral venous pressure, respectively, taken as

$$p_{a,eye} = 0.5(p_{ICA,r} + p_{ICA,l}) - L_{f\text{-}b}\rho g \cos\alpha, \tag{3.73}$$

and

$$p_{v,eye} = \max\big(CVP,\, EVP\big), \tag{3.74}$$

with episcleral venous pressure defined as

$$EVP = p_{svc} - \rho g\left(\frac{L_H}{2} + \frac{L_{svc}}{2}\right)\sin\alpha - L_{f\text{-}b}\rho g \cos\alpha\,, \tag{3.75}$$

and where $L_{f\text{-}b} = 0.03$ m is the perpendicular distance between the globe and the mid-coronal plane [189].

To integrate the ocular model with the global CVS model, arterial eye input ($Q_{a,eye}$) and venous eye output ($Q_{v,eye}$) flow rates shall be determined. These are obtained from the mass conservation and the pressure constitutive law (equation (3.19)) applied to the ocular arterial and venous blood compartments, that is

$$Q_{a,eye} = C_{ag}\frac{d}{dt}\big(dp_{a,eye} - IOP\big) + Q_{eye}\,, \tag{3.76}$$

$$Q_{v,eye} = Q_{eye} - C_{vg}\frac{d}{dt}\big(dp_{v,eye} - IOP\big)\,, \tag{3.77}$$

with the eye blood flow rate $Q_{eye} = (p_{a,eye} - p_{v,eye})/R_{eye}$, and the eye resistance $R_{eye} = 4676$ mmHg s/ml such that mean $Q_{eye} \simeq 1$ ml/min [286].

3.7 Short-term regulation mechanisms

The present CVS model includes 3 different short-term control mechanisms aimed at maintaining the overall homeostasis even under various working conditions (*e.g.*, at various postures, gravity acceleration levels, or cardiac rhythms such as during fibrillated beating). The short-term regulation mechanisms implemented in the present model are those already anticipated in chapter 1 of the present thesis, where their functioning principles are described in further detail. Thus, the short-term mechanisms of homeostatic control accounted for in the present work are (i) baroreflex control of central arterial pressure, (ii) cardiopulmonary reflex control of central venous pressure, and (iii) cerebral autoregulation/CO_2 reactivity (although CO_2 will not be considered to the aim of the present work) of cerebral blood flow. The functioning principles and a sketch of the underlying operational flow mediated by such control mechanisms is depicted in Figure 3.14.

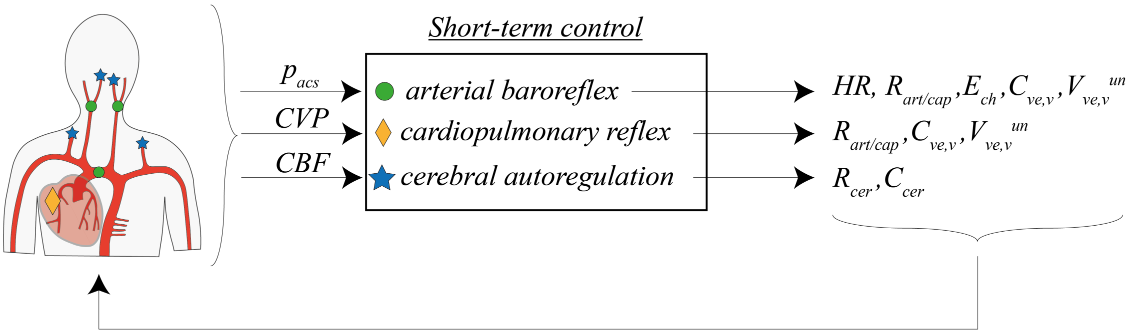

Figure 3.14: Schematic representation of short-term control mechanisms (baroreflex, cardiopulmonary reflex and cerebral autoregulation) functioning and operational flow. p_{acs} is aortic-carotid sinus pressure, CVP is central venous pressure and CBF si cerebral blood flow.

In this section, we provide only the mathematical details and equations regulating baroreflex, cardiopulmonary reflex and cerebral autoregulation controls, with all parameter settings reported in appendix B.

3.7.1 Baroreflex model

The baroreceptor model is taken from [177, 48, 74] and accounts for the inotropic effect of both ventricles (control of cardiac contractility, that is chambers maximum elastance $E_{ch,max}$), the chronotropic effect (control of the heart rate HR), as well as the control of the systemic vasculature including peripheral arteriolar (R_{art}) and capillary (R_{cap}) resistances (thus, control of total peripheral resistance TPR), unstressed volume of the venular/venous system ($V_{ve/v}^{un}$), and venular/venous compliance ($C_{ve/v}$, venous tone), as represented in Figure 3.14. Tuning and calibration of the parameters controlling sympathetic and parasympathetic activity is made accordingly to reported behaviors and cardiovascular responses observed during posture changes [43, 241, 23]. In the model, mean aortic-carotid sinus pressure (p_{pacs}) (average of aortic arch, right and left carotid sinus pressure) drives the extent of sympathetic and parasympathetic autonomic responses governing efferent organ y_m (HR, $E_{ch,max}$, $R_{art/cap}$, $V^{un}_{ve/v}$, $C_{ve/v}$) with respect to its target value. For arterial baroreflex, the assumed target pressure corresponds to the supine mean aortic-carotid sinus pressure.

Current mean aortic-carotid sinus pressure $\bar{p}_{acs}$ is determined by averaging pressure signals related to the three baroreflex sensors location (aortic arch $p_{AA}(t)$, right and left carotid sinus $p_{cs,R}(t)$ and $p_{cs,L}(t)$) over the RR cardiac cycle:

$$\bar{p}_{acs} = \frac{1}{3RR}\int_{RR}\Big(p_{AA}(t) + p_{cs,R}(t) + p_{cs,L}(t)\Big)\,dt. \tag{3.78}$$

Then, sympathetic (n_s) and parasympathetic (n_p) activities are determined as

$$n_s(\bar{p}_{acs}) = \frac{1}{1+\left(\dfrac{\bar{p}_{acs}}{\bar{p}_{acs,tg}}\right)^{\nu}} \quad , \quad n_p(\bar{p}_{acs}) = \frac{1}{1+\left(\dfrac{\bar{p}_{acs}}{\bar{p}_{acs,tg}}\right)^{-\nu}}, \tag{3.79}$$

where, for arterial baroreflex, $\bar{p}_{acs,tg} = 89.01$ mmHg, and ν is the steepness of response, assumed equal to 7. Being $y_m(t)$ the generic efferent organ ($R_{i,art}$, $R_{i,cap}$, $V^{un}_{i,v}$, $V^{un}_{i,ve}$, $C_{i,v}$, $C_{i,ve}$, $E_{ch,max} = E_{ch,A} + E_{ch,B}$, HR, with subscript i denoting 0D body macro-regions from head to legs, see section 3.2), controlled by arterial baroreflex, its time evolution is given by

$$\frac{dy_m}{dt} = \frac{1}{\tau_m}\Big(- y_m + \alpha_m n_s(\bar{p}_{acs}) - \beta_m n_p(\bar{p}_{acs}) + \gamma_m\Big), \tag{3.80}$$

with parameters α_m, β_m, γ_m and τ_m reported in appendix B, Table B.9.

3.7.2 Cardiopulmonary reflex model

Similarly to arterial baroreflex, cardiopulmonary reflex [93, 136] are introduced in the present model to control the low pressure side (*i.e.*, venous) of the circulation. cardiopulmonary low-pressure receptors are located into the right atrium, so that and estimation of the central venous pressure (CVP) can be sensed. Cardiopulmonary target pressure is therefore assumed equal to supine CVP, and sympathetic/parasympathetic activities are computed as a function of the current $CVP = p_{ra}$ (right atrial pressure) with respect to the target value. However, differently from arterial baroreflex,cardiopulmonary reflex controls only peripheral resistances ($R_{art/cap}$) and venous tone ($V^{un}_{ve/v}$ and $C_{ve/v}$).

The current cardiopulmonary pressure control $\bar{p}_{cp}$ is therefore taken as

$$\bar{p}_{cp} = \frac{1}{RR}\int_{RR} p_{ra}(t)\,dt, \tag{3.81}$$

with $n_{s,cp}(\bar{p}_{cp})$ and $n_{p,cp}(\bar{p}_{cp})$ in turn defined as

$$n_{s,cp}(\bar{p}_{cp}) = \frac{1}{1+\left(\dfrac{\bar{p}_{cp}}{\bar{p}_{cp,tg}}\right)^{\nu}} \quad , \quad n_{p,cp}(\bar{p}_{cp}) = \frac{1}{1+\left(\dfrac{\bar{p}_{cp}}{\bar{p}_{cp,tg}}\right)^{-\nu}}, \tag{3.82}$$

and where target pressure $\bar{p}_{cp,tg} = 7.02$ mmHg, and $\nu = 7$. Efferent organs control equation (3.80) used in arterial baroreflex control applies also to cardiopulmonary reflex. Parameters $\alpha_{cp,m}$, $\gamma_{cp,m}$ and $\tau_{cp,m}$ referred to variable $y_{cp,m}$ are enclosed in appendix B, Table B.9.

3.7.3 Cerebral autoregulation model and CO_2 reactivity

Cerebral autoregulation - ensuring constant cerebral blood flow (CBF) to the human brain via cerebral vessel vasoconstriction/dilation - is implemented into the cerebrovascular model by Ursino & Giannessi [259] (section 3.5). The scope of the model is to modify cerebral pial arteriolar compliances and resistances as non-linear function of the mismatch between the current local blood flow (fractions of the overall CBF) and a given reference values taken as target, as displayed in Figure 3.14. Cerebral compliances vary between bounding maximum and minimum values, whereas arteriolar resistances are determined exploiting Poiseuille's law.

Cerebral pial arteriolar resistances and compliances are controlled by cerebral autoregulation and CO_2 reactivity . To each of the six distal regions, the following equations apply:

$$\begin{cases} \tau_{aut}\frac{dx_{aut,i,j}}{dt} = -x_{aut,i,j} + G_{aut}\left(\frac{Q_{di,j}-Q_{ndi,j}}{Q_{ndi,j}}\right), \ \ \text{i=m,a,p; j=l,r,} \\ \tau_{CO_2}\frac{dx_{CO_2,i,j}}{dt} = -x_{CO_2,i,j} + G_{CO_2}A_{CO_2,i,j}\log_{10}\left(\frac{p_{aCO_2}}{p_{aCO_2 n}}\right), \ \ \text{i=m,a,p; j=l,r,} \end{cases}, \tag{3.83}$$

where the subscript n denotes the basal values and

$$A_{CO_2,i,j} = \frac{1}{1+\exp\{[-k_{CO_2}(Q_{di,j}-Q_{ndi,j})/Q_{ndi,j}] - b_{CO_2}\}}, \ \ \text{i=m,a,p; j=l,r.} \tag{3.84}$$

Distal compliances and resistances are expressed as

$$\begin{cases} C_{di,j} = \dfrac{C_{d0i,j}\left[(1-\Delta C_{di,j}/2)+(1+\Delta C_{di,j}/2)e^{\frac{x_{CO_2,i,j}-x_{aut,i,j}}{k_{C_{di,j}}}}\right]}{1+e^{\frac{x_{CO_2,i,j}-x_{aut,i,j}}{k_{C_{di,j}}}}}, \\ R_{di,j} = \frac{k_{R_{di,j}}C^2_{d0i,j}}{V^2_{di,j}}, \ \ \text{i=m,a,p; j=l,r,,} \end{cases} \tag{3.85}$$

where

$$\begin{cases} \Delta C_{di,j} = \begin{cases} 2s_1, & \text{if } \ x_{CO_2,i,j} < x_{aut,i,j}, \\ 2s_2, & \text{if } \ x_{CO_2,i,j} \geq x_{aut,i,j}, \end{cases} & \text{i=m,a,p; j=left,right} \\ k_{C_{di,j}} = \begin{cases} \dfrac{C_{d0i,j}s_1}{2}, & \text{if } \ x_{CO_2,i,j} < x_{aut,i,j}, \\ \dfrac{C_{d0i,j}s_2}{2}, & \text{if } \ x_{CO_2,i,j} \geq x_{aut,i,j}, \end{cases} & \text{i=m,a,p; j=l,r} \end{cases} . \tag{3.86}$$

Parameter settings of cerebral autoregulation and CO_2 reactivity controls are reported in appendix B, Table B.10.

3.8 Numerical methods

In order to obtain time signals of all dependent variables at any point throughout the 1D domain (vessels cross section area $A(x,t)$, blood flow rate $Q(x,t)$, blood pressure $p(x,t)$) as well as in all 0D compartments ($Q(t)$, $p(t)$, but also blood volume $v(t)$), suitable numerical schemes shall be adopted to discretize partial and ordinary derivative equations introduced in the present chapter, in order to obtain approximated numerical solutions [74, 204]. Thus, in this section, brief detailing regarding spatial discretization of the 1D arterial model counterpart and time integration of the overall CVS model is reported. An overall summary of the general CVS model time marching algorithm is also enclosed at the end of the present section.

3.8.1 Spatial discretization

Partial differential equations (3.3)-(3.8) describing blood motion throughout the 1D arterial tree - including all 63 large 1D arteries listed in Figure 3.2 and Table A.1 - are discretized according to a Discontinuous Galerkin Finite Elements approach [74, 204]. To this end, the conservative form of equations (3.3)-(3.8) is obtained, as

$$\frac{\partial \mathbf{U}}{\partial t} + \frac{\partial \mathbf{F}}{\partial x} + \mathbf{S} = 0, \tag{3.87}$$

where $\mathbf{U} = (A,\, Q)^T$ is the vector of state (conservative) variables, while definitions of $\mathbf{F} = \mathbf{F}(\mathbf{U})$ (flux vector) and $\mathbf{S}$ (source term vector) are reported in appendix A, equation (A.6).

Then, the following bilinear form is obtained from the weak formulation of (3.87) by introducing the test function $\psi(x)$:

$$\left(\frac{\partial \mathbf{U}}{\partial t}, \psi\right)_\Omega + \left(\frac{\partial \mathbf{F}}{\partial x}, \psi\right)_\Omega + \left(\mathbf{S}, \psi\right)_\Omega = 0, \tag{3.88}$$

where with Ω the domain of integration has been denoted (*i.e.*, each element of the spatial discretization), and $(a, b)_\Omega = \int_\Omega a\, b\, d\Omega$. Then, integrating by parts

$$\int_\Omega \frac{\partial \mathbf{U}}{\partial t}\psi,\, d\Omega + [\mathbf{F}(\mathbf{U})\psi]_{\partial\Omega} - \int_\Omega \mathbf{F}(\mathbf{U})\frac{d\psi}{dx}\, d\Omega + \int_\Omega \mathbf{S}\psi\, d\Omega = 0, \tag{3.89}$$

which will be integrated over each element of the spatial discretization (details on the spatial discretization of the 1D arterial network are reported in appendix A, Table A.1, including the number of elements used to discretize each 1D arterial vessel), and where $\partial\Omega$ identifies the boundary of the domain Ω, that is $\partial\Omega = \Gamma_\Omega$, and thus terms $[\mathbf{F}(\mathbf{U})\psi]_{\partial\Omega}$ are evaluated on each element boundaries through Lax-Friedrichs approximation for internal boundaries between adjacent elements, or via the method of characteristics (described in section 3.1) for external boundaries.

A piece-wise linear representation (through lagrangian polynomials) is adopted, approximating thus $A \approxeq A_1\phi_1(\xi) + A_2\phi_2(\xi)$ and $Q \approxeq Q_1\phi_1(\xi) + Q_2\phi_2(\xi)$ at each element, with shape functions $\phi_1(\xi)$ and $\phi_2(\xi)$ defined as the lagrangian functions:

$$\phi_1(\xi) = \frac{1-\xi}{2}, \qquad \phi_2(\xi) = \frac{1+\xi}{2}, \tag{3.90}$$

where the normalized coordinate $\xi \in [-1,\, 1]$ is defined such that

$$\xi = x_1\frac{1-\xi}{2} + x_2\frac{1+\xi}{2}, \tag{3.91}$$

with x_1 and x_2 the spatial coordinates of the single element $\Omega_e = [x_1,\, x_2]$ of the piece-wise representation.

Taking then the test function $\psi = (\psi_1,\, \psi_2)$ as identical to the shape functions ϕ_1, ϕ_2 defined above, form (3.89) can be re-arranged as

$$\frac{\partial \mathbf{Y}_{1D}}{\partial t} = \mathbf{M}\mathbf{G}, \tag{3.92}$$

where $\mathbf{Y}_{1D} = \left(\begin{smallmatrix} A_1 & A_2 \\ Q_1 & Q_2 \end{smallmatrix}\right)$ is the matrix of area and flow rate weights at elements nodes, $\mathbf{M} = \left(\begin{smallmatrix} 2 & -1 \\ -1 & 2 \end{smallmatrix}\right)$ is the mass matrix, and $\mathbf{G}$ is the known term matrix at right-hand side, whose definition is reported below

$$\begin{aligned} \mathbf{G} = {} & \frac{1}{l_e}\int_{-1}^{1}\begin{pmatrix} -F_1(A,Q) & F_1(A,Q) \\ -F_2(A,Q) & F_2(A,Q) \end{pmatrix} d\xi + \\ & -\frac{2}{l_e}\begin{pmatrix} -F_1(A_1,Q_1) & F_1(A_2,Q_2) \\ -F_2(A_2,Q_1) & F_2(A_2,Q_2) \end{pmatrix} - \int_{-1}^{1}\begin{pmatrix} -S_1(A,Q)\psi_1 & S_1(A,Q)\psi_2 \\ -S_2(A,Q)\psi_1 & S_2(A,Q)\psi_2 \end{pmatrix} d\xi \end{aligned}, \tag{3.93}$$

recalling definitions of components F_1, F_2, S_1, and S_2 reported in appendix A, equation (A.6).

3.8.2 Time integration

System (3.92) together with all ordinary differential equations governing 0D model compartments and short-term regulation mechanisms (sections 3.2-3.7) are integrated in time according to a 2-step Runge-Kutta time marching scheme [74]. That is, given $\mathbf{f}$ the generic state vector containing all time-marching variables (belonging 1D, 0D and short-term control models), time integration is performed in two separate half-steps, according to the following scheme:

- first half-step, from $\mathbf{f}^n$ at time t^n to $\mathbf{f}^{n+\frac{1}{2}}$ at time $t^{n+\frac{1}{2}}$:

$$\mathbf{f}^{n+\frac{1}{2}} = \mathbf{f}^n + \frac{\Delta t}{2}\frac{d\mathbf{f}^n}{dt} \tag{3.94}$$

- second half-step, from $\mathbf{f}^n$ at time t^n to $\mathbf{f}^{n+1}$ at time t^{n+1}, exploiting the state vector $\mathbf{f}^{n+\frac{1}{2}}$ previously integrated at time $t^{n+\frac{1}{2}}$:

$$\mathbf{f}^{n+1} = \mathbf{f}^n + \Delta t\frac{d\mathbf{f}^{n+\frac{1}{2}}}{dt} \tag{3.95}$$

3.8.3 General algorithm

In conclusion, in this paragraph we report the overall flow of operations performed by the CVS model at each time step of the integration. That is, we list the sequence of operations composing the overall algorithm followed by the presented CVS model, including initialization performed at the beginning of the simulation, spatial discretization and time marching of all variables at each time step, computation of boundary conditions and 1D-0D coupling at interfaces. The general CVS model algorithm is therefore reported below.

1. start of algorithm;
2. simulation settings and saving parameters (posture, gravity, heart pacing rhythm, saving directory);
3. model initialization: 1D arterial network geometry, 0D parameters, initial values, vectors pre-allocation;
4. (alternative to point 3) model initialization performed by loading the final variables state and settings of a previous simulation;
5. time loop integration:
   (a) integrate 1D model equations (3.92) to the first half-step at time $t^{n+\frac{1}{2}}$ according to equation (3.94);
   (b) integrate baroreflex and cardiopulmonary reflex to the first half-step at time $t^{n+\frac{1}{2}}$;

   (c) integrate 0D model equations (section 3.2) to the first half-step at time $t^{n+\frac{1}{2}}$;
   (d) update time t to $t^{n+\frac{1}{2}}$ and update gravity acceleration g and tilt angle α accordingly, if necessary;
   (e) update cardiac elastance values according to equations (3.28), (3.29), (3.27) to the first half-step at time $t^{n+\frac{1}{2}}$;
   (f) integrate 0D cerebrovascular (section 3.5) and ocular (section 3.6) model equations to the first half-step at time $t^{n+\frac{1}{2}}$;
   (g) update boundary conditions for the 1D domain using solution obtained at time $t^{n+\frac{1}{2}}$;
   (h) integrate baroreflex and cardiopulmonary reflex to the second half-step at time t^{n+1} according to equation (3.95);
   (i) integrate 0D model equations (section 3.2) to the second half-step at time t^{n+1};
   (j) update time t to t^{n+1} and update gravity acceleration g and tilt angle α accordingly, if necessary;
   (k) update cardiac elastance values according to equations (3.28), (3.29), (3.27) to the second half-step at time t^{n+1};
   (l) update boundary conditions for the 1D domain using 0D solution obtained at time t^{n+1};
   (m) integrate 1D model equations (3.92) to the second half-step at time t^{n+1};
   (n) integrate 0D cerebrovascular (section 3.5) and ocular (section 3.6) model equations to the second half-step at time t^{n+1};
   (o) save solution and perform another time integration step;

6. end of algorithm.

Chapter 4

Case study: mathematical modeling of atrial fibrillation

(the contents of the present chapter have been previously published in [216])

Atrial fibrillation (AF) is the most common form of sustained cardiac arrhythmia, and is often strongly associated with advanced age and other comorbidities [88]. Its occurrence in clinical evidences has constantly grown during the last decades, reaching a three-fold increase over the last 50 years [230]. Additionally, recent epidemiological predictions show a further increase, with an estimation of 16-17 million cases reached by 2050 in US and Europe [119]. Given this important epidemiological situation, thorough comprehension of the pathophysiology of this form of cardiac arrhythmia is strongly advisable. Among the consequences of AF, patients with ongoing arrhythmia may present ischemic chest pain, ECG abnormalities and troponin release, even in the absence of classical obstructive epicardial coronary disease [283, 185, 262]. A possible mechanism underlying this association is AF-induced microvascular dysfunction, determining a limited coronary flow reserve even in the presence of normal epicardial coronary arteries [283, 207]. Yet, a direct detrimental hemodynamic consequence of the irregular RR beating intervals elicited during AF occurrence [8, 225, 217, 218] has not been extensively established so far, especially as a plausible alternative, or even as additional mechanism hampering correct perfusion of the cardiac muscle [116]. Given the frequent coexistence of AF and coronary artery disease (CAD) [179] and the lack of reliable clinical data regarding the prognostic effect of AF in patients with stable CAD [219], evaluating the rhythm-specific impact on the coronary circle appears as clinically relevant.

Use of computational modeling in cardiology is a growing field of interest, progressively adopted in many different contexts, such as cardiac electrophysiology [168] and cardiovascular fluid dynamics [254, 158]. Indeed, mathematical modeling represents a powerful tool of investigation to explore the complex process of fluid dynamics involved in numerous clinical scenarios, integrating empirical findings and providing quantitative insights into physiological and pathophysiological aspects of the cardiovascular system. To mention one, a previous version of the multiscale CVS and coronary circulation model presented in this thesis has demonstrated that AF implies direct epicardial coronary flow impairment, particularly at higher ventricular rates, as well as an imbalance of the oxygen demand and supply ratio [227].

Thus, in this chapter, a previous version of computational model of the human cardiovascular and coronary vascular system presented in this thesis (Chapter 3) is introduced and used to deepen the current comprehension of coronary perfusion of the different layers of the myocardium during AF at various beating frequency.

4.1 Model description

The numerical simulations conducted to the aim of this investigation are carried out through a previous version of the CVS model briefly recalled in the following. The adopted version of the CVS model is a multiscale 1D-0D description of the human vasculature and cardiac circulation, arranged in a closed-loop layout and not accounting for the influence of gravity throughout the circulation. The model architecture is sketched in Figure 4.1, and can also be found in previous works by our group [76, 74, 75], with the most evident topological difference with respect to the current version of the model presented in chapter 3 being the subdivision of the 0D systemic peripheral circulation and venous return into only two separate macro-regions, namely upper body and lower body circulations. These compartments, eventually connecting at the level of superior and inferior venae cavae, together reach the right atrium and thus connect to the cardiopulmonary circulation, which is the same as presented in chapter 3, apart from the introduction of intrathoracic pressure which is not present in this version of the model, plus cardiopulmonary reflex, which are not included as additional short-term regulatory mechanism. Thus, homeostatic regulation is only performed by baroreflex response. The multiscale representation of coronary arteries and coronary microvasculature is modeled as proposed by Mynard and Smolich [160, 162], and is analogue to the coronary vasculature model description reported in 3 (schematized on the left side of Figure 4.1), connecting directly to the right atrium jointly with veane cavae circulations.

In Figure 4.2 an example of blood flow Q across the three myocardial layers of the LAD III (vessel No. 57, hereinafter referred to as simply LAD) is reported, under normal sinus rhythm (SR, *i.e.*, not fibrillated) at $HR = 75$ bpm. Blood flow rates through subepicardial, midwall and subendocardial layers are named as Q_{EPI}, Q_{MID}, Q_{ENDO}, respectively, with mean flow ($\bar{Q}$) ENDO-to-EPI ratio of about 1.32,

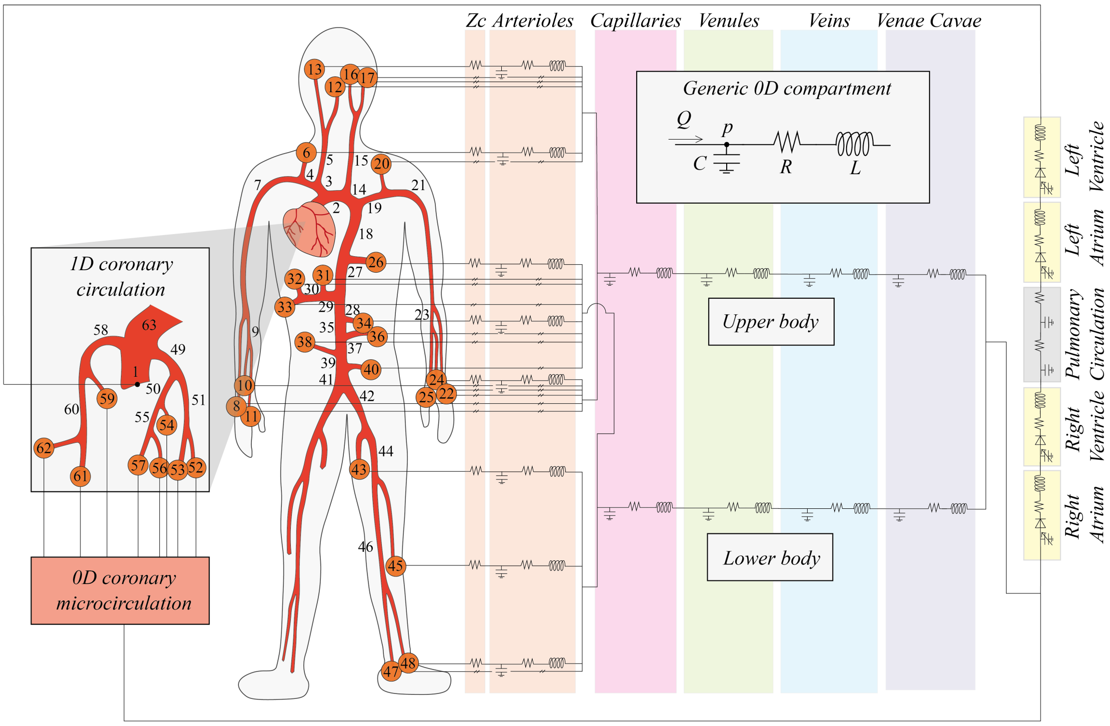

Figure 4.1: Illustration of the multiscale cardiovascular model used to study coronary perfusion of the myocardium during AF. The 1D arterial tree is sketched in red, while remaining 0D systemic circulation of upper and lower body, and cardiopulmonary circulation are schematized as electrical circuits on the right (the generic RLC lumped compartment is reported on top, with R vascular hydraulic resistance, C vessels compliance, and L vessels inertance). Vertical rectangles (orange, pink, green and blue, from left to right) divide the 0D peripheral circulation into arteriolar, capillary, venular, venous and venae cavae compartments. Image taken from [216].

according to the reported literature ranges [59].

4.2 Numerical simulation of atrial fibrillation

The model is employed to inquire into deep coronary hemodynamics under different heart beating rhythms, that is (i) during physiological sinus rhythm (SR), and (ii) under atrial fibrillation (AF). We focus on three mean ventricular rates (mean HR frequency): 75, 100 and 125 bpm, which are externally imposed as inputs of the present model, meaning that in these simulations HR is not controlled freely by short-term regulation mechanisms (*i.e.*, baroreflex response). On the contrary, HR is provided externally to the model from a RR time series previously

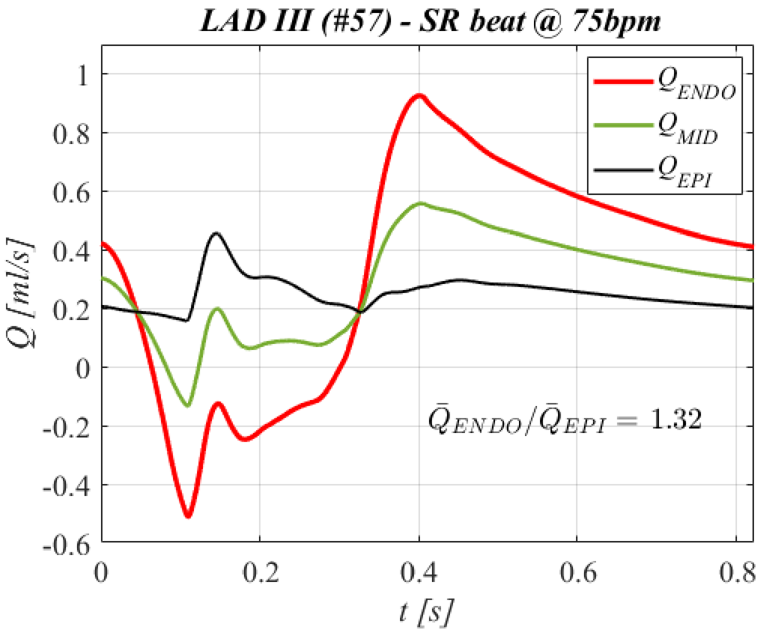

Figure 4.2: Example of blood flow rate Q across the three myocardial layers (ENDO, MID, EPI) under SR at $HR = 75$ bpm.

extracted to the scope of the study. To allow for proper comparison between SR and AF rhythms, the model is assumed to represent supine (*i.e.*, no gravitational effects are included to the aim of the present study) resting conditions (*i.e.*, not exercise), thus the simulations reproduce AF with variable ventricular response and SR/tachycardic right atrial pacing in non-exercising patients.

The RR beating extraction procedure is described in further detail in the previous works by our group [227, 223]. In summary, the SR beating series follow a pinknoise-like time correlation, and are extracted from a Gaussian distribution (Figure 4.3, small top panels) with mean value $\mu = \frac{60}{HR}$ (where $HR = 75$, 100, 125 bpm) and standard deviation $\sigma = cv * \mu$ ($cv = 0.07$ for SR, where cv is the coefficient of variation). Differently, AF RR beating series are uncorrelated in time and extracted from a modified Gaussian distribution with an exponential correction (Figure 4.3, small top panels with rate parameter $\gamma = -9.2\frac{60}{HR} + 14.6$ [6] and $cv = 0.24$. Furthermore, during AF, the typical atrial kick experienced at the end of ventricular diastole to achieve full emptying of the corresponding filling atrial chamber, has been removed from both right and left atria [223] by imposing no final atrial contraction through the associated atrial time-varying elastance function (equation (3.28) in chapter 3). For each case study (*i.e.*, mean beating frequency $HR = 75$, 100, 125 bpm), a number $N_B = 2000$ of RR beatings are extracted for both cardiac rhythms (SR and AF), as depicted in Figure 4.3.

The present study focuses especially on the microcirculatory districts representing the natural termination of the largest 1D epicardial coronary arteries: (i) vessel No. 57, that is left anterior descending coronary artery (LAD), (ii) vessel No. 53 for left circumflex coronary artery (LCx), (iii) and vessel No. 61 for right main coronary artery (RCA) (refer to figure 4.1). Due to the scope of the study, aimed at understanding the detrimental effect of AF onto coronary arteries myocardial perfusion, the attention is primarily devoted to coronary arterial blood flow rate time series Q pertaining to each myocardial microcirculation layer (EPI, MID and ENDO) - denoted as $Q_{EPI}(t)$, $Q_{MID}(t)$ and $Q_{ENDO}(t)$ (refer to Figures 4.2 and 3.11, in chapter 3) - under both sinus and fibrillated rhythm (subscripts SR and AF, respectively). Representative flow rate time series $Q(t)$ across the three myocardial layers of the LAD coronary microvascular district are depicted in Figure 4.4 as example, under SR and AF conditions, for $HR = 75$ and 125 bpm.

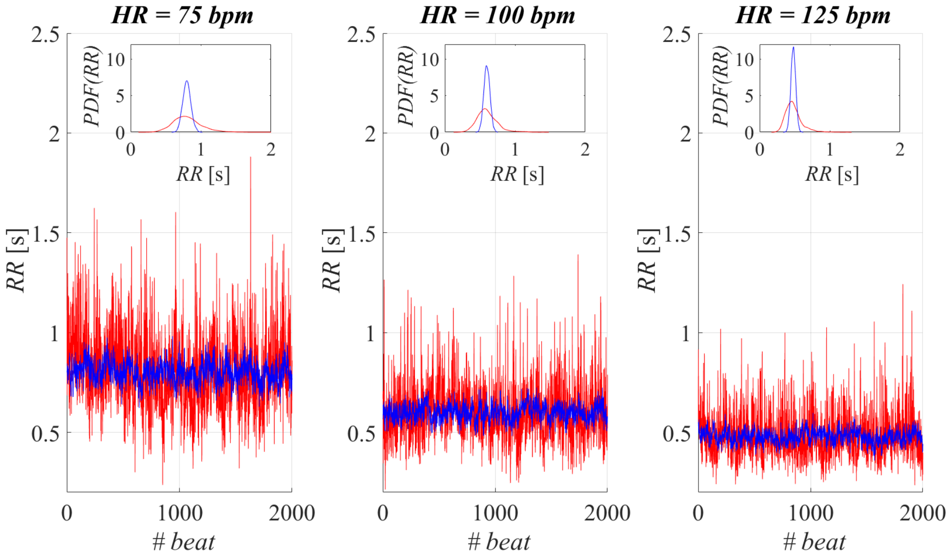

Figure 4.3: RR beating series extraction ($N_B = 2000$), with SR rhythm depicted in blue and AF in red, for each of the three mean pacing frequency ($HR = 75$, 100, 125 bpm). On top of each panel, PDFs (probability distribution functions) of RR beating series are reported for each cardiac rhythm. Image taken from [216].

4.3 Effect of AF at increasing frequency on the perfusion of myocardial layers

For a generic myocardial layer (EPI, MID, or ENDO) and ventricular rate (75, 100, or 125 bpm), mean beat-to-beat flow distributions $Q_{SR,b}$ and $Q_{AF,b}$ ($Nb = 2000$ beats each) are computed by averaging flow rate $Q(t)$ time series over the cardiac

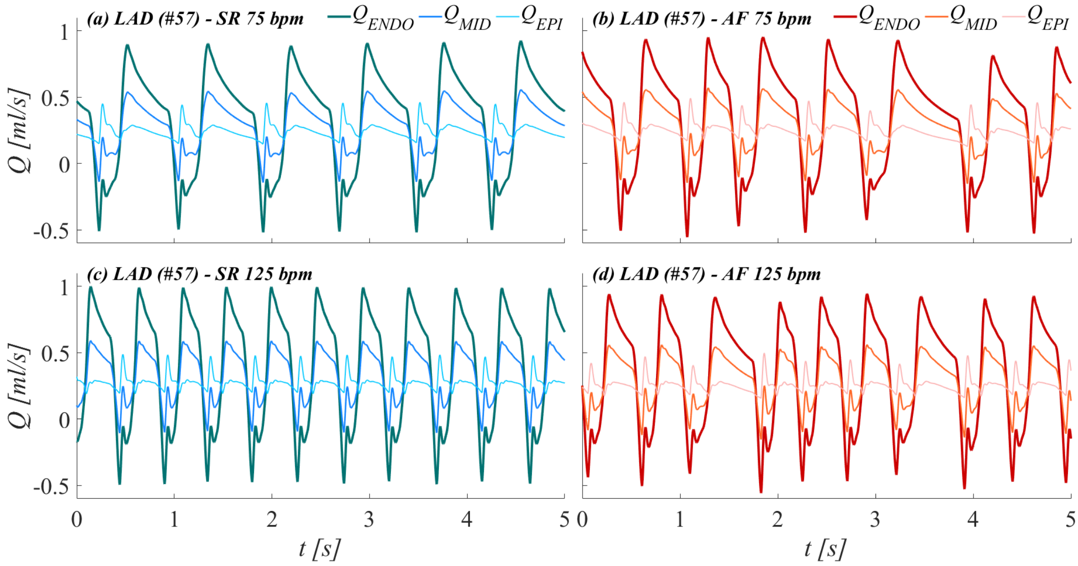

Figure 4.4: Example fow rate $Q(t)$ time series across the three layers of the LAD coronary artery (No. 57) microvascular district under SR (blue) and AF (red) pacing rhythms at $HR = 75$ and 125 bpm pacing frequency. Image taken from [216].

cycle, that is

$$Q_{SR,b} = \frac{1}{RR_{SR,b}} \int_{RR_{SR,b}} Q_{SR}(t)\,dt, \qquad Q_{AF,b} = \frac{1}{RR_{AF,b}} \int_{RR_{AF,b}} Q_{AF}(t)\,dt, \tag{4.1}$$

with subscript b indicating the b-th mean flow rate obtained from the b-th heartbeat, with RR-length $RR_{SR,b}$ or $RR_{AF,b}$ depending on the considered cardiac rhythm. Thus, a set of 9 beat-to-beat flow rate distributions $Q_{SR,b}$ and $Q_{AF,b}$ are collected for each cardiac rhythm (SR and AF), that is for all 3 myocardial layers under the 3 mean pacing frequencies (see Figure 4.5).

Mean flow rate values $\bar{Q}_{SR}$ and $\bar{Q}_{AF}$ are then calculated from these latter distributions as

$$\bar{Q}_{SR} = \frac{1}{N_b} \sum_{b=1}^{N_b} Q_{SR,b}, \qquad \bar{Q}_{AF} = \frac{1}{N_b} \sum_{b=1}^{N_b} Q_{AF,b}, \tag{4.2}$$

for each myocardial layer and pacing frequency. Then, following an inter-layer vs. inter-frequency approach, according to Figure 4.5, differences of AF-to-SR ratio mean values $\bar{Q}_{AF}/\bar{Q}_{SR}$ are evaluated across different layers and frequencies. Significance of results is tested through statistical tests of hypothesis:

- direct $\bar{Q}_{SR}$ vs. $\bar{Q}_{AF}$ comparison is assessed via Wilcoxon's test for medians, at each given cardiac layer and frequency, as well as across layers and among frequencies under a given cardiac rhythm (SR or AF);

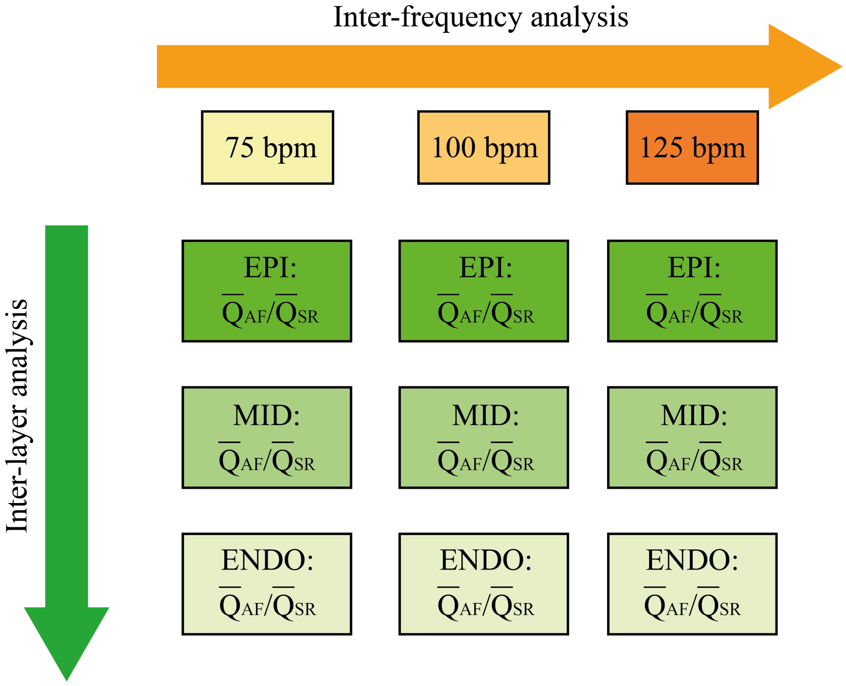

Figure 4.5: Illustration of the inter-frequency vs. inter-layer analyses with flow rate Q distributions (and mean values $\bar{Q}$) across the 3 myocardial layers and at the 3 mean pacing frequencies. Image taken from [216].

- ANOVA tests are performed instead on $Q_{AF,b}/\bar{Q}_{SR}$ distributions, across layers and among frequencies;
- t-Student tests are performed to evaluate significance of regression trend interpolating $Q_{AF,b}/\bar{Q}_{SR}$ distributions across the 3 myocardial layers, at a given pacing frequency.

P-values equal or lower than 0.05 are considered statistically significant.

Table 4.1 reports mean $\bar{Q}_{AF}$, $\bar{Q}_{SR}$, and their ratio $\bar{Q}_{AF}/\bar{Q}_{SR}$ over all myocardial layers for the six possible configurations, that is AF at 75, 100, and 125 bpm, or SR at 75, 100, and 125 bpm. It is evident how, at all simulated ventricular rates and independently of the myocardial layer, $\bar{Q}_{AF}$ is significantly lower than corresponding $\bar{Q}_{SR}$ (p-values < 0.001 for all $\bar{Q}_{AF}$ vs. $\bar{Q}_{SR}$ comparisons).

The inter-layer and inter-frequency ANOVA test results, with corresponding p-values, are reported in Tables 4.2 and 4.3, respectively. In addition, Figure 4.6 displays, for each coronary microvascular district, the $\bar{Q}_{AF}/\bar{Q}_{SR}$ ratio across myocardial layers for each investigated ventricular rate HR. The inter-layer analysis evidences that, for each simulated ventricular rate, $\bar{Q}_{AF}/\bar{Q}_{SR}$ is progressively decreased going from epicardial to endocardial layers in the distal left coronary artery districts (LAD and LCx, both reporting p-values < 0.001 at all frequencies, Table 4.2), while this is not the case for the distal RCA district (p-value 0.669, 0.409, 0.186 for 75 bpm, 100 bpm and 125 bpm simulations, respectively, Table 4.2). Inter-frequency analysis, instead, highlights how $\bar{Q}_{AF}/\bar{Q}_{SR}$ is progressively worsened as the ventricular rates is increased. In fact, in all the investigated distal coronary mirovascular districts, we observe a significant decrease in $\bar{Q}_{AF}/\bar{Q}_{SR}$ evaluated at a given myocardial layer when comparing the different ventricular rates (p-values < 0.001 for all layer-specific comparisons, Table 4.3).

Ultimately, no significant differences emerge from inter-frequency analysis assessing potential differences in the slopes of $Q_{AF,b}/\bar{Q}_{SR}$ across cardiac layers, albeit a trend towards significance is evident when comparing the slopes of interpolating lines across $Q_{AF,b}/\bar{Q}_{SR}$ distribution from EPI to ENDO layers at 75 and 125 bpm, in the left microvascular coronary artery districts (see Figure 4.6, p-values 0.129 for both LAD and LCx, Table 4.4). Table 4.4 reports all slope values of the HR-specific $Q_{AF,b}/\bar{Q}_{SR}$ regression lines obtained for each microvascular district (p-values for pairwise comparisons).

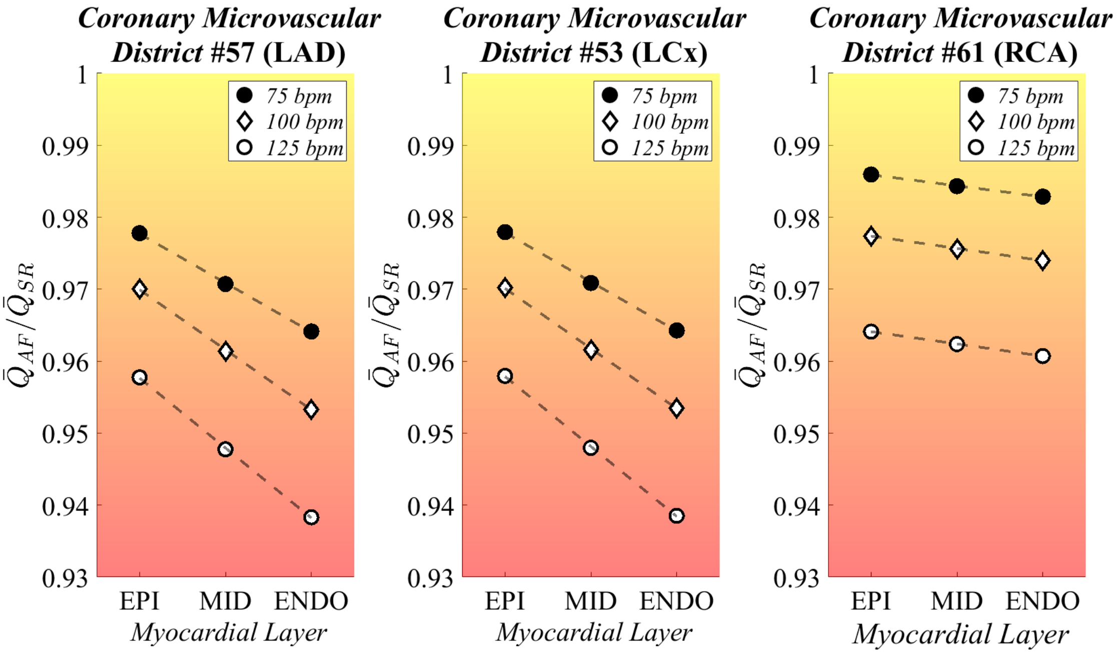

Figure 4.6: $\bar{Q}_{AF}/\bar{Q}_{SR}$ ratios at each simulated frequency across the myocardial layers, for the 3 considered coronary microvascular districts. HR-specific regression lines (dashed lines) are also reported. Image taken from [216].

Thus, the main findings of the present computational analysis, based on a detailed mathematical modeling of the coronary hemodynamics and their downstream microcirculatory districts under a pathological state of relevant clinical interest - namely, atrial fibrillation -, are the following:

Table 4.1: Beat-to-beat analysis for $\bar{Q}_{AF}$, $\bar{Q}_{SR}$, and $\bar{Q}_{AF}/\bar{Q}_{SR}$ across myocardial layers and pacing frequencies. Values reported as mean (std.dev.). Table taken from [216].

	$\bar{Q}_{AF}$ [ml/s]	$\bar{Q}_{SR}$ [ml/s]	p-value	$\bar{Q}_{AF}/\bar{Q}_{SR}$	AF-SR reduction (%)
LAD					
75 bpm					
EPI	0.2451 (0.0201)	0.2507 (0.0067)	< 0.001	0.9778	-2.222%
MID	0.2749 (0.0235)	0.2832 (0.0074)	< 0.001	0.9707	-2.928%
ENDO	0.3138 (0.0348)	0.3255 (0.0097)	< 0.001	0.9641	-3.587%
100 bpm					
EPI	0.2583 (0.0155)	0.2663 (0.0061)	<0.001	0.9700	-2.998%
MID	0.2891 (0.0215)	0.3007 (0.0075)	<0.001	0.9614	-3.859%
ENDO	0.3294 (0.0391)	0.3455 (0.0114)	<0.001	0.9533	-4.667%
125 bpm					
EPI	0.2644 (0.0150)	0.2761 (0.0037)	<0.001	0.9578	-4.225%
MID	0.2954 (0.0188)	0.3117 (0.0057)	<0.001	0.9478	-5.224%
ENDO	0.3360 (0.0418)	0.3581 (0.0113)	<0.001	0.9383	-6.169%
LCx					
75 bpm					
EPI	0.3364 (0.0275)	0.3440 (0.0091)	<0.001	0.9779	-2.206%
MID	0.3773 (0.0321)	0.3886 (0.0102)	<0.001	0.9709	-2.913%
ENDO	0.4306 (0.0475)	0.4466 (0.0133)	<0.001	0.9643	-3.573%
100 bpm					
EPI	0.3544 (0.0212)	0.3652 (0.0083)	<0.001	0.9702	-2.980%
MID	0.3967 (0.0292)	0.4125 (0.0102)	<0.001	0.9616	-3.841%
ENDO	0.4519 (0.0534)	0.4740 (0.0155)	<0.001	0.9535	-4.650%
125 bpm					
EPI	0.3627 (0.0144)	0.3786 (0.0022)	<0.001	0.9580	-4.204%
MID	0.4052 (0.0255)	0.4275 (0.0062)	<0.001	0.9480	-5.203%
ENDO	0.4609 (0.0570)	0.4911 (0.0223)	<0.001	0.9385	-6.149%
RCA					
75 bpm					
EPI	0.0389 (0.0045)	0.0394 (0.0015)	<0.001	0.9859	-1.406%
MID	0.0476 (0.0052)	0.0484 (0.0017)	<0.001	0.9843	-1.569%
ENDO	0.0554 (0.0058)	0.0564 (0.0019)	<0.001	0.9829	-1.714%
100 bpm					
EPI	0.0409 (0.0037)	0.0419 (0.0013)	<0.001	0.9774	-2.259%
MID	0.0501 (0.0041)	0.0514 (0.0015)	<0.001	0.9756	-2.438%
ENDO	0.0583 (0.0045)	0.0599 (0.0016)	<0.001	0.9740	-2.602%
125 bpm					
EPI	0.0418 (0.0028)	0.0434 (0.0009)	<0.001	0.9641	-3.589%
MID	0.0513 (0.0031)	0.0533 (0.0010)	<0.001	0.9624	-3.763%
ENDO	0.0596 (0.0032)	0.0620 (0.0011)	<0.001	0.9607	-3.929%

Table 4.2: ANOVA test results for inter-layer analysis of $Q_{AF,b}/\bar{Q}_{SR}$ across the different myocardial layers at a given pacing frequency. Table taken from [216].

Inter-layer analysis	
Layer	p-value
LAD	
75 bpm	< 0.001
100 bpm	< 0.001
125 bpm	< 0.001
LCx	
75 bpm	< 0.001
100 bpm	< 0.001
125 bpm	< 0.001
RCA	
75 bpm	0.669
100 bpm	0.409
125 bpm	0.186

- AF exerts direct hemodynamics consequences on the coronary microcirculation and subsequent perfusion of the myocardium, which might partly explain angina-like symptoms, particularly at higher ventricular rates (HR), if superimposed on a susceptible substrate (*i.e.*, hypertensive microvascular coronary disease, AF-related endothelial dysfunction);

- considering a constant mean ventricular rate, AF, decreases mean blood flow at all myocardial layers when compared to SR, and progressively even more going from subepicardial to subendocardial layer;

- given a specific myocardial layer, higher ventricular rates during AF relate to a more pronounced reduction in microvascular blood flow and thus myocardial perfusion, if compared to the corresponding SR simulation.

As anticipated, it has been extensively described that AF patients may suffer from ischemic chest pain, with associated electrocardiographic changes (ST depression), even in case of normal epicardial coronary arteries [283, 185, 262]. In particular, the magnitude of ischemic electrocardiographic alterations during ongoing AF - specially at high ventricular rates - do not seem to be predictive of obstructive epicardial coronary artery disease, differently from SR where electrocardiographic changes are clear predictors of obstructive epicardial coronary disease [197]. This latter finding, despite apparently ambiguous, is partly explained by AF-induced

Table 4.3: ANOVA test results for inter-frequency analysis of $Q_{AF,b}/\bar{Q}_{SR}$ across the different simulated frequencies across a given myocardial layer. Table taken from [216].

Inter-frequency analysis	
HR	p-value
LAD	
EPI	< 0.001
MID	< 0.001
ENDO	< 0.001
LCx	
EPI	< 0.001
MID	< 0.001
ENDO	< 0.001
RCA	
EPI	< 0.001
MID	< 0.001
ENDO	< 0.001

Table 4.4: Inter-frequency analysis comparing the slope of interpolating line across the three layer-specific $Q_{AF,b}/\bar{Q}_{SR}$ distribution for each coronary microvascular district (myocardial layers conventionally indexed as EPI = 1, MID = 2, ENDO = 3, SE: standard error). Table taken from [216].

	Slope coeff.	**SE**	**Comparison**	**p-value**
LAD				
75 bpm	-0.0068	0.0014	75 vs. 100 bpm	0.432
100 bpm	-0.0083	0.0013	100 vs. 125 bpm	0.446
125 bpm	-0.0097	0.0013	75 vs 125 bpm	0.129
LCx				
75 bpm	-0.0068	0.0014	75 vs. 100 bpm	0.432
100 bpm	-0.0083	0.0013	100 vs. 125 bpm	0.429
125 bpm	-0.0097	0.0012	75 vs. 125 bpm	0.116
RCA				
75 bpm	-0.0015	0.0017	75 vs. 100 bpm	0.926
100 bpm	-0.0017	0.0013	100 vs. 125 bpm	1.000
125 bpm	-0.0017	0.00093	75 vs. 125 bpm	0.918

coronary microvascular dysfunction, previously documented *in vivo* and accounting for a limited coronary flow reserve in AF patients. However, another possible mechanism may be the direct hemodynamic influence exerted by the typically irregular AF rhythm on coronary hemodynamics. The coronary circulation is peculiar, blood flow is prominent during diastole (see section 1.2 in chapter 1), due to the complex interplay between the forcing pressure (aortic pressure) and the extravascular forces (myocytes contraction and left ventricular end-diastolic pressure) compressing the microvasculature of the different myocardial layers, in particular the subendocardium [59]. Surprisingly, this mechanism has not yet been thoroughly investigated in this context, although clinical data in humans clearly demonstrated that the irregular AF beating produces detrimental hemodynamic effects in terms of decreased cardiac output and increased biventricular filling pressure [40]. Our group was the first to demonstrate that AF can exert direct epicardial coronary flow impairment and oxygen supply-demand ratio unbalancing based on a multiscale computational model [227]. Therefore, in the present study, the purpose was to to deepen the comprehension of the direct hemodynamic effect of AF on the coronary circulation, by designing a novel *in silico* approach implementing a higher order, multiscale 1D-0D computational model enriched by detailed mathematical description of the coronary microcirculatory districts. The study suggest thus detrimental consequences that an irregular rhythm *per se* exerts on microvascular coronary blood flow. On top of AF-related endothelial dysfunction, the altered rhythm may itself directly decrease myocardial blood flow, particularly at the subendocardial level. This reduction in myocardial perfusion appears to be dependent on the ventricular rate, with greater reduction observed at higher rates during AF, another potential element favoring a stricter rate control target in patients with permanent AF [217, 7].

Furthermore, our findings are in line with previous evidence on animals: Saito *et al.* [220] demonstrated that mechanically-induced AF diminishes coronary flow reserve in anesthetized open-chest dogs, particularly in subendocardial layers (subendocardial blood flow was reduced by 22%, while subepicardial blood flow by 9% only). Similarly, Kochiadakis *et al.* [115] showed a reduced coronary flow reserve in humans elicited in experimentally induced AF compared to right atrial pacing at a similar heart rate, even though they did not assess potential differences in blood flow distribution across myocardial wall.

The computational framework here adopted is not merely able to describe AF-induced direct hemodynamic effects only, but also unique details and cause-effect relationships regarding the possible mechanisms underlying these phenomena. In fact, as reported in Table 4.5, an in-depth analysis of two key-factors shaping coronary hemodynamics, such as the driving pressure (aortic pressure) and the most relevant extravascular force (left ventricular end-diastolic pressure, p_{LVED}) suggests that: (i) the reduced coronary flow during AF, compared to SR, at higher ventricular rates correlates to a drop in mean aortic pressure (and consequent reduction of cardiac output and coronary circulation driving pressure); (ii) the AF-driven greater reduction in subendocardial perfusion, with respect to the other cardiac layers, in the left-sided coronary arteries (LAD and LCx), correlates to a significantly increased left ventricular end diastolic pressure, compared to right ventricle end-diastolic pressure p_{LVED} given the lower absolute values of right ventricular pressures. This picture is even further worsened at faster ventricular rates.

Table 4.5: Summary statistics of mean aortic pressure (MAP), left ventricular end-diastolic pressure (p_{LVED}) and right ventricular end-diastolic pressure (p_{RVED}). Values reported as mean ± SD (standard deviation). Table taken from [216].

Cardiac Parameters			
	MAP [mmHg]	p_{LVED} [mmHg]	p_{RVED} [mmHg]
SR 75	92.71 ± 2.10	15.37 ± 0.18	10.61 ± 0.25
AF 75	90.9 ± 6.29	15.73 ± 0.70	11.49 ± 0.75
p-value	< 0.001	< 0.001	< 0.001
SR 100	97.20 ± 1.94	15.49 ± 0.22	9.18 ± 0.21
AF 100	94.77 ± 4.92	15.78 ± 0.78	10.91 ± 1.07
p-value	< 0.001	< 0.001	< 0.001
SR 125	100.03 ± 1.25	15.85 ± 0.22	9.82 ± 0.55
AF 125	96.59 ± 3.44	16.10 ± 0.83	11.51 ± 1.21
p-value	< 0.001	< 0.001	< 0.001

Concluding remarks

The following limitations connected to the mathematical modeling of coronary hemodynamics have to be acknowledge in light of the conclusions drawn from the present study. Primarily, the coronary microvascular model includes a passive autoregulation mechanism accounting for coronary vessels resistance variation in response to blood volume changes occurring to the coronary microvascular beds, but does not directly account for metabolic regulations, as well as for AF-induced endothelial dysfunction. In addition, the presence of other comorbidities and the potential hemodynamic effects of rate control drugs is not taken into account in our framework. In spite of this, considering that our analysis focuses mostly on the assessment of the pure hemodynamic effects of AF on coronary circulation, our simplified but powerful computational framework, as well as the use of standardized conditions regardless of any other baseline clinical feature potentially altering the mechanical properties of both cardiac vessels and muscle, allows to explore the standalone impact that the irregular AF beating exerts on the coronary circulation.

Chapter 5

Modeling posture-driven acute cardiovascular and hemodynamic changes

(the contents of the present chapter have been previously published in [68, 65, 64])

In spite of the influence of gravity and posture changes onto the human CVS has been recognized and investigated for decades [92, 23, 43, 241], a number of aspects still need further elucidation. Among the most intriguing issues, the key-role played by autonomic and autonomous regulation mechanisms in preserving global homeostasis - or their inefficient intervention due to pathological conditions - has still to be fully understood, especially during changes of posture. These aspects are crucial to grasp how regulation and adequate blood pressure and perfusion levels are maintained during active and passive orthostatic stress (refer to chapter 2 for further details). Indeed, a number of autonomic disorders or dysautonomias (*e.g.*, orthostatic hypotension, orthostatic intolerance and syncope [81]), can prevent efficiency of the CVS response to gravitational stress. These problems are also relevant to space medicine, committed to devising new strategies to counteract autonomic deconditioning following long-term permanence in space [41, 91]. In the context of autonomic medicine, head-up tilt (HUT) and tilt-down table tests are used as fundamental diagnostic and prognostic clinical tools, being widely employed to study autonomic disorders [36].

In addition, beside the huge hemodynamic alterations experienced by the human CVS when undergoing orthostatic stress [43, 23] (chapter 2), such as during stand up, sitting or HUT, the dynamics of pressure and flow waves traveling throughout the arterial tree is also crucial to investigate and monitor to fully understand the overall CVS functioning [151, 274, 183, 247, 174, 50] (see chapter 1, section 1.3). Indeed, despite the wide literature covering the subject of arterial wave dynamics and coping to various working conditions, their dependency on body posture still remains unclear. However, a few efforts have been made to obtain *in vivo* measurements of arterial wave reflection indices upon varying posture [14, 13, 101, 102]. These studies highlight that central (*i.e.*, ascending aorta, aortic arch) wave reflection seems to be reduced when passing from supine to upright posture, in spite of the widely acknowledged CVS stiffening - mirrored by the globally increased wave velocity - driven by augmented peripheral resistance and reduced systemic venous tone and compliance [278, 231, 271]. Therefore, previous results remain contradictory, requiring further elucidation. Moreover, it is interesting to note how the CVS is optimized from the point of view of waves transmission and reflection phenomena, at least while lying in the supine position. This means that direct (*i.e.*, forward) waves are transmitted with low losses across arterial bifurcations and tapered vessels [278, 49], as a consequence the optimal cross-section area matching between parent and daughter vessels. On the other hand, reflected waves are trapped and cannot travel back along the arterial tree, resulting in the so-called 'wave trapping' effect, an advantageous CVS working condition documented by many researchers [49, 276, 272]. Indeed, this latter CVS configuration represents a natural protection of the heart against reflected waves, meanwhile reducing cardiac workload due to the enhanced forward waves propagation. Nevertheless, despite the fact that most of human life takes place in a standing posture, no investigation has been conducted on whether and how this favorable CVS configuration encountered at supine position is maintained or lost along with body posture changes, such as during HUT or upright standing.

In this picture, the present chapter has a twofold aim: (i) to investigate systemic, cardiopulmonary and coronary circulation response to passive HUT, introducing the first multiscale model version designed to this end; and (ii) to further exploit the model to describe complex dynamics of pressure and flow wave patterns along the arterial tree in response to orthostatic stress.

5.1 *In silico* simulation of HUT

The mathematical model introduced in this chapter is used to inquire into the short-term hemodynamic alterations elicited by passive tilt from supine to upright posture. The steady-state and transient model response is assessed in terms of main hemodynamic parameters, including mean arterial pressure (MAP), heart rate (HR), stroke volume (SV), cardiac output (CO), total peripheral resistance (TPR), central venous pressure (CVP), regional blood volumes, cardiac work and indices of oxygen consumption and cardiac performance. The study includes also a systematic investigation of the previous CVS parameters response to increasing tilting rate from supine to 70° HUT, and *vice versa* from 70° HUT to supine position.

5.1.1 Model description

The multiscale model of the human CVS employed in this study is a previous version [68, 65, 64] of the model introduced in chapter 3 of the present thesis. In particular, the model combines the same 1D representation of the arterial network - including all 63 1D arteries listed in appendix A, Table A.1, where no partial collapse model is applied to carotid and vertebral arteries - with the 0D model counterpart of the systemic microcirculation, venous return and cardiopulmonary circulation. No ocular model is attached to the version of the model adopted in this chapter, whereas the head-cerebral circulation is described as a pure sequence of RLC compartments for the arteriolar, capillary, venular and venous head districts, including a simple model of cerebral autoregulation, and no detailed circuital model of the cerebrovascular circulation is enclosed.

5.1.2 HUT simulation

Passive tilting simulations are based on Heldt's modeling approach [93], that is according to the following relationship:

$$\alpha(t) = \begin{cases} \alpha^{sup}\,, & t < t_{tilt,0} \\ \alpha^{sup} + \dfrac{\alpha^{up} - \alpha^{sup}}{2}\left(1 - \cos\left(\pi \dfrac{t - t_{tilt,0}}{\Delta t_{tilt}}\right)\right), & t_{tilt,0} \leq t \leq t_{tilt,0} + \Delta t_{tilt} \\ \alpha^{up}\,, & t > t_{tilt,0} + \Delta t_{tilt} \end{cases}, \tag{5.1}$$

where tilt angle $\alpha(t)$, starting from the supine position ($\alpha^{sup} = 0$) at $t_{tilt,0}$, reaches the desired tilted posture α^{up} within a given rotation period Δt_{tilt}. Tilt angles specifically selected for the present investigation are 30°, and 70°, while 90° (*i.e.*, upright) is simulated for the wave dynamics analysis presented in the following section. All levels of α^{up} are reached keeping a constant tilting rate.

5.1.3 *In vivo* HUT model validation

To the aim of validating our CVS model, *in vivo* clinical measurements were carried out at the Città della Salute e della Scienza Hospital in Turin, at the "Autonomic Unit" laboratory of the Department of Medical Sciences, University of Turin. Hence, fourteen healthy male volunteers - coherently with the model setup - were enrolled and tested, all respecting age (20-30 yo), weight (50-95 kg) and height (160-200 cm) requirements (subjects anthropometric features are reported in Table 5.1 and in [68]).

The experimental study involved continuous heart rate HR and finger arterial pressure recording via the Finapres Finometer MIDI device [63], with height correction unit to derive brachial arterial pressure [90]. By the same instrument, also

Table 5.1: Subjects anthropometric features.

Subject	**Age**	**Weight [kg]**	**Height [cm]**
1	26	60	175
2	26	73	175
3	26	78	182
4	25	78	190
5	26	82	175
6	26	74	171
7	26	92	198
8	29	70	187
9	23	75	186
10	26	80	175
11	28	68	178
12	27	75	182
13	29	80	178
14	24	82	180

stroke volume SV, cardiac output CO and total peripheral resistance TPR were acquired/derived. Two digital sphygmomanometers were used to measure punctual heart rate, systolic, mean and diastolic arterial pressure at brachial and calf level, as a baseline measurement to calibrate the Finapres signals. To perform tilt table tests, a standard TTPD2-AV-HD dynamic bed was used, with a nominal tilting velocity of 10° for every 2.5 s. The experimental protocol included two separate sessions of tilt: (i) the first one reaching an inclination of 30° starting from the supine position, and returning then to the supine position, to be followed by a (ii) second session with tilt from supine to 70° and then back again to supine. Each upright tilted posture was maintained for 5 minutes, to favor Finometer continuous recording and thus capture the complete transient response to change of posture, as well as to record the new steady-state post-tilt condition with respect to the previous corresponding supine basal status.

Table 5.2, showing the supine baseline condition against the steady-state hemodynamic response to two modeled levels of tilt, *i.e.*, 30° and 70°, reports steady-state pre- and post-tilt model outcomes compared to literature parameters ranges and *in vivo* measures obtained from our HUT experiments. As evidenced by Table 5.2, the model reproduces fairly well the global hemodynamic response to passive change from supine to upright posture to different levels of tilt. In particular, relative variations with respect to supine baseline levels fall within literature ranges, although almost all parameters match also available absolute ranges. The only exception regards our *in vivo* SV, CO and TPR data, which tend to be overestimated by the Finometer due to its limited absolute accuracy, in spite of the high capability of capturing parameter variations [37].

Table 5.2: Comparison between literature data (≊: no significant variation, – : no data available), our *in vivo* findings (in square brackets) and model outcomes for steady-state supine, HUT 30° and 70°. Literature data references reported in chapter 2. Table taken from [68].

Variable	**Supine**		**HUT 30°**		**HUT 70°**	
	Literature [Measured]	Model	Literature [Measured]	Model	Literature [Measured]	Model
Brachial *MAP* [mmHg]	66÷105 [85±10]	82	-5%÷+23% [86±8]	89 (+9%)	-3%÷+33% [89±7]	90 (+10%)
Tibial *MAP* [mmHg]	75÷110 [93±10]	85	110÷175 [141±16]	135	150÷200 [179±17]	173
HR [bpm]	69÷77 [64±14]	69	≊÷+13% [66±12]	73 (+6%)	+7%÷+34% [79±12]	86 (+25%)
SV [ml]	59÷119 [121±20]	75	-13%÷-25% [100±16]	61 (-19%)	-20%÷+40% [82±18]	50 (-33%)
CO [l/min]	3.9÷8.7 [7.7±3.2]	5.2	-13%÷-17% [6.8±1.6]	4.4 (-15%)	-4%÷-21% [6.8±1.4]	4.2 (-19%)
TPR [mmHg s/ml]	0.79÷1.32 [0.55±0.10]	0.83	+17%÷+28% [0.65±0.13]	1.08 (+30%)	+3%÷+44% [0.71±0.24]	1.15 (+39%)

Steady-state model validation is further achieved through modeled brachial pressure waveform comparison with experimental signals extracted by the Finometer, at supine and HUT 70° positions. Indeed, a number of 50/60 consecutive brachial pressure waveforms are normalized in time (with respect to the single RR heartbeat duration), and averaged for each subject. Then, the ensemble average pressure waveform is obtained by averaging all fourteen subject-specific waves, re-scaled with respect to their time-averaged mean pressure. Standard deviation bands are computed including both intra- and inter-subject variances as

$$
\begin{aligned}
\sigma^2 &= \frac{1}{N_1 + \cdots + N_M}\left(\sum_{i=1}^{N_1}\Big(x_{i,1} - \mu\Big)^2 + \cdots + \sum_{i=1}^{N_M}\Big(x_{i,M} - \mu\Big)^2\right) \\
&\approx \frac{1}{M}\Big(\sigma_1^2 + \cdots + \sigma_M^2 + \Big(\mu_1 - \mu\Big)^2 + \cdots + \Big(\mu_M - \mu\Big)^2\Big),
\end{aligned}
\tag{5.2}
$$

where M is the number of subjects, x_i is the time series of the considered hemodynamic variable, and N denotes subjects sample size. The outcomes of this pressure waveform validation are depicted in Figure 5.1. Overall, the model is able to reproduce fairly accurately the average measured pressure waveform both prior and after HUT to 70°; the dicrotic notch and the secondary peak position appear as delayed approximately to the same extent for the simulated and measured waveforms, with the simulated wave always comprised within the standard deviation bands of the measured average signal, except for the foot of the wave. This local discrepancy can be likely due to the signal smoothing caused by the averaging operation, with consequent overestimation of diastolic and underestimation of systolic pressure.

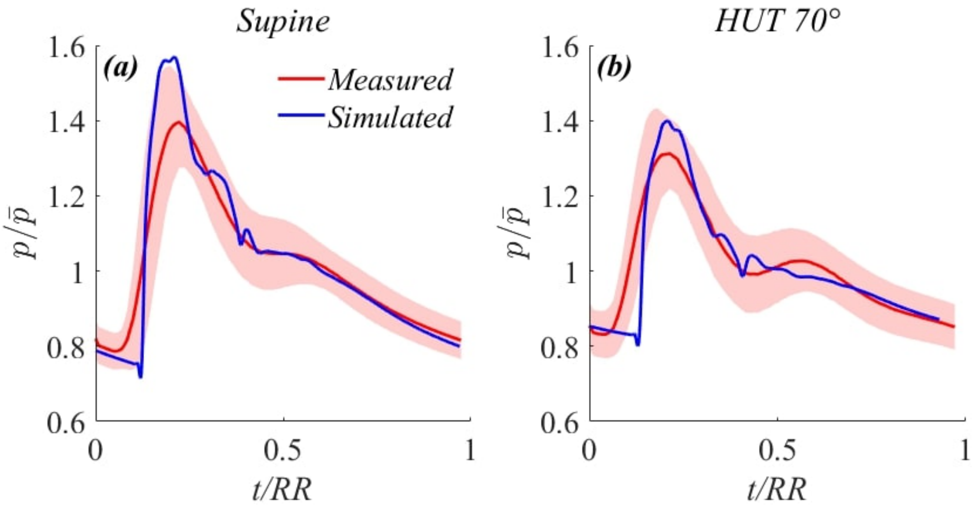

Figure 5.1: Simulated (blue) and measured (red, with standard deviation bands) steady-state brachial pressure waveforms for supine (a) and 70° HUT (b). $\bar{p}$ denotes brachial MAP. Image taken from [68].

Furthermore, Figure 5.2 reports beat-to-beat hemodynamic parameters transient response to 70° HUT at 4°/s. Results shown are referred to the supine position, in terms of ratio or absolute difference depending on the considered variable. In general, good agreement is found between *in vivo* and model outcomes, with all simulated parameters falling within the standard deviation band about the mean of the related experimental signal. The brachial MAP initial drop is caused by the sudden fluid migration from upper to lower regions (and consequent reduction in ventricular filling), which is subsequently well recovered by means of regulation mechanisms intervention. Simulated under- and overshoots are in line with observations reported in other studies [93, 285, 256]. In spite of subjects averaging tends to smooth strong fluctuations that are not in phase among subjects (Figure 5.2, panel b), standard deviation band peaks are always well comparable with modeled signals over- and undershoots.

5.1.4 Overall cardiovascular response to simulated HUT

In this paragraph, results are organized by describing first a global picture of the most relevant steady-state behaviors following tilt to 70°, from the 1D arterial tree up to 0D venous return compartments. Secondly, the role of tilting rate onto the transient response to 70° HUT and tilt back to supine is systematically investigated.

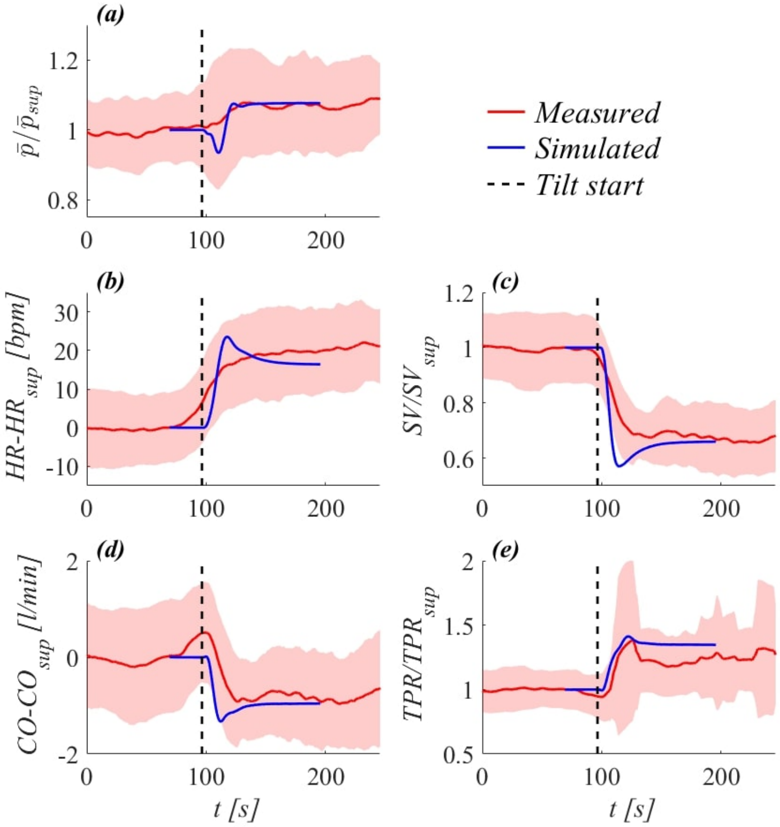

Figure 5.2: Simulated (blue) and experimental (red, with standard deviation bands) transient hemodynamic response to 70° HUT at 4°/s. Image taken from [68].

Steady-state CVS response to HUT: overview

Figure 5.3 shows steady-state pressure and flow rate time signals taken at distinct body sites, both from the 1D (along the arterial tree) and the 0D (left ventricle) model counterparts. As a main consequence of the HR increase elicited by tilt to 70°, post-tilt signals are shifted out of phase with respect to supine condition, due to the altered systole-to-diastole ratio within the single heartbeat duration. In fact, as the HR rises, systole duration tends to prevail with respect to diastole, resulting in a different balance of the two cardiac phases. Moreover, Figure 5.3 shows how flow rate amplitude reduction at all sites reflects the drop in CO typically observed upon acute response to change of posture [43, 23, 241], with flow mean value diminishing significantly up to -20% at the aortic valve (panel c) and all along the aorta (bottom diagrams of panels d-h). Pressure signals appear as shifted up or down depending on the positive or negative effect of gravity (top diagrams of panels b, d-h) because of the hydrostatic pressure contribution associated with the column of blood measured from the heart to each considered site. This outcome implies arterial mean pressure values more than doubled at tibial level, as already widely confirmed [43, 23, 241] (Table 5.2). Conversely, reduced mean arterial pressure is detected at carotid/cerebral level (panel b), leading to changes in cerebral perfusion pressure and thus driving the prompt intervention of autoregulation mechanisms aimed at preserving cerebral blood flow. Finally, due to heart chambers emptying following downward blood shift at tilt up, left ventricle end-diastolic volume is considerably decreased, leading to a marked stroke work reduction (area of the left ventricle pressure-volume loop, panel a), which is a proxy of cardiac energy supply.

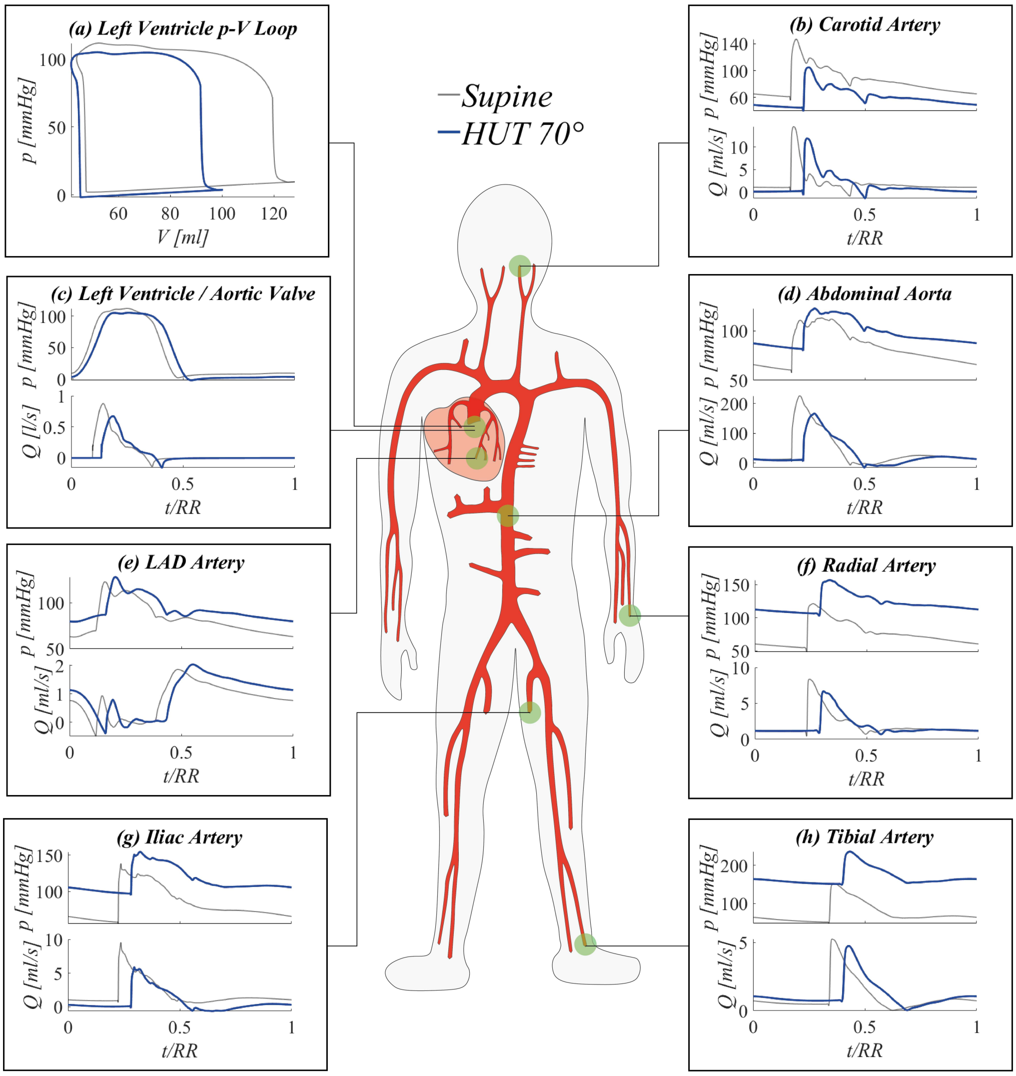

Figure 5.3: simulated steady-state results at 70° HUT (blue) and in supine position (grey). Image taken from [68].

Steady-state CVS response to HUT: 1D arterial pressure patterns

Pressure patterns and related alterations following tilt to 70° are detailed to a closer perspective in Figure 5.4. Considering eight distinct sites along the aorta and the arterial tree (from the aortic arch down to the lower extremity of the posterior tibial artery) relative differences of mean, systolic and diastolic arterial pressure between 70° HUT and supine position are depicted in panels a-b. Pressure changes are reported both taking into account (top panel a, 70° HUT-to-supine pressure variations Δp) and subtracting (bottom panel b, Δp^*) the hydrostatic contribution $\rho g z \sin \alpha$, where z is the height difference between the considered site and the aortic valve (assumed as the arterial hydrostatic indifference point, HIP).

Panel a of Figure 5.4 shows systolic, mean and diastolic pressures rising with increasing distance from the heart, reaching values more than doubled at feet level (mean pressure $\bar{p}$ +125.8%). At the summit of the aortic arch, a mean pressure reduction is registered, diminished by 1.5% with respect to the supine condition. When the hydrostatic pressure contribution is accounted for (panel a), diastolic pressure increases monotonically proceeding along the feetward direction, and more than systolic pressure. Conversely, when the hydrostatic contribution is virtually removed (panel b), diastolic pressure is still markedly augmented with respect to its supine value, by a value as high as +20% on average, although almost uniformly throughout the considered arterial path. We recall that, despite the global reduction in venular and venous compliance accompanied by the augmented total peripheral resistance, the observed diastolic pressure increase in the absence of hydrostatic contribution is driven by the different interplay between systole and diastole as a consequence of the augmented HR, which tends to lengthen systole leaving ventricles shorter time to relax (*i.e.*, diastolic pressure remains high). Conversely, systolic pressure appears to reduce slightly along the arterial tree. Mean pressure undergoes only small alterations (+0.7%÷+3%), following a non-monotonic trend from head to feet, with a peak revealed at thoracic level. In addition, results displayed in Figure 5.4 underline the importance of the hydrostatic pressure contribution onto mean pressure variation following HUT. While hydrostatic contribution alone represents almost the entire pressure change registered at the lower extremities (only +0.7% found for $\bar{p}$ at tibial level), central regions instead show much larger mean pressure changes (+2/3%) with respect to supine, when hydrostatic terms are not enclosed. The reason for such behavior can be found in the regulatory action of the baroreflex mechanisms, together with the effect of intrathoracic pressure reduction onto venous return and cardiac filling, both of which influence mostly central arterial vessels.

Moreover, Figure 5.4b reports also relative variations of pulse pressure with respect to supine values. As expected from clinical evidences [43, 23, 241], pulse pressure is reduced along the entire aorta at 70° HUT, particularly because of the increased diastolic pressure. Pulse pressure partially recovers proceeding along the feetward direction, likely because of the combined effect of arterial vessels stiffening and vasoconstriction promoted by regulatory actions enhanced by the baroreflex and cardiopulmonary reflex controls. The overall pulse pressure drop mirrors the reduction revealed for cardiac stroke work (SW, area of p-V loop, Figure 5.3a), which decreases by 33% at 70° HUT, highlighting the different working condition faced by the CVS when undergoing passive HUT.

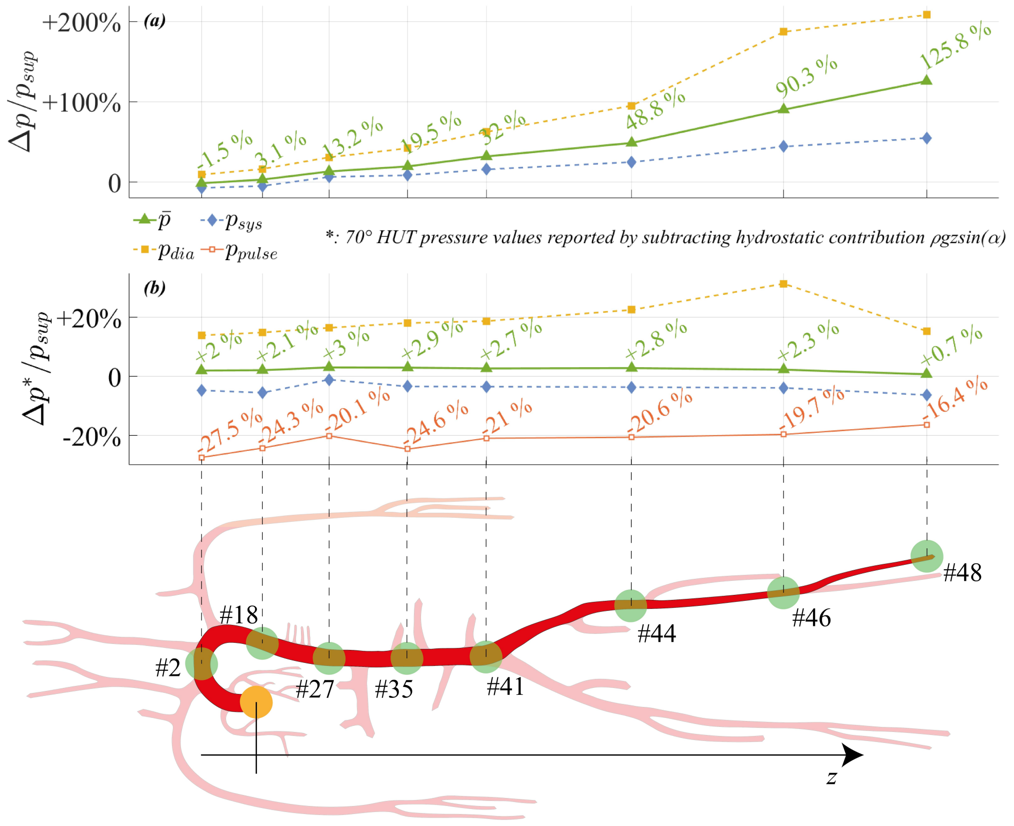

Figure 5.4: Relative pressure variations between steady-state 70° HUT and supine position at different sites along the aorta and legs arteries, with the hydrostatic contribution taken into account ($\Delta p/p$, panel a), and neglected ($\Delta p^*/p$, panel b). Image taken from [68].

Steady-state CVS response to HUT: 0D systemic circulation

The posture-driven CVS response of the 0D systemic vasculature is illustrated in Figure 5.5, where systemic distal arterioles, capillary and venular beds, systemic venous return encompassing venous and venae cavae compartments are represented. Three representative body regions are selected to analyze gravity effects onto this side of the circulation, that is head, abdomen and legs (a-c panels in Figure 5.5).

Steady-state and time-normalized pressure signals are presented for each mentioned 0D compartment, evidencing the same signals phase shifting already encountered for 1D signals depicted in Figure 5.3 caused by the different interplay between systole and diastole following HR modulation.

Pressure variations along the 0D systemic circulation are ruled mostly by (i) resistive effects - especially in microvascular compartments (arteriole, capillary) - and (ii) hydrostatic pressure effects (which are instead negligible in the systemic microcirculation, namely in arterioles, capillaries and venules). The deepest pressure drops is revealed at arteriolar and capillary levels, regardless of the body position: in fact, such compartments provide the highest vascular resistance, being responsible for lowering blood pressure to a value suitable for gas exchange. Thus, pressure drops occurring through arteriolar and capillary compartments shall be present at any body posture.

A further relevant pressure drop emerges along the legs region (panel c) between veins and venae cavae compartments, at 70° HUT. Such pressure drop is instead exclusively due to the related hydrostatic pressure component registered between leg veins and the following abdominal vena cava compartment, due to a vertical anatomical distance of approximately 0.5 m between the above said compartments, causing the reported 40 mmHg pressure decay. On the other hand, almost no hydrostatic pressure drops are revealed at abdominal level (panel b), as abdominal veins are assumed to have no dominant vertical anatomical dimension. Head veins (panel a), instead, may reach negative levels of intraluminal pressure upon 70° HUT, because of their elevated position with respect to the heart, although their tone does not vary significantly thanks to their peculiar extravascular and non-collapsible condition (chapter 2) [92, 98, 131, 120, 23].

Transient dynamic CVS response to HUT

In this paragraph, the effect of different tilting rates on the CVS transient response to 70° HUT is systematically investigated. In Figure 5.6, the model outcomes in response to five different tilting rates ranging from 35°/s to 1.4°/s are reported.

From an overall point of view, the same steady-state post-tilt condition is approached by all variables at all different tilting rates, implying that the post-tilt steady-state configuration is independent of the selected tilting velocity, with the transitory duration inversely related to the rate of tilt. Brachial mean arterial pressure (denoted as $\bar{p}$, panel a) exhibits a non-monotonic variation at all tilting rates, apart from the slowest case, *i.e.*, 1.4°/s (50 s tilting duration), where the initial pressure drop is almost absent. This different behavior encountered at 1.4°/s is likely dictated by the prompt compensation mediated by the regulatory mechanisms acting efficiently at such a slow tilting rate. Notice that the fastest case (*i.e.*, 35°/s, reaching 70° HUT in 2 s) may potentially be problematic for orthostatic intolerant subjects, as such a rapid posture variation to upright, especially when combined

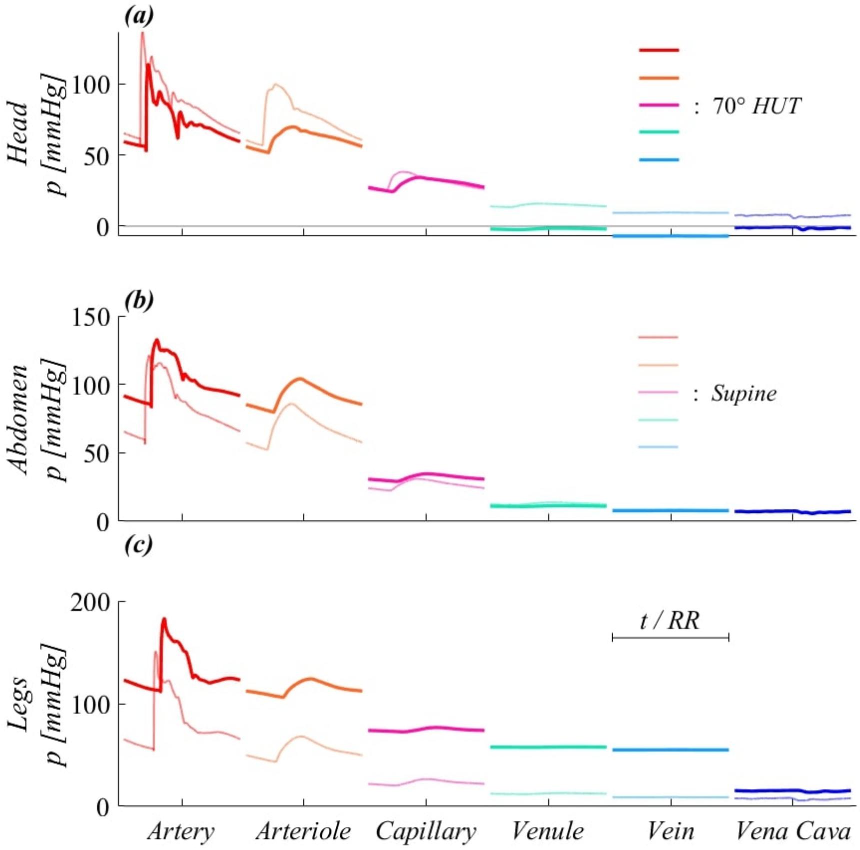

Figure 5.5: Steady-state 0D compartments pressure signals at supine (thin, light colored lines) and 70° HUT (thick, dark colored lines). Panels refer to different body regions: (a) head , (b) abdomen , (c) legs. Image taken from [68].

with total absence of additional compensatory mechanisms (muscle pumping action of calf, legs and diaphragm), can lead to dizziness and loss of consciousness.

All variables generally present under- and overshoots, although no oscillatory behavior is ever observed, except for mean brachial arterial pressure $\bar{p}$, showing a modest positive peak is detected following the initial deep drop, particularly at faster tilting rates. In all cases, under- and overshoots amplitude is progressively damped as the tilting rate is slowed down, showing a more and more nearly-monotonic response at slowest tilting rates. An interesting behavior is registered for CO (panel d) at the fastest tilting rate, where an evident initial rapid increase is revealed. A possible reason for this initial positive peak can be found in the rapid HR rise (panel b) driving the initial CO increase, compensating and overcoming the reduction in SV (panel c), and thus counteracting temporarily the effect of peripheral vasoconstriction (*i.e.*, increased TPR, panel e). In fact, TPR shows also remarkable behaviors especially at higher tilting rates, for which the sudden initial resistance increase is decelerated by following intervention of the remaining slower efferent organs (venous tone regulation), and then adjusted (*i.e.*, fastened) again to counteract abrupt effects of posture variation.

Another peculiar response is observed for CVP (panel f), decreasing as primary consequence of intrathoracic pressure drop upon assuming upright posture (chapter 2). Since intrathoracic pressure decreases monotonically with increasing tilt angle, the related CVP undershoot exhibited at faster tilting rates must be due to different mechanisms, *e.g.*, a delay in venous return restoring. Vascular volume increase registered in the lower limbs (panel h) and the corresponding decrease detected at central level (panel g) are widely debated, particularly concerning plausible stress-relaxation mechanisms aimed at delaying venous vascular filling [95]. However, volume shifts predicted by our model is in good agreement with available clinical findings [95], with an amount of approximately 400 ml of fluid being transferred from upper to lower body regions within 10÷60 s (chapter 2). Moreover, at all simulated tilting rates cerebral autoregulation succeeds in maintaining nearly unchanged cerebral blood flow, thus preserving correct cerebral perfusion with only little decrease revealed at steady-state post-tilt CBF (panel i).

Lastly, considering TTI (tension time index, given as $TTI = p_{lv,mean} \cdot RR$, that is mean left ventricle pressure times the cardiac cycle length) and SW responses (panels l and m, respectively), it is fairly evident how the system is engaged to balance gravitational load experienced during acute change of posture: once the upright posture is approached, the overall working performance and energy supply provided by the CVS are considerably reduced (CO -19%, SW -33% at steady-state 70° HUT, with respect to supine) in response to a diminished oxygen consumption (TTI, energy demand) caused by the decrease in mean left ventricle pressure (-6%) and RR interval (-20%). This implies an overall less demanding condition for the CVS functioning, elicited by the partially reduced circulating blood volume following blood pooling in the lower extremities (although considering TTI/min and other indices of oxygen consumption would lead to less evident mismatches, see following chapter 6).

Some authors have dealt also with reverse tilt from upright to supine posture, both from a modeling and a clinical perspective [93, 45, 241, 256, 248]. To address this problem, in the present study we investigate also the transient dynamic CVS response following tilt-down from 70° to supine position, focusing onto the same hemodynamic parameters already analyzed in Figure 5.6. Here, Figure 5.7 displays te CVS response following tilt-down from 70° at only two different tilting velocities (*i.e.*, 4°/s and 1.4°/s), compared to the corresponding tilt-up cases (reported in blue). Overall, HUT under- and overshoots correspond to related over- and undershoots of the analogue tilt-down case, respectively, although with different amplitude and time of occurrence. Tilt-down peaks are generally more

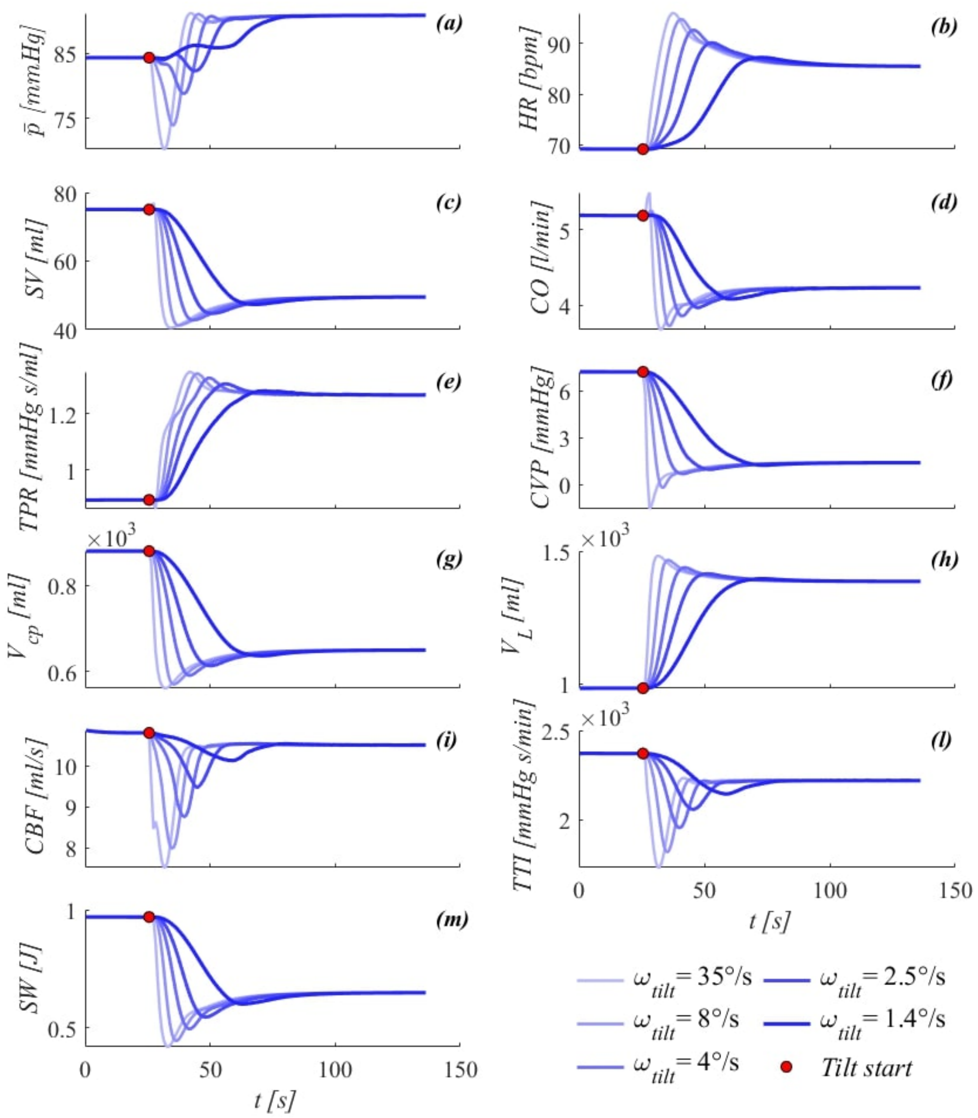

Figure 5.6: Simulated transient CVS response to passive HUT from supine position to 70° at different tilting rates. Red points denote tilting starting point. Image taken from [68].

pronounced, likely because of the non-symmetric (slower) intervention of parasympathetic activity with respect to sympathetic activity mediated by baroreflex and cardio-pulmonary reflex control. For instance, considering the case of brachial mean arterial pressure $\bar{p}$, the latter shows almost monotonic increase during tilt-up to 70° at 1.4°/s, with barely visible oscillation after the first ramp; differently, upon tilt-down from 70° to supine, $\bar{p}$ exhibits by a first evident peak followed by subsequent non-monotonic decrease to the steady-state supine value.

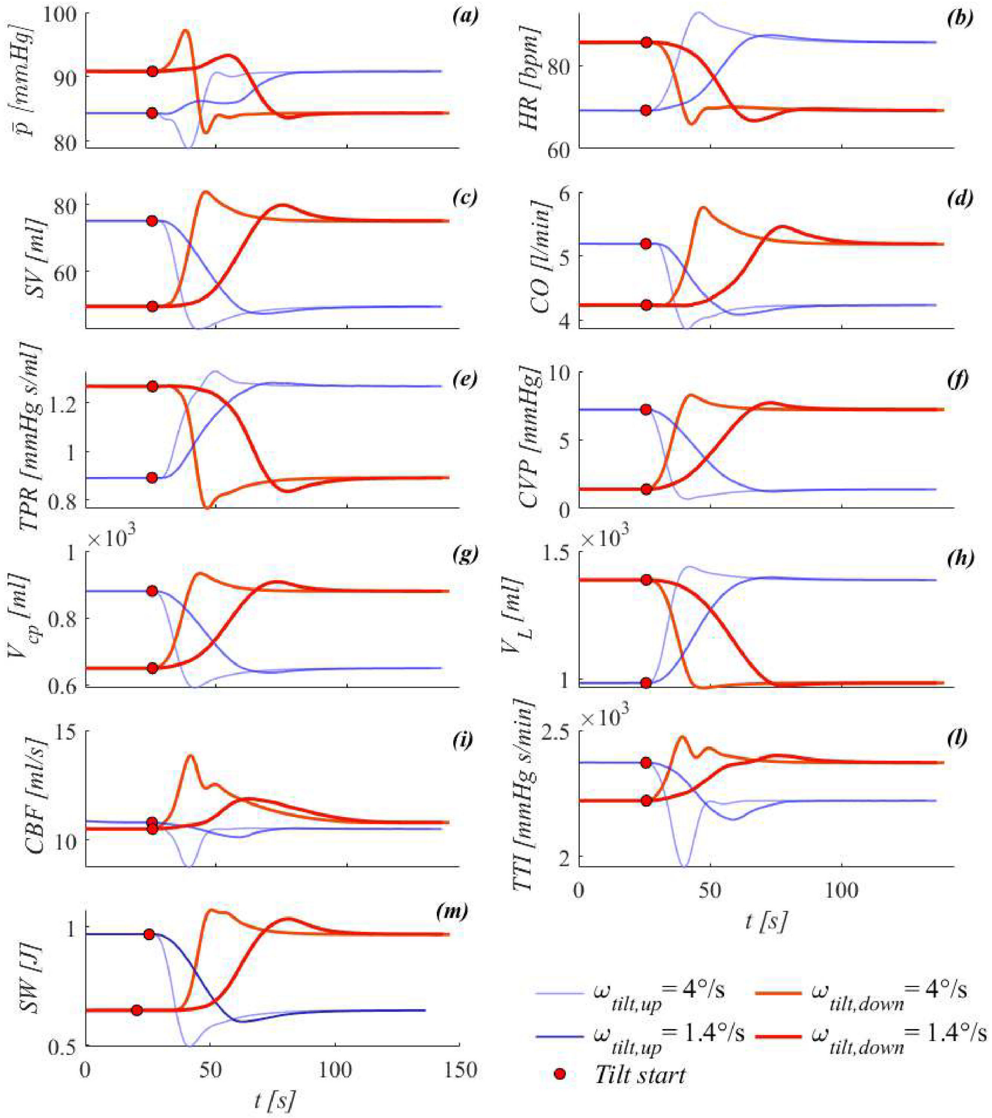

Figure 5.7: Simulated transient CVS response to passive tilt-down from 70° to the supine position at two different tilting rates. Corresponding tilt-up transients are also reported (blue lines) for comparison Red points mark tilting starting point. Image taken from [68].

5.1.5 Effects of simulated HUT on the coronary circulation

In spite of the overall CVS response to passive change of posture widely discussed so far in the present thesis [43, 256], understanding of peculiar hemodynamics involved in specific vasculature - such as the coronary circulation - still lacks exhaustive comprehension [23]. To date, little is known regarding the effect of passive orthostatic stress onto perfusion of the cardiac muscle [268]. Therefore, the mathematical model of the CVS presented in this work can be exploited in this context as diagnostic tool, in order to explore the coronary vasculature coping to gravitational load.

In the present analysis, we use the modeling approach to investigate the coronary hemodynamic response to simulated HUT from supine to 70°. To this end, we focus in particular on two main parameters shaping coronary hemodynamics, namely coronary perfusion pressure (CPP) and coronary blood flow (CBF). Observations are conducted regarding left/right coronary arteries blood flow unbalance, myocardial layers perfusion and coronary vasculature resistance behavior. Further details on this study can be found in [65].

Figure 5.8 illustrates the most relevant hemodynamic alterations detected in the coronary vasculature upon passive HUT to 70°. Defining CPP as the difference between aortic diastolic pressure ($p_{aor,dia}$, which is increased by about 8 mmHg after tilting to 70° with respect to supine) and right atrium end-diastolic pressure (p_{raed}, dropped from 7.9 mmHg at supine posture to 1.6 mmHg at 70° HUT), we observe a CPP increase of +26% with respect to supine posture (bottom right table in Figure 5.8). As CPP can be considered as the main coronary blood flow driving pressure, it is also reasonably taken as a proxy of CBF.

Actual CBF is obtained as the summation of beat-to-beat mean flow rate $\bar{Q}$ through left main coronary artery (LMCA) and right main coronary artery (RMCA), and it is shown in the bottom diagram of Figure 5.8 (blue line). Despite the upstream SV and CO reduction (see Table 5.2), a marked increase in LMCA+RMCA blood flow from 4.46 ml/s to 5.28 ml/s (+18%, bottom right table in Figure 5.8) is detected after tilting to 70° HUT. The simultaneous rise seen for CPP and CBF can be explained by systemic pulse pressure contraction (Figure 5.4, mainly due to the augmented diastolic pressure) together with concomitant intrathoracic pressure drop (linked to the decreased p_{raed}, as well as all cardiac pressures).

On the other hand, coronary vasculature hydraulic resistance ($R_{cor,eq}$) is approximated as the equivalent resistance of all the 0D microcirculatory districts describing the 0D coronary myocardial microvasculature, although no significant variation is detected for this quantity when tilting from supine to 70° HUT, as almost no blood migration towards the coronary microvascular bed occurs (we recall that coronary vasculature resistance depends on the inverse of coronary blood volume squared). In addition, due to $R_{cor,eq}$ invariance, almost no CBF differences emerge from an inter-layer point of view: single-myocardial layers flow rate changes by +18% in total subendocardial (ENDO) and by +18% in total subepicardial (EPI) vessels (that is, sum of flow over all 0D districts) going from supine to 70° HUT, as reported in the bottom right table of Figure 5.8 as well as in the small tables on the right and left sides of the same figure. From a left-to-right heart perspective instead, a little unbalance is highlighted towards right coronary arteries: +21% blood flow through RMCA - shown in the small table on top left side of Figure 5.8 - with respect to left coronary arteries (+17% flow through LMCA, +18% and +16% through LAD and LCx coronary arteries, refer to small tables on top right side of Figure 5.8). A potential explanation for this left-to-right unbalance may be the different intrachamber pressure associated with the adjacent ventricle, leading to higher left coronary arteries flow obstruction with respect to right side.

Thus, present analysis shows that passive upright posture enhances CBF likely because of the augmented CPP. Our results are qualitatively in agreement with those by Vrachatis *et al.* [268]), considering that only indirect measurements of CBF variation following change of posture are reported in their work. As already stated in chapter 4 appositely dedicated to coronary hemodynamics upon fibrillated heart rhythm, we acknowledge that our model lacks of additional coronary flow regulation mechanisms - such as metabolic and myogenic CBF regulation - other than passive adjustment of vascular resistance. Such mechanisms would probably limit CBF growth elicited by HUT-induced augmented CPP and HR rise.

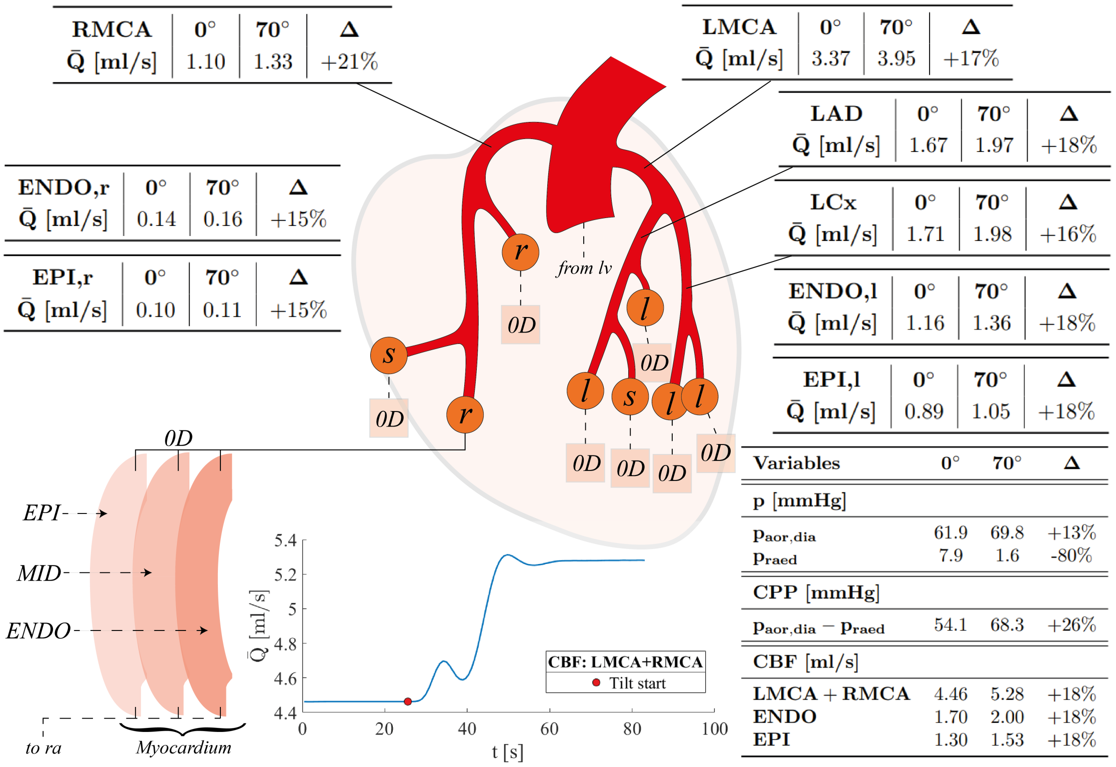

Figure 5.8: Illustration of coronary hemodynamics response to passive HUT. $\bar{Q}$ is beat-to-beat mean blood flow rate, $p_{aor,dia}$ and p_{raed} are aortic diastolic pressure and right atrium end-diastolic pressure, respectively. Image taken from [65].

5.2 Arterial wave dynamics during HUT

The concept of traveling waves and wave dynamics throughout the human vasculature has already been anticipated in chapter 1, and it is here resumed to provide further elaboration on this topic, including results from one of our studies devoted to explore the impact of postural changes onto arterial wave-connected phenomena [64].

The importance of understanding wave patterns lies in the fact that they reflect the mechanical and geometric characteristics of the arterial system, thus serving as proxies of the arterial vasculature health and working condition. Indeed, arterial pressure and flow waves originate at the aortic root level by means of periodic left ventricle contraction and relaxation cycles. These waves enter the arterial tree through the aortic valve, traveling then down the aorta and the successive bifurcations of the entire arterial tree, eventually reaching all arterial peripheral branches. Meanwhile, waves keep being continuously reflected, giving rise to backward propagating waves [274, 183, 182, 278] that travel the opposite direction, from arterial periphery toward central aorta. Therefore, at any considered point of the arterial tree, local measured pressure and flow waves are the result of the superposition of forward and backward components traveling waves. However, in spite of the huge amount of research conducted to grasp arterial wave dynamics [151, 274, 183, 247, 174, 50] especially at standard supine posture, little is known concerning wave transmission and reflection phenomena on a standing subject.

In the present section, we aim to bridge this gap by elucidating the posture-induced wave dynamics elicited by simulated orthostatic stress. To this end, in [64] we conducted a numerical investigation of the arterial wave dynamics upon simulated head-up tilt from supine to upright standing posture, resorting to the same mathematical model of the CVS presented in this chapter. Details on the particular model calibration adopted to the scope of this study can be found in [64]. Results presented in this section include (i) pressure and flow wave analysis (WA); (ii) investigation and quantification of wave reflections originated at all parts of the arterial network (*i.e.*, reflections at arterial bifurcations [278, 163, 49] in the forward and backward directions, reflections due to arterial vessels tapering [163, 232, 1], reflections produced at peripheral terminal branches [278, 163, 151]); (iii) wave intensity analysis (WIA) [183, 182, 163, 161]; and (iv) assessment of backward wave trapping [49, 276, 272] along the aorta and its response to body posture variation.

5.2.1 Wave analysis and wave intensity analysis

Wave Separation

Considering pressure P and flow Q signals taken at a given point of the arterial network, they can be expressed as the summation of their respective forward (subscript f) and backward (subscript b) traveling components as

$$P = P_f + P_b\,, \tag{5.3}$$

$$Q = Q_f + Q_b\,. \tag{5.4}$$

From the water-hammer equation [163] it follows that $P_{f,b} = \pm\, Z_c Q_{f,b}$ (taking the sign '+' for forward waves, subscript f, whereas the sign '$-$' for backward waves, subscript b), and where Z_c is the local vessel characteristic impedance. Thus, forward and backward components of P and Q signals can be expressed as

$$P_{f,b} = \frac{P \pm Z_c Q}{2}, \tag{5.5}$$

$$Q_{f,b} = \frac{Q \pm P/Z_c}{2}. \tag{5.6}$$

To compute Z_c from local, simultaneous P and Q signals, we apply the so-called PQ-method, while the PU-loop method is used instead to directly estimate local wave velocity c, from P and flow velocity, U (*i.e.*, Q/A, where A is the vessel cross-section area) signals [163, 113, 181, 100]. These methods are illustrated in Figure 5.9d-e, where Z_c and ρc (ρ is blood density) are determined as the slope of the corresponding linear tracts of the associated loop.

According to Figure 5.9, for a given 1D arterial vessel v of length L_v, $e = 1 \dots N_v$ are segments used to discretized it, each of length L_e. For each single segment e, panels a-c display local pressure, flow and velocity time signals. Thus, panels d and e illustrate the PQ- and PU-loops, respectively, whereas panels g-h report the separated forward (forw, green) and backward (back, red) components of pressure, flow and velocity waveforms for the e-th segment, with PP_f and PP_b being the pulse pressure of the forward and backward pressure signals, respectively. Panel f shows the frequency content of the input impedance Z_{in} in terms of its modulus $|.|$ and phase $\angle.$, resulting from Fourier decomposition of the pressure and flow signals associated with the e-th segment (R_{down} is the downstream resistance with respect to the considered site, and Z_c can be taken as Z_{in} at high frequencies, which are deemed to be reflection-less [100]).

Table 5.3 reports local wave speed c computed along the 1D arterial network, at the supine and standing postures. It is evident how wave speed is progressively increased while moving along the aortic-wise direction, at a given posture. A further increase in local wave speed is also detected at each site when passing from supine to upright standing posture, as a consequence of arterial vessels adaptation promoted to fight orthostatic stress [287, 193, 200]. Such posture-induced c increase is found as statistically significant (Wilcoxon test) at all considered sites apart from the iliac bifurcation (#41, p-value = 0.125), likely due to its limited number of segments. The largest percentage increase in local c is seen in leg arteries, with standing wave speed almost +45% higher than supine, whereas at carotids level we observe a

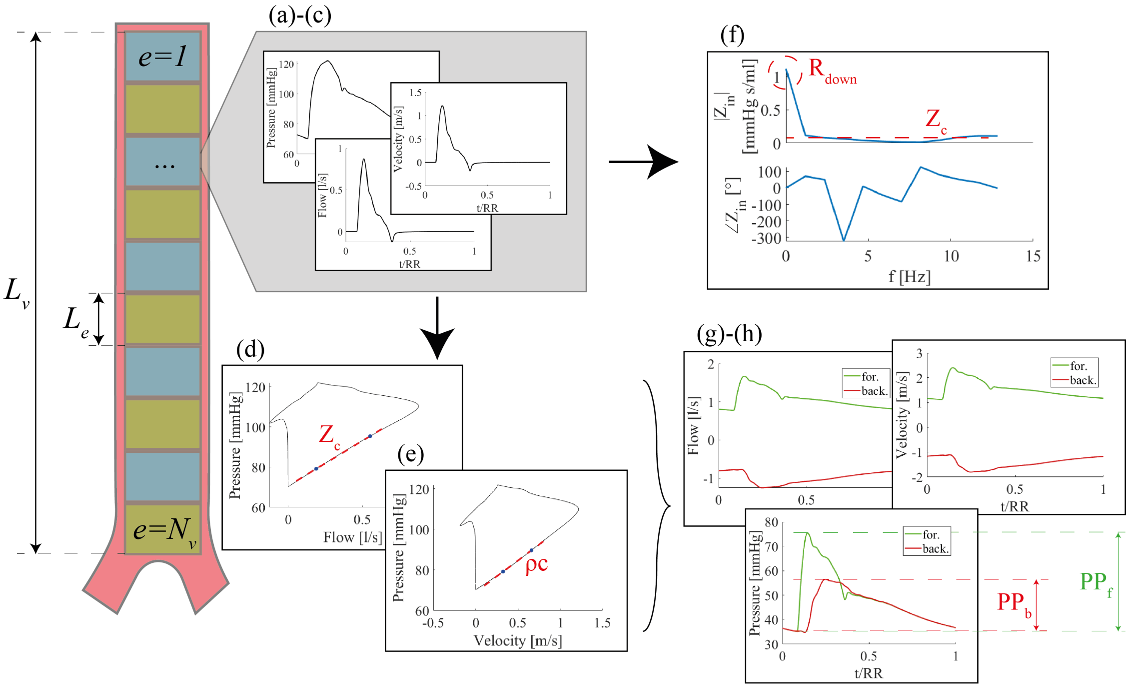

Figure 5.9: Wave analysis operational flow performed at the aortic root, vessel No. 1.

Table 5.3: Standing vs. supine wave velocity (c, mean ± std.dev) along the arterial tree. Table taken from [64].

Vessel	c [m/s]			
Aorta	supine	standing	Δ%	p-value
Ascending #63	3.89 ± 0.14	4.10 ± 0.14	+5.3%	0.031
Arch #14	4.24 ± 0.22	4.45 ± 0.22	+5.0%	0.008
Thoracic #18	4.32 ± 0.14	4.59 ± 0.11	+6.1%	0.002
Abdominal #39	4.85 ± 0.15	5.64 ± 0.15	+16.4%	0.002
Iliac bif. #41	5.06 ± 0.07	6.32 ± 0.09	+24.9%	0.125
Carotid				
External carotid #13	6.77 ± 0.15	6.55 ± 0.12	-3.2%	0.031
Legs				
Tibial #48	7.42 ± 0.11	10.78 ± 0.38	+45.2%	0.002

slight c decrease (-3%), likely caused by cerebral arteriolar vasodilation mediated by cerebral autoregulation.

Top diagrams in all panels of Figure 5.10 show the separated components of pressure and flow waves, along with their alteration following orthostatic stress.

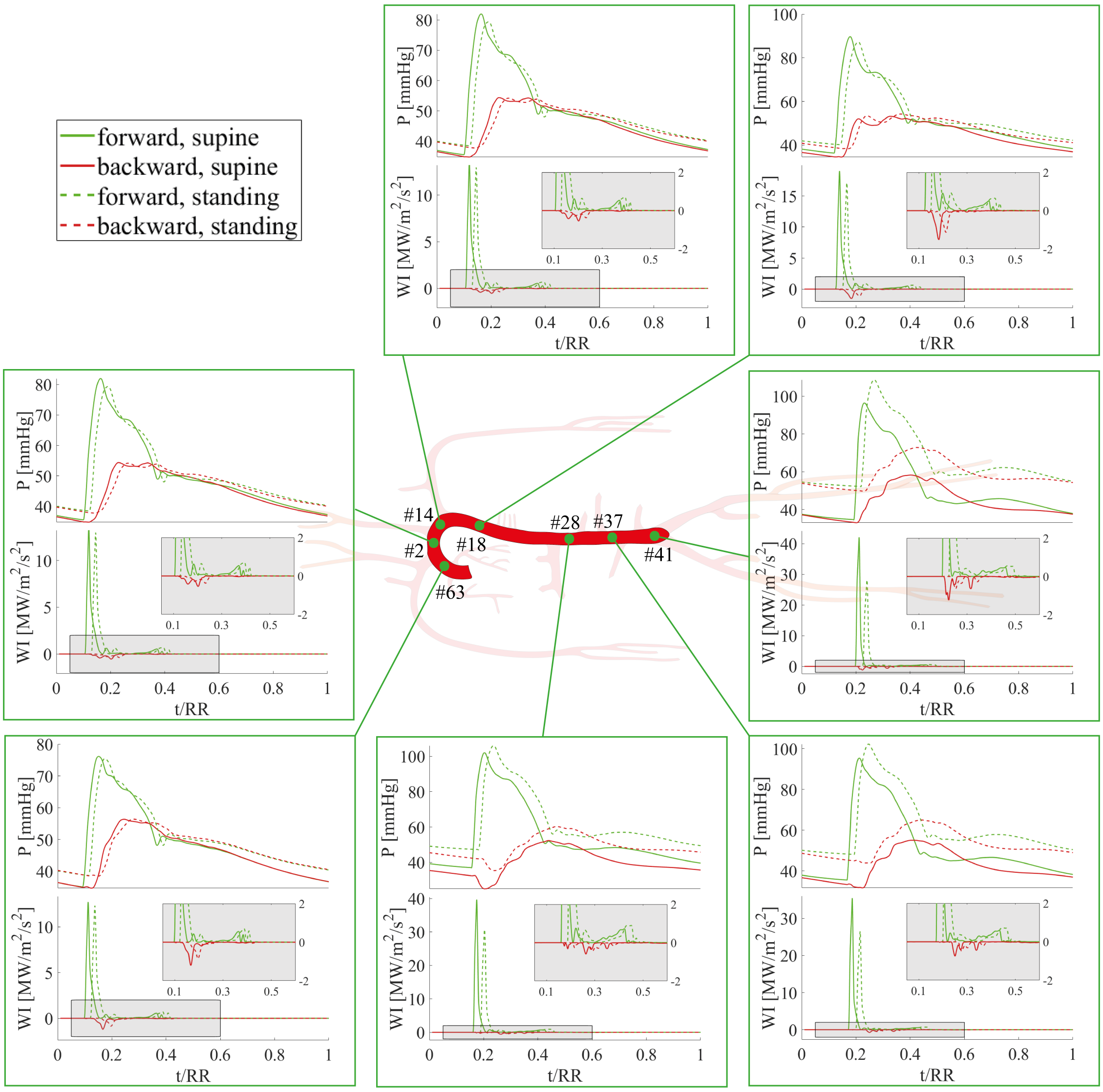

Figure 5.10: Forward (green) and backward (red) components of traveling pressure waves (top side of panels) and associated wave intensity (WI) profiles (bottom side of panels) at different sites along the aorta at supine (solid lines) and standing (dashed lines) posture. Image taken from [64].

Forward and backward pressure waves present the same behavior observed for the total (forward + backward) pressure signals after passive tilting to the standing posture (section 5.1, [68]), with both pressure components reduced in amplitude following global pulse pressure contraction, as well as the HR-driven signals phase shifting discussed previously in this section.

Wave reflection

Quantitative WA is conducted considering additional indices: the reflection magnitude RM and the reflection index RI (both evaluating the amount of wave reflection with respect to forward traveling waves amplitude at a given location) [278, 273], and the augmentation index AI (giving a measure of the influence of the reflected wave onto the forward traveling wave resulting in the total local pressure wave) [278, 163]. Such parameters are defined as:

$$RM = \frac{PP_b}{PP_f}\,, \quad RI = \frac{PP_b}{PP_f + PP_b}\,, \quad AI = \frac{AP}{PP}\,, \tag{5.7}$$

where PP_b and PP_f are backward and forward pulse pressures components, respectively, while PP is the pulse pressure of the total (forward + backward) pressure signal. AP is the augmentation pressure [278, 163], that is the difference between the systolic pressure and the pressure at the inflection point, taken as positive if the inflection point precedes systole and negative otherwise. RM and RI then are computed for each arterial vessel by using mean PP_f and PP_b values computed at all single vessel segments e (Figure 5.9), while AI is computed at a single point located in the middle of the ascending aorta (No. 1) and the interosseous (No. 24) artery.

Results for arterial local PP_f, PP_b and reflection magnitude RM for the supine and standing postures are presented in Table 5.4 (refer to [64] for RI results). Interestingly, while PP_f is decreased to almost the same extent throughout the entire arterial tree (apart from the tibial artery #48) tilting from supine to upright standing (about -8% ÷ -10% with respect to the supine values), PP_b shows a wider range of variation, with reductions similar to those observed for PP_f only in the thoracic-abdominal aortic tracts, whereas PP_b is seen to drop much deeper within the ascending aorta-aortic arch (-17%), carotid arteries (-31%), and terminal tibial arteries (-20%). As a result, RM shows significant reductions (-3% ÷ -8%) going from supine to upright standing posture for the central aortic (ascending aorta, arch of aorta and initial thoracic aorta) regions, in line with findings reported by other researchers [49, 25, 14] (Davis *et al.* [51] report that aortic RM dropped from 0.55 ± 0.05 to 0.48 ± 0.05 going from supine to standing). Moreover, RM eventually recovers up to almost negligible variations towards the thoracic-abdominal aortic tracts and the iliac bifurcation. RM shows marked fall also at carotid (-26%) and tibial (-27%) level, with the latter being caused also by the +8.7% increase in PP_f.

Table 5.5 shows the computed values for the augmentation index AI - often taken as a proxy of arterial stiffness [271] - before and after tilting from supine to upright standing, at central (aorta) and peripheral (finger) level. Both central and peripheral AIs drop when undergoing passive orthostatic stress, as also observed in other studies [51, 14, 13, 102, 101] (Davis *et al.* [51] registered aortic AI falling from 18% ± 11% to 1% ± 11% changing from supine to standing posture). Such AI decrease should also be considered in light of the conclusions by Wilkinson *et*

Table 5.4: Standing vs. supine forward pulse pressure (PP_f), backward pulse pressure (PP_b) and reflection magnitude (RM) computed along the arterial tree. Table taken from [64].

Vessel	PP_f [mmHg]			PP_b [mmHg]			RM		
Aorta	supine	standing	Δ%	supine	standing	Δ%	supine	standing	Δ%
#1	40	37	-9.9%	22	18	-17.3%	0.54	0.49	-8.2%
#63	41	37	-10.4%	22	18	-17.1%	0.53	0.49	-7.5%
#2	47	41	-11.9%	20	16	-16.1%	0.42	0.40	-4.9%
#18	53	47	-11.9%	19	16	-14.8%	0.35	0.34	-3.4%
#37	60	54	-9.6%	23	21	-9.3%	0.39	0.39	+0.3%
#41	62	57	-8.7%	25	23	-8.3%	0.41	0.41	+0.5%
Carotid									
#13	61	57	-6.3%	24	17	-31%	0.40	0.29	-26.4%
Legs									
#48	79	85	+8.7%	34	27	-20.9%	0.44	0.32	-27.2%

al. [284], who suggest that elevated heart rate provokes linear falling of AI regardless of the body posture.

Table 5.5: Standing vs. supine central (aortic) and peripheral (finger) augmentation index (AI). Table taken from [64].

Site	supine	standing	Δ%
Central AI (#1)	0.22	0.13	-40%
Peripheral AI (#24)	-0.40	-0.48	-21%

The increase in arterial wave speed together with the augmented total peripheral resistance (TPR) should be accompanied by a simultaneous increase of arterial wave reflections and, therefore, of the associated indices RM, RI, AI [14, 13, 51]. To explain the paradoxical results reported above and by the cited authors we inquire into the specific mechanisms involved in wave reflection generation, quantifying their role in giving rise to reflected waves by means of the pressure reflection coefficient, R_p [278, 163, 133, 151, 113]. In this analysis we account for reflections produced: (i) at arterial bifurcations, (ii) by arterial tapering, and (iii) by peripheral resistance, defined as

$$R_p = \begin{cases} \dfrac{Z_{c,d} - Z_{c,p}}{Z_{c,d} + Z_{c,p}} & \text{at bifurcations}\,, \\ \sum_{e=1}^{N_v} \dfrac{Z_{c,e+1} - Z_{c,e}}{Z_{c,e+1} + Z_{c,e}} & \text{due to tapering}\,, \\ \dfrac{R_{down} - Z_{c,out}}{R_{down} + Z_{c,out}} & \text{at 1D terminal branches}\,, \end{cases} \tag{5.8}$$

respectively, where subscripts d and p indicate daughters and parent vessels of a bifurcation, with $Z_{c,d}$ computed according to the specific daughter vessels combination (*e.g.*, vessels in parallel). $Z_{c,out}$ is the characteristic impedance of the corresponding 1D terminal artery outlet. Significance of R_p distributions over arterial vessels between postures is tested via Wilcoxon non-parametric test for paired samples.

Figures 5.11-5.12 show that R_p related to neither arterial bifurcations (both in the forward and backward directions) nor vessels tapering varies significantly changing posture from supine to standing. Therefore, such mechanisms do not cause the wave reflection reduction detected at central level. Given the abrupt TPR rise promoted upon upright tilting, wave reflection at peripheral sites shows the largest variation in terms of R_p with respect to the supine levels. Bottom diagram of Figure 5.12 highlights that R_p at peripheral sites grows markedly at almost all arterial terminal branches, apart from external/internal carotids and vertebral arteries (No. 6, 12, 13, 16, 17, 20) reaching cerebral vasculature. These vessels report a decrease in R_p going from supine to upright, and interestingly they are the only ones showing an increase in parent-to-daughter vessels cross-section area (see [64]) and a decrease in local wave speed c (Table 5.3). The reason for such peculiar behavior is likely determined by cerebral autoregulation, acting such that cerebral vessels tend to vasodilate in response to downward blood migration elicited by upright posture assumption, in order to preserve stable levels of cerebral perfusion. Indeed, RM tends to decrease (Table 5.4, -26% at right external carotid artery) as PP_b is strongly reduced at terminal carotid arteries (-31% at right external carotid). This strong decrease of wave reflection occurs at each of the six cerebral arteries terminal branches, giving rise to weakened backward waves propagating back to the arch of aorta, explaining the reduced reflection indices found at central level.

Wave intensity patterns

Wave intensity (WI) is defined as the power per unit vessel area carried by successive ‘wavefronts’ (infinitesimal waves) dP, dU and dQ which cumulatively return the original waves P, U and Q, respectively, that is

$$WI = dP\,dU\,. \tag{5.9}$$

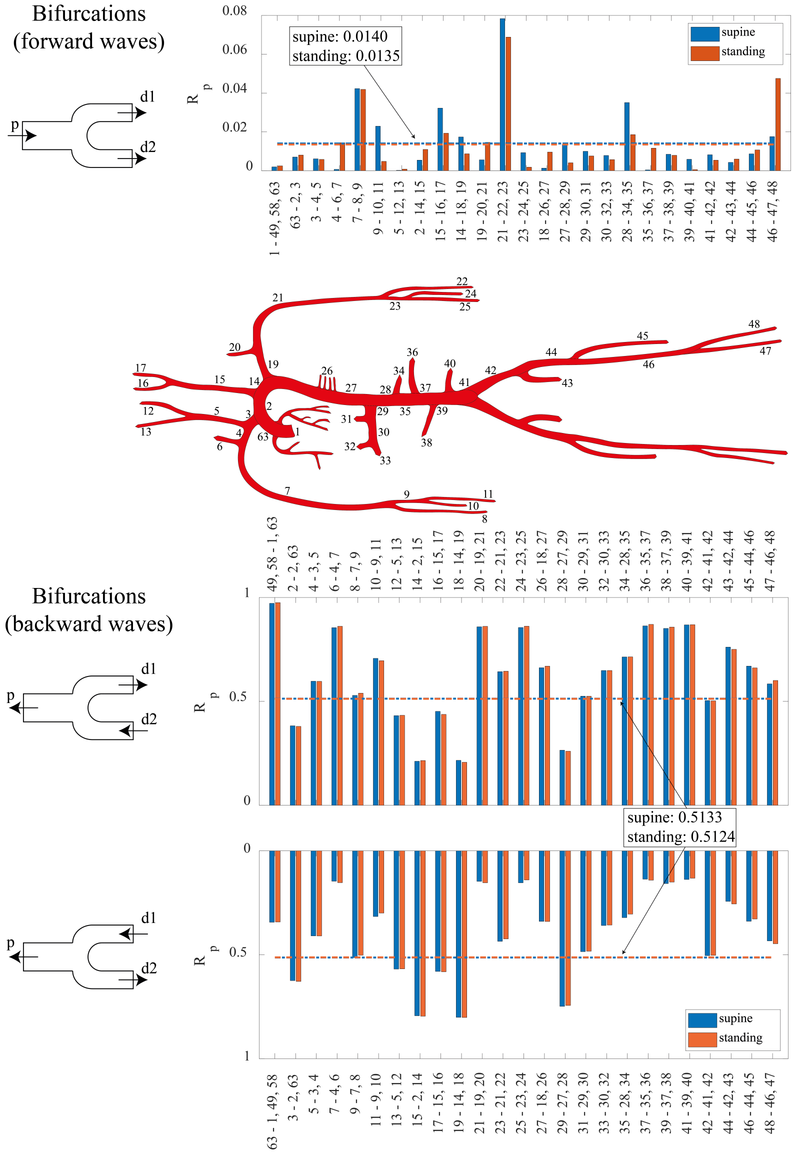

Figure 5.11: Pressure reflection coefficient R_p at supine (blue bars) and standing (orange bars) postures computed at arterial bifurcations. Image taken from [64].

Usually, a different version of equation (5.9) is used to avoid the sampling frequency dependence of dP and dU, by taking time derivatives [163]:

$$WI = \frac{dP}{dt}\frac{dU}{dt}\,. \tag{5.10}$$

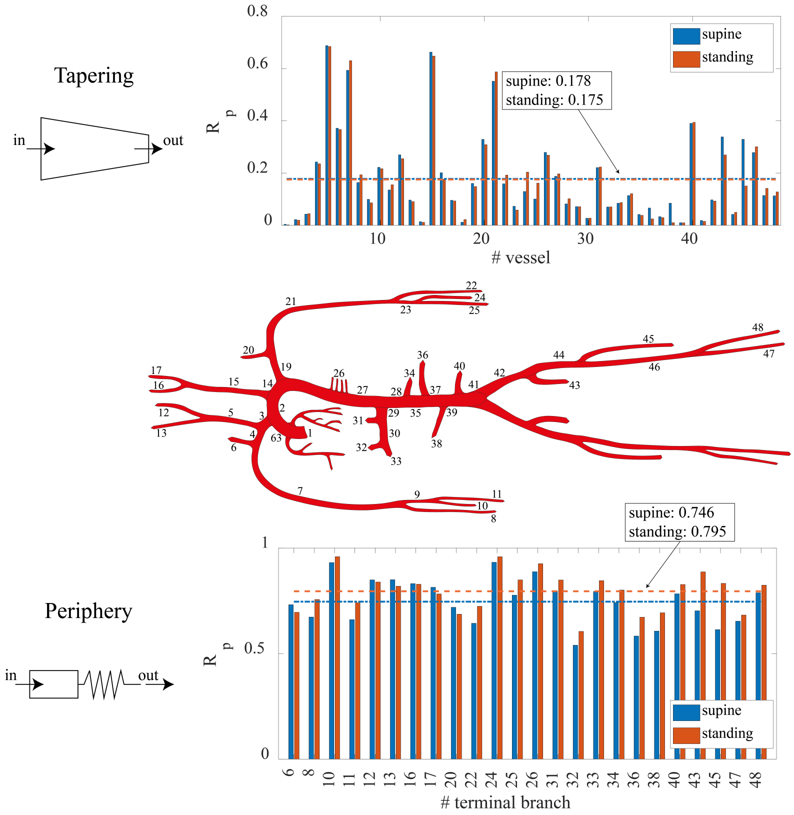

Figure 5.12: Pressure reflection coefficient R_p at supine (blue bars) and standing (orange bars) postures associated with arterial vessels tapering (top diagram) and peripheral resistance (bottom diagrams). Image taken from [64].

Similarly to wave separation seen above, also WI can then be separated into its forward (WI_f) and backward (WI_b) components, as

$$WI_{f,b} = \frac{dP_{f,b}}{dt}\frac{dU_{f,b}}{dt}\,. \tag{5.11}$$

Then, by applying equations (5.5)-(5.6) (with $U = Q/A$) to (5.11), the following expressions for forward (WI_f) and backward (WI_b) wave intensity are obtained:

$$WI_{f,b} = \pm\frac{1}{4\rho c}\left(\frac{dP}{dt} \pm \rho c\frac{dU}{dt}\right)^2 , \tag{5.12}$$

taking the sign '+' for WI_f, whereas '−' for WI_b.

Figure 5.13 shows an example of WI computation performed at the entrance of the aorta (No. 1, first segment) at supine posture. The different peaks of forward and backward WI profiles correspond to increase or decrease of related P_f and P_b

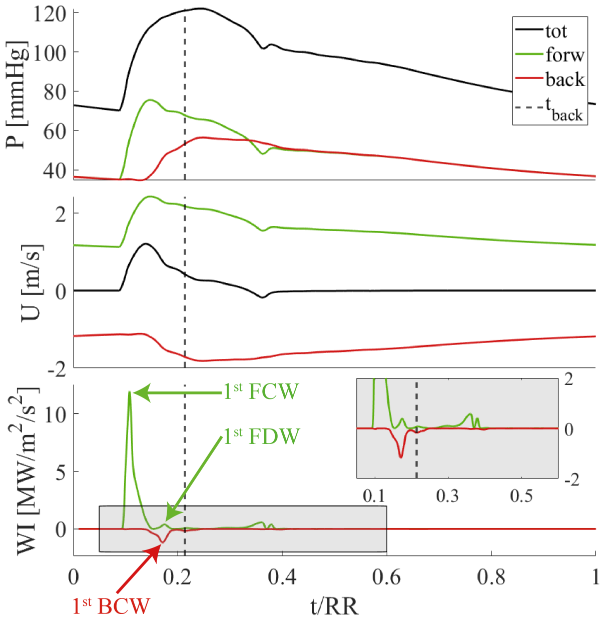

Figure 5.13: Example of WI computation at the entrance of the aorta ($e = 1$) obtained from forward and backward pressure/flow velocity signals. Image taken from [64].

signals. WI_f peaks are typically named as forward compression wave (FCW) if corresponding to P_f signal local increase (such as for the first, strong forward WI peak, corresponding to the FCW originated from left ventricle contraction). Differently, a WI_b peak is named as a forward decompression/expansion wave (FDW) if it corresponds to a P_f signal local local decrease (such as for the late-systolic expansion wave originated by the aortic valve closure, at the dicrotic notch). The same nomenclature is used for WI_b peaks, with the first, evident backward WI peak represented in 5.13 being a backward compression wave (BCW) originated by the downstream reflection of the first FCW introduced previously.

WI profiles at multiple sites along the arterial tree are shown in Figure 5.10. Following the aortic-wise direction, from the aortic arch (No. 2) up to the iliac bifurcation (No. 41), the first forward compression wave (FCW) moves forward in time regardless of the body position, thus reaching the selected site after longer time. Additionally, the first FCW amplitude appears as progressively increased from upper to lower aorta - at fixed posture - due to anatomical vessels narrowing. On the other hand, passing from supine to standing posture, the first FCW wave appears as noticeably reduced at a given aortic site, potentially because of the increased local cross-section area caused by blood shift and the hydrostatic pressure contribution below heart level. Despite forward WI profiles look qualitatively similar among the considered sites and postures, WI_b profiles change profoundly from one site to another due to the effect of various backward traveling waves reaching the considered site from near downstream sites.

5.2.2 Wave trapping and moving horizon

Because of the scarce propagation of backward waves at bifurcations (Figure 5.11), it is commonly believed that reflected waves originated at each reflection site cannot travel back up the entire arterial tree reaching the aortic root, due to re-reflections determining a condition of backward wave trapping [49, 276, 272]. In light of this, Davies *et al.* [49] claim the existence of a 'horizon effect' in the human aorta, explaining why backward reflected waves seem not to come from a unique point of reflection located at the iliac bifurcation, as it was widely believed. Instead, according to the authors [49], reflected waves are produced from multiple reflection sites distributed along the whole aortic length. Due of backward wave trapping, only backward waves reflected from downstream points which are close enough are detectable at a given upstream site, as depicted in Figure 5.14 and further evidenced by backward WI profiles shown in Figure 5.10. In these plots, taken at successive points along the aorta, it can be seen how the first BCWs (red peaks) seem to move downstream as we proceed along the aorta, shifting forward the corresponding reflection site and behaving thus like a moving horizon beyond which reflected waves are no longer visible (Figure 5.14 shows the moving horizon shifting downstream).

Therefore, following the work of Davies *et al.* [49], we aim to estimate the elapsed time between the first FCW and subsequent backward waves return (time of reflection, ToR) at different sites along the arterial tree. Considering the average speed of waves downstream the selected site (*i.e.*, $\bar{c}_{down}$), the corresponding point of the aorta at which reflection takes place (point of reflection, PoR) is obtained, as illustrated in Figure 5.14. Then, ToR is computed as the difference between the average arrival time of backward waves (t_{back}) and the arrival time of the first FCW, where t_{back} is defined as

$$t_{back} = \frac{\int_{RR} t\, WI_b\, dt}{\int_{RR} WI_b\, dt}. \tag{5.13}$$

PoR is then computed as

$$PoR = \frac{ToR \cdot \bar{c}_{down}}{2}\,, \tag{5.14}$$

where $\bar{c}_{down}$ is computed as the average wave speed over the aortic sites downstream the current one, up to the iliac bifurcation.

Figure 5.15 reports - at different sites and postures - the arrival time of the first FCW (circles and solid interpolating lines) and the average arrival time of backward waves (equation (5.13), asterisks and dashed interpolating lines). The

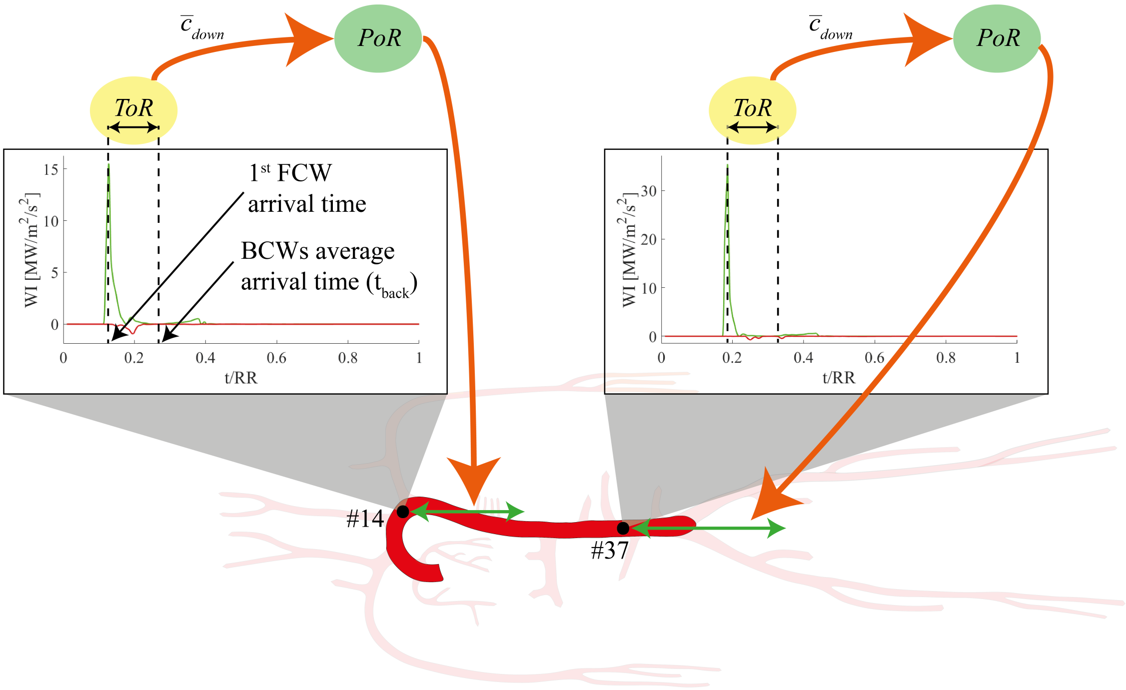

Figure 5.14: Time of reflection (ToR) and point of reflection (PoR) computation at two different sites along the aorta. Image taken from [64].

elapsed time of reflection ToR and the distal point of reflection PoR are then reported in Table 5.6. For the supine position, results appear to be very good agreement with Davies *et al.* [49]. Furthermore, tilting to standing position does not alter the ToR to a significant extent, while standing PoR are shifted more downstream with respect to the corresponding supine values (specifically, by about +5% at the aortic root, and up to about +27% at the iliac bifurcation). This effect is connected to the different site-specific increase of $\bar{c}_{down}$, which rises by about +12% at the aortic root, and by almost +25% at the iliac bifurcation due to upright tilting. The present results prove thus how backward wave trapping is preserved after posture changes, guaranteeing the supine favorable functioning of the human arterial circulation, while protecting the heart and the aortic valve against reflected waves.

Concluding remarks

In summary, our study suggests that passive upright tilt causes an overall increase of mean arterial pressure, heart rate and peripheral resistance, together with a decrease of stroke volume, cardiac output and central venous pressure. Pressure and flow rate waveform analysis along the arterial tree, in combination with with

Table 5.6: Standing vs. supine $\bar{c}_{down}$ and PoR along the aorta tree. Table taken from [64].

Vessel	$\bar{c}_{down}$ [m/s]			PoR [m]		
Aorta	supine	standing	Δ%	supine	standing	Δ%
No. 1	4.53	5.09	+12.4%	0.213	0.224	+5.2%
No. 63	4.55	5.18	+13.9%	0.189	0.200	+5.8%
No. 2	4.61	5.29	+14.9%	0.208	0.222	+6.9%
No. 14	4.64	5.41	+16.8%	0.200	0.217	+8.2%
No. 18	4.69	5.54	+18.2%	0.150	0.166	+10.9%
No. 27	4.77	5.69	+19.4%	0.208	0.246	+17.9%
No. 28	4.86	5.79	+19.1%	0.305	0.332	+8.6%
No. 35	4.94	5.89	+19.1%	0.311	0.339	+8.7%
No. 37	4.97	6.00	+20.8%	0.303	0.341	+12.7%
No. 39	5.03	6.18	+22.9%	0.245	0.287	+16.9%
No. 41	5.06	6.32	+24.9%	0.186	0.236	+27.2%

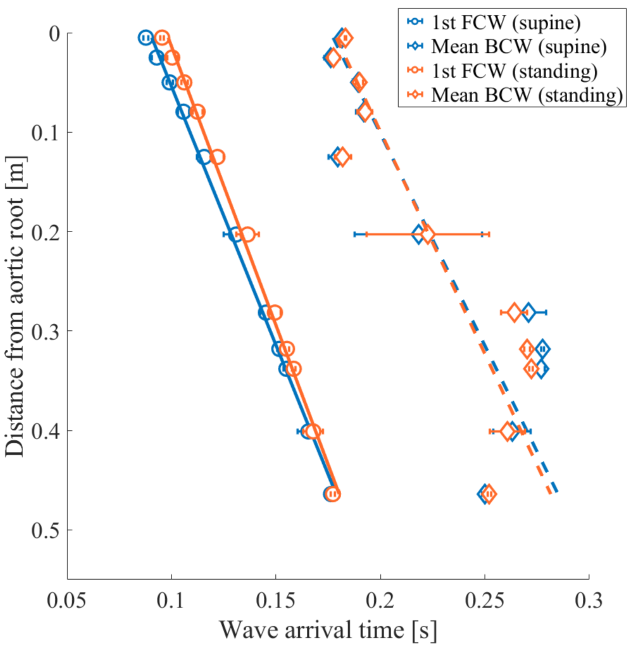

Figure 5.15: First FCW arrival times (circles and solid interpolating lines) and average BCW arrival times (asterisks and dashed interpolating lines) at supine (blue) and standing (orange) position along the arterial tree. Image taken from [64].

mechano-energetic (stroke work) and oxygen consumption (time-tension index) parameters, evidences how the CVS reaches a less stressed condition at passive upright posture than supine, with a slight impairment of the energy supply-demand ratio.

Furthermore, the tilt-up vs. down transient dynamic response is not symmetric, plus being non-linearly affected by the tilting rate and showing stronger under- and parameter overshoots as the duration of tilt is reduced. Besides, our numerical framework evidences also how coronary perfusion results as improved during passive orthostatic stress. Moreover, our work shows the CVS excellent conservation of wave dynamics even upon orthostatic stress. In spite of all remarkable hemodynamic alterations following head-up tilting, the standing posture does not lead to larger production of wave reflections, since all computed pressure reflection coefficients do not increase in a relevant way. In addition, all indices of wave reflection reveal a reduced reflected waves amplitude at central level, likely because of the diminished reflected waves amplitude coming from cerebral district, due to cerebral autoregulation-driven vasodilation. However, these indices show almost null variation with respect to supine values proceeding towards the lower thoracic and abdominal aorta. Thus, the supine favorable functioning of the human arterial circulation is guaranteed with posture changing to standing, as wave trapping is maintained as a protection for the heart and the aortic valve against reflected waves along with the preservation of the near-optimum area matching at bifurcations for the efficient transmission of forward waves.

Chapter 6

Modeling the cardiovascular and cerebral response to parabolic flight

(the contents of the present chapter have been previously published in [66, 224])

In recent years, a considerable number of parabolic flight experiments have been conducted with the purpose of collecting information about human physiology coping to reduced gravity, particularly considering the role of the human CVS. Yet, only simple and non-invasive *in vivo* measurements (such as HR, finger or brachial MAP) have been acquired in general. Most authors focus on the main hemodynamic parameters response to different single phases of flight [159, 20, 190, 33, 18, 137], although some report also continuous monitoring of the investigated parameters [140, 201, 173] throughout the whole experiment. In [159], the authors present a detailed analysis of the role of posture in shaping the hemodynamic response to parabolic flight. In other works, different aspects are explored instead, such as post-flight induced orthostatic intolerance [229], the impact of the Valsalva maneuver [228] or the particular response to different reduced-gravity environments (*e.g.*, Moon, Mars) [282, 17]. Only few studies [234, 173] report non-invasive estimation of central aortic pressure, derived through transfer function reconstruction. However, understanding of central hemodynamics is crucial also in order to adequately grasp and predict the CVS response to actual weightlessness.

Additionally, beside global hemodynamic changes introduced above, proper understanding of the cerebral circulation response to 0g (induced by parabolic flight) has also received little attention, to date [57]. However, a large number of reported neurological symptoms revealed after exposure to microgravity could be linked to cerebral hemodynamics alterations. It is also widely believed that cerebral hemodynamics changes are among the main causes for spaceflight associated neuro-ocular syndrome (SANS, see chapter 2, section 2.2.1) [129, 130, 294]. The emerging picture is that microgravity-induced alterations of hemodynamics at the brain level are multifaceted and definitive data are currently missing. This gap is partially due to the limited number of available data, to the high individual variability, as well as to the different duration and functioning of ground analogs [57]. Plus, direct and local clinical measures are intrinsically hard to obtain, as the currently adopted techniques usually fail to capture the cerebral microvascular hemodynamics. Moreover, since the most of existing measures are beat-averaged, it is not possible to assess how hemodynamic pulsatility of crebrovascular signals and intra-beat variability change in 0g with respect to 1g, and whether these may exert negative or harmful consequences onto the cerebrovascular health.

In this perspective, numerical modeling has showed promising results to investigate the human CVS functioning and response to various conditions [68, 10, 280, 76]. Yet, the only attempts to numerically reproduce parabolic flight are presented by Gerber *et al.* [80], who designed numerical simulations of the characteristic g variation occurring during a standard parabolic flight profile (chapter 2, section 2.2.2) by adopting a lumped parameterization of the human circulation, though assuming fictitious time transitions to achieve model stability. Thus, to fully exploit the potentialities of the computational approach, in the present study we adopt a previous version of the multiscale 1D-0D mathematical model of the CVS presented in chapter 3 to simulate the posture-depending hemodynamic response and the cerebrovascular hemodynamics coping to gravity changes elicited by simulated parabolic flight. Specifically, in this chapter we report results published in [66, 224] about (i) the study of the dynamic response of some crucial parameters - such as central MAP - not generally observed during parabolic flights due to their difficult invasive measurement; (ii) the assessment of the transient cardiac mechano-energetic response and related cardiac performance; (iii) the discussion on the role of microgravity-induced elevated ICP as plausible mechanism inducing long-term spaceflight visual impairment (and SANS); and (iv) the analysis of cerebral hemodynamics during parabolic flight-induced microgravity at supine posture, particularly focused on the impact of hemodynamic signals pulsatility on the overall cerebrovascular health.

6.1 Numerical simulation of parabolic flight

6.1.1 CVS model

The multiscale CVS model adopted to the aim of this study is described in our previous works [66, 224]. The model encompasses the same 1D arterial tree as introduced in chapter 3 - including the hyperbolic partial collapse model by Drzewiecki *et* *al.* [56] adopted to deal with very low hypergravity-induced carotid and vertebral arterial pressure - linked to 0D analogs of the systemic peripheral microcirculation (arteriolar, capillary and venular) and the venous return (veins and venae cavae). The 0D model counterpart is organized into five separate body regions, from head to legs, as presented in chapter 3, although no ocular and cerebrovascular models are present in the head circulation (as already done in chapter 5). ITP dependency onto current body posture (tilt angle α) and gravity acceleration g is modeled through equation (3.35) introduced in chapter 3, with ITP behavior during parabolic flight at different posture shown in Figure 6.2.

In the global 1D-0D CVS model, 0D head veins are subject to the action of extravascular ICP, that is cerebrospinal fluid pressure (see chapter 2, section 2.1.1), which is modulated with posture in the present version of the model as detailed in the following. At supine posture, baseline ICP is taken as large as 10 mmHg. Then, the relation governing ICP with body posture is obtained by taking the difference between Davson equation for tilted and supine posture, as proposed by [98]:

$$ICP_{tilt} = ICP_{sup} + CVP_{tilt} - CVP_{sup} - \Delta p^{h}_{H\text{-}ra}\,, \tag{6.1}$$

where $\Delta p^{h}_{H\text{-}ra}$ is the head-right atrium hydrostatic pressure difference, determined according to Stevino's law as $\Delta p^{h}_{H\text{-}ra} = \rho g \Delta h_{H\text{-}ra} \sin\alpha$, with $\Delta h_{H\text{-}ra}$ the vertical anatomical distance between the head and the right atrium, while α is the tilt angle. Furthermore, to account for jugular vein collapsibility, only the gravity gradient associated with the fluid column extending from the head to the jugular vein point of collapse at zero transmural pressure - that is $\Delta h_{H\text{-}jv}$ - is considered (here represented simply by Δh_H, assuming the jugular vein as corresponding to the superior vena cava compartment). The relation implemented for tilt angles $\alpha \geq \alpha_{collapse}$ thus reads

$$ICP_{tilt} = ICP_{sup} - CVP_{sup} - \Delta p^{h}_{H\text{-}jv}\,, \tag{6.2}$$

where $\alpha_{collapse}$ is the angle for which superior vena cava pressure $p_{svc} \leq 0$. Intracranial pressure has been introduced only for cerebral veins.

6.1.2 Cerebrovascular model

The cerebrovascular 0D model used to characterize the impact of parabolic flight onto cerebral hemodynamics at supine posture is taken from [259] (and described in detail in chapter 3, section 3.5). The cerebrovascular model consists of an open-loop, standalone lumped parameterization of the main cerebral large arteries of the circle of Willis, distal cerebral pial circulation and cerebral capillary-venous circulation. The model is schematically illustrated in Figure 6.1. The open-loop cerebrovascular model is used in combination with two time-series inputs: central (aortic) pressure (P_a) directly taken from the 1D-0D global cardiovascular model, and dural sinus pressure (P_{vs}), which can be approximated as equal to CVP at supine posture, when jugular veins are completely distended [128, 259] (CVP in turn is taken from the 1D-0D global model).

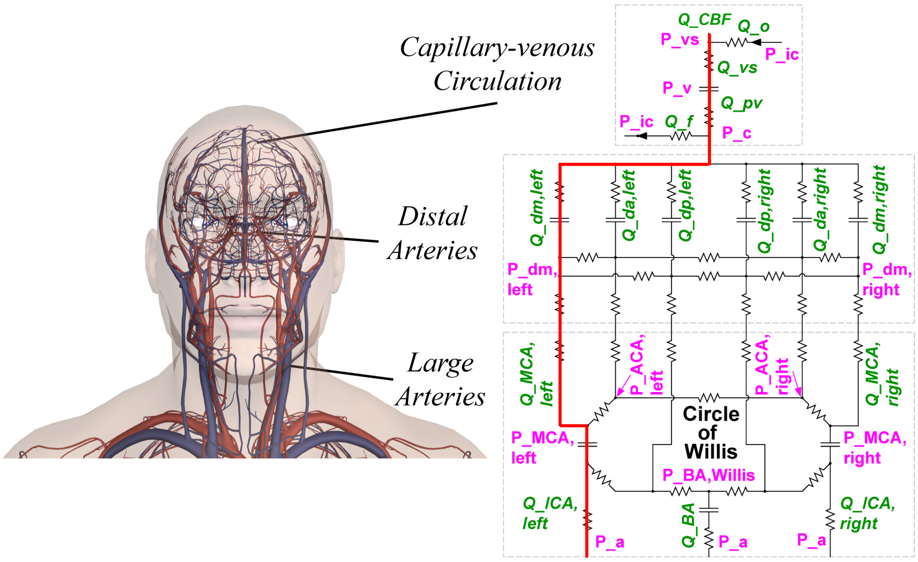

Figure 6.1: Schematic architecture of the 0D cerebrovascular model adopted in this study in combination with the 1D-0D global CVS model. Image taken from [224].

6.1.3 Parabolic flight profile

A standard parabolic flight profile is designed on the basis of data reported by various parabolic flight experimental campaigns [140, 20, 190, 159, 201, 33, 137, 173, 234, 18, 282, 17, 229, 228]. The duration of each phase of flight (hyper- and microgravity) is typically of about 20 s, with fast transitions of a few seconds between each phase. The implemented g/g_0 time profile is illustrated in Figure 6.2, together with the corresponding sketch of the parabolic flight trajectory and ITP profile at each simulated posture. Specifically, gravity transitions between flight phases are modeled as cosinusoidal functions of time:

$$\frac{g}{g_0} = \left(\frac{g}{g_0}\right)_i \pm \frac{1}{2}\left[\left(\frac{g}{g_0}\right)_f - \left(\frac{g}{g_0}\right)_i\right] \cdot \left[1 \mp \cos\left(\frac{t - t_i}{\Delta t_{i-f}}\pi\right)\right], \tag{6.3}$$

taking the upper signs for increasing g/g_0 (g_0=9.81 m/s^2), whereas the lower signs for descending g/g_0. Subscripts i and f refer to the initial and final gravity acceleration magnitude of the corresponding transition, respectively, with t_i and Δt_{if}

being the transition starting time and the transition phase duration, respectively. Al gravity transitions are simulated at a fixed time rate of ±0.36 g/s, with lengths of all gravity transition phases Δt_{i-f} (*i.e.*, $\Delta t_{1g-1.8g}$, $\Delta t_{1.8g-0g}$ and *vice versa*) reported in Table 6.1, together with time duration of each flight phase ($T^{I}_{1.8g}$ and $T^{II}_{1.8g}$ for the first and second hypergravity phases, and T_{0g} for the microgravity phase, respectively).

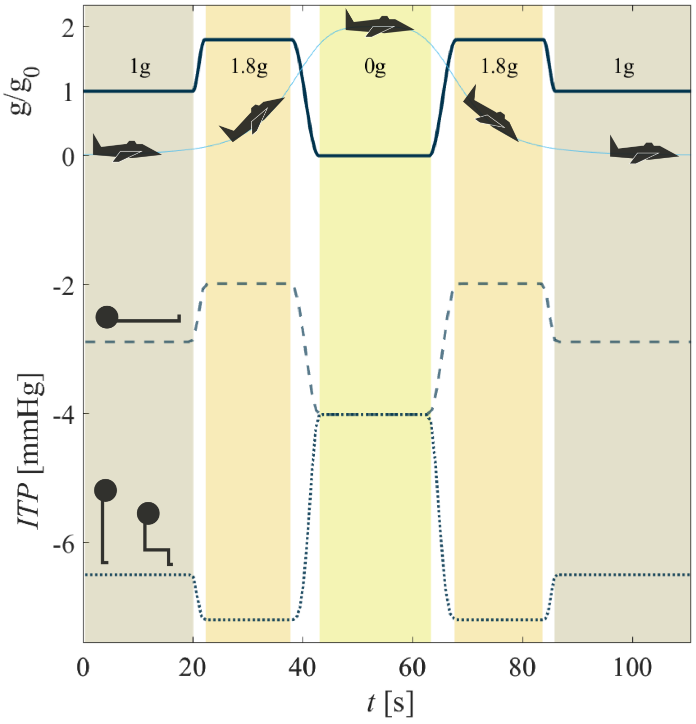

Figure 6.2: Simulated parabolic flight g/g_0 profile (on top) and related ITP response at different postures (supine: dashed line; seated and standing: dotted line). Image taken from [66].

Table 6.1: Parabolic flight profile parameters. Table taken from [66].

Param.	$\Delta t_{1g-1.8g}$	$T^{I}_{1.8g}$	$\Delta t_{1.8g-0g}$	T_{0g}	$\Delta t_{0g-1.8g}$	$T^{II}_{1.8g}$	$\Delta t_{1.8g-1g}$
Value [s]	2.2	15.8	5.0	20.0	5.0	15.8	2.2

6.2 Overall cardiovascular response to simulated parabolic flight

6.2.1 Global hemodynamics and effect of posture

The model outcomes for global hemodynamics parameters over each parabolic flight phase at various postures (supine, seated, and standing) are listed in Table 6.2 together with literature reference data reported for validation [140, 20, 190, 159, 201, 33, 137, 173, 234, 18, 282, 17, 229, 228]. All single-phase time average values are evaluated over the last 10 s of each flight phase. Table 6.2 therefore shows that the global hemodynamic response to parabolic flight at different postures is reproduced accurately by the CVS model.

In our model the gravity term is introduced along the body longitudinal axis only (*i.e.*, along the head-feet direction). However, gravity contributes to shape the model response even at supine posture through ITP dependency on g (equation (3.35) in chapter 3), triggering modest but still visible hemodynamic changes in the same direction as those observed in the literature [20, 159, 190, 201, 18, 140, 169]. Because of ITP variation indeed, simulated supine 1g differs slightly from supine 0g during parabolic flight (as well as from seated and standing 0g), as ITP approaches a similar value upon microgravity at all postures - lower than 1g in supine posture - thus leading to improved venous return and enhanced ventricular filling, accompanied by HR reduction. Thus, compared with initial and final 1g phases, the 20 s microgravity phase shows an overall hemodynamic relaxation at all postures.

In addition, Table 6.2 highlights how the first and second hypergravity phases elicit CVS responses to a different extent. The MAP drop evidenced at the second 1.8g phase is much larger than during the first one, with standing posture being even more influenced than seated. Also SV and CO decrease more during the second 1.8g, with corresponding HR reaching higher levels to compensate such blood pressure falls. The possible reasons for such different response to 1.8 phases could be the different TPR increment mediated by arterial baroreflex and cardiopulmonary reflex, with the weaker TPR response following the second 1.8g phase likely due to the 20 s microgravity phase preceding the 0g-1.8g transition. In fact, during 0g, TPR approaches an overall vasodilated state, therefore the fast transition from 0g to 1.8g elicits a strong TPR increment, although the resulting resistance reached after pull-out (0g-1.8g) is lower than that observed after the initial pull-up (1g-1.8g) phase, due to the different pre-transition state.

Through the model, it is possible to predict the transient behavior of several hemodynamic variables over the parabolic flight maneuver. In our published work [66] readers will find further detail and additional information regarding global hemodynamics parameters response to simulated parabolic flight at different postures (*e.g.*, HR, SV, CO, TPR, thoracic blood volume). In the following, we

Table 6.2: Model outcomes and literature measured data (in squared brackets) of global hemodynamics parameters at different posture and flight phase. Symbols identify trends for the corresponding parameters with respect to 1g conditions (≊: not clear trend, ↑: parameter increase, ↓: parameter decrease). Table taken from [66].

Posture	**Parameter**	**1g**	**1.8g**	**0g**	**1.8g**	**1g**
Supine	MAP [mmHg]	87 [73÷101]	85 [68÷98] ≊	89 [78÷96] ≊	84 [68÷95] ≊	87 [75÷95]
	HR [bpm]	70 [60÷89]	74 [60÷88] ≊	66 [61÷91] ≊	73 [61÷84] ≊	70 [60÷88]
	SV [ml]	76 (123%) [132%÷134%]	71 (115%) [126%÷142%] ≊	82 (133%) [125%÷151%] ≊↑	72 (116%) [124%÷138%] ≊	76 (123%) [130%÷136%]
	CO [l/min]	5.3 (109%) [106%÷108%]	5.2 (107%) [97%÷121%] ≊	5.4 (111%) [98%÷122%] ≊↑	5.2 (108%) [91%÷115%] ≊	5.3 (109%) [103%÷109%]
	TPR [mmHg·min/l]	16.1 (82%) [80%÷82%]	15.9 (81%) [70%÷90%] ≊	16.4 (83%) [71%÷89%] ≊	15.9 (80%) [77%÷87%] ≊	16.2 (82%) [77%÷87%]
Seated	MAP [mmHg]	97 [85÷105]	96 [90÷110] ≊↓	88 [70÷101] ↓	84 [80÷105] ≊↓	97 [80÷110]
	HR [bpm]	74 [63÷86]	99 [74÷113] ↑	68 [62÷90] ↓	108 [74÷109] ↑	75 [67÷93]
	SV [ml]	68 (110%) [50÷111]	48 (78%) [40÷90] ↓	87 (142%) [70÷125] ↑	41 (67%) [50÷100] ↓	68 (110%) [50÷100]
	CO [l/min]	5.0 (104%) [4.0÷8.5]	4.8 (98%) [4.0÷8.9] ↓	5.9 (122%) [5.0÷9.9] ↑	4.5 (92%) [4.5÷8.9] ↓	5.0 (104%) [4.0÷8.0]
	TPR [mmHg·min/l]	19.4 (98%) [11.8÷22.2]	20.1 (102%) [12.5÷25.0] ≊↑	14.8 (75%) [9.1÷16.7] ↓	18.8 (95%) [10.0÷22.2] ≊	19.4 (98%) [11.8÷22.2]
Standing	MAP [mmHg]	95 [90÷102]	89 [95÷105] ≊↑	87 [75÷97] ↓	70 [90÷94] ≊↓	95 [88÷98]
	HR [bpm]	79 [69÷104]	105 [82÷117] ↑	69 [60÷90] ↓	110 [80÷119] ↑	80 [73÷102]
	SV [ml]	62 (100%) [39÷77]	43 (69%) [28÷70] ↓	88 (142%) [41÷117] ↑	35 (57%) [85%÷109%] ↓	61 (99%) [97%÷105%]
	CO [l/min]	4.9 (100%) [4.3÷5.7]	4.5 (92%) [83%÷99%] ↓	6.0 (124%) [7.9÷15.1] ↑	3.9 (80%) [92%÷124%] ↓	4.9 (100%) [99%÷103%]
	TPR [mmHg·min/l]	19.8 (100%) [100%]	20.0 (101%) [102%÷130%] ≊↑	14.6 (74%) [63%÷83%] ↓	17.9 (91%) [79%÷107%] ≊	19.8 (100%) [94%÷98%]

report only the transient response of central aortic root MAP (*i.e.*, $cMAP$), in Figure 6.3, due to its key-role in shaping and explaining the overall CVS functioning upon parabolic flight at various postures. Figure 6.3 underlines that the response of $cMAP$ is triggered proportionally to the body posture, with stronger response revealed at standing posture than at seated and, lastly, at supine posture. Standing posture entails also the strongest $cMAP$ variations compared to 1g pre-flight, reaching values as low as 70 mmHg (first 1.8g peak) and 45 mmHg (second 1.8g peak), primarily caused by sudden blood pooling in the lower extremities. Indeed, during hypergravity, HR is raised up to 100÷110 bpm at seated and standing

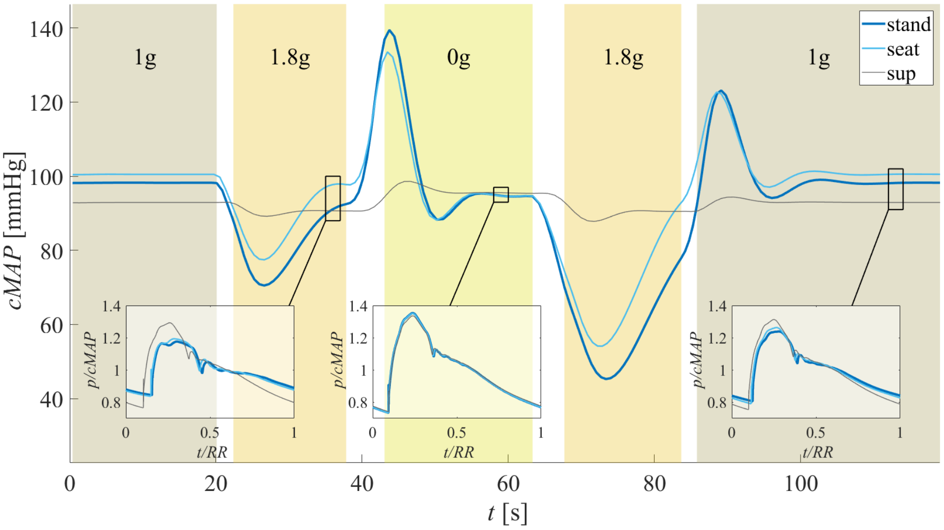

Figure 6.3: Central aortic MAP response to parabolic flight at different postures. Normalized aortic root pressure waveform ($p/cMAP$) at each reported in the insets at 1.8g, 0g and final 1g phases. Image taken from [66].

postures, together with concomitant vasoconstriction of peripheral vessels (TPR augmented by +10%÷+20% with respect to 1g) (Table 6.2) to promptly counteract the observed $cMAP$ drop. Consequently, at 1.8g also CO initially drops by -22%÷-47% at seated and standing postures, with respect to 1g, to recover then up to values slightly below 1g pre-flight conditions. At supine posture, the model behaves in a similar way but to a much lower extent compared to seated and standing, owing to the compression of the thoracic cavity with resulting higher ITP, determining a slightly reduced venous return to the heart and as such weakly affecting all hemodynamic variables (Table 6.2). During the 20 s of microgravity, instead, given the marked blood volume transfer to central regions, $cMAP$ is raised to almost 130÷140 mmHg (Figure 6.3) together with SV and CO. Then, following the overall CVS relaxation including HR reduction and peripheral vasodilation, near pre-flight hemodynamic values are approached (Table 6.2).

In Figure 6.3, by analyzing the shape of the aortic pressure waveform revealed at various postures and flight phases, it is possible to identify a number of aspects: (i) aortic pulse pressure, already shortened at 1g standing and seated postures compared to supine, undergoes further contraction with increasing gravity from 1g (right inset of Figure 6.3) to 1.8g (left inset) especially at seated and standing postures; (ii) entering microgravity (central inset) restores almost the same pressure waveform as in 1g supine, and no evident difference is found among postures in this phase; (iii) by focusing on the pressure waveform diastolic minimum, systolic maximum and dicrotic notch, it emerges that parabolic flight induces a marked signal phase shifting, especially at standing and seated posture and during 1.8g phases. This shifting is mainly determined by HR variation, responsible for the alteration of the systolic-diastolic duration balance over the heartbeat.

6.2.2 Mechano-energetic indices

To grasp the global CVS mechano-energetic balance (*i.e.*, cardiac oxygen demand-supply ratio) during parabolic flight, the behavior of various oxygen consumption indices is investigated, such as the rate-pressure product RPP, the tension-time index TTI and the pressure-volume area PVA [277], defined as

$$RPP = p_{aor,sys} \cdot HR, \quad TTI = p_{lv,mean} \cdot RR, \quad PVA = PE + SW,$$

where $p_{aor,sys}$ is aortic systolic pressure, $p_{lv,mean}$ is mean left ventricle pressure computed over a single heartbeat, and PE is left ventricle potential energy, defined as $PE = p_{lves}(V_{lves} - V_{lv}^{un})/2 - p_{lved}(V_{lved} - V_{lv}^{un})/2$, with p_{lves}, p_{lved}, V_{lves}, V_{lved} and V_{lv}^{un} being left ventricle end-systolic and end-diastolic pressures, end-systolic and end-diastolic volumes, and unstressed volume, respectively.

The corresponding energy supply parameters are considered as well, represented mainly by cardiac stroke work SW (area of the left ventricle p-V loop). Cardiac efficiency is also assessed by means of the ejection fraction EF and the cardiac energy supply vs. demand ratio, respectively defined as:

$$EF = \frac{SV}{V_{LVED}}, \quad \frac{SW}{PVA}$$

where stroke volume SV and the maximum available left ventricular volume (*i.e.*, left ventricle end-diastolic volume, V_{LVED}) are involved. To allow for the comparison between flight phases and postures, all these indices are expressed in a per-minute fashion by multiplicating their beat-average value by the heart rate HR (*i.e.*, $SW/min = SW \cdot HR$, $PVA/min = PVA \cdot HR$, $TTI/min = TTI \cdot HR$).

Figure 6.4 reports the transient behavior of energy demand indices RPP and TTI/min jointly with the corresponding energy supply index SW/min (indicated as percentage value of their respective 1g supine level). SW/min computed at both standing and seated initial 1g phase is similar to the corresponding supine value, whereas seated and standing RPP is higher than the corresponding supine value initial 1g phase. Initial 1g TTI/min instead is almost unchanged at all postures. Successively, reaching the first 1.8g phase RPP rises up to 135% at seated and standing postures (mostly dictated by the augmented HR), unlike SW/min which initially falls to 68% (seated) and 55% (standing) due to cardiac emptying (*i.e.*, SV drop), recovering then to about 95% and 84% at seated and standing postures, respectively. TTI/min initially drops by -22% at seated and -29% at standing posture, at the first 1.8g phase, but then recovers up to 100% and 96%, respectively.

Notice that percentage SW/min remains always lower than RPP and TTI/min during the first 1.8 phase, evidencing a substantial energy demand-supply unbalance. Supine posture shows very weak indices variations over the first 1.8g phase while the second 1.8g phase following microgravity exhibits an overall similar behavior, although with further pronounced undershoots - especially at seated and standing postures - due to the sudden gravity variation from 0g to 1.8g, starting from a globally much more relaxed CVS configuration. During the 20 s microgravity phase, instead, after a first strong peak registered for all indices, oxygen demand (RPP and TTI/min) fall at all postures to values below or close to corresponding 1g pre-flight states, and comparable with supine 1g pre-flight (98%÷102% for RPP and TTI/min, respectively), likely owing to the decelerated HR. Conversely, energy supply remains high (SW/min about 114% at seated and standing postures, 106% at supine posture) also in late microgravity, due to the augmented ventricular filling revealed at this phase. At the end of the parabolic flight maneuver, all indices approaches the same 1g pre-flight values, even though the strong variation observed during the pull-out phase is not perfectly symmetric with respect to the previous pull-up, as already discussed above for global hemodynamic parameters.

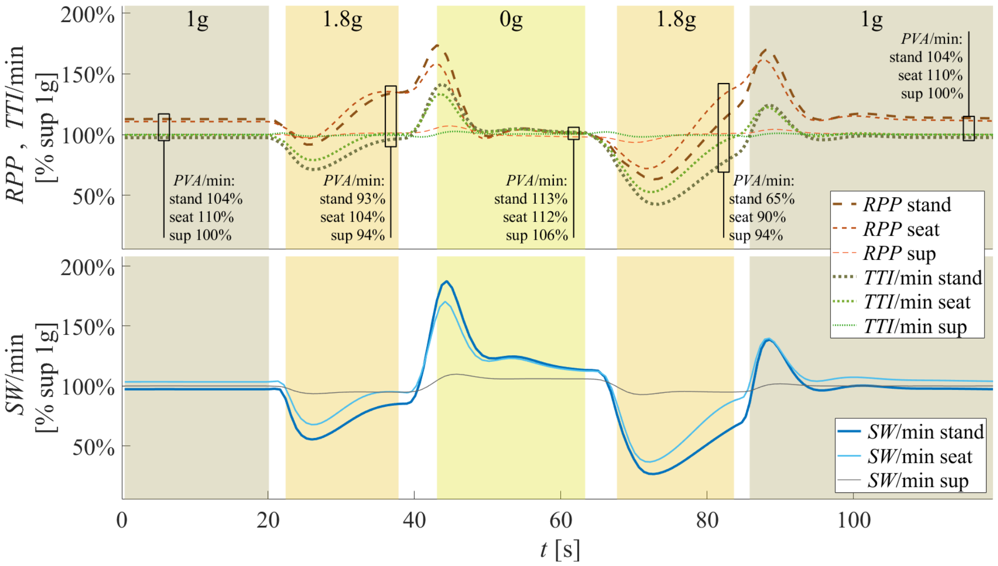

Figure 6.4: Oxygen demand indices (top panel) and left ventricle energy supply (bottom panel) computed during parabolic flight at different posture. Image taken from [66].

Figure 6.4 reports also punctual percentage values of PVA/min for each late-phase of the parabolic flight. This index of oxygen consumption behaves quite the opposite with respect to RPP. Indeed, PVA/min decreases at all postures during 1.8g phases, whereas it rises again in microgravity compared to 1g supine. The reason for such behavior may lie in the strict dependence of PVA/min on SW/min, explaining the similar transient response of these two parameters. However, also PVA/min confirms the above mentioned energy demand-supply unbalance when compared to corresponding levels of SW/min, which are found higher during 1.8g phases and lower in the 0g phase, respectively.

Figure 6.5 illustrates the transient response of the indices of cardiac efficiency to parabolic flight at various postures, that is EF and SW/PVA. These two indices behave qualitatively similarly, although while EF represents the emptying performance of the heart, that is how much the left ventricle succeeds in ejecting blood during systole, SW/PVA instead is an index of the cardiac energy demand-supply ratio. As evidenced in Figure 6.5, both indices fall during first 1.8g phase at seated and standing posture, because of the strong SV and SW/min reduction (Figure 6.4), as well as also during the second 1.8g phase. This SW/PVA decrease detected at 1.8g phases therefore confirms the cardiac oxygen demand vs. energy supply unbalance, determined by the stronger SW/min reduction compared to PVA/min (Figure 6.4). Both indices are markedly increased at seated and standing postures during microgravity, due to the improved cardiac filling and higher ventricular work. Thus, in microgravity the energy demand vs. supply unbalance is inverted, with SW/min rising more than PVA/min (Figure 6.4). At supine posture the behavior of EF and SW/PVA is very weakly affected during the entire parabolic flight maneuver.

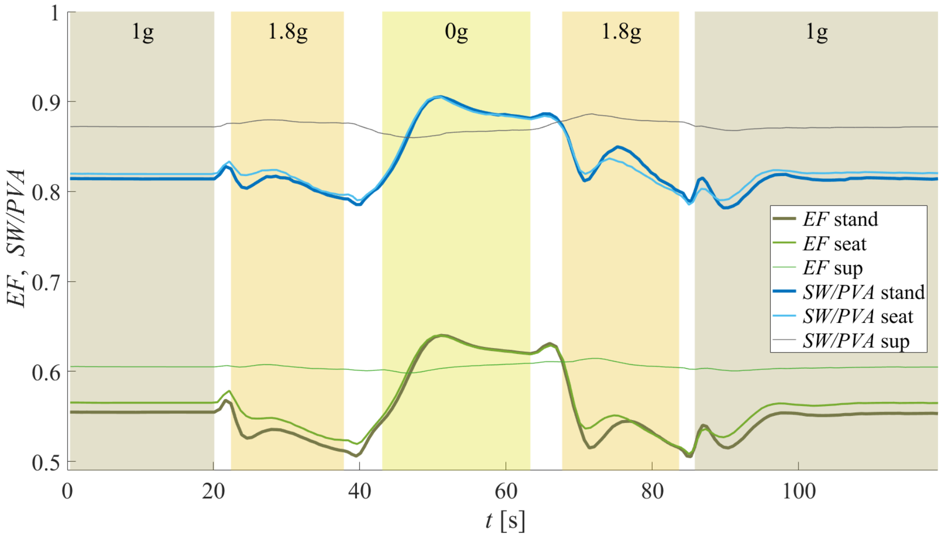

Figure 6.5: Ventricular efficiency indices computed during parabolic flight at different posture. Image taken from [66].

6.2.3 ICP and CVP

With the present version of the model, we report also the results of a preliminary analysis on the parabolic flight-induced changes occurring to cerebrospinal fluid dynamics and ICP, in combination with possible development of serious visual impairment and related ocular changes commonly associated with SANS onset (chapter 2, section 2.2.1) [169, 291, 294, 128]. Researchers have hypothesized that the chronically elevated ICP elicited during prolonged 0g can potentially represent a determinant risk factor for SANS insurgence [169, 291, 294, 128]. Indeed, on Earth, due to normal circadian rhythm, ICP changes daily from slightly negative values at standing to ~12 mmHg at supine posture (according to [251] the physiological range is 5-15 mmHg), whereas such alternation of high and low levels of ICP is completely removed in microgravity.

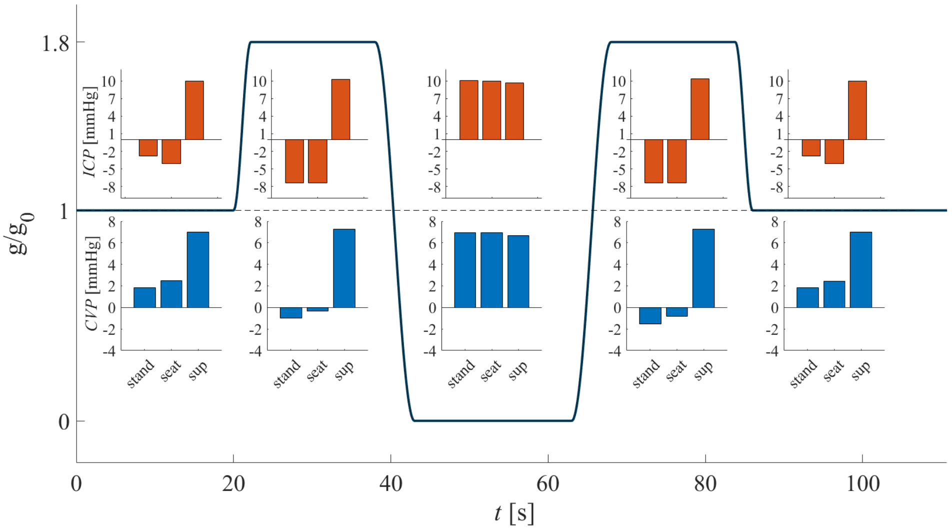

Figure 6.6: Phase-average values of CVP (blue bars) and ICP (orange bars) during parabolic flight at different postures. Image taken from [66].

The present version of the model is integrated with the ICP vs. posture model suggested by Holmlund *et al.* [98] (equations (6.1)-(6.2)). Figure 6.6 depicts single-phase average values of CVP (driver of ICP, according to equations (6.1)-(6.2)) and ICP at all considered postures. From such analysis it emerges that, during both hypergravity phases, standing/seated CVP and ICP fall to values even more negative with respect to 1g levels, while supine values do not change dramatically. At late-0g phase, CVP and ICP reaches similar values for all postures, which are in turn slightly lower than corresponding 1g supine values, in agreement with data reported by Lawley *et al.* [128] (likely because of reduced ITP and, thus, CVP

revealed at 0g [266, 170, 169]). Therefore, the model confirms that ICP is mildly-elevated in microgravity (though not to a pathological extent), at all postures, with prolonged maintenance of such chronic condition during long-term missions potentially contributing to the occurrence detrimental consequences for the ocular apparatus, albeit further investigation is definitely needed on this aspect.

6.3 Cerebrovascular response to simulated parabolic flight

In the present section, we present the results of the analyses published in [224] on the cerebrovascular response to simulated parabolic flight, by resorting to the combined 0D cerebrovascular and 1D-0D global CVS models presented above, in section 6.1. A general overview of the cerebral hemodynamics triggered by parabolic flight at supine posture is first proposed in Figure 6.7. Panels of Figure 6.7 show pressure (P) and flow rate (Q) signals along the left internal carotid-middle cerebral artery (ICA-MCA) pathway (P_a is central aortic pressure), down to the (left) distal pial arteriolar circulation (distal middle cerebral artery, subscript $dm, left$) and capillary-venous cerebral circulation (subscripts c and pv). Here, intracranial pressure and cerebral blood flow are denoted as P_{ic} and Q_{CBF}, respectively. Beside beat-averaged signals (thick lines), steady state values referred to each flight phase (computed over the last 10 s of each phase) are also reported in Figure 6.7. In general, steady-state pressure values show slight (within 3%) albeit significant variations at all different phases of flight with respect to 1g (t-Test for paired-sample), whereas lower and non-significant variations are seen for flow rates. In addition, Figure 6.7 reveals also that over- and undershoots of beat-averaged and continuous signals are not of the same extent throughout the different cerebrovascular districts, as described in detailed in the following.

To provide a thorough quantification of the observed proximal-to-distal differences, Figure 6.8 compares beat-averaged P (panel a) and Q (panel b) signals to respective single-beat pulsatile values ($\Delta P = P_{max} - P_{min}$, panel c, and $\Delta Q = Q_{max} - Q_{min}$, panel d). All signals are normalized with respect to the corresponding 1g (beat-averaged or pulsatile) value. Thus, normalized beat-averaged P (panel a) evidences a protective behavior especially for the distal-capillary regions: here, indeed, over- and undershoots tend to extinguish earlier in time than in proximal districts. Therefore, it is hypothesized that in the distal pial circulation cerebral autoregulation damps out sudden changes induced at proximal level, explaining the observed outcomes. Moreover, at 0g, $\bar{P}/\bar{P}_{1g}$ is found always greater than 1 at 0g, up to distal level, while in the capillary-venous districts $\bar{P}/\bar{P}_{1g}$ is always less than 1. The contrary holds instead during 1.8g phases. Beat-averaged Q signals (panel b) present no time lag, with $\bar{Q}/\bar{Q}_{1g}$ always found either < 1 or > 1 at all flight phases and in all districts (the most stressed is on average the distal

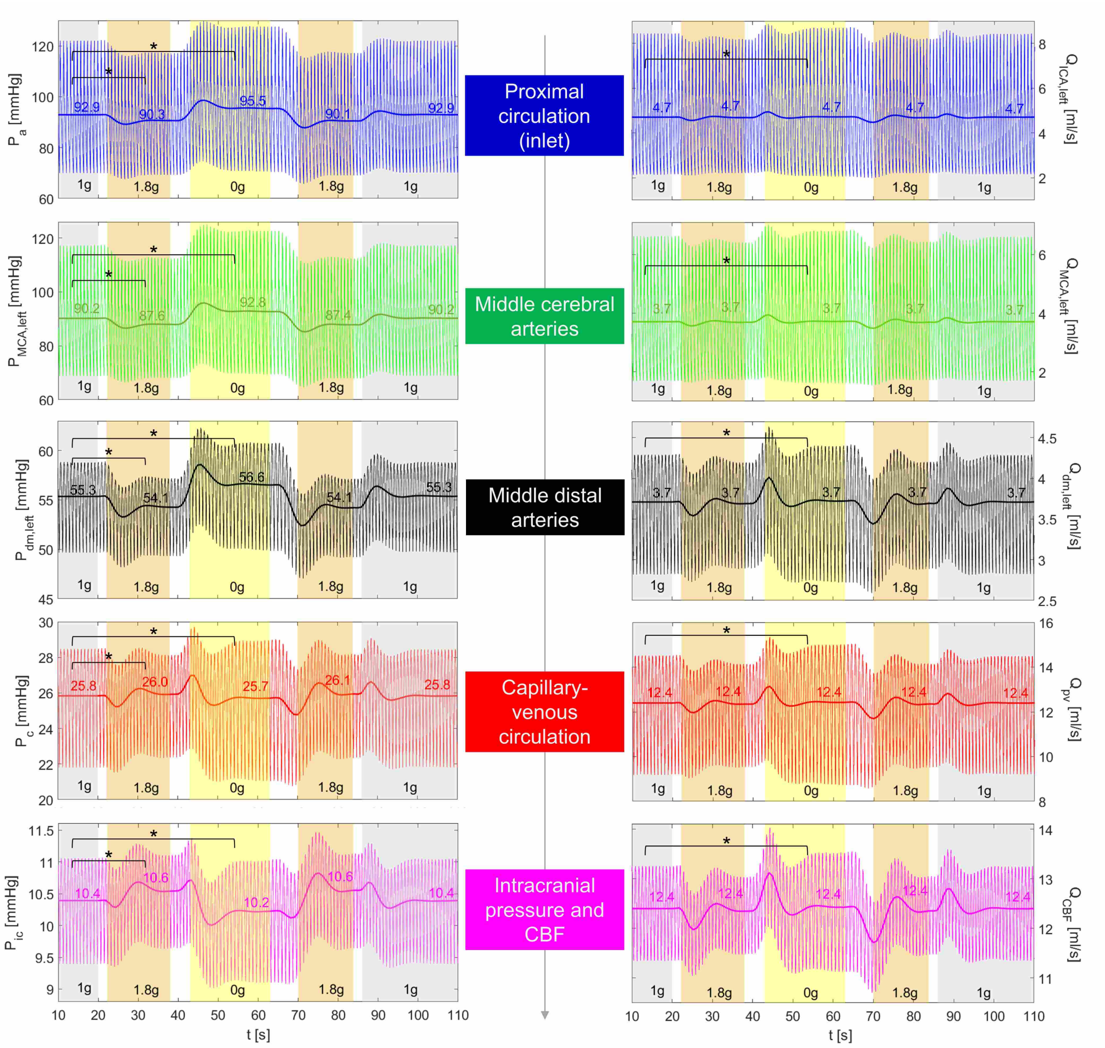

Figure 6.7: Overview pressure (left) and flow rate (right) signals throughout the cerebrovascular model during simulated parabolic flight at supine posture. Asterisks denote significant (p-value<0.05) parameter differences. Image taken from [224].

pial district).

Intracranial pressure (P_{ic}) shows a very slight decrease during 20 s microgravity (-0.2 mmHg compared to 1g), in line with [128, 57]. Thus, as already presented in the preliminary analysis for ICP reported in the previous section 6.2, our findings confirm that in supine posture P_{ic} remains at mildly-elevated levels, showing even a slight increase (+2%) in the hypergravity phase. The slight beat-averaged P_{ic} variation observed between steady-state 1g and 0g phases is comparable to those revealed in the upstream cerebral compartments ($< 3\%$) and can mainly be due to

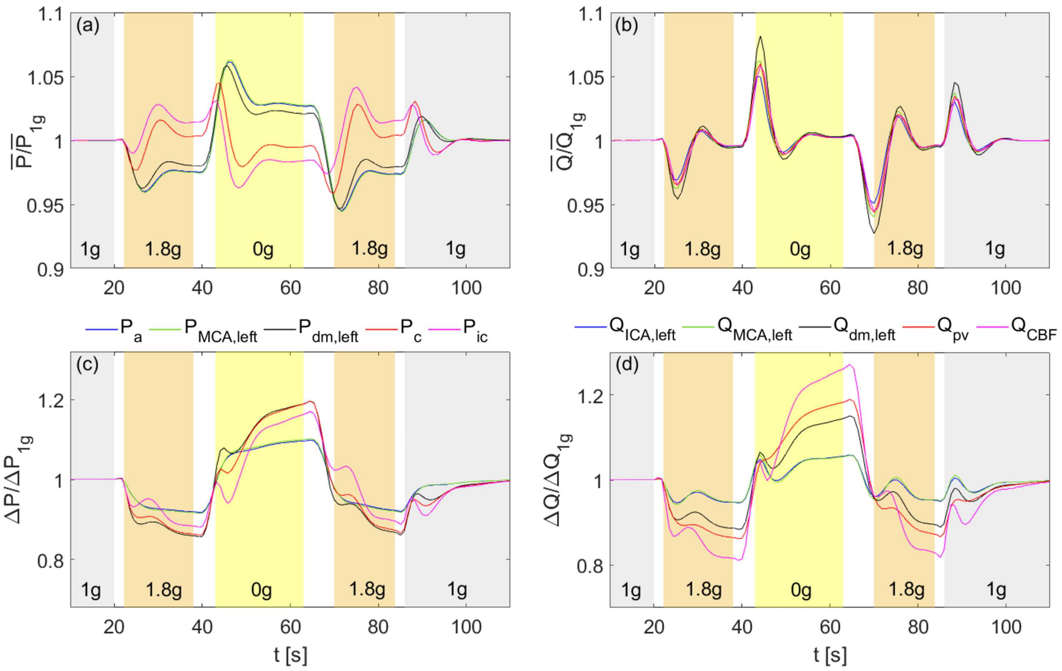

Figure 6.8: Normalized beat-averaged and single-beat pulsatile values of pressure and flow rate signals throughout the cerebrovascular model during simulated parabolic flight at supine posture. Image taken from [224].

cerebral autoregulation intervention.

By observing single-beat pulsatile values ΔP and ΔQ reported in panels c and d of Figure 6.8 instead, it can be observed that, differently from beat-averaged values, pulsatile P and Q vary widely during both 1.8g and 0g flight phases, without usually reaching steady-state. In particular, upon 0g, pulsatile values increase by up to 20-30% in the distal-capillary circulation, while not exceeding 5-10% in the large arteries region. Thus, the protective and maintenance effects seen for beat-averaged pressure and flow signals, respectively, are lost. Pulsatility variations (positive in 0g or negative in 1.8g) increase even further in the proximal-to-distal direction with respect to the 1g phase. There is therefore an amplifying effect of pulsatility towards deep cerebral circulation, due to the complex interplay between the different mechanical-structural characteristics of cerebral circulation, represented as a combination of resistances and compliances of different size [225]. Both P and Q signals present thus a pulsatile values contraction during hypergravity, while an amplification is found during microgravity, with respect to the 1g levels. This behavior is also further exacerbated by central hemodynamics, as a consequence of the aortic pulse pressure increase and decrease observed at central level [68] as a consequence of posture or gravity changes: while in the deep cerebral circulation the reduced proximal pulsatility is further reduced at 1.8g following also the reduced aortic pulse pressure, similarly the increased proximal pulsatility results as further amplified in 0g also because of simultaneous aortic pulse pressure widening.

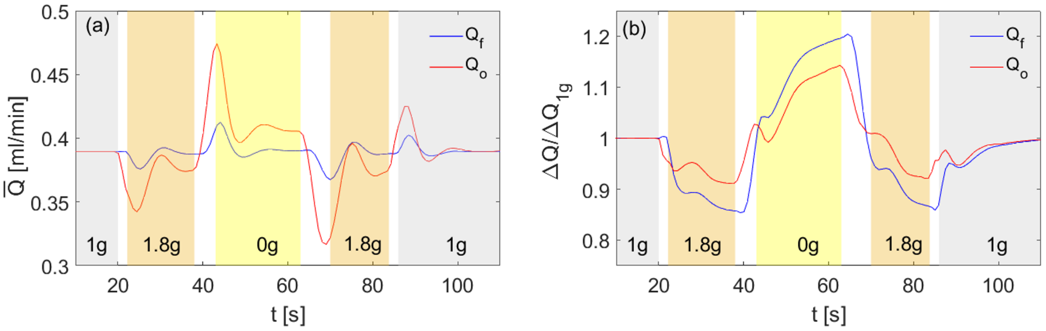

Figure 6.9: CSF formation (Q_f, blue lines) and absorption (Q_o, red lines) during simulated parabolic flight at supine posture. Image taken from [224].

Figure 6.9 instead illustrates the response of the CSF circulation, in terms of formation and absorption CSF rates, that is Q_f and Q_o, respectively. Given that Q_f is driven by pressure difference $P_c - P_{ic}$, whereas Q_o is determined by $P_{ic} - P_{vs}$, the CSF dynamics is strictly related to P_{ic} behavior. In fact, recent *in vivo* measures report an increase of brain ventricular volume in the subarachnoid space - that is where the CSF is formed - and a widespread spatial redistribution of CSF after long-term spaceflight [15, 3, 107, 264]. Thus, the fact that such larger volumes are observed in astronauts reporting SANS-related symptoms suggest that altered CSF and fluid accumulation in brain ventricles may play a role in SANS onset [15, 3].

Our simulated beat-averaged Q_f results (panel a) highlights a CSF formation flow rate peak in early 0g, which is rapidly damped by means of cerebral autoregulation intervention. CSF absorption rate instead, in the same panel, shows that: (i) formation and absorption rates matching observed at 1g is impaired during altered gravity, even at late-phase steady-states of parabolic flight; (ii) CSF accumulation is prevented by a higher CSF absorption rate (at least upon short-term 0g). Similarly to what has been reported previously for distal variables, even in the CSF circulation the hemodynamic pulsatility (panel b) is intensified at 0g, with a more evident increase (+20%) detected for Q_f.

Lastly, in Figure 6.10 we report the result of the investigation on the comparison between cerebral perfusion pressure CPP (defined as $P_a - P_{ic}$), and cerebral blood flow Q_{CBF} during supine parabolic flight. By comparing beat-averaged values of CPP and Q_{CBF} (panel a), it emerges how transient response over- and undershoots are in general more pronounced for CPP than for Q_{CBF}, resulting thus in higher absolute variations of stead-state phase averaged CPP than Q_{CBF} values. Indeed,

CPP is seen to slightly (albeit significantly, t-test for paired samples) increase at 0g steady-state, as confirmed by [173], while barely significant variations are found for Q_{CBF} upon analogous transition. Observing pulsatile CPP and Q_{CBF} instead (panel b), the higher Q_{CBF} pulsatility revealed at 0g is underestimated by CPP, and the reduced Q_{CBF} pulsatility found at 1.8g is in turn underestimated (in module) by CPP. Therefore, CPP can be considered a good proxy of Q_{CBF} even during parabolic flight, even though it does not take into account the effects of vasodilatation/constriction due to cerebral autoregulation mechanisms, showing particularly important effects especially in the distal circulation. Cerebral autoregulation in fact is aimed at varying distal cerebrovascular resistance such that nearly-constant mean Q_{CBF} is preserved (chapter 1, section 1.4) at all flight phases (in spite of CPP).

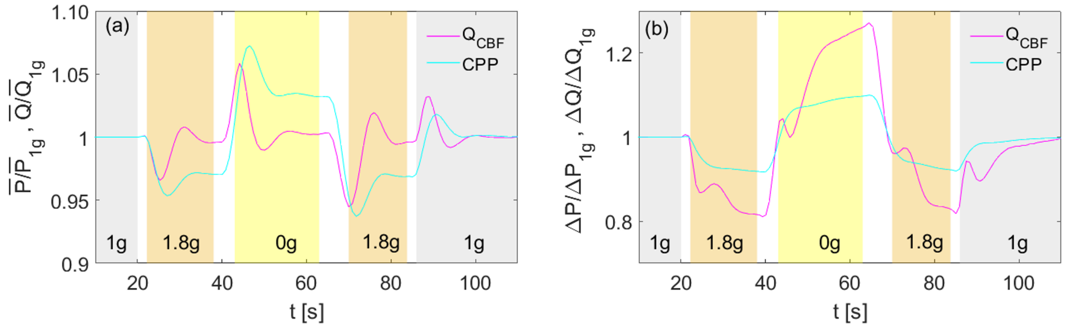

Figure 6.10: Beat-averaged and pulsatile values of the cerebral perfusion pressure (CPP) and cerebral blood flow (Q_{CBF}) during simulated parabolic flight at supine posture. Image taken from [224].

Concluding remarks

In conclusion, the modeling approach shows good capability of reproducing known global hemodynamics response to parabolic flight at different postures, representing a powerful tool of investigation for hemodynamic variables poorly observed in actual short-term microgravity. Moreover, the analysis of cardiac energy demand-supply parameters during parabolic flight sheds light onto the different mechanisms affecting central and global hemodynamics upon entering short-term hyper- and microgravity environments of simulated parabolic flight. The model therefore reveals promising potentialities for future aerospace applications, ranging from short-term microgravity exposure to a better implementation of in-flight countermeasures. Moreover, findings of the present study confirm that, despite showing over- and under-shoots, beat-averaged pressure and flow rate steady state values do not vary remarkably between 0g and 1g because of cerebral autoregulation. On the contrary, in microgravity we observe an augmented hemodynamic pulsatility which increases towards the deep cerebral microcirculation. Such greater pulsatility, inducing a higher variability of maximum and minimum values within single heartbeats, is observed also for other important cerebral markers, such as intracranial pressure, cerebrospinal fluid inflows and outflow, and cerebral blood flow. The proposed approach moreover offers novel insights on how hemodynamic alterations - such as cerebral hypoperfusion and intracranial pressure fluctuations - may contribute to explain neurovestibular dysfunctions emerging during short-term exposure to 0g, including the onset of nausea, SANS and cognitive fatigue.

Chapter 7

Modeling the ocular, cerebral and cardiovascular response during 6° HDT

(part of the contents of the present chapter have been previously published in [69, 67])

Ground-based analogues of human spaceflight have been widely adopted in recent years to resemble the acute and long-term cardiovascular response and later adaptation to microgravity [91, 269, 238, 24]. Among the most diffused analogues of human spaceflight (summarized in chapter 2), 6° head-down tilt (HDT) in particular has gathered wide popularity to mimic the fluid shift revealed in astronauts entering actual weightlessness - *i.e.*, microgravity - during space missions (or parabolic flight) [188].

Therefore, to help ensure healthiness and survival of astronauts undergoing short- and long-term permanence in space [291, 21, 41], remarkable efforts have been devoted to inquire into SANS risks and causes, including the design of possible countermeasures, by resorting to 6° HDT as a terrestrial analogue of spaceflight [175, 99, 150, 198, 125, 126, 210, 279, 281, 189]. The vast majority of these studies explored the relationship between the pressure within the eye globe, *i.e.*, intraocular pressure (IOP), and the pressure in the retrobulbar space, that is cerebrospinal fluid pressure (ICP); or, alternatively, the relationship between IOP and blood pressure at the level of the eye (particularly arterial). The pressure difference between IOP and ICP, called ocular translaminar pressure (TLP), is believed to play a relevant role in the development of SANS. In particular, reduced (or reversed) TLP may compromise the spherical shape of the eye [128, 294, 99, 150].

In addition, elevated ocular perfusion pressure (OPP, defined as the difference between eye arterial pressure and IOP) has also been hypothesized as a potential risk for edema formation [189]. In this context, despite past investigations concerning cerebrovascular responsiveness to HDT have been conducted [57, 42, 210], no clear link between cerebral hemodynamics and the ocular apparatus has been established and thoroughly explained.

To confirm such hypotheses, a number of IOP measures have been collected at 6° HDT and upon acute and long-permanence in 0g [4, 39, 55, 144, 143]. Nevertheless, given the harmful and difficult nature of invasive ICP measurements instead [62, 297], direct (*in vivo*) ICP values associated with posture variation (*e.g.* during 6° HDT) are rare in the literature [191, 5], while completely missing onboard of actual space missions (0g), to date (albeit some results have been reported during parabolic flight [128]).

In the present chapter, thus, we present the acute cerebrovascular and ocular response to 6° HDT and to understanding their interaction and potentially dangerous effects on ocular changes. To accomplish this, we resort to the CVS model integrated with the ocular-cerebrovascular circulation as introduced in chapter 3 of the present thesis. To validate the CVS model, we conducted *in vivo* human experiments to measure cardiovascular and ocular parameters during short-term (10 min) of 6° HDT from 80° head-up tilt (HUT). Additionally, the cardiovascular and ocular response and adaptation to 6° HDT is explored during longer duration experiments, with subjects of both genders maintained on the tilting bed for approximately one hour. Once validated, the new multiscale model is used to investigate the cerebrovascular dynamics elicited by simulated posture change from 80° HUT to 6° HDT at different levels of the brain (from proximal arterial to distal, capillary, and venous cerebral sites), explaining the mechanisms shaping IOP and cephalic blood volume responses, and thus contributing to the understanding of the relationship between cerebral hemodynamics and ocular responses.

7.1 *In vivo* HDBR

A cohort of twelve healthy volunteers (equally distributed by gender: 6 males, 6 females) were recruited to take part in the experiments. Demographic and anthropometric characteristics of subjects enrolled in the study are reported in Table 7.1. All subjects were instructed to avoid intense exercise and caffeine within 12h prior to the study, and they were appositely screened by completing a questionnaire in order to report history of previous or ongoing cardiovascular or ocular conditions, diseases, or any other exclusion criteria. The whole experimental protocol involving human participants was approved by the Human Research Protection Program of Texas A&M University (Institutional Review Board number IRB2022-1070), in compliance to the Declaration of Helsinki (1964) and its later amendments. Informed consent was obtained from all participants included in the study upon completion of the screening questionnaire.

Table 7.1: Subject demographic and athropometric features ($n = 12$, 6 males + 6 females). BSA is body surface area (Du Bois method [58]).

ID	age [ys]	weight [kg]	height [cm]	BSA [m^2]
M01	20	77	179	1.954
M02	21	82	177	1.990
M03	28	79	170	1.905
M04	26	78	179	1.967
M05	33	85	172	1.962
M06	31	65	180	1.828
F01	22	57	163	1.607
F02	27	57	152	1.526
F03	24	52	150	1.967
F04	25	50	160	1.501
F05	25	85	157	1.855
F06	25	58	161	1.606

7.1.1 Experimental setup and protocol

The global experimental study is composed of three different sessions, respectively referred to as experiment 1, 2 and 3:

- **Experiment 1:** 10-minute 6° HDT session from upright (80°);
- **Experiment 2:** 60-minute 6° HDT session from supine (0°);
- **Experiment 3:** 60-minute 6° HDT session from upright (80°).

The experimental protocol includes an additional baseline session, during which the subjects are placed in a seated position, with a first set of cardiovascular measures (described below) collected after 5 minutes of rest. During all three experimental sessions, the subjects are positioned on an inversion tilt table (Figure 7.1a) in the initial position (80° or 0°), and after 5 minutes of rest, a first set of cardiovascular measures is collected at the initial position. The subjects are then tilted to 6° HDT, and (after 5 min of adjustment rest) multiple sets of cardiovascular measures are collected every 10 minutes throughout the whole HDT duration (only one measurement taken for experiment 1). The subjects spent thus a total of 10 minutes and 60 minutes at 6° head-down position in experimental sessions 1 and 2-3, respectively. At the end of the head-down position, the subjects are then tilted back to the corresponding initial position pertaining to each session, and two last sets of cardiovascular measures are collected after 5 min and 15 minutes from tilt back, respectively. For safety reasons, the subjects remain strapped to the tilt table for the whole duration of the experiments.

Each set cardiovascular measures includes the following measurements: (i) brachial arterial pressure (sphygmomanometer, Omron cuff), (ii) heart rate, cardiac output, and stroke volume (Innocor inert gas rebreathing, Cosmed, Figure 7.1b), (iii) intraocular pressure (eye tonometer, iCare, Figure 7.1c), (iv) left and right common carotid artery and internal jugular vein cross section area (ultrasound imagery, Butterfly iQ+, Figure 7.1d) and (v) blood flow velocity (Doppler ultrasound, Butterfly iQ+, Figure 7.1d). Additionally, (vi) subjects' finger arterial pressure is recorded continuously using a Finometer NOVA (plethysmography, Finapres Medical Systems, Figure 7.1e), corrected at brachial-heart level with a height correction unit, and periodically calibrated with brachial pressure acquired through the sphygmomanometer (i).

7.1.2 Acute 6° HDT from 80° HUT and 0° supine

In this section, we report results from our *in vivo* experimental campaign in terms of global hemodynamics parameters (arterial pressure, HR, CO, SV, TPR), ocular (IOP) and common carotid artery (CCA)/internal jugular vein (IJV) (*i.e.* cross-section area A). For each measured data-point, the corresponding mean pressure values (systolic SAP, mean MAP or diastolic DAP) are computed by averaging the continuous pressure signal acquired by the Finometer NOVA (instrument vi) over 1 minute of recorded time, starting from immediately after the Innocor gas rebreathing (instrument ii). Further information regarding the adopted instrumentation, usage and calibration of devices, and other operational procedure can be found in [69, 281, 279]. Additionally, at almost all measured data-point, data are non-normally distributed ($\mathrm{p} \sim$ 1e-15, two-tailed Kolmogorov-Smirnov test for normality) Thus, statistical significance of parameter differences between different time-points, experiments have been tested via non-parametric Wilcoxon test for paired samples (two-tailed), while Wilcoxon test for unpaired samples have been adopted to test gender differences instead.

Global hemodynamics

Results from the three experiments for the measured parameters of global hemodynamics are displayed in all panels of Figures 7.2-7.3. Each parameter results are presented for both genders (blue and pink curves), at each measured time-point and during each of the three experiments. At each single time-point, results are reported as mean (circles and thick lines) ± SE (bars, denoting the standard error of the mean), with single-subject parameters values also included as thin, colored lines (blue for males, pink for females).

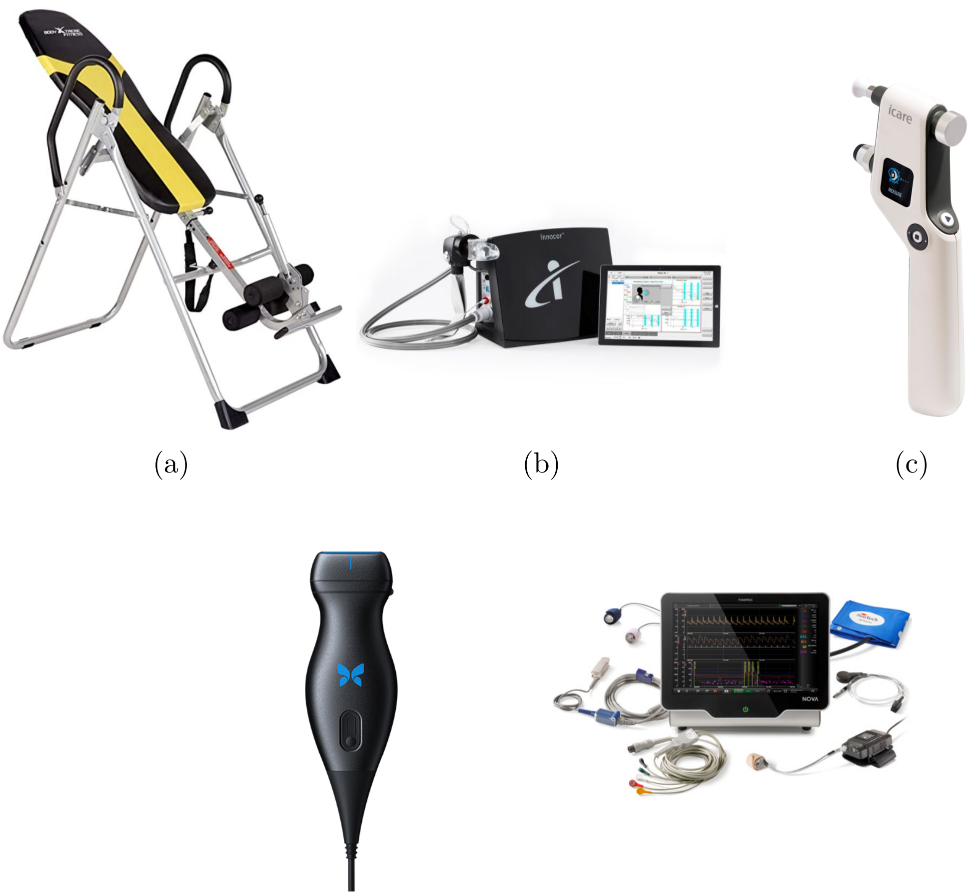

(a) (b) (c)

(d) (e)

Figure 7.1: Devices used within the experimental HDT sessions: inversion table, Cosmed Innocor, iCare tonometer, Butterfly iQ+, Finapres Finometer NOVA, from a to e.

As shown in Figures 7.2-7.3, the tilt maneuver from 80° HUT to 6° HDT (experiments 1 and 3) causes an important headward fluid shift from the lower to the upper body [188, 238]. The resulting augmented cardiac filling leads to the rise in SV (Figure 7.2c) and CO (Figure 7.3a), accompanied by a drop in HR (Figure 7.2b), a rise in TPR (Figure 7.3b) and a slight decrease of MAP (Figure 7.2a), modulated by the short-term regulation mechanisms. Successively, parameters response for the post-tilt 80° HUT position, for experiments 1 and 3, are similar to the corresponding pre-tilt values for all parameters. IOP (Figure 7.3c) follows the same trend revealed by CO and SV, dictated by the headward fluid shift to the cephalic compartments, showing an acute rise when tilting from 80° HUT to 6° HDT in experiments 1 and 3. Results of experiment 2 are instead weaker and less pronounced compared to experiments 1 and 3, although always in the same

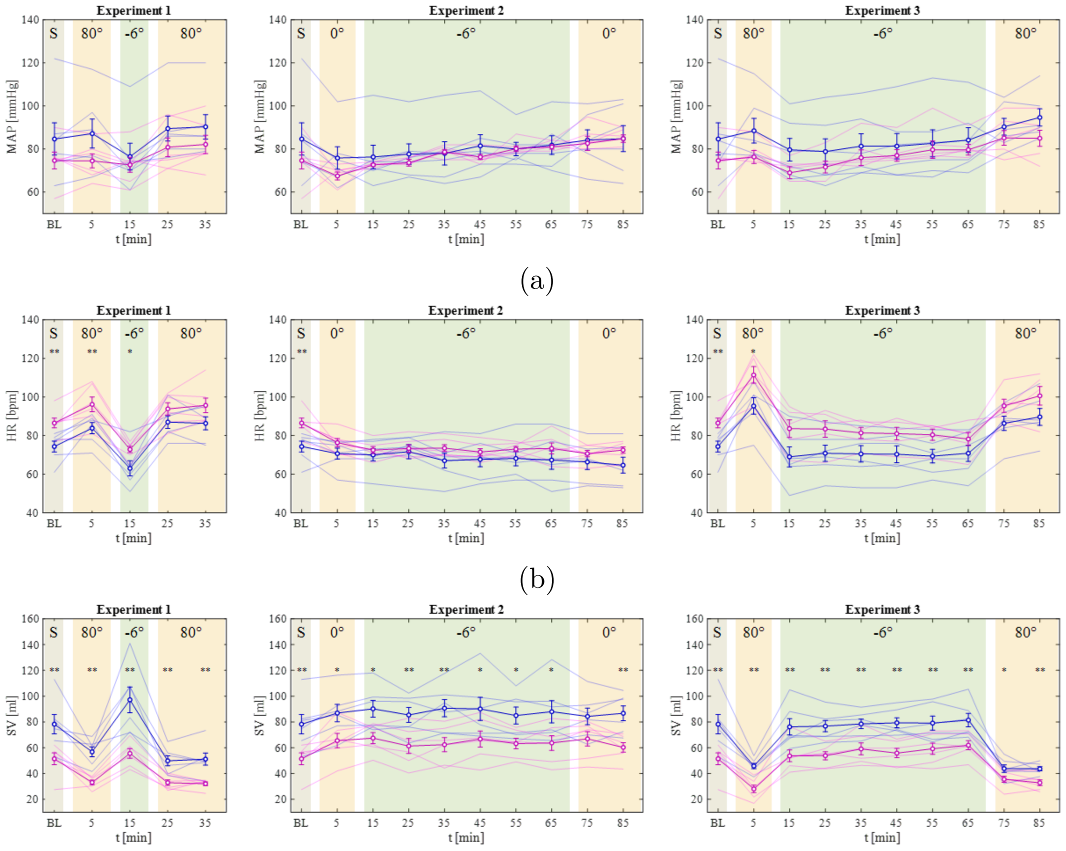

(a)

(b)

(c)

Figure 7.2: Global hemodynamics parameters results from experiments 1-3 (I) (*: $p < 0.10$, **: $p < 0.05$ through Wilcoxon unpaired test between genders).

direction, with only slight parameters differences revealed between 0° (supine) and 6° HDT positions.

Figures 7.2-7.3 display also some preliminary results of statistical tests for differences between genders, with not much difference (*i.e.*, not statistically significant, through Wilcoxon test for independent samples) revealed for MAP and IOP, although a few time-points show significant differences between genders for HR and TPR. SV and CO instead are found almost always significantly different between males and females (Figures 7.2c and 7.3a), with male values always significantly greater than females due to the different baseline heart size associated with both genders [244, 211], respectively.

Our results align also with previous experimental cardiovascular data reported by other authors [24, 238, 139, 125, 198]. Blomqvist *et al.* [24] report $HR = 68 \pm 2$ bpm, $CO = 7.4 \pm 0.5$ l/min, $SV = 108 \pm 7$ ml, systolic arterial pressure SAP $= 104 \pm 3$ mmHg, and diastolic arterial pressure $DAP = 59 \pm 6$ mmHg (diastolic)

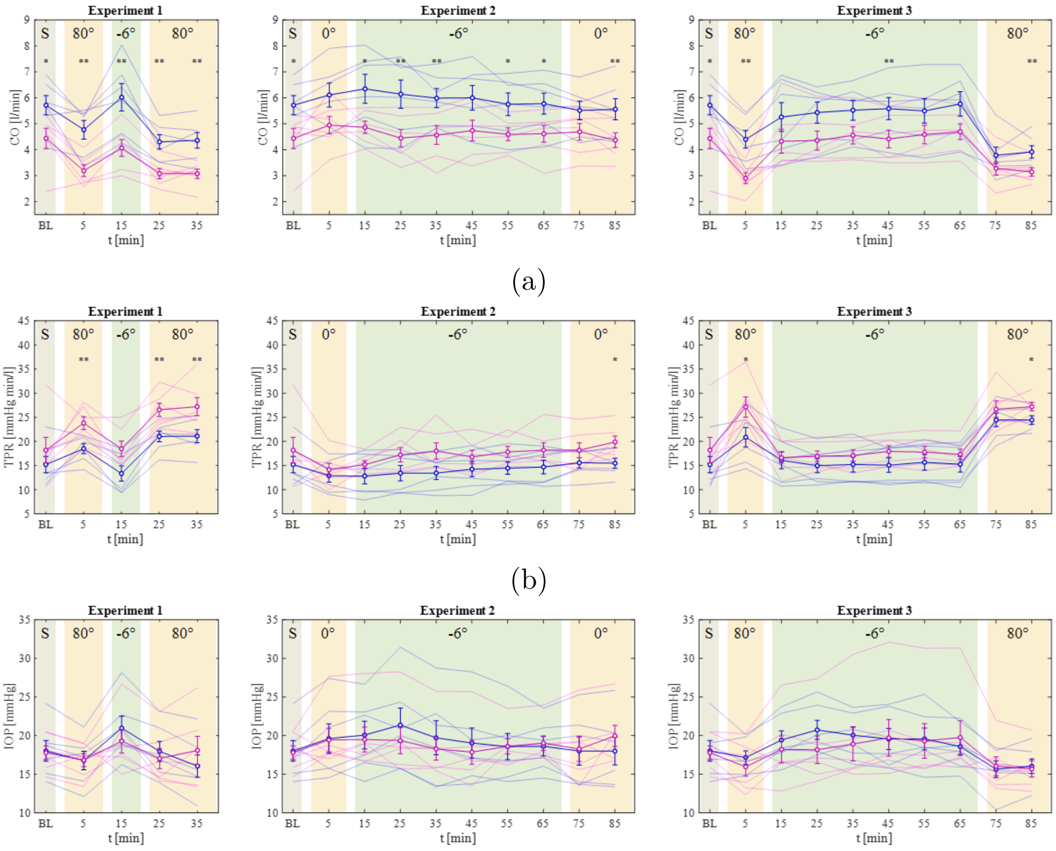

(a)

(b)

(c)

Figure 7.3: Global hemodynamics parameters results from experiments 1-3 (II) (*: $p < 0.10$, **: $p < 0.05$ through Wilcoxon unpaired test between genders).

after a 30-minute tilt to 5° HDT ($n = 10$ male individuals, baseline supine data: $HR = 75 \pm 4$ bpm, $CO = 7.7 \pm 0.4$ l/min, $SV = 102 \pm 7$ ml, $SAP = 106 \pm 3$ mmHg, and $DAP = 65 \pm 2$ mmHg). Shiraishi *et al.* [238] performed a 6° HDT and compared the observed findings with baseline seated measures ($n = 10$ male individuals). They report that MAP decreases from 86 ± 2 mmHg to 77 ± 2 mmHg, that HR decreases from 68 ± 2 bpm to 57 ± 2 bpm, and that CO increases from 4.6 ± 0.3 l/min to 5.3 ± 0.3 l/min. Linder *et al.* [139] report an IOP increase of approximately 3.5 mmHg on 10 individuals when tilting from the upright 90° position to 6° HDT, while Laurie *et al.* [125] report a smaller IOP increase of 0.7 mmHg from 8 male subjects tilted to 6° HDT, compared to seated position.

Trends of parameters response have also been tested via Mann-Kendall test for trends (with Sen's method) [147, 32], in order to assess whether the observed parameters present or not significant trends of variation throughout both phases of the 1-hour exposure to 6° HDT, separately during experiments 2 and 3. Results in terms of parameter slopes (computed between time-points at minute 5 and 65 of experiments 2 and 3) are reported in Table 7.2, with asterisks highlighting those parameters showing a significant positive or negative trend of variation. As evidenced in Table 7.2, almost all parameters show some degree of trend throughout the 1-hour exposure to 6° HDT, in both considered experiments. However, only a few parameters report significant results, with inconsistencies emerging between the two experiments despite the analogue subjects conditions. Thus, we hypothesize that the initial (pre-tilt) position may play a role, especially over short-to-mid time exposure to 6° HDT. However, it should be considered also that the small sample size of our experiments (*i.e.*, 6 subjects for each gender) may limit the power of statistical tests consistently, requiring thus for a bigger sample size, that is recruiting a higher number of subjects to strengthen test results and thus produce reliable inferences.

Table 7.2: Test for trend results, *: $p < 0.10$, **: $p < 0.05$ (Mann-Kendall test [147, 32]).

	Males		**Females**	
Parameter	**Experiment 2**	**Experiment 3**	**Experiment 2**	**Experiment 3**
SAP [mmHg/min]	0.1900	0.2500*	0.1000	0.2400**
MAP [mmHg/min]	0.1367	0.1000	0.1667**	0.1667**
DAP [mmHg/min]	0.1000	0.1750**	0.0733	0.1708**
HR [bpm/min]	-0.1000	~ 0	~ 0	-0.1000
CO [l/min/min]	-0.0143	0.0037	-0.0015	0.0077
SV [ml/min]	-0.0992	0.0928	-0.0249	0.1884*
IOP [mmHg/min]	-0.0422	-0.0200	~ 0	0.02
VO_2 [l/min/min]	~ 0	~ 0	~ 0	~ 0
TPR [mmHg s/ml/min]	0.0395	0.0063	0.0446	0.0178
$A_{CCA,r}$ [mm^2/min]	0.0145	0.0216	0.0935	0.0483
$A_{CCA,l}$ [mm^2/min]	0.0376	0.0278	-0.0130	0.0524
$A_{IJV,r}$ [mm^2/min]	0.2201	0.4904	0.2373	0.6623**
$A_{IJV,l}$ [mm^2/min]	0.1257	0.1624	0.1829	0.7995*

Common carotid arteries and Jugular veins characteristics

Measurement of common carotid artery (CCA) and internal jugular vein (IJV) characteristics (cross-section area and blood flow velocity) conducted through ultrasounds imaging (measures iv-v listed above) and related results are presented in this paragraph. Following the work by Whittle & Diaz-Artiles [279] on the analysis of CCA and IJV cross-section area at various degrees of HUT and HDT, in our study we developed a new procedure to compute CCA and IJV cross-section area

A (that is, A_{CCA} and A_{IJV}, respectively) by exploiting the Image Processing Toolbox available in MATLAB. The newly devised procedure is sketched in Figure 7.4, where steps 1-4 illustrate the computation strategy adopted to calculate left and right (subscripts l and r) A_{CCA} and A_{IJV} starting from ultrasound images acquired at each measured time-point, during all the three experiments. Step 1 in Figure 7.4 shows the single ultrasound image loading onto the Image Segmenter tool, where the case of a right-side CCA and IJV cross-section is displayed, corresponding to a given time-point taken at 6° HDT position. The successive step 2 consists of adopting the guided segmentation tool to draw and cut through the edges of the selected vessel cross-section (*e.g.*, IJV cross-section, as shown in the figure). Then, the image is converted into a binary black and white matrix of pixels and further into a matrix of integer/double precision values of 1s or 0s, depending on whether the pixel is situated within (white, *i.e.*, assigned value 1) or outside (black, *i.e.*, assigned value 0) the contoured area. The summation of all 1 values then gives the extent of the considered vessel cross-section area in pixel units, which can then be converted into mm^2 through a scale conversion factor determined on the basis of the image scale (automatically reported by the ultrasound imaging device on the right side of the picture, and maintained along with images size and resolution throughout all the experiments and tested subjects). The scale factor adopted for all images is $1\ \text{mm}^2 = 548$ px, with the only exception of subject F06 (experiment 3 only), for which a different scale factor of $1\ \text{mm}^2 = 625$ px is adopted. The final values of $A_{CCA,r}$, $A_{CCA,l}$, $A_{IJV,r}$, and $A_{IJV,l}$ assumed to the end of this study are then computed at each time-point of each experiment, for each considered subject, by averaging either two or three distinct corresponding area values computed by two or three different operators, respectively, depending on whether the first two computed area values differ by more than 10%.

Results for $A_{CCA,r}$, $A_{CCA,l}$, $A_{IJV,r}$, and $A_{IJV,l}$ at each time-point taken over the three experiments and for all tested subjects are reported in Figures 7.5 and 7.6 as mean (thick lines and circles) ± SE (bars, that is the standard error of the mean) together with all single-subject values (thin, colored lines). In particular, Figure 7.5 shows that left and right CCA do not show large variations among the performed experiments, although evident differences emerge when tilting from 80° HUT to 6° HDT, despite considering a high pressure zone such as carotid arteries. On the contrary, IJV areas (Figure 7.6) show much wider variations when tilting to 6° HDT from upright, reaching values largely bigger than corresponding A_{CCA}s, despite starting from a general condition of collapsed veins (*i.e.*, $A_{IJV} = 0$ and intravascular pressure equal to extravascular pressure) at upright standing/seated posture.

A remarkable number of significant differences between genders emerge at all positions, in particular, A_{CCA}s are found in general significantly bigger in males than in females, at all postures and during all performed experiments. Conversely, A_{IJV}s (especially left-sided) appear to grow more in females than in males approaching

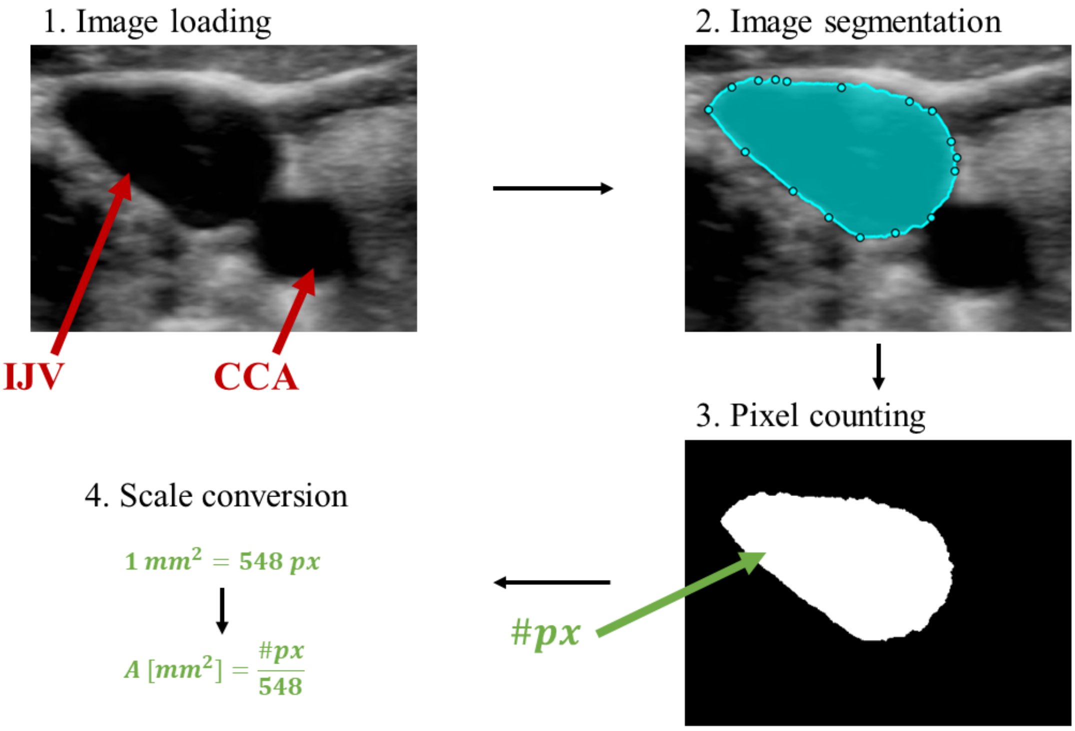

Figure 7.4: Cross-section area computation strategy.

and during 6° HDT, with a few significant cases revealed at several time-points along the 6° HDT phase of experiments 2 and 3. This latter result should also be considered in light of the dominance side (left or right neck side) of subjects involved in the study, because of which left or right IJV may result as more prone to sustain pressure excursions than the corresponding opposite side, by showing larger cross-section area distensibility or by counteracting collapse at upright standing/seated posture. Thus, further investigation is definitely required on this topic.

Lastly, results on trend analysis are also reported for computed $A_{CCA,r}$, $A_{CCA,l}$, $A_{IJV,r}$, and $A_{IJV,l}$, and reported in Table 7.2. Mann-Kendall tests evidence that, in spite of a slight trend towards increasing cross-section area seem to be visible by looking at CCA and IJV (especially) cross-section behavior during permanence at 6° HDT position in Figures 7.5-7.6, these are found to be significant only for female subjects undergoing experiment 3. Still, this outcome may be explained in light of the limited size of the sample adopted for this investigation, although it should be stressed once again that even the initial (pre-tilt) position may play a role in the subsequently observed response over time. Further elucidation is needed also on this aspect.

A second, interesting analysis has also been initiated concerning CCA and IJV

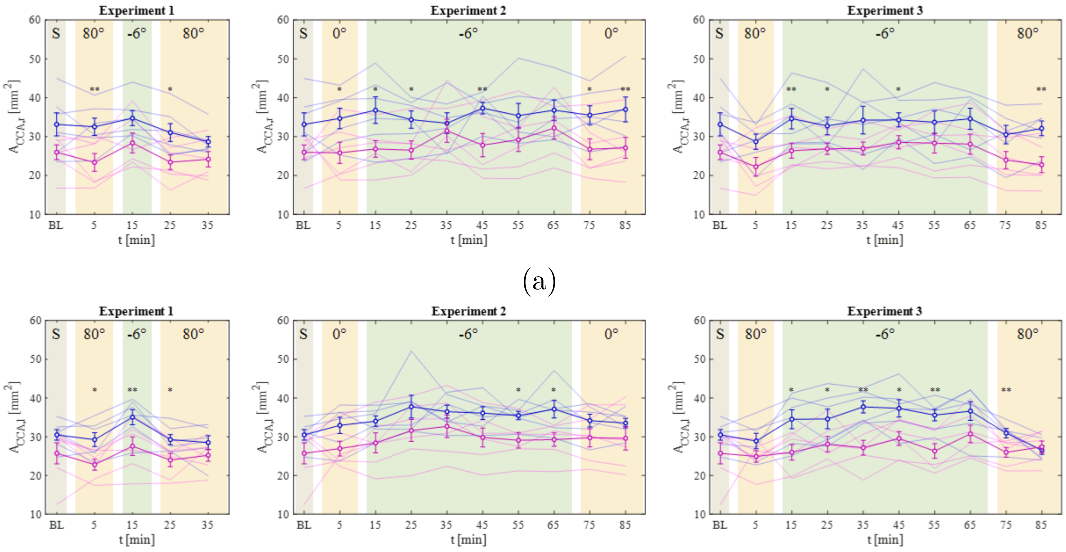

(a)

(b)

Figure 7.5: Common carotid artery cross-section area from experiments 1-3 (*: $p < 0.10$, **: $p < 0.05$ through Wilcoxon unpaired test between genders).

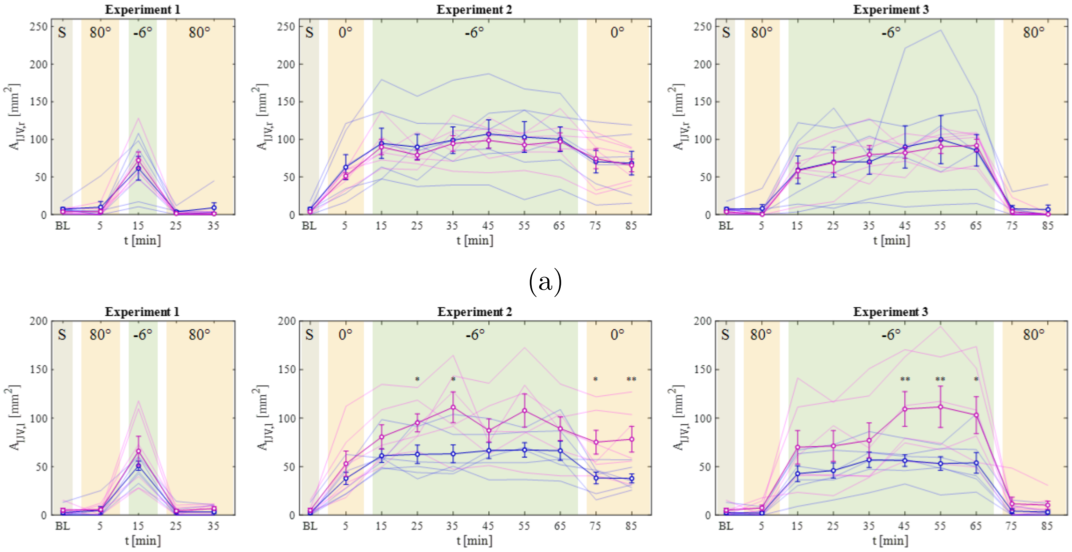

(a)

(b)

Figure 7.6: Internal jugular vein cross-section area from experiments 1-3 (*: $p < 0.10$, **: $p < 0.05$ through Wilcoxon unpaired test between genders).

characteristics during 6° HDT, involving observation and classification particularly of jugular blood flow velocity patterns acquired through ultrasound imaging and Doppler analysis (measure v above). This classification is based on the seminal work

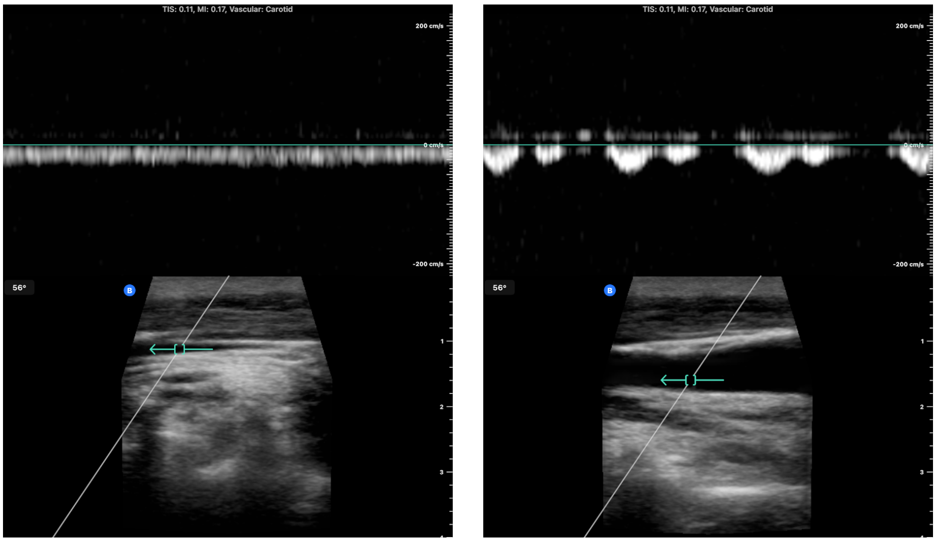

(a) (b)

Figure 7.7: Example of grade 1 (a) and grade 2 (b) IJV blood flow rate classification according to Marshall-Goebel [149].

by Marshall-Goebel *et al.* [149], who proposed to characterize the typical patterns observed for IJV blood flow on astronauts participating in long-duration spaceflight missions, taking ultrasound images of their IJV blood flows before, during and after spaceflight at various postures (*i.e.*, seated, supine, and 15° HDT). The purpose of the study by Marshall-Goebel is linked to the fact that prolonged exposure to microgravity during long-term space missions is believed to result in a chronic headward blood shift and consequent cephalic fluid accumulation compared to the upright posture on Earth, with unknown consequences onto cerebral healthiness. The classification of IJV blood flow patterns proposed by Marshall-Goebel [149] is as follows

- Grade 1: forward flow never returning to zero;
- Grade 2: mostly forward flow that may occasionally return to zero (*i.e.*, occasional reverse flow occurs);
- Grade 3: even forward and reverse flow (*i.e.*, net flow stasis);
- Grade 4: mostly retrograde flow (dangerous, indicating severe cephalic congestion, jugular venous flow stasis and potential thrombosis).

Figures 7.7a and 7.7b, acquired during our experimental campaign on subjects undertaking 6° HDT, show a case of grade 1 (a) and grade 2 (b) jugular flow, respectively. Based on the preliminary data and results obtained from our experiments, grade 1 flow has been detected in 79 times (91.86%) out of 86 available at

80° HUT position, with only 7 (8.14%) grade 2 cases and no grades 3 and 4 revealed at this position. At 0° (supine), 27 (37.50%) grade 1 flows, 43 (59.72%) grade 2 flows and only 2 (2.78%) grade 3 flows are observed over a total of 72 available observations. Finally, at 6° HDT position 114 (38.38%) grade 1 flows, 182 (61.28%) grade 2 flow and only 1 (0.34%) grade 3 flow are detected out of 297 total available cases. It should be noted also that all 3 grade 3 cases revealed in our investigation are associated with the same subject, during the same experiment. No grade 4 flow have been detected in our experimental investigation so far. Definitive outcomes of this study will be made available in the future publications by our group.

7.2 *In silico* HDT

The adopted numerical framework of the closed-loop, multiscale model of the human CVS have been introduced and described in detail in chapter 3 of the present thesis. In particular, the model of cerebrovascular circulation and the ocular compartment presented in sections 3.5-3.6 and used to the aim of the present section are displayed separately in Figures 3.12, 3.13, and together in Figure 7.8.

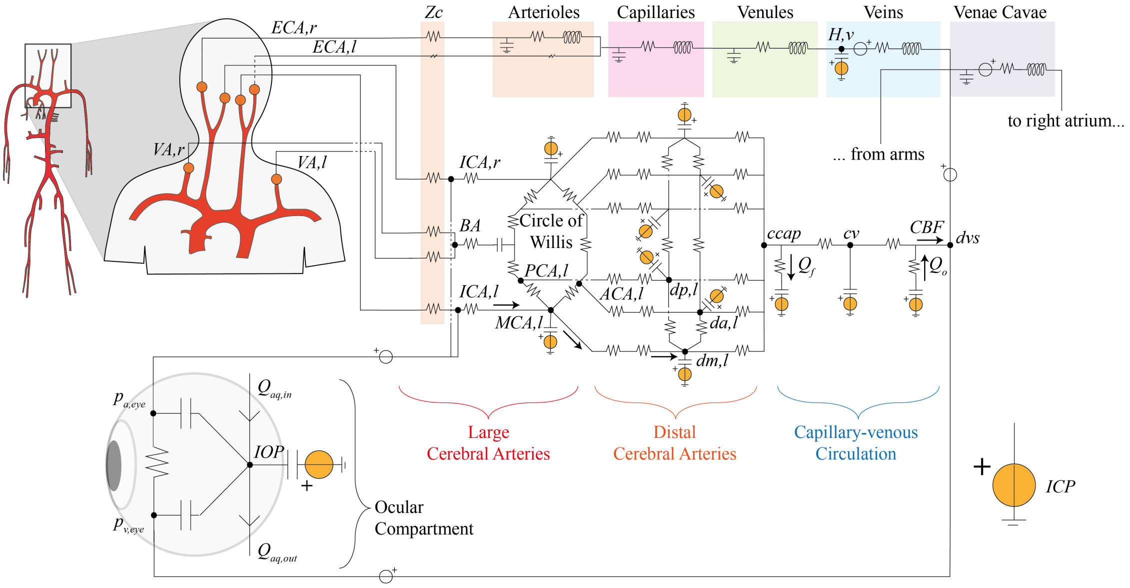

Figure 7.8: Architecture of the CVS model with emphasis on the cerebrovascular and ocular compartments. Image taken from [69].

7.2.1 Model validation

In vivo data resulting from our short-term (10 minutes) HDT experiment used for validation and corresponding model outcomes in terms of cardiovascular and ocular parameters are displayed in Figure 7.9 (only the 6 male subjects are considered for the purpose of the present model validation, p-values computed via Wilcoxon test for paired samples). Since we aim to provide the typical acute response to 6° HDT for a generic subject (and not subject-specific), to reduce the inter-subject variability we recruited 6 young healthy male volunteers with anthropometric features as homogeneous and comparable as possible to those on which the model is calibrated. Results show that the model is able to accurately reproduce the global cardiovascular and ocular response to the tilt maneuver between 80° HUT and 6° HDT, with all model predictions lying within the experimental data box plots (inter-quartile bands or whiskers). For all parameters, pre- and post-tilt 80° HUT positions are non-significantly different from each other ($p > 0.05$). Conversely, most parameters show statistically significant differences between pre- and post-tilt 80° HUT and 6° HDT positions ($p < 0.05$; with only *MAP* $p < 0.10$ between pre-tilt 80° HUT and 6° HDT).

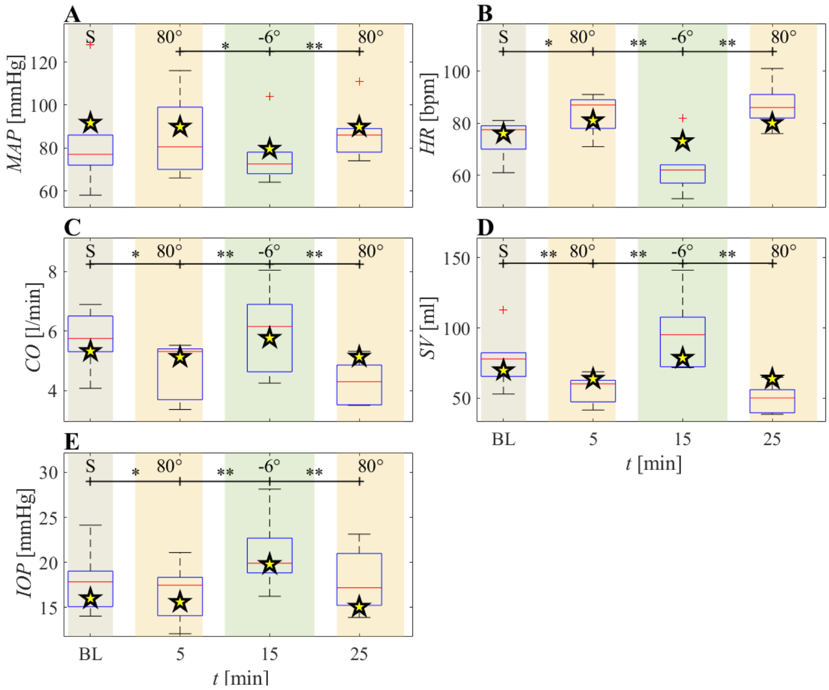

Figure 7.9: Experimental data (box plots) vs. *in silico* modeled results of global cardiovascular and ocular parameters (*: $p < 0.10$, **: $p < 0.05$). Image taken from [69].

7.2.2 Ocular and cerebrovascular interaction during short-term 6° HDT

In the following, the cerebrovascular model is investigated by exploring blood pressure and flow rate responses to 6° HDT, following a proximal-to-distal pathway. Figure 7.10 reports hemodynamic signals at left (subscript l) internal carotid artery (ICA, panel F), left middle cerebral artery (MCA, panel D), left distal middle cerebral artery (dm, panel B), and then at cerebral capillary ($ccap$, panel C), cerebral venous (cv, panel C), and dural venous sinus (dvs, panel A) sites. As it can be seen, blood pressure rises at the beginning of the 6° HDT at all considered sites, due to the change in the hydrostatic pressure associated with change of posture.

Figure 7.10 reports also arterial and venous pressures at the level of the eye (panel E), sharing a similar behavior to the cerebral arterial and distal-capillary-venous compartments in response to 6° HDT. Specifically, mean (beat-averaged) eye arterial pressure is raised by 19.6 mmHg (+30%) approaching 6° HDT from 80° HUT. This mean pressure increase is less than the mean pressure increase detected at cerebral arterial level (+21.4 mmHg, +33%, at left ICA), because of the forward position of the eyes compared to the body mid-coronal plane. Thus, at 6° HDT position the lower eye arterial pressure is caused by the slightly more elevated position of the eye with respect to the rest of the cerebral circulation. Besides, mean eye venous pressure rises by about 5.5 mmHg (+260%) upon tilting from 80° HUT to 6° HDT.

Blood flow rates at all cerebrovascular sites (panels F, D, B and C) present a much more homogeneous response to 6° HDT than compared to pressure. The first initial flow rate increase observed at all sites at the beginning of the tilt maneuver – caused by the headward fluid shift – is rapidly extinguished restoring almost the same pre-tilt flow rate levels, shortly after reaching -6°. This is made possible by cerebral autoregulation, acting onto distal pial circulation by increasing arteriolar resistance (+13%) and reducing the corresponding compliance (-17%) so that an almost unchanged level of cerebral blood flow (CBF) is guaranteed [42] (panel A).

Figure 7.11 summarizes mean (beat-averaged) and pulse (max - min, at single-beat) pressures and flow rates before and after the 6° HDT from 80°, at steady-state and at each considered cerebrovascular site (from left ICA, to cerebral capillary-venous compartments). It is evident how 6° HDT position drives blood pressure to increase all over the cerebral vasculature [57], with mean ICA,l pressure at 80° HUT of about 65.8 mmHg (aortic MAP about 92.8 mmHg) vs. 6° HDT mean ICA,l pressure of about 87.2 mmHg, which is much more similar to the post-tilt aortic MAP of about 86.1 mmHg. Yet, the post-to-pre tilt difference of mean pressure resulting from the HDT maneuver is not homogeneous throughout the considered cerebrovascular sites: +21.4 mmHg (+32.5%) registered at ICA,l and +21.1 mmHg (+33.3%) at MCA,l, while +16.2 mmHg (+44.4%) at dm,l, and +12 mmHg (+83.3%) at $ccap$), and even +11.3 mmHg (+271.4%) at cv. Thus, not

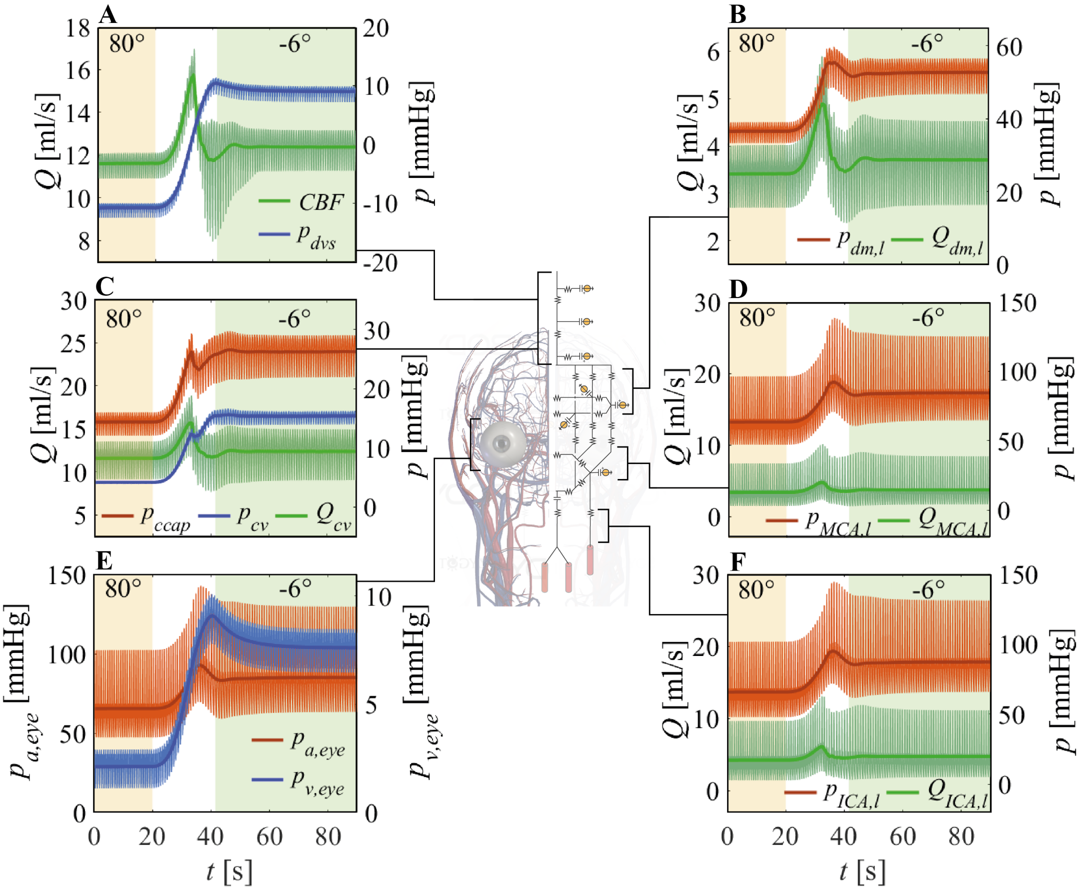

Figure 7.10: Ocular-cerebrovascular pressure and flow rate time responses to 6° HDT. Image taken from [69].

only the absolute pressure difference decreases between 80° HUT and 6° HDT moving from proximal to distal/capillary-venous cerebral compartments, but it can be observed that the relative (*i.e.*, percentage) post-to-pre tilt differences show an increasing trend when proceeding along the same cerebral pathway. These findings can be explained by the reduction of distal pial arteriolar compliances mediated by cerebral autoregulation to counteract the abrupt *CBF* increase triggered by HDT, in combination with the non-linear behavior of the cerebral venous compliance (modeled as inversely related to cerebral venous pressure). Furthermore, mean *dvs* pressure at the outflow of the cerebrovascular compartment goes from -10.8 mmHg to 9 mmHg tilting head-down from 80° HUT, that is, +19.8 mmHg (+183.2%), similarly to left *ICA* pressure (absolute variation). This latter mean *dvs* pressure growth differs from the previously mentioned increasing trend revealed along the *ICA*-*cv* pathway, potentially because of the presence of downstream superior vena cava (*svc*) pressure (mean values -0.5 mmHg at 80° HUT, 7.9 mmHg at 6° HDT)

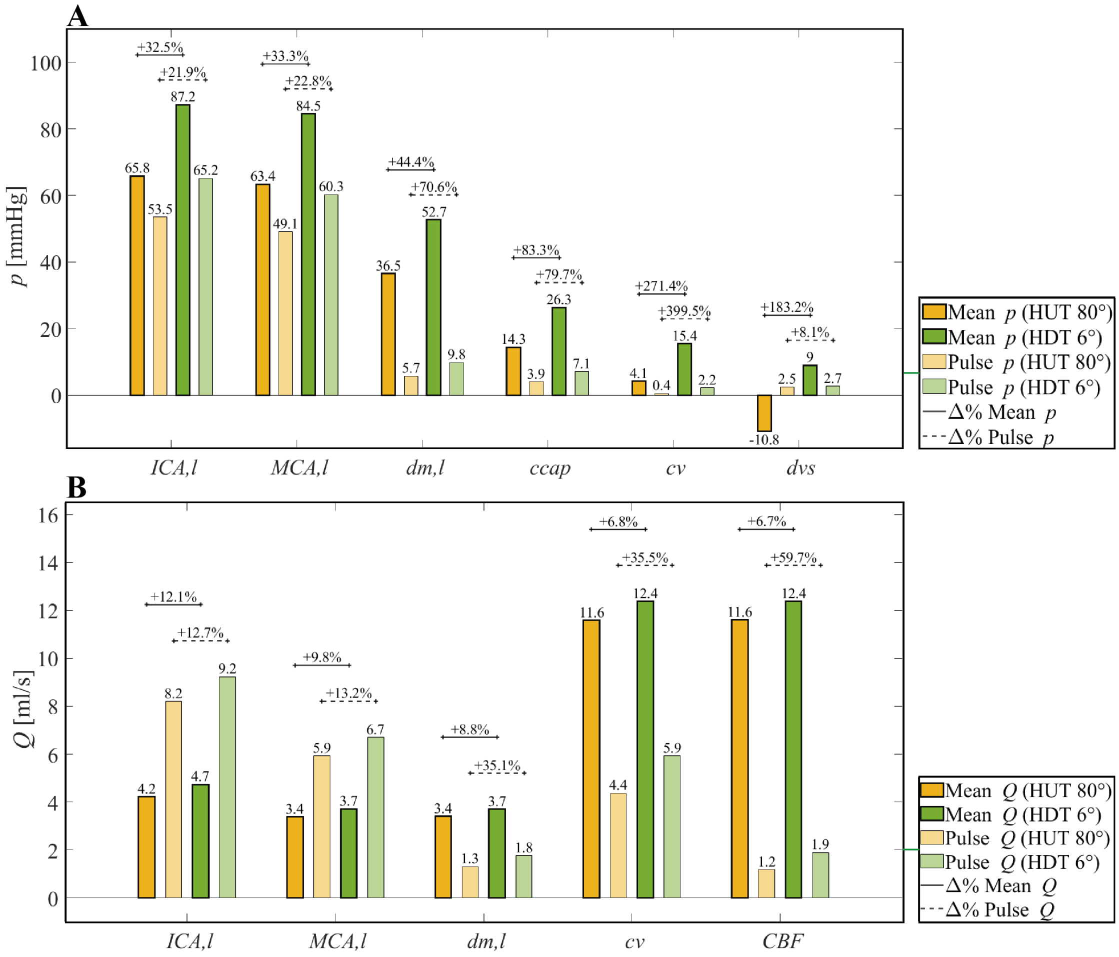

Figure 7.11: Cerebrovascular mean and pulse pressure/flow rate at steady-state pre- vs. post-tilt. Image taken from [69].

and the related central venous pressure *CVP* (2.1 mmHg at 80° HUT, 7.6 mmHg at 6° HDT), exerting their influence especially onto the closer upstream cerebral compartments. Indeed, it can be noted that mean *dvs* pressure registered at 80° HUT is given by 80° HUT *svc* pressure and subtracting the corresponding hydrostatic term related to the *svc*-head distance (about 10 mmHg at 80° HUT).

Besides, Figure 7.11A shows also how pulse pressure tends to increase at all sites when tilting from 80° HUT to 6° HDT, reflecting the global pulse pressure increase widely documented at central (aortic) level when undergoing similar changes of posture [23, 68]. Specifically, the change found for cerebrovascular pulse pressure is lower (in percentage) at proximal arterial sites (*ICA,l*: +11.7 mmHg, +21.9%; *MCA,l*: +11.2 mmHg, +22.8%) than in the downstream distal and capillary-venous sites (from +4.1 mmHg, +70.6% at *dm,l* to +1.8 mmHg, +399.5% at *cv*). This behavior should be considered in light of the cerebral autoregulation contribution, reducing cerebral arteriolar compliance, and thus further contributing to enlarge pulse pressure amplitude. On the other hand, pulse pressure revealed at *dvs* level is not much affected by HDT maneuver (+0.2 mmHg, +8.1%), which is similar to the pulse pressure response of *svc* (+0.2 mmHg, +8.1%) and *CVP* (+0.2 mmHg, +12.5%) for the above mentioned reasons.

Flow rate mean values are reported instead in Figure 7.11B, sharing similar responses to 6° HDT across the different cerebrovascular compartments. Because of cerebral autoregulation, especially at distal sites (*dm,l*), very limited (+0.3 ml/s, +8.8%) mean flow rate variations are observed in response to 6° HDT. The adjacent sites show a similar behavior, with limited mean flow rate variation following 6° HDT (mean flow rate at *ICA,l*: +0.5 ml/s, +12.1% ; *MCA,l*: +0.3 ml/s, +9.8%; *cv*: +0.8 ml/s, +6.8%). As expected, *CBF* is maintained at nearly-constant level during the entire posture change maneuver [42], with +0.8 ml/s (+6.7%) detected variation. Flow rate pulse values, also represented in Figure 7.11, panel B, present an increase along the proximal to distal/capillary-venous direction (*ICA,l*: +12.7%, *MCA,l*: +13.2%, *dm,l*: +35.5% and *CBF*: +59.7%), similarly to what has been observed for the corresponding sites pulse pressures.

To elucidate the role of posture changes specifically onto the ocular apparatus, in the next paragraphs we focus and discuss the role of ocular-cephalic pressures and volumes response during the tilt maneuver from 80° HUT to 6° HDT. Figure 7.12 highlights the model ocular compartment, underlining its interplay and link with the communicating cerebrovascular circulation. Indeed, the relationship between *IOP* and *ICP* (*i.e.*, the translaminar pressure $TLP = IOP - ICP$), as well as between *IOP* and the arterial pressure at eye level (ocular perfusion pressure $OPP = p_{a,eye} - IOP$) are believed to play a crucial role in the development of SANS [125, 99, 150, 128, 294].

Panel A of Figure 7.12 depicts *IOP* and *ICP* transient responses to 6° HDT from 80° HUT. It can be observed that *ICP* increases in response to tilt down from -0.1 mmHg to about 10.9 mmHg. Lawley *et al.* [128] report *ICP* to increase from 4 ± 1 mmHg to 14 ± 2 mmHg when tilting subjects from 90° HUT (seated) to 0° supine, while *ICP* increases even further (an additional +1.8 ± 0.5 mmHg) when tilting from 0° supine to 6° HDT. Holmlund *et al.* [98] report instead *ICP* to pass from -0.9 ± 3.5 mmHg at 69° HUT to 10.4 ± 1.5 mmHg at 0° supine. In all cases, *ICP* is found to increase by approximately 10/12 mmHg when changing posture from upright to supine/head-down. *IOP* instead changes from 15.8 mmHg to 19.9 mmHg (in line also with documented *IOP* measurements in actual microgravity [4, 39, 144, 143]). In addition, we find that pulse *ICP* rises from 0.01 mmHg (80° HUT) to 1.7 mmHg (6° HDT), while pulse *IOP* increases from 6.9 mmHg (80° HUT) to 8.7 mmHg (6° HDT).

Therefore, both *IOP* and *ICP* (beat-averaged) grow along with the HDT maneuver, mostly driven the fluid shift to the upward-cephalic compartments and

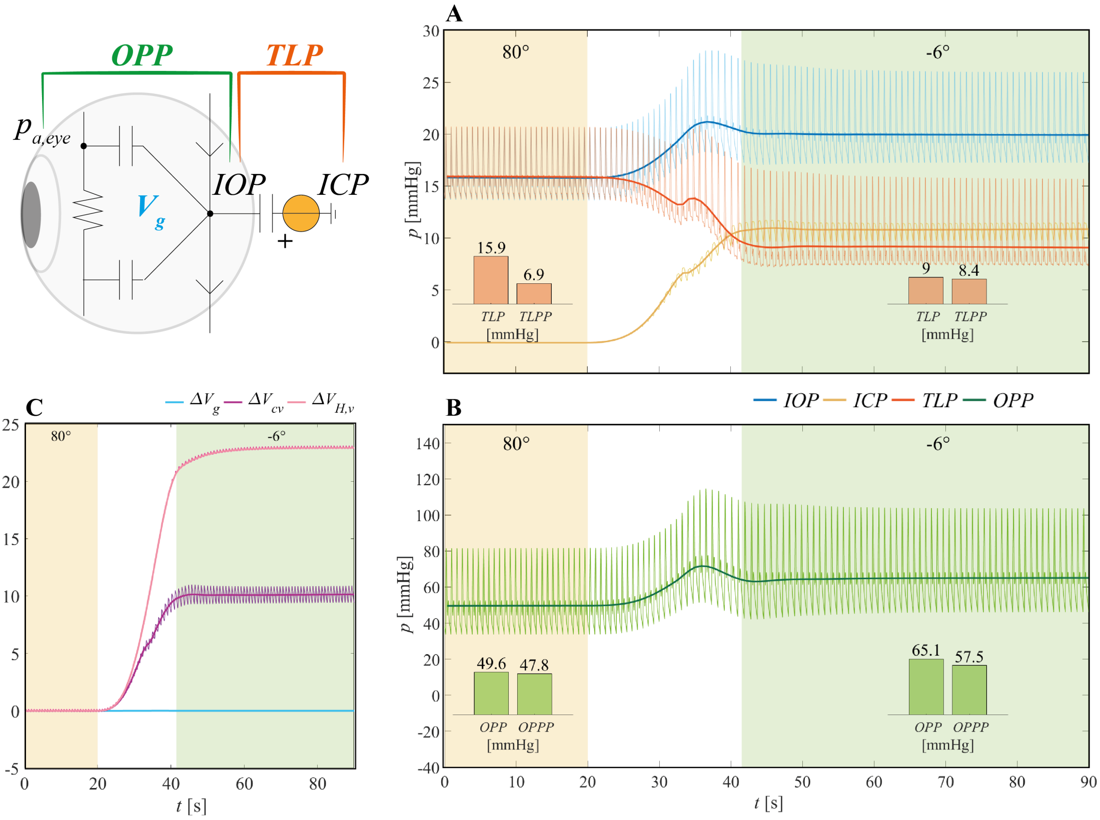

Figure 7.12: Ocular-cephalic compartment response to head-down tilt maneuver from 80° HUT to 6° HDT in terms of ocular pressures and ocular-cephalic volumes. Image taken from [69].

related blood pressure increase at eye and cerebral level. From the present results it emerges that *ICP* is increased to a higher extent than *IOP* in response to HDT, causing mean *TLP* to drop from 15.9 mmHg (pre-tilt at 80° HUT) to 9 mmHg (post-tilt, 6° HDT). This *TLP* contraction of about -43% – albeit here purely acute – is deemed to play a crucial role in contributing to SANS development in astronauts undergoing actual missions in microgravity [128, 294]. Also pulse (max - min) *TLP* (*TLPP*) results as altered after HDT to -6°, as it is widened by +1.5 mmHg (from 6.9 mmHg to 8.4 mmHg, +22%) as a consequence of the augmented pulse *IOP* and *ICP*.

Figure 7.12, panel B, illustrates instead the response of *OPP* to HDT from 80° HUT to -6°. Differently from *TLP*, beat-averaged *OPP* goes up from 49.6 mmHg to 65.1 mmHg (+31%) being driven by the augmented arterial pressure at eye level (+19.6 mmHg, see Figure 7.10, panel E), that is rising more than the more limited *IOP* increase discussed above (+4.1 mmHg, Figure 7.12, panel A). Thus, the larger

OPP revealed at 6° HDT translates into an increasing perfusion pressure directly applied to the ocular apparatus [250], potentially leading to formation of optic disk edema [189]. Similarly to *TLPP*, also pulse *OPP* (*OPPP*) tends to increase while reaching 6° HDT, that is by +9.7 mmHg (from 47.8 mmHg at 80° HUT to 57.5 mmHg at 6° HDT, +20%).

Finally, due to SANS association with cephalic volume congestion caused by head-ward fluid shift [99, 128, 16, 130, 169, 279], the model is used to inquire into the acute ocular-cerebrovascular volume variations elicited during 6° HDT maneuver. In this context, panel C of Figure 7.12 depicts the absolute volume differences, with respect to the pre-tilt 80° HUT levels, caused by 6° HDT onto the volume of eye globe (V_g), of the cerebral veins (V_{cv}), and of the extra-cerebral head veins ($V_{H,v}$, refer to Figure 7.8 and chapter 3 for the exact definition of such compartments). From this analysis it emerges that, beside the fact that almost no volume change is revealed for the ocular globe ($\Delta V_g \simeq +0.005$ ml after HDT), both cerebral and extra-cerebral venous volumes are highly impacted by the headward fluid shift, showing a deep compartmental volume increase while tilting from the upright position to 6° HDT. Therefore, although *IOP* is raised as a consequence of reaching 6° HDT, the volume of the eye globe stays nearly-unchanged, appearing to be almost independent of posture variations. Conversely, the marked cephalic congestion highlighted by the cerebral and extra-cerebral blood volume accumulation evidences how the retrobulbar space can exert higher compression forces onto the ocular globe and, over prolonged time, may even lead to structural remodeling and permanent changes [145].

Concluding remarks

In conclusion, our numerical framework can accurately resemble the ocular and cardiovascular response to acute 6° HDT, representing thus a promising tool to investigate the complex physiological mechanisms contributing to the development of SANS. Our results from short-term (10 min) simulated 6° HDT show increased hemodynamic pulsatility in the proximal-to-distal/capillary-venous cerebral direction, a marked decrease (-43%) in ocular translaminar pressure, and an increase (+31%) in ocular perfusion pressure, suggesting a plausible explanation of the underlying mechanisms at the onset of ocular globe deformation and edema formation over longer time scales. Furthermore, our experimental results on longer (60 min) exposure to 6° HDT from upright and from supine can lead to a better understanding of gender differences in the hemodynamic response to posture changes and ground-based reproduced micrograviity, including also the insightful contribution of our preliminary investigation on common carotid artery and internal jugular vein characteristics in terms of cephalic congestion and plausible associated disturbances.

Conclusions

The present doctoral thesis pursues the objective of introducing and exploring the state of the art of cardiovascular modeling applied to clinical and spaceflight-related scenarios. In particular, in the present work we discussed the most widely acknowledged issues related to cardiac arrhythmias such as atrial fibrillation, to change of posture on Earth and related hemodynamic consequences, to varying gravity aboard of parabolic flights, and to head-down tilt to mimic astronauts undergoing space missions in true microgravity. To address such problems, we developed and presented a computational tool; namely, a multiscale 1D-0D closed-loop mathematical model of the human circulation, including also the ocular and cerebrovascular circulations, sub-models of short-term regulation responses plus a number of additional features strictly connected to the dynamics of the physiological response to posture and gravity changes on Earth and in space.

Through our analyses, we highlighted that:

i. considering the clinical case study of atrial fibrillation effects onto perfusion of the myocardium - tackled to show promising applicability of our numerical tool even to cases of clinical interest - we found that this condition induces a series of detrimental consequences onto perfusion of the myocardial muscles - compared to normal sinus rhythm - particularly proceeding towards deeper myocardial layers and at higher ventricular frequencies;

ii. passive posture changes at normal Earth gravity (1g) drives a series of autonomic responses aimed at maintaining the system homeostasis. Specifically, heart rate, cardiac contractility and peripheral resistance are promoted to fight hypotension and blood flow migration to and pooling in the lower extremities, at upright posture, while venous tone is diminished. As a result, central mean arterial pressure tends to reach slightly higher values at upright posture than supine, while central venous pressure drops because of thoracic pressure expansion and consequent intrathoracic pressure falling, enabling augmented venous return;

iii. approaching of passive upright posture highlights an energy demand-supply unbalance, with reduced energy produced by the heart (stroke work) in contrast to augmented (rate pressure product) oxygen consumption, compared to supine posture;

iv. through wave analysis and wave intensity analysis, we revealed how, despite orthostatic-induced augment arterial stiffness and consequent increased wave velocity, wave reflections at central levels seem to be reduced because of weakened backward waves being reflected from the cerebral region, likely due to cerebral autoregulation modifying cerebral arteriolar resistance and caliber in order to maintain suitable level of cerebral blood flow. Additionally, the wave trapping mechanisms protecting the heart and the aortic valve from reflected waves produced all over the arterial tree is preserved along with body posture changes;

v. parabolic flight simulated by means of our model induces a number of cardiovascular changes, including exacerbated mechano-energetic unbalance especially at standing and seated posture during hypergravity phases, which appears then to be reversed - that is, higher energy production than energy demand - at microgravity phases. Parabolic flight maneuver shows also potentially harmful conditions at cerebrovascular level, during simulated flight at supine posture. Particularly, hemodynamic pulsatility of pressure and flow signals increases at deep cerebral level - despite the observed beat-averaged signals damping operated by cerebral autoregulation - leading to higher peak values, potentially threatening cerebrovascular health;

vi. acute exposure to 6° head-down tilt as analogue of spaceflight is of great interest to space medicine and bioastronautics, especially in the context of understanding SANS and orthostatic intolerance experienced by astronauts upon landing on Earth after long space missions. Our experimental study points out significant trends of variation of hemodynamic variables during 1-hour exposure to 6° head-down position, including also internal jugular vein size engorgement indicating potential cephalic venous congestion and flow stasis (assessed through jugular venous flow Doppler analysis). Our numerical simulations of 6° head-down tilt from upright (80°) instead highlights that the intraocular - intracranial pressure balance (*i.e.*, translaminar pressure) can potentially be compromised upon tilting head-down, especially after long periods, leading to eventual ocular compression, eyeball shape alteration and consequent visual complications; furthermore, elevated ocular perfusion pressure revealed at 6° head-down position can in turn elicit ocular edema formation over prolonged time.

The mathematical model presented in this thesis may even be further expanded in future works, in view of possible applications to the simulation of additional clinical conditions. Upon preliminary calibration, the model can be used to investigate the insurgence and impact of dysautonomias, autonomic disorders, specific vascular incompetencies, by acting on the specific behavior of the related dependent vasculature variables, showing remarkable potential in the framework of clinical assessments where direct invasive measurements are difficult - if not impossible - to carry out. The advantage of relying on a computational approach lies also in the fact that specific cause-effect relationships between different processes - at the basis of the observed cardiovascular behaviors - can be explained clearly and more easily such as through appositely designed parametric studies. Furthermore, the model can be exploited to explore the impact of different altered-gravity environments (lunar, martian or other conditions of interest to the aim of space exploration), as to simulate the long-exposure cardiovascular adaptation to 0g. In this regard, the possible mitigation of the microgravity-induced cardiovascular deconditioning and SANS occurrence may also be further deepened through the computational approach made possible by our computational framework. Besides, numerical modeling would also facilitate the development of appropriate countermeasures (*e.g.*, simulating the use of artificial gravity on the human circulation as done in lower body negative pressure and centrifugation experiments) to fight such related cardiovascular deconditioning. Further analyses and experimental investigation are advisable concerning mid and long-term effects of 6° head-down tilt. These could be mainly devoted to increase the current sample size, in order to strengthen the significance of our statistical analysis, as well as to dive deep into topics such as gender differences in the cardiovascular response, or carotid and jugular veins characteristics in association with cephalic venous congestion, thrombosis and SANS reported in 0g/6° head-down tilt.

It is therefore clear how important numerical tools can be in the context of human subjects research, especially nowadays, given the ever increasing power and accessibility of computational frameworks at associated reduced costs. Thus, we strongly advice further investigation on these aspects, as improving responsiveness, reliability, robustness, scalability and adaptability of computational models can be determinant to bridge the current gaps, as well as to provide assistance in the diagnostics and prediction processes, helping clinicians and engineers find better solutions to existing cardiovascular problems, both on Earth and in space.

Appendix A

1D model settings and definitions

$$\beta = \frac{4}{3}\frac{2\pi A\delta^2 + 3A^2 - 4\sqrt{\pi}A^{3/2}\delta}{(\pi\delta^2 + 2A - 2\sqrt{\pi A}\delta)^2} \tag{A.1}$$

$$N_4 = \frac{8\nu\sqrt{\pi}A^2}{\delta(-4A^{3/2} + 6A\delta\sqrt{\pi} - 4\sqrt{A}\pi\delta^2 + \pi^{3/2}\delta^3)} \tag{A.2}$$

$$\begin{aligned}\frac{\partial}{\partial t}\begin{pmatrix} A \\ Q \end{pmatrix} &= \begin{pmatrix} 0 & 1 \\ \sum_{j=1}^{3} \frac{jA^j B_{j+1}}{\rho} - \beta\frac{Q^2}{A^2} + \frac{\widehat{EI}}{\rho}\frac{mA_b^m}{A^m} & 2\beta\frac{Q}{A} \end{pmatrix} \frac{\partial}{\partial x}\begin{pmatrix} A \\ Q \end{pmatrix} + \\ &+ \begin{pmatrix} 0 \\ \sum_{j=1}^{4} \frac{A^j}{\rho}\frac{dB_j}{dx} - N_4\frac{Q}{A} - Ag\sin\gamma\sin\alpha \end{pmatrix}\end{aligned} \tag{A.3}$$

$$\frac{\partial\lambda_{1,2}}{\partial x} = -\beta\frac{Q}{A}\frac{\partial A}{\partial x} + \beta\frac{1}{A}\frac{\partial Q}{\partial x} \pm \frac{(.)}{2\sqrt{\beta(\beta-1)\frac{Q^2}{A^2} + \sum_{j=1}^{3}\frac{jA^jB_{j+1}}{\rho} + \frac{\widehat{EI}}{\rho}\frac{mA_b^m}{A^m}}}, \tag{A.4}$$

where

$$\begin{aligned}(.) = {} & \frac{\partial A}{\partial x}\left(\frac{B_2}{\rho} + 4\frac{B_3}{\rho}A + 9\frac{B_4}{\rho}A^2 + 2\frac{Q^2\beta(1-\beta)}{A^3}\right) + \\ & + \frac{A}{\rho}\left(\frac{dB_2}{dx} + 2A\frac{dB_3}{dx} + 3A^2\frac{dB_4}{dx}\right) + 2\frac{Q}{A^2}\beta(\beta-1)\frac{\partial Q}{\partial x} + \\ & - m^2\frac{\widehat{EI}}{\rho}\frac{A_b^m}{A^{m+1}}\frac{\partial A}{\partial x}\end{aligned} \tag{A.5}$$

$$
\begin{aligned}
&\frac{\partial \mathbf{U}}{\partial t} + \frac{\partial \mathbf{F}}{\partial x} + \mathbf{S} = \\
&\frac{\partial}{\partial t}\begin{pmatrix} A \\ Q \end{pmatrix} + \frac{\partial}{\partial x}\begin{pmatrix} F_1 \\ F_2 \end{pmatrix} + \begin{pmatrix} S_1 \\ S_2 \end{pmatrix} = \\
&= \frac{\partial}{\partial t}\begin{pmatrix} A \\ Q \end{pmatrix} + + \frac{\partial}{\partial x}\begin{pmatrix} Q \\ \beta \frac{Q^2}{A} + \sum_{j=2}^{4} \frac{(j-1A^j B_j)}{j\rho} - B_5\sqrt{A}\frac{\partial Q}{\partial x} - \widehat{EI}\frac{A}{\rho}\left(\frac{A_b^m}{A^m} - 1\right) + \frac{A}{\rho}p_b \end{pmatrix} + \\
&\begin{pmatrix} 0 \\ \sum_{j=1}^{4} \frac{dB_j}{dx} + \frac{B_5}{\rho\sqrt{A}}\frac{\partial A}{\partial x}\frac{\partial Q}{\partial x} + \frac{\widehat{EI}}{\rho}\left(\frac{A_b^m}{A^m} - 1\right)\frac{\partial A}{\partial x} - \frac{p_b}{\rho}\frac{\partial A}{\partial x} - N_4\frac{Q}{A} - Ag\sin\gamma\sin\alpha \end{pmatrix} = 0
\end{aligned}
\tag{A.6}
$$

Table A.1: Geometric features of the 1D arterial tree (l: vessel length, D_{in} : vessel inlet diameter, D_{out}: vessel outlet diameter, h_{wall}: vessel wall thickness, γ: vessel orientation with respect to the frontal transverse body axis, #e the number of elements used to discretize the corresponding vessel).

No.	Artery	l [mm]	D_{in} [mm]	D_{out} [mm]	h_{wall} [mm]	γ [°]	#e
1	Ascending Aorta I	10	29.40	29.30	1.63	-90	2
2	Aortic Arch I	20	24.10	24	1.32	0	4
3	Brachiocephalic Artery	34	19.40	18	0.86	-45	6
4/19	R/L Subclavian Artery I	34	12.90/11	9/8.5	0.67	-30/-45	6
5/15	R/L Common Carotid Artery	94/119	15.10/12.40	7/6	0.63	-90	10
6/20	R/L Vertebral Artery	149/148	4.10/3.80	2.80	0.45	-90	10
7/21	R/L Subclavian II, Axillary & Brachial Arteries	422	8.90/8.40	4.70	0.66	+90	10
8/22	R/L Radial Artery	235	3.70/3.30	3.10/2.80	0.43	+90	10
9/23	R/L Ulnar Artery I	67	3.70/4	3.40/4	0.49	+90	10
10/24	R/L Interosseous Artery	79	2.10/1.80	1.80	0.28	+90	10
11/25	R/L Ulnar Artery II	171	3.20/4.10	2.80/3.70	0.49	+90	10
12/16	R/L Internal Carotid Artery	178	5.70/5	4.30/4.30	0.39	-90	10
13/17	R/L External Carotid Artery	41	5/4.50	4.50/4.30	0.42	-90	6
14	Aortic Arch II	39	22	20.80	1.27	0	8
18	Thoracic Aorta I	52	20	18.90	1.20	+90	10
26	Intercostal Arteries	80	12.60	9.50	1.20	0	10
27	Thoracic Aorta II	104	16.50	12.90	1.16	+90	10
28	Abdominal Aorta I	53	12.20	12.20	1.08	+90	10
29	Celiac Artery I	20	7.80	6.90	0.64	0	4
30	Celiac Artery II	25	5.20	4.90	0.64	0	4
31	Hepatic Artery	66	5.40	4.40	0.49	0	10
32	Gastric Artery	71	3.20	3	0.45	-90	10
33	Splenic Artery	63	4.20	3.90	0.54	0	10
34	Superior Mesenteric Artery	59	7.90	7.10	0.69	+90	10
35	Abdominal Aorta II	20	11.50	11.30	0.8	+90	4
36/38	R/L Renal Artery	32	4.94	4.94/5.2	0.53	0	6
37	Abdominal Aorta III	20	11.20	11.20	0.8	+90	4
39	Abdominal Aorta IV	106	11	11	0.8	+90	10
40	Inferior Mesenteric Artery	50	4.70	3.20	0.43	+90	8
41	Abdominal Aorta V	20	10.80	10.40	0.8	+90	4
42	Common Iliac Artery	59	7.90	7	0.76	+45	10
43	Inner Iliac Artery	50	4	4	0.4	+45	8
44	External Iliac Artery	144	6.40	6.10	0.55	+90	10
45	Deep Femoral Artery	126	4	3.70	0.49	+90	10
46	Femoral Artery	443	5.20	3.80	0.5	+90	10
47	Anterior Tibial Artery	343	2.60	2.30	0.39	+90	10
48	Posterior Tibial Artery	321	3.10	2.80	0.45	+90	10
49	Left Main Coronary Artery	12	4.50	4.50	0.4	0	4
50	Left Anterior Descending Coronary Artery I	18	3.74	3.74	0.4	+60	4
51	Circumflex Coronary Artery I	32	3.60	3.60	0.4	+60	4
52	Marginal Coronary Artery	73	2.52	2.52	0.3	+90	6
53	Circumflex Coronary Artery II	43	3	3	0.2	+90	6
54	Diagonal Coronary Artery	65	2.40	2.40	0.3	+90	6
55	Left Anterior Descending Coronary Artery II	22	3.29	3.29	0.3	+90	6
56	Septal Coronary Artery II	45	2.39	2.39	0.2	0	6
57	Left Anterior Descending Coronary Artery III	100	2.72	2.72	0.3	+90	4
58	Right Coronary Artery I	50	4.05	4.05	0.4	+60	6
59	Acute Marginal Coronary Artery I	34	2.52	2.52	0.3	0	6
60	Right Coronary Artery II	48	3.55	3.55	0.4	+90	6
61	Acute Marginal Coronary Artery II	23	2.11	2.11	0.2	+60	6
62	Right Coronary Artery III (Posterior Descending Artery)	89	3.21	3.21	0.3	+60	8
63	Ascending Aorta II	30	29.3	28.8	1.63	-90	6

Appendix B

0D model settings and definitions

Table B.1: 0D arteriolar settings. R arteriolar resistance, C compliance, L inertance, V^{un} and V unstressed and total blood volume.

Arteriolar #id	R [mmHg s/ml]	C [mmHg/ml]	L [mmHg s/ml]	V^{un} [ml]	V [ml]
Vertebral 6/20	25.88	0.013	0.019	4.2	4.72
Radial 8/22	17.03	0.014	0.018	3.6	4.16
Interosseous 10/24	393.70	0.0009	0.070	3.6	3.63
Ulnar II 11/25	19.69	0.014	0.018	3.6	4.16
Internal Carotid 12/16	23.60	0.015	0.017	4.2	4.8
External Carotid 13/17	21.85	0.015	0.017	4.2	4.8
Intercostals 26	5.61	0.054	0.009	6.9	9.06
Hepatic 31	16.24	0.021	0.015	30.6	31.44
Gastric 32	8.91	0.033	0.012	9.3	10.62
Splenic 33	21.33	0.014	0.018	11.6	12.16
Superior Mesenteric 34	3.85	0.081	0.007	15.9	19.14
Renal 36/38	4.31	0.068	0.008	5.9	8.62
Inferior Mesenteric 40	30.74	0.011	0.02	11.9	12.34
Inner Iliac 43	23.48	0.014	0.018	3.5	4.06
Deep Femoral 45	13.37	0.023	0.014	14.4	15.32
Anterior Tibial 47	14.03	0.023	0.014	14.4	15.32
Posterior Tibial 48	30.44	0.010	0.021	14.4	14.80

Table B.2: 0D systemic and pulmonary circulation parameters values. R, C, L, V^{un} and V are lumped compartmental hydraulic resistance, compliance, inertance, unstressed volume and total blood volume, respectively. H, A, UA, LA and L refer to the head, arms, upper and lower abdomen and legs body regions. *svc*, *ivc* and *avc* are superior, inferior and abdominal veane cavae compartments, while *pa* and *pv* denote pulmonary arterial and venous compartments, respectively.

Compartment	R [mmHg s/ml]	C [mmHg/ml]	L [mmHg s/ml]	V^{un} [ml]	V [ml]
Capillary					
H	5.0048	0.0029	0.00150	2.50	2.58
A	1.8876	0.0058	0.00065	46.71	46.88
UA	1.0611	0.0121	0.00051	111.64	112.00
LA	0.5598	0.0226	0.00039	71.32	72.00
L	0.9550	0.0140	0.00037	56.86	57.28
Venule					
H	1.6038	0.0853	0.00260	8.67	9.69
A	0.6043	0.1780	0.00120	173.66	175.80
UA	0.3397	0.4470	0.00093	414.64	420.00
LA	0.1784	0.6760	0.00096	261.89	270.00
L	0.3061	0.5500	0.00061	208.20	214.80
Vein					
H	0.6653	0.91	0.00290	20.03	20.03
A	0.2200	3.71	0.00130	333.64	363.32
UA	0.0653	49.50	0.00100	515.20	868.00
LA	0.0455	23.80	0.00078	367.60	558.00
L	0.1422	18.00	0.00067	299.92	443.92
Vena Cava					
svc	0.00055	5.0	0.00005	30	60
ivc	0.00055	7.5	0.00005	55	100
avc	0.00055	7.5	0.00005	15	60
Pulmonary					
pa	0.08	3.8	-	44.3	89.9
pv	0.005	20.5	-	232.8	396.8

Table B.3: Anatomical length of head (H), arms (A), lower/upper abdomen (LA, UA), legs (L) venous and venae cavae (*svc*, *ivc*, *avc*) compartments.

Compartment	Length [m]
H	0.25
A	0.55
UA	0
LA	0
L	1.00
svc	0.07
ivc	0.15
avc	0.07

Table B.4: Parameter settings for the cardiac model, extracted from [74]. E_A, E_B are cardiac elastances amplitude and baseline values, V^{un}, V are unstressed and total chamber volumes, t_{ac}, T_{ac}, t_{ar}, T_{ar}, T_{vc}, T_{vr} denote atria and ventricles contraction/relaxation starting time and duration. R, L, B are valve's resistance, inertance and Bernoulli's coefficient, k_p, k_q, k_f, k_v indicate valve's geometric effects parameters (normalized by the valve's momentum of inertia).

Chamber	***ra***	***rv***	***la***	***lv***
E_A [ml/mmHg]	0.06	0.55	0.07	2.75
E_B [ml/mmHg]	0.14	0.08	0.11	0.10
V^{un} [ml]	6	12	6	7
V [ml]	91.9	116.3	109.9	109.4
t_{ac} [s]	$0.8RR$	-	$0.8RR$	-
T_{ac} [s]	$0.17RR$	-	$0.17RR$	-
t_{ar} [s]	$t_{ac} + T_{ac}$	-	$t_{ac} + T_{ac}$	-
T_{ar} [s]	T_{ac}	-	T_{ac}	-
T_{vc} [s]	-	$0.3\sqrt{RR}$	-	$0.3\sqrt{RR}$
T_{vr} [s]	-	$0.5T_{vc}$	-	$0.5T_{vc}$
Valve	***tv***	***puv***	***mv***	***aov***
$R_{va} \cdot 10^{-6}$ [mmHg s/ml]	4.5	4.5	4.5	4.5
$L_{va} \cdot 10^{-6}$ [mmHg s/ml]	3.75	3.75	3.75	3.75
$B_{va} \cdot 10^{-6}$ [mmHg s^2/ml^2]	4.80	5.67	4.80	5.67
$k_{p,va}$ [rad/(mmHg s^2)]	5500	5500	5500	5500
$k_{q,va}$ [rad/(ml s)]	2	2	2	2
$k_{f,va}$ [rad/(ml s)]	50	50	50	50
$k_{v,va}$ [rad/(ml s)]	3.5	3.5	3.5	3.5

Table B.5: 0D Coronary microvascular districts general parameter settings. p_{rv} and p_{lv} are right and left ventricular pressures, respectively.

Parameter	**Value**		
Region (G)	Right Ventricle	Septum	Left ventricle
Vessel No.	59, 61	56, 62	52, 53, 54, 57
W_G [hg] 0.46	0.54	1.04	
$R_{0,j,T,G}$ [mmHg s/ml]	[2903 , 2364 , 2030]	[934 , 827 , 719]	[1048 , 927 , 806]
γ_j	[0.31 , 0.33 , 0.36]	[0.31 , 0.33 , 0.36]	[0.31 , 0.33 , 0.36]
$\gamma_{CEP,j}$	[0.2 , 0.6 , 1] p_{rv}	[p_{rv} , $0.5(p_{rv} + p_{lv})$, p_{lv}]	[0.2 , 0.6 , 1] p_{lv}
$C_{1,T}$ [ml/(mmHg hg)]	0.026		
$C_{3,T}$ [ml/(mmHg hg)]	0.127		
$V_{0,1,T}$ [ml/hg]	2.5		
$V_{0,3,T}$ [ml/hg]	8		
ϕ_{SIP} [ml]	8.9		

Table B.6: Parameters values of 0D large cerebral arteries (R: resistances, C: compliances).

Parameter	Value
$R_{ICA,l}$	0.1707 mmHg s/ml
$R_{ICA,r}$	0.1707 mmHg s/ml
R_{BA}	0.1350 mmHg s/ml
$R_{MCA,l}$	0.4326 mmHg s/ml
$R_{MCA,r}$	0.4326 mmHg s/ml
$R_{PCA1,l}$	0.2292 mmHg s/ml
$R_{PCA1,r}$	0.2292 mmHg s/ml
$R_{ACA1,l}$	1.1374 mmHg s/ml
$R_{ACA1,r}$	1.1374 mmHg s/ml
$R_{PCA2,l}$	1.0819 mmHg s/ml
$R_{PCA2,r}$	1.0819 mmHg s/ml
$R_{ACA2,l}$	0.4868 mmHg s/ml
$R_{ACA2,r}$	0.4868 mmHg s/ml
$R_{PCoA,l}$	27.2936 mmHg s/ml
$R_{PCoA,r}$	27.2936 mmHg s/ml
R_{ACoA}	4.4768 mmHg s/ml
$C_{ICA,l}$	0.0034 ml/mmHg
$C_{ICA,r}$	0.0034 ml/mmHg
C_{BA}	0.0017 ml/mmHg

Table B.7: Parameters values of 0D distal arteries (R: resistances).

Parameter	Value
$R_{cam,l}$	105 mmHg s/ml
$R_{cam,r}$	105 mmHg s/ml
$R_{cpm,l}$	120 mmHg s/ml
$R_{cpm,r}$	120 mmHg s/ml
R_{caa}	22 mmHg s/ml
R_{cpp}	75 mmHg s/ml

Table B.8: Parameters values of 0D cerebral capillary-venous compartments (R: resistances, k: constants, p: pressures).

Parameter	Value
R_f	$2.3 \cdot 10^3$ mmHg s/ml
R_o	526.3 mmHg s/ml
R_{cv}	0.880 mmHg s/ml
R_{dvs1}	0.366 mmHg s/ml
k_E	0.077 ml^{-1}
k_{ven}	0.155 ml^{-1}
p_{v1}	-2.5 mmHg

Table B.9: Arterial baroreflex and cardiopulmonary reflex parameter settings. $E_{rv/lv,max}$ is maximum right/left ventricle elastance ($E_{rv/lv,A} + E_{rv/lv,B}$), subscript i for resistances, compliances and unstressed volumes indicates the corresponding body region (from head to legs). Each m-th organ-specific parameter is normalized by the initial value of the corresponding efferent organ variable (denoted by superscripts 0).

Arterial Baroreflex				
y_m	α_m	β_m	γ_m	τ_m
HR/HR^0	0.75	0.75	1.00	5
$E_{rv/lv,max}/E^0_{rv/lv,max}$	0.40	-	0.80	5
$R_{i,art/cap}/R^0_{i,art/cap}$	5.00	-	-1.50	10
$C_{i,ve/v}/C^0_{i,ve/v}$	-0.60	-	1.30	30
$V^{un}_{i,ve/v}/V^{un,0}_{i,ve/v}$	-0.40	-	1.20	30
Cardiopulmonary Reflex				
$y_{cp,m}$	$\alpha_{cp,m}$	$\beta_{cp,m}$	$\gamma_{cp,m}$	$\tau_{cp,m}$
$R_{cp,i,art/cap}/R^0_{cp,i,art/cap}$	2.50	-	-0.25	15
$C_{cp,i,ve/v}/C^0_{cp,i,ve/v}$	-0.60	-	1.30	30
$V^{un}_{cp,i,ve/v}/V^{un,0}_{cp,i,ve/v}$	-0.40	-	1.20	30

Table B.10: Parameters values of cerebral autoregulation and CO_2 reactivity control mechanisms (τ: time-delay parameters, G: gains, k, s and b: constants, Q: flow rates, C: compliances, p: pressures).

Parameter	Value
τ_{aut}	20 s
G_{aut}	0.9
τ_{CO_2}	40 s
G_{CO_2}	4.0
k_{CO_2}	15
b_{CO_2}	0.5
P_{aCO_2n}	40 mmHg
P_{aCO_2}	40 mmHg
s_1	7
s_2	0.4
$Q_{ndm,left}$	3.75 ml/s
$Q_{ndm,right}$	3.75 ml/s
$Q_{nda,left}$	1 ml/s
$Q_{nda,right}$	1 ml/s
$Q_{ndp,left}$	1.5 ml/s
$Q_{ndp,right}$	1.5 ml/s
$k_{R_{dm,left}}$	$3.4278 \cdot 10^{4}$ mmHg^{-3} s/ml
$k_{R_{dm,right}}$	$3.4278 \cdot 10^{4}$ mmHg^{-3} s/ml
$k_{R_{da,left}}$	$1.2848 \cdot 10^{5}$ mmHg^{-3} s/ml
$k_{R_{da,right}}$	$1.2848 \cdot 10^{5}$ mmHg^{-3} s/ml
$k_{R_{dp,left}}$	$0.8622 \cdot 10^{5}$ mmHg^{-3} s/ml
$k_{R_{dp,right}}$	$0.8622 \cdot 10^{5}$ mmHg^{-3} s/ml
$C_{d0m,left}$	0.06 ml/mmHg
$C_{d0m,right}$	0.06 ml/mmHg
$C_{d0a,left}$	0.016 ml/mmHg
$C_{d0a,right}$	0.016 ml/mmHg
$C_{d0p,left}$	0.024 ml/mmHg
$C_{d0p,right}$	0.024 ml/mmHg

Nomenclature

Roman Symbols

$\boldsymbol{g}$	gravity acceleration vector
Δh	fluid column hydrostatic height
$\mathbf{u}$	velocity vector
ϕ_{SIP}	SIP constant parameter
$\widehat{EI}$	normalized vessel flexural rigidity
A	local vessel cross-section area
A_b	buckling cross-section area
A_{eff}	compartment effective area
A_{in1D}	1D arterial inlet cross-section area
A_{out1D}	1D arterial outlet cross-section area
art, cap, ven, v, svc, ivc, avc	0D vascular districts
B	Bernoulli's coefficient
$B_1 \dots B_5$	pressure constitutive law coefficients
C	vessels compliance
c_0	local wave velocity
C_g	ocular globe compliances
$E_{ch,A}$	cardiac chamber's elastance amplitude
$E_{ch,B}$	cardiac chamber's elastance baseline value
E_{ch}	cardiac chamber's elastance function
e_{ch}	cardiac chamber's normalized shape-elastancee function
g_0	gravity acceleration magnitude on Earth
g_x	gravity vector $x - wise$ component
H, A, UA, LA, L	body 0D macro regions
k_{vc}	valve's closing rate
k_{vo}	valve's opening rate

L	vessels inertance
l_{eff}	compartment effective length
$L_{f\text{-}b}$	perpendicular distance between the globe and the mid-coronal plane
$L_{i,j}$	compartments characteristic vertical anatomical lengths
N_4	viscous coefficient
n_p	parasympathetic activity
n_s	sympathetic activity
p	blood pressure
p^t	vessels transmural pressure
p^{ext}	extravascular pressure
p_b	buckling cross-section pressure
p_{AA}	aotic arch pressure
p_{art0D}	0D arteriolar pressure
$p_{cs,R/L}$	right/left carotid sinus pressure
p_{dvs}	dural venous sinus pressure
p_{in1D}	1D arterial inlet pressure
p_{out1D}	1D arterial outlet pressure
p_{ra}	right atrial pressure
p_{svc}	superior vena cava pressure
Q	local blood flow rate
$Q_{a,eye}$	arterial eye inflow
Q_{ao}	aortic blood flow
$Q_{v,eye}$	venous eye outflow
R	vessels hydraulic resistance
r	cylindrical radial coordinate
r_v	local vessel radius
R_{eye}	eye hydraulic resistance
RR	heartbeat duration
t	time
u_r	cylindrical radial velocity component
$u_x \dots u_z$	velocity cartesian components
u_θ	cylindrical angular velocity component
V	vessels total blood volume

V^{un}	vessels unstressed blood volume
V_g	ocular globe volume
$x \dots z$	spatial cartesian coordinates
x_{ves}	vessel longitudinal axis
y_b	transverse body axis
z_b	longitudinal body axis
Z_c	characteristic impedance
EF	ejection fraction
P_{ic}	intracranial pressure (Chapter 6 nomenclature)
WI	wave intensity

Greek Symbols

α	tilt angle
β	Coriolis coefficient
γ	angle between vessel longitudinal axis and transverse body axis
$\lambda_{1,2}$	left,right characteristic lines
μ	blood dynamic viscosity
∇	nabla operator
ω	cardiac pulsation
ρ	blood density
θ	cylindrical angular coordinate

Acronyms / Abbreviations

BA	basilar artery
CBF	cerebral blood flow
CEP	cavity-induced extracellular pressure
cv	cerebral veins
EVP	episcleral venous pressure
ICA	internal carotid artery
IMP	intramyocardial pressure
MCA	middle cerebral artery
SIP	shortening-induced intracellular pressure
AI	augmentation index
AP	augmentation pressure
$ccap$	cerebral capillary

CO	cardiac output
CPP	coronary/cerebral perfusion pressure
CVP	central venous pressure
DAP	diastolic arterial pressure
HR	heart rate
ICP	intracranial pressure
IOP	intraocular pressure
IPP	intrapleural pressure
ITP	intrathoracic pressure
MAP	mean arterial pressure
PoR	point of reflection
PP	pulse pressure
$pulMAP$	pulmonary mean arterial pressure
PVA	pressure-volume area
RI	reflection index
RM	reflection magnitude
RPP	rate pressure product
RPP	rate pressure product
SAP	systolic arterial pressure
SV	stroke volume
SVR	systemic vascular resistance
SW	stroke work
TA	thoracic admittance
$TCVP$	transmural central venous pressure
TLP	translaminar pressure
ToR	time of reflection
TPR	total peripheral resistance
TTI	tension time index
AF	atrial fibrillation
BCW	backward compression wave
BSA	body surface area
CCA	common carotid artery
CI	cardiac index

COI	chronic orthostatic intolerance
CSF	cerebrospinal fluid
CVS	cardiovascular system
ENDO	subendocardium
EPI	subepicardium
EVA	extra vehicular activity
FCW	forward compression wave
FDW	forward decompression wave
HDBR	head-down bed rest
HDBS	head-down bed stress
HIP	hydrostatic indifference point
IJV	internal jugular vein
ISS	International Space Station
LAD	left anterior descendind coronary artery
LBNP	lower body negative pressure
LCx	left circumflex coronary artery
LMCA	left main coronary artery
MID	midwall
OH	orthostatic hypotesion
PWV	pulse wave velocity
RCA	right coronary artery
RMCA	right main coronary artery
rSAS	retrobulbar subarachnoid space
SANS	spaceflight-associated neuro ocular syndrome
SR	sinus rhythm
WI	water immersion

Bibliography

[1] Shima Abdullateef, Jorge Mariscal-Harana, and Ashraf W Khir. "Impact of tapering of arterial vessels on blood pressure, pulse wave velocity, and wave intensity analysis using one-dimensional computational model". In: *International Journal for Numerical Methods in Biomedical Engineering* 37.11 (2021), e3312. DOI: `10.1002/cnm.3312`.

[2] Jordi Alastruey et al. "Lumped parameter outflow models for 1-D blood flow simulations: effect on pulse waves and parameter estimation". In: *Communications in Computational Physics* 4.2 (2008), pp. 317–336. URL: `https://global-sci.org/intro/article_detail/cicp/7792.html`.

[3] Noam Alperin et al. "Role of cerebrospinal fluid in spaceflight-induced ocular changes and visual impairment in astronauts". In: *Radiology* 285.3 (2017), p. 1063. DOI: `10.1148/radiol.2017174039`.

[4] Allison P Anderson et al. "Acute effects of changes to the gravitational vector on the eye". In: *Journal of Applied Physiology* 120.8 (2016), pp. 939–946. DOI: `10.1152/japplphysiol.00730.2015`.

[5] Morten Andresen et al. "Effect of postural changes on ICP in healthy and ill subjects". In: *Acta Neurochirurgica* 157 (2015), pp. 109–113. DOI: `10.1007/s00701-014-2250-2`.

[6] Matteo Anselmino et al. "A computational study on the relation between resting heart rate and atrial fibrillation hemodynamics under exercise". In: *PloS One* 12.1 (2017), e0169967. DOI: `10.1371/journal.pone.0169967`.

[7] Matteo Anselmino et al. "Rate control management of atrial fibrillation: may a mathematical model suggest an ideal heart rate?" In: *PloS One* 10.3 (2015), e0119868. DOI: `10.1371/journal.pone.0119868`.

[8] Matteo Anselmino et al. "Transient cerebral hypoperfusion and hypertensive events during atrial fibrillation: a plausible mechanism for cognitive impairment". In: *Scientific Reports* 6.1 (2016), p. 28635. DOI: `10.1038/srep28635`.

[9] D Antle et al. “Lower limb blood flow and mean arterial pressure during standing and seated work: Implications for workplace posture recommendations”. In: *Preventive Medicine Reports* 10 (2018), pp. 117–122. DOI: `10.1016/j.pmedr.2018.02.016`.

[10] Ana Diaz Artiles, Thomas Heldt, and Laurence R Young. “Effects of artificial gravity on the cardiovascular system: computational approach”. In: *Acta Astronautica* 126 (2016), pp. 395–410. DOI: `10.1016/j.actaastro.2016.05.005`.

[11] E Asmussen. “The distribution of the blood between the lower extremities and the rest of body”. In: *Acta Physiologica Scandinavica* 5.1 (1943), pp. 31–38. DOI: `10.1111/j.1748-1716.1943.tb02030.x`.

[12] André E Aubert et al. “What happens to the human heart in space?-parabolic flights provide some answers”. In: *ESA Bulletin* 119 (2004), pp. 30–38. URL: `https://ui.adsabs.harvard.edu/abs/2004ESABu.119...30A`.

[13] Alberto Avolio, Mark Butlin, and Ke Xu. “Reflections on determinants of augmentation index”. In: *Journal of Hypertension* 30.2 (2012), pp. 267–268. DOI: `10.1097/HJH.0b013e32834f96e0`.

[14] Alberto Avolio and Gianfranco Parati. “Reflecting on posture”. In: *Journal of hypertension* 29.4 (2011), pp. 655–657. DOI: `10.1097/HJH.0b013e328345852a`.

[15] Giuseppe Barisano et al. “The effect of prolonged spaceflight on cerebrospinal fluid and perivascular spaces of astronauts and cosmonauts”. In: *Proceedings of the National Academy of Sciences* 119.17 (2022), e2120439119. DOI: `10.1073/pnas.2120439119`.

[16] Grant Alexander Bateman and Alexander Robert Bateman. “A perspective on spaceflight associated neuro-ocular syndrome causation secondary to elevated venous sinus pressure”. In: *npj Microgravity* 8.1 (2022), p. 3. DOI: `10.1038/s41526-022-00188-6`.

[17] Paula Beck et al. “Modeling human orthostatic responses on the Moon and on Mars”. In: *Clinical Autonomic Research* 28.3 (2018), pp. 325–332. DOI: `10.1007/s10286-018-0527-x`.

[18] Frank Beckers et al. “Parasympathetic heart rate modulation during parabolic flights”. In: *European Journal of Applied Physiology* 90.1 (2003), pp. 83–91. DOI: `10.1007/s00421-003-0854-y`.

[19] J Gordon Betts et al. *Anatomy and physiology. OpenStax*. Accessed: 10.11.2020. 2013. URL: `https://openstax.org/details/books/anatomy-and-physiology-2e`.

[20] Nana-Yaw Bimpong-Buta et al. “Comprehensive Analysis of Macrocirculation and Microcirculation in Microgravity During Parabolic Flights”. In: *Frontiers in Physiology* (2020), p. 960. DOI: `10.3389/fphys.2020.00960`.

[21] Elizabeth Blaber, Helder Marçal, and Brendan P Burns. "Bioastronautics: the influence of microgravity on astronaut health". In: *Astrobiology* 10.5 (2010), pp. 463–473. DOI: `10.1089/ast.2009.0415`.

[22] P Blanco and R Feijóo. "A dimensionally-heterogeneous closed-loop model for the cardiovascular system and its applications". In: *Medical Engineering & Physics* 35.5 (2013), pp. 652–667. DOI: `10.1016/j.medengphy.2012.07.011`.

[23] C Gunnar Blomqvist and H Lowell Stone. "Cardiovascular adjustments to gravitational stress". In: *NASA. Lyndon B. Johnson Space Center, Spacelab Life Sciences 1: Reprints of Background Life Sciences Publications* (1991). URL: `https://ntrs.nasa.gov/citations/19910016260`.

[24] C Gunnar Blomqvist et al. "Early cardiovascular adaptation to zero gravity simulated by head-down tilt". In: *Acta Astronautica* 7.4 (1980), pp. 543–553. DOI: `10.1016/0094-5765(80)90043-0`.

[25] Bas van den Bogaard et al. "Arterial wave reflection decreases gradually from supine to upright". In: *Blood Pressure* 20.6 (2011), pp. 370–375. DOI: `10.3109/08037051.2011.588484`.

[26] PM Brodrick and GS Ingram. "The antigravity suit in neurosurgery: cardiovascular responses in seated neurosurgical patients". In: *Anaesthesia* 43.9 (1988), pp. 762–765. DOI: `10.1111/j.1365-2044.1988.tb05751.x`.

[27] M Broomé et al. "Closed-loop real-time simulation model of hemodynamics and oxygen transport in the cardiovascular system". In: *Biomedical Engineering Online* 12.1 (2013), pp. 1–20. DOI: `10.1186/1475-925X-12-69`.

[28] A Bryan, J Milic-Emili, and D Pengelly. "Effect of gravity on the distribution of pulmonary ventilation". In: *Journal of Applied Physiology* 21.3 (1966), pp. 778–784. DOI: `10.1152/jappl.1966.21.3.778`.

[29] JC Buckey Jr et al. "Central venous pressure in space". In: *Journal of Applied Physiology* 81.1 (1996), pp. 19–25. DOI: `10.1152/jappl.1996.81.1.19`.

[30] A Buda, G MacKenzie, and E Wigle. "Effect of negative intrathoracic pressure on left ventricular outflow tract obstruction in muscular subaortic stenosis". In: *Circulation* 63.4 (1981), pp. 875–881. DOI: `10.1161/01.CIR.63.4.875`.

[31] W Buhre et al. "Effects of the sitting position on the distribution of blood volume in patients undergoing neurosurgical procedures". In: *British Journal of Anaesthesia* 84.3 (2000), pp. 354–357. DOI: `10.1093/oxfordjournals.bja.a013439`.

[32] Jeff Burkey. “Mann-Kendall Tau-b with Sen’s Method (enhanced)”. In: *MATLAB Central File Exchange* (2023). Accessed: June 14, 2023. URL: https://www.mathworks.com/matlabcentral/fileexchange/11190-mann-kendall-tau-b-with-sen-s-method-enhanced.

[33] Enrico Gianluca Caiani et al. “The role of echocardiography in the assessment of cardiac function in weightlessness—Our experience during parabolic flights”. In: *Respiratory Physiology & Neurobiology* 169 (2009), S6–S9. DOI: 10.1016/j.resp.2009.07.007.

[34] C van Campen et al. “Cerebral blood flow changes during tilt table testing in healthy volunteers, as assessed by Doppler imaging of the carotid and vertebral arteries”. In: *Clinical neurophysiology practice* 3 (2018), pp. 91–95. DOI: 10.1016/j.cnp.2018.02.004.

[35] Keirh H Carlson et al. “Effect of body position on intraocular pressure and aqueous flow.” In: *Investigative Ophthalmology & Visual Science* 28.8 (1987), pp. 1346–1352. URL: https://iovs.arvojournals.org/article.aspx?articleid=2160155.

[36] W Cheshire and D Goldstein. “Autonomic uprising: the tilt table test in autonomic medicine”. In: *Clinical Autonomic Research* 29.2 (2019), pp. 215–230. DOI: 10.1007/s10286-019-00598-9.

[37] K Chin and R Panerai. “Comparative study of Finapres devices”. In: *Blood Pressure Monitoring* 17.4 (2012), pp. 171–178. DOI: 10.1097/MBP.0b013e328356e1b3.

[38] Christophe Chiquet et al. “Changes in intraocular pressure during prolonged (7-day) head-down tilt bedrest”. In: *Journal of Glaucoma* 12.3 (2003), pp. 204–208. DOI: 10.1097/00061198-200306000-00004.

[39] Ki-young Chung et al. “Diurnal pattern of intraocular pressure is affected by microgravity when measured in space with the pressure phosphene tonometer (PPT)”. In: *Journal of Glaucoma* 20.8 (2011), pp. 488–491. DOI: 10.1097/IJG.0b013e3181f464d2.

[40] David M Clark et al. “Hemodynamic effects of an irregular sequence of ventricular cycle lengths during atrial fibrillation”. In: *Journal of the American College of Cardiology* 30.4 (1997), pp. 1039–1045. DOI: 10.1016/S0735-1097(97)00254-4.

[41] Gilles Clément. *Fundamentals of space medicine*. Vol. 23. Springer Science & Business Media, 2011. DOI: 10.1007/978-1-4419-9905-4.

[42] William H Cooke, Guy L Pellegrini, and Olga A Kovalenko. “Dynamic cerebral autoregulation is preserved during acute head-down tilt”. In: *Journal of Applied Physiology* 95.4 (2003), pp. 1439–1445. DOI: 10.1152/japplphysiol.00524.2003.

[43] T Coonan and C Hope. “Cardio-respiratory effects of change of body position”. In: *Canadian Anaesthetists’ Society Journal* 30.4 (1983), pp. 424–437. DOI: `10.1007/BF03007869`.

[44] Richard Courant and David Hilbert. *Methods of mathematical physics: partial differential equations*. John Wiley & Sons, 2008. DOI: `10.1002/9783527617210`.

[45] L Critchley et al. “Non-invasive continuous arterial pressure, heart rate and stroke volume measurements during graded head-up tilt in normal man”. In: *Clinical Autonomic Research* 7.2 (1997), pp. 97–101. DOI: `10.1007/BF02267754`.

[46] Ronita L Cromwell et al. “Overview of the NASA 70-day bed rest study”. In: *Medicine and Science in Sports and Exercise* 50.9 (2018), p. 1909. DOI: `10.1249/MSS.0000000000001617`.

[47] Marek Czosnyka et al. “Cerebrospinal fluid dynamics”. In: *Physiological Measurement* 25.5 (2004), R51. DOI: `10.1088/0967-3334/25/5/R01`.

[48] M Danielsen and J Ottesen. “A baroreceptor model”. In: *Applied Mathematical Models in Human Physiology*. SIAM, 2004, pp. 157–196.

[49] Justin E Davies et al. “Attenuation of wave reflection by wave entrapment creates a “horizon effect” in the human aorta”. In: *Hypertension* 60.3 (2012), pp. 778–785. DOI: `10.1161/HYPERTENSIONAHA.111.180604/-/DC1.`.

[50] Justin E Davies et al. “Evidence of a dominant backward-propagating “suction” wave responsible for diastolic coronary filling in humans, attenuated in left ventricular hypertrophy”. In: *Circulation* 113.14 (2006), pp. 1768–1778. DOI: `10.1161/CIRCULATIONAHA.105.603050`.

[51] Shyrin CAT Davis et al. “Active standing reduces wave reflection in the presence of increased peripheral resistance in young and old healthy individuals”. In: *Journal of Hypertension* 29.4 (2011), pp. 682–689. DOI: `10.1097/HJH.0b013e328343cda9`.

[52] S De Cort, J Innes, and A Guz. “Effect of positive and negative step changes in intrathoracic pressure on left ventricular function in conscious man”. In: *The Journal of Physiology* 472.1 (1993), pp. 513–520. DOI: `https://doi.org/10.1113/jphysiol.1993.sp019959`.

[53] L Dell’Italia and R Walsh. “Application of a time varying elastance model to right ventricular performance in man”. In: *Cardiovascular Research* 22.12 (1988), pp. 864–874. DOI: `10.1093/cvr/22.12.864`.

[54] Ana Diaz-Artiles, Thomas Heldt, and Laurence R Young. “Computational model of cardiovascular response to centrifugation and lower body cycling exercise”. In: *Journal of Applied Physiology* 127.5 (2019), pp. 1453–1468. DOI: `10.1152/japplphysiol.00314.2019`.

[55] J Draeger et al. "Self-tonometry under microgravity conditions". In: *The Clinical Investigator* 71 (1993), pp. 700–703. DOI: 10.1007/BF00209723.

[56] Gary Drzewiecki et al. "Vessel growth and collapsible pressure-area relationship". In: *American Journal of Physiology-Heart and Circulatory Physiology* 273.4 (1997), H2030–H2043. DOI: 10.1152/ajpheart.1997.273.4.H2030.

[57] Jichen Du et al. "Alterations in cerebral hemodynamics during microgravity: A literature review". In: *Medical Science Monitor: International Medical Journal of Experimental and Clinical Research* 27 (2021), e928108–1. DOI: 10.12659/MSM.928108.

[58] Delafield Du Bois and Eugene F Du Bois. "Clinical calorimetry: tenth paper a formula to estimate the approximate surface area if height and weight be known". In: *Archives of Internal Medicine* 17.6_2 (1916), pp. 863–871. DOI: 10.1001/archinte.1916.00080130010002.

[59] Dirk J Duncker and Robert J Bache. "Regulation of coronary blood flow during exercise". In: *Physiological Reviews* 88.3 (2008), pp. 1009–1086. DOI: 10.1152/physrev.00045.2006.

[60] Łukasz Dziuda et al. "Development and evaluation of a novel system for inducing orthostatic challenge by tilt tests and lower body negative pressure". In: *Scientific Reports* 8.1 (2018), p. 7793. DOI: 10.1038/s41598-018-26173-2.

[61] H Edgell, A Robertson, and R Hughson. "Hemodynamics and brain blood flow during posture change in younger women and postmenopausal women compared with age-matched men". In: *Journal of Applied Physiology* 112.9 (2012), pp. 1482–1493. DOI: 10.1152/japplphysiol.01204.2011.

[62] Karen Brastad Evensen and Per Kristian Eide. "Measuring intracranial pressure by invasive, less invasive or non-invasive means: limitations and avenues for improvement". In: *Fluids and Barriers of the CNS* 17.1 (2020), pp. 1–33. DOI: 10.1186/s12987-020-00195-3.

[63] FMS. "Finapres Medical Systems non-invasive hemodynamic". In: (2021). Accessed: 18.06.2021. URL: https://www.finapres.com/.

[64] Matteo Fois, Luca Ridolfi, and Stefania Scarsoglio. "Arterial wave dynamics preservation upon orthostatic stress: a modelling perspective". In: *Royal Society Open Science* 10.3 (2023), p. 221257. DOI: 10.1098/rsos.221257.

[65] Matteo Fois, Luca Ridolfi, Stefania Scarsoglio, et al. "Cardiovascular response to orthostatic stress: multiscale modeling with focus on the coronary circulation". In: *CMBE22-7 th International Conference on Computational & Mathematical Biomedical Engineering.* Vol. 1. ISBN: 978-0-9562914-6-2. Computational and scientific consultancy services Ltd. 2022, pp. 336–339.

[66] Matteo Fois, Luca Ridolfi, and Stefania Scarsoglio. “In silico study of the posture-dependent cardiovascular performance during parabolic flights”. In: *Acta Astronautica* 200 (2022), pp. 435–447. DOI: `10.1016/j.actaastro.2022.08.018`.

[67] Matteo Fois et al. “An in silico-in vivo framework for the acute ocular and cardiovascular response to 6° head-down tilt”. In: *ESB-ITA 2023 - XII Annual Meeting of the Italian Chapter of the European Society of Biomechanics, Turin*. 2023.

[68] Matteo Fois et al. “Cardiovascular Response to Posture Changes: Multiscale Modeling and in vivo Validation During Head-Up Tilt”. In: *Frontiers in Physiology* 13 (2022). DOI: `10.3389/fphys.2022.826989`.

[69] Matteo Fois et al. “Linking cerebral hemodynamics and ocular microgravity-induced alterations through an in silico-in vivo head-down tilt framework”. In: *npj Microgravity* 10.22 (2024). DOI: `10.1038/s41526-024-00366-8`.

[70] Luca Formaggia, Daniele Lamponi, and Alfio Quarteroni. “One-dimensional models for blood flow in arteries”. In: *Journal of Engineering Mathematics* 47 (2003), pp. 251–276. DOI: `10.1023/B:ENGI.0000007980.01347.29`.

[71] Luca Formaggia et al. “Numerical modeling of 1D arterial networks coupled with a lumped parameters description of the heart”. In: *Computer Methods in Biomechanics and Biomedical Engineering* 9.5 (2006), pp. 273–288. DOI: `10.1080/10255840600857767`.

[72] Kenneth James Franklin. “Valves in veins: an historical survey”. In: *Proceedings of the Royal Society of Medicine* 21.1 (1927), pp. 1–33. DOI: `10.1177/003591572702100101`.

[73] Branko Furst. “The effect of gravity and upright posture on circulation”. In: *The Heart and Circulation: An Integrative Model*. Springer, Cham, 2020, pp. 319–341. DOI: `10.1007/978-3-030-25062-1_24`.

[74] C Gallo. “A multiscale modelling of the cardiovascular fluid dynamics for clinical and space applications”. PhD thesis. Politecnico di Torino, 2021.

[75] C Gallo et al. “Testing a patient-specific in-silico model to noninvasively estimate central blood pressure”. In: *Cardiovascular Engineering and Technology* 12.2 (2021), pp. 144–157. DOI: `10.1007/s13239-020-00512-9`.

[76] Caterina Gallo, Luca Ridolfi, and Stefania Scarsoglio. “Cardiovascular deconditioning during long-term spaceflight through multiscale modeling”. In: *npj Microgravity* 6.1 (2020), p. 27. DOI: `10.1038/s41526-020-00117-5`.

[77] W James Gardner and Donald F Dohn. “The antigravity suit (G-suit) in surgery: Control of blood pressure in the sitting position and in hypotensive anesthesia”. In: *Journal of the American Medical Association* 162.4 (1956), pp. 274–276. DOI: `10.1001/jama.1956.72970210001006`.

[78] Z Garrett, J Pearson, and A Subudhi. “Postural effects on cerebral blood flow and autoregulation”. In: *Physiological Reports* 5.4 (2017), e13150. DOI: 10.14814/phy2.13150.

[79] Manuel Gehlen, Vartan Kurtcuoglu, and Marianne Schmid Daners. “Is posture-related craniospinal compliance shift caused by jugular vein collapse? A theoretical analysis”. In: *Fluids and Barriers of the CNS* 14 (2017), pp. 1–11. DOI: 10.1186/s12987-017-0053-6.

[80] Benjamin Gerber et al. “A computer simulation of short-term adaptations of cardiovascular hemodynamics in microgravity”. In: *Computers in Biology and Medicine* 102 (2018), pp. 86–94. DOI: 10.1016/j.compbiomed.2018.09.014.

[81] D Goldstein. *Principles of autonomic medicine.* e-book online resource, 2017. DOI: https://doi.org/10.1002/j.1552-4604.1994.tb04977.x.

[82] Adam G Goodwill et al. “Regulation of coronary blood flow”. In: *Comprehensive Physiology* 7.2 (2017), p. 321. DOI: 10.1002/cphy.c160016.

[83] N Goswami et al. “Teaching fluid shifts during orthostasis using a classic paper by Foux et al.” In: *Advances in Physiology Education* 35.4 (2011), pp. 330–335. DOI: 10.1152/advan.00071.2011.

[84] Nandu Goswami et al. “Lower body negative pressure: physiological effects, applications, and implementation”. In: *Physiological Reviews* 99.1 (2019), pp. 807–851. DOI: 10.1152/physrev.00006.2018.

[85] Nandu Goswami et al. “Short-arm human centrifugation with 0.4 g at eye and 0.75 g at heart level provides similar cerebrovascular and cardiovascular responses to standing”. In: *European Journal of Applied Physiology* 115 (2015), pp. 1569–1575. DOI: 10.1007/s00421-015-3142-8.

[86] Marlene S Grenon et al. “Why is orthostatic tolerance lower in women than in men? Renal and cardiovascular responses to simulated microgravity and the role of midodrine”. In: *Journal of Investigative Medicine* 54.4 (2006), pp. 180–190. DOI: 10.2310/6650.2006.05064.

[87] AI Grigoriev, AR Kotovskaya, and GA Fomina. “The human cardiovascular system during space flight”. In: *Acta Astronautica* 68.9-10 (2011), pp. 1495–1500. DOI: 10.1016/j.actaastro.2009.11.013.

[88] ESC Scientific Document Group et al. “2020 ESC Guidelines for the diagnosis and management of atrial fibrillation developed in collaboration with the European Association of Cardio-Thoracic Surgery (EACTS)”. In: *European Heart Journal* (2020). DOI: 10.1093/eurheartj/ehaa612.

[89] Andrea Guala et al. “Modelling and subject-specific validation of the heart-arterial tree system”. In: *Annals of Biomedical Engineering* 43.1 (2015), pp. 222–237. DOI: 10.1007/s10439-014-1163-9.

[90] I Guelen et al. “Finometer, finger pressure measurements with the possibility to reconstruct brachial pressure”. In: *Blood Pressure Monitoring* 8.1 (2003), pp. 27–30. DOI: `10.1097/00126097-200302000-00006`.

[91] Hanns-Christian Gunga et al. “The Cardiovascular System in Space”. In: *Cardiovascular system, red blood cells, and oxygen transport in microgravity*. Springer, 2016. Chap. 2, pp. 11–34. DOI: `10.1007/978-3-319-33226-0`.

[92] John E Hall and Michael E Hall. *Guyton and Hall textbook of medical physiology 12th Edition*. ISBN: 978-1-4160-4574-8. Elsevier Health Sciences, 2011.

[93] T Heldt. “Computational models of cardiovascular response to orthostatic stress”. PhD thesis. Massachusetts Institute of Technology, 2004. DOI: `/hdl.handle.net/1721.1/28761`.

[94] Thomas Heldt et al. “Computational modeling of cardiovascular response to orthostatic stress”. In: *Journal of Applied Physiology* 92.3 (2002), pp. 1239–1254. DOI: `10.1152/japplphysiol.00241.2001`.

[95] K van Heusden et al. “Mathematical modeling of gravitational effects on the circulation: importance of the time course of venous pooling and blood volume changes in the lungs”. In: *American Journal of Physiology-Heart and Circulatory Physiology* 291.5 (2006), H2152–H2165. DOI: `10.1152/ajpheart.01268.2004`.

[96] H Hinghofer-Szalkay. “Gravity, the hydrostatic indifference concept and the cardiovascular system”. In: *European Journal of Applied Physiology* 111.2 (2011), pp. 163–174. DOI: `10.1007/s00421-010-1646-9`.

[97] Petter Holmlund et al. “Human jugular vein collapse in the upright posture: implications for postural intracranial pressure regulation”. In: *Fluids and Barriers of the CNS* 14 (2017), pp. 1–7. DOI: `10.1186/s12987-017-0065-2`.

[98] Petter Holmlund et al. “Venous collapse regulates intracranial pressure in upright body positions”. In: *American Journal of Physiology-Regulatory, Integrative and Comparative Physiology* 314.3 (2018), R377–R385. DOI: `10.1152/ajpregu.00291.2017`.

[99] Alex S Huang, Michael B Stenger, and Brandon R Macias. “Gravitational influence on intraocular pressure: implications for spaceflight and disease”. In: *Journal of Glaucoma* 28.8 (2019), p. 756. DOI: `10.1097/IJG.0000000000001293`.

[100] Alun D Hughes and Kim H Parker. “Forward and backward waves in the arterial system: impedance or wave intensity analysis?” In: *Medical & Biological Engineering & Computing* 47.2 (2009), pp. 207–210. DOI: `10.1007/s11517-009-0444-1`.

[101] William E Hughes and Darren P Casey. “Aortic wave reflection during orthostatic challenges: influence of body position and venous pooling”. In: *American Journal of Hypertension* 30.2 (2017), pp. 166–172. DOI: `10.1093/ajh/hpw138`.

[102] Auke MT Huijben et al. “Aortic augmentation index and pulse wave velocity in response to head-up tilting: effect of autonomic failure”. In: *Journal of Hypertension* 30.2 (2012), pp. 307–314. DOI: `10.1097/HJH.0b013e32834f09ee`.

[103] Y Ishbulatov et al. “Mathematical modeling of the cardiovascular autonomic control in healthy subjects during a passive head-up tilt test”. In: *Scientific Reports* 10.1 (2020), pp. 1–11. DOI: `10.1038/s41598-020-71532-7`.

[104] H Ito et al. “Database of normal human cerebral blood flow, cerebral blood volume, cerebral oxygen extraction fraction and cerebral metabolic rate of oxygen measured by positron emission tomography with 15 O-labelled carbon dioxide or water, carbon monoxide and oxygen: a multicentre study in Japan”. In: *European Journal of Nuclear Medicine and Molecular Imaging* 31.5 (2004), pp. 635–643. DOI: `10.1007/s00259-003-1430-8`.

[105] Ken ichi Iwasaki et al. “Cerebral circulation during mild+ Gz hypergravity by short-arm human centrifuge”. In: *Journal of Applied Physiology* 112.2 (2012), pp. 266–271. DOI: `10.1152/japplphysiol.01232.2011`.

[106] R Jacob, B Dierberger, and G Kissling. “Functional significance of the Frank-Starling mechanism under physiological and pathophysiological conditions”. In: *European Heart Journal* 13.suppl_E (1992), pp. 7–14. DOI: `10.1093/eurheartj/13.suppl_E.7`.

[107] Steven Jillings et al. “Macro-and microstructural changes in cosmonauts’ brains after long-duration spaceflight”. In: *Science Advances* 6.36 (2020), eaaz9488. DOI: `10.1126/sciadv.aaz9488`.

[108] A Jose and D Collison. “The normal range and determinants of the intrinsic heart rate in man”. In: *Cardiovascular Research* 4.2 (1970), pp. 160–167. DOI: `10.1093/cvr/4.2.160`.

[109] L Karpeles and R Huff. “Blood volume of representative portions of the musculoskeletal system in man”. In: *Circulation Research* 3.5 (1955), pp. 483–489. DOI: `10.1161/01.RES.3.5.483`.

[110] J Keijsers et al. “A 1D pulse wave propagation model of the hemodynamics of calf muscle pump function”. In: *International Journal for Numerical Methods in Biomedical Engineering* 31.7 (2015), e02714. DOI: `10.1002/cnm.2714`.

[111] J Keijsers et al. “Global sensitivity analysis of a model for venous valve dynamics”. In: *Journal of Biomechanics* 49.13 (2016), pp. 2845–2853. DOI: `10.1016/j.jbiomech.2016.06.029`.

[112] Marc Kermorgant et al. "Effects of venoconstrictive thigh cuffs on dry immersion-induced ophthalmological changes". In: *Frontiers in Physiology* 12 (2021), p. 692361. DOI: 10.3389/fphys.2021.692361.

[113] AW Khir and Kim H Parker. "Measurements of wave speed and reflected waves in elastic tubes and bifurcations". In: *Journal of Biomechanics* 35.6 (2002), pp. 775–783. DOI: 10.1016/S0021-9290(02)00025-8.

[114] Richard E. Klabunde. *Factors Promoting Venous Return - Respiratory Activity.* Accessed: 16.04.2021. 2016. URL: https://www.cvphysiology.com/Cardiac%5C%20Function/CF018.

[115] GE Kochiadakis et al. "Effect of acute atrial fibrillation on phasic coronary blood flow pattern and flow reserve in humans". In: *European Heart Journal* 23.9 (2002), pp. 734–741. DOI: 10.1053/euhj.2001.2894.

[116] George E Kochiadakis and Eleftherios M Kallergis. "Impact of atrial fibrillation on coronary blood flow: a systematic review". In: *Journal of Atrial Fibrillation* 5.3 (2012). DOI: 10.4022/jafib.458.

[117] Bruce M Koeppen and Bruce A Stanton. *Berne and Levy physiology 7th Edition.* ISBN: 978-0-323-39394-2. Elsevier Health Sciences, 2018.

[118] T Korakianitis and Y Shi. "Numerical simulation of cardiovascular dynamics with healthy and diseased heart valves". In: *Journal of Biomechanics* 39.11 (2006), pp. 1964–1982. DOI: 10.1016/j.jbiomech.2005.06.016.

[119] Jelena Kornej et al. "Epidemiology of atrial fibrillation in the 21st century: novel methods and new insights". In: *Circulation research* 127.1 (2020), pp. 4–20. DOI: 10.1161/CIRCRESAHA.120.316340.

[120] K Kosugi et al. "Posture-induced changes in the vessels of the head and neck: evaluation using conventional supine CT and upright CT". In: *Scientific Reports* 10.1 (2020), pp. 1–12. DOI: 10.1038/s41598-020-73658-0.

[121] Charles Laing et al. "Effect of novel short-arm human centrifugation-induced gravitational gradients upon cardiovascular responses, cerebral perfusion and g-tolerance". In: *The Journal of Physiology* 598.19 (2020), pp. 4237–4249. DOI: 10.1113/JP273615.

[122] N Lassen. "Cerebral blood flow and oxygen consumption in man". In: *Physiological Reviews* 39.2 (1959), pp. 183–238. DOI: 10.1152/physrev.1959.39.2.183.

[123] K Lau and C Figueroa. "Simulation of short-term pressure regulation during the tilt test in a coupled 3D–0D closed-loop model of the circulation". In: *Biomechanics and Modeling in Mechanobiology* 14.4 (2015), pp. 915–929. DOI: 10.1007/s10237-014-0645-x.

[124] Stéphane Laurent et al. “Aortic stiffness is an independent predictor of all-cause and cardiovascular mortality in hypertensive patients”. In: *Hypertension* 37.5 (2001), pp. 1236–1241. DOI: `10.1161/01.HYP.37.5.1236`.

[125] Steven S Laurie et al. “Effects of short-term mild hypercapnia during head-down tilt on intracranial pressure and ocular structures in healthy human subjects”. In: *Physiological Reports* 5.11 (2017), e13302. DOI: `10.14814/phy2.13302`.

[126] Steven S Laurie et al. “Optic disc edema after 30 days of strict head-down tilt bed rest”. In: *Ophthalmology* 126.3 (2019), pp. 467–468. DOI: `10.1016/j.ophtha.2018.09.042`.

[127] Steven S Laurie et al. “Risk of Spaceflight Associated Neuro-ocular Syndrome (SANS)”. In: *NASA Human Research Program - Human Health Countermeasures Element*. National Aeronautics and Space Administration, Lyndon B. Johnson Space Center, Houston, Texas, 2022. URL: `https://humanresearchroadmap.nasa.gov/risks/risk.aspx?i=105`.

[128] Justin S Lawley et al. “Effect of gravity and microgravity on intracranial pressure”. In: *The Journal of Physiology* 595.6 (2017), pp. 2115–2127. DOI: `10.1113/JP273557`.

[129] Andrew G Lee et al. “Space flight-associated neuro-ocular syndrome (SANS)”. In: *Eye* 32.7 (2018), pp. 1164–1167. DOI: `10.1038/s41433-018-0070-y`.

[130] Andrew G Lee et al. “Spaceflight associated neuro-ocular syndrome (SANS) and the neuro-ophthalmologic effects of microgravity: a review and an update”. In: *npj Microgravity* 6.1 (2020), p. 7. DOI: `10.1038/s41526-020-0097-9`.

[131] R Leggett and L Williams. “Suggested reference values for regional blood volumes in humans”. In: *Health Physics* 60.2 (1991), pp. 139–154. DOI: `10.1097/00004032-199102000-00001`.

[132] J Rodney Levick. *An introduction to cardiovascular physiology.* ISBN: 0-750-61028-X. Butterworth-Heinemann, 1991.

[133] Ye Li, Kim H Parker, and Ashraf W Khir. “Using wave intensity analysis to determine local reflection coefficient in flexible tubes”. In: *Journal of Biomechanics* 49.13 (2016), pp. 2709–2717. DOI: `10.1016/j.jbiomech.2016.06.004`.

[134] F Liang et al. “Biomechanical characterization of ventricular–arterial coupling during aging: a multi-scale model study”. In: *Journal of Biomechanics* 42.6 (2009), pp. 692–704. DOI: `10.1016/j.jbiomech.2009.01.010`.

[135] F Liang et al. "Multi-scale modeling of the human cardiovascular system with applications to aortic valvular and arterial stenoses". In: *Medical & Biological Engineering & Computing* 47.7 (2009), pp. 743–755. DOI: `10.1007/s11517-009-0449-9`.

[136] E Lim et al. "A cardiovascular mathematical model of graded head-up tilt". In: *PloS One* 8.10 (2013), e77357. DOI: `10.1371/journal.pone.0077357`.

[137] Ulrich Limper, Peter Gauger, and Luis EJ Beck. "Upright cardiac output measurements in the transition to weightlessness during parabolic flights". In: *Aviation, Space, and Environmental Medicine* 82.4 (2011), pp. 448–454. DOI: `10.3357/ASEM.2883.2011`.

[138] Christina Lindén et al. "Normal-tension glaucoma has normal intracranial pressure: a prospective study of intracranial pressure and intraocular pressure in different body positions". In: *Ophthalmology* 125.3 (2018), pp. 361–368. DOI: `10.1016/j.ophtha.2017.09.022`.

[139] Barry J Linder, Gory L Trick, and Mirchel L Wolf. "Altering body position affects intraocular pressure and visual function." In: *Investigative Ophthalmology & Visual Science* 29.10 (1988), pp. 1492–1497. URL: `https://iovs.arvojournals.org/article.aspx?articleid=2177869`.

[140] Jiexin Liu et al. "Haemodynamic adaptation during sudden gravity transitions". In: *European Journal of Applied Physiology* 112.1 (2012), pp. 79–89. DOI: `10.1007/s00421-011-1956-6`.

[141] G London et al. "Tilt test in essential hypertension. Differential responses in heart rate and vascular resistance". In: *Hypertension* 10.1 (1987), pp. 29–34. DOI: `10.1161/01.HYP.10.1.29`.

[142] J Ludbrook. "Functional aspects of the veins of the leg". In: *American Heart Journal* 64.5 (1962), pp. 706–713. DOI: `10.1016/0002-8703(62)90257-0`.

[143] COL Thomas H Mader et al. "Intraocular pressure and retinal vascular changes during transient exposure to microgravity". In: *American Journal of Ophthalmology* 115.3 (1993), pp. 347–350. DOI: `10.1016/S0002-9394(14)73586-X`.

[144] Thomas H Mader. "Intraocular pressure in microgravity". In: *The Journal of Clinical Pharmacology* 31.10 (1991), pp. 947–950. DOI: `10.1002/j.1552-4604.1991.tb03654.x`.

[145] Thomas H Mader et al. "Optic disc edema, globe flattening, choroidal folds, and hyperopic shifts observed in astronauts after long-duration space flight". In: *Ophthalmology* 118.10 (2011), pp. 2058–2069. DOI: `10.1016/j.ophtha.2011.06.021`.

[146] A Malhotra et al. "Blood pressure changes in the leg on standing". In: *The Journal of Clinical Hypertension* 4.5 (2002), pp. 350–354. DOI: 10.1111/j.1524-6175.2002.00767.x.

[147] Henry B Mann. "Nonparametric tests against trend". In: *Econometrica: Journal of the Econometric Society* (1945), pp. 245–259. DOI: 10.2307/1907187.

[148] Karina Marshall-Bowman, Michael R Barratt, and C Robert Gibson. "Ophthalmic changes and increased intracranial pressure associated with long duration spaceflight: an emerging understanding". In: *Acta Astronautica* 87 (2013), pp. 77–87. DOI: 10.1016/j.actaastro.2013.01.014.

[149] Karina Marshall-Goebel et al. "Assessment of jugular venous blood flow stasis and thrombosis during spaceflight". In: *JAMA Network Open* 2.11 (2019), e1915011–e1915011. DOI: 10.1001/jamanetworkopen.2019.15011.

[150] Karina Marshall-Goebel et al. "Intracranial and intraocular pressure during various degrees of head-down tilt". In: *Aerospace Medicine and Human Performance* 88.1 (2017), pp. 10–16. DOI: 10.3357/AMHP.4653.2017.

[151] Donald A McDonald. *Blood flow in arteries*. Williams & Wilkins, 1974. DOI: 10.1201/b13568.

[152] J Mead and E Gaensler. "Esophageal and pleural pressures in man, upright and supine". In: *Journal of Applied Physiology* 14.1 (1959), pp. 81–83. DOI: 10.1152/jappl.1959.14.1.81.

[153] F Melchior et al. "Simulation of cardiovascular response to lower body negative pressure from 0 to-40 mmHg". In: *Journal of Applied Physiology* 77.2 (1994), pp. 630–640. DOI: 10.1152/jappl.1994.77.2.630.

[154] Parvin Mohammadyari, Giacomo Gadda, and Angelo Taibi. "Modelling physiology of haemodynamic adaptation in short-term microgravity exposure and orthostatic stress on Earth". In: *Scientific Reports* 11.1 (2021), p. 4672. DOI: 10.1038/s41598-021-84197-7.

[155] S Møller et al. "Effects of tilting on central hemodynamics and homeostatic mechanisms in cirrhosis". In: *Hepatology* 40.4 (2004), pp. 811–819. DOI: 10.1002/hep.1840400410.

[156] David Montero and Sven Rauber. "Brain perfusion and arterial blood flow velocity during prolonged body tilting". In: *Aerospace Medicine and Human Performance* 87.8 (2016), pp. 682–687. DOI: 10.3357/AMHP.4546.2016.

[157] William H Morgan et al. "The influence of cerebrospinal fluid pressure on the lamina cribrosa tissue pressure gradient." In: *Investigative Ophthalmology & Visual Science* 36.6 (1995), pp. 1163–1172. URL: https://arvojournals.org/arvo/content%5C_public/journal/iovs/933186/1163.pdf.

[158] Paul D Morris et al. “Computational fluid dynamics modelling in cardiovascular medicine”. In: *Heart* 102.1 (2016), pp. 18–28. DOI: `10.1136/heartjnl-2015-308044`.

[159] Chiaki N Mukai et al. “Acute hemodynamic responses to weightlessness during parabolic flight”. In: *The Journal of Clinical Pharmacology* 31.10 (1991), pp. 993–1000. DOI: `10.1002/j.1552-4604.1991.tb03662.x`.

[160] J Mynard, D Penny, and J Smolich. “Scalability and in vivo validation of a multiscale numerical model of the left coronary circulation”. In: *American Journal of Physiology-Heart and Circulatory Physiology* 306.4 (2014), H517–H528. DOI: `10.1152/ajpheart.00603.2013`.

[161] Jonathan P Mynard and Joseph J Smolich. “Novel wave power analysis linking pressure-flow waves, wave potential, and the forward and backward components of hydraulic power”. In: *American Journal of Physiology-Heart and Circulatory Physiology* 310.8 (2016), H1026–H1038. DOI: `10.1152/ajpheart.00954.2015`.

[162] Jonathan P Mynard and Joseph J Smolich. “One-dimensional haemodynamic modeling and wave dynamics in the entire adult circulation”. In: *Annals of Biomedical Engineering* 43.6 (2015), pp. 1443–1460. DOI: `10.1007/s10439-015-1313-8`.

[163] Jonathan P Mynard et al. “Measurement, analysis and interpretation of pressure/flow waves in blood vessels”. In: *Frontiers in Physiology* (2020). DOI: `10.3389/fphys.2020.01085`.

[164] M Mynard J Davidson, D Penny, and J Smolich. “A simple, versatile valve model for use in lumped parameter and one-dimensional cardiovascular models”. In: *International Journal for Numerical Methods in Biomedical Engineering* 28.6-7 (2012), pp. 626–641. DOI: `https://doi.org/10.1002/cnm.1466`.

[165] Emily S Nelson et al. “Acute effects of posture on intraocular pressure”. In: *PLoS One* 15.2 (2020), e0226915. DOI: `10.1371/journal.pone.0226915`.

[166] Emily S Nelson et al. “The impact of ocular hemodynamics and intracranial pressure on intraocular pressure during acute gravitational changes”. In: *Journal of Applied Physiology* 123.2 (2017), pp. 352–363. DOI: `10.1152/japplphysiol.00102.2017`.

[167] Michael J Neufeld and John B Charles. “Practicing for space underwater: inventing neutral buoyancy training, 1963–1968”. In: *Endeavour* 39.3-4 (2015), pp. 147–159. DOI: `10.1016/j.endeavour.2015.05.006`.

[168] Steven A Niederer, Joost Lumens, and Natalia A Trayanova. “Computational models in cardiology”. In: *Nature Reviews Cardiology* 16.2 (2019), pp. 100–111. DOI: `10.1038/s41569-018-0104-y`.

[169] Peter Norsk. “Adaptation of the cardiovascular system to weightlessness: surprises, paradoxes and implications for deep space missions”. In: *Acta Physiologica* 228.3 (2020), e13434. DOI: 10.1111/apha.13434.

[170] Peter Norsk et al. “Fluid shifts, vasodilatation and ambulatory blood pressure reduction during long duration spaceflight”. In: *The Journal of Physiology* 593.3 (2015), pp. 573–584. DOI: 10.1113/jphysiol.2014.284869.

[171] Peter Norsk et al. “Vasorelaxation in space”. In: *Hypertension* 47.1 (2006), pp. 69–73. DOI: 10.1161/01.HYP.0000194332.98674.57.

[172] Shigehiko Ogoh and Takashi Tarumi. “Cerebral blood flow regulation and cognitive function: a role of arterial baroreflex function”. In: *The Journal of Physiological Sciences* 69.6 (2019), pp. 813–823. DOI: 10.1007/s12576-019-00704-6.

[173] Shigehiko Ogoh et al. “Effect of an acute increase in central blood volume on cerebral hemodynamics”. In: *American Journal of Physiology-Regulatory, Integrative and Comparative Physiology* 309.8 (2015), R902–R911. DOI: 10.1152/ajpregu.00137.2015.

[174] Nobuyuki Ohte et al. “Clinical usefulness of carotid arterial wave intensity in assessing left ventricular systolic and early diastolic performance”. In: *Heart and Vessels* 18.3 (2003), pp. 107–111. DOI: 10.1007/s00380-003-0700-5.

[175] Joshua Ong, Andrew G Lee, and Heather E Moss. “Head-down tilt bed rest studies as a terrestrial analog for spaceflight associated neuro-ocular syndrome”. In: *Frontiers in Neurology* 12 (2021), p. 648958. DOI: 10.3389/fneur.2021.648958.

[176] C Onizuka et al. “Arterial blood pressure response to head-up tilt test and orthostatic tolerance in nurses”. In: *Environmental Health and Preventive Medicine* 20.4 (2015), pp. 262–270. DOI: 10.1007/s12199-015-0455-5.

[177] J Ottesen, M Olufsen, and J Larsen. *Applied mathematical models in human physiology*. SIAM, Philadelphia, 2004. DOI: 10.1137/1.9780898718287.

[178] Christian Otto. “The Visual Impairment Intracranial Pressure (VIIP) Risk in Spaceflight”. In: *Handbook of Bioastronautics*. Springer, 2021. Chap. 51, pp. 641–673. DOI: 10.1007/978-3-319-12191-8_93.

[179] Douglas L Packer et al. “Effect of catheter ablation vs antiarrhythmic drug therapy on mortality, stroke, bleeding, and cardiac arrest among patients with atrial fibrillation: the CABANA randomized clinical trial”. In: *Jama* 321.13 (2019), pp. 1261–1274. DOI: 10.1001/jama.2019.0693.

[180] Meenakshi Pandiarajan and Alan R Hargens. “Ground-based analogs for human spaceflight”. In: *Frontiers in Physiology* (2020), p. 716. DOI: 10.3389/fphys.2020.00716.

[181] Kim H Parker. "An introduction to wave intensity analysis". In: *Medical & Biological Engineering & Computing* 47.2 (2009), pp. 175–188. DOI: 10.1007/s11517-009-0439-y.

[182] Kim H Parker and CJH Jones. "Forward and backward running waves in the arteries: analysis using the method of characteristics". In: *J. Biomech Eng.* 112.3 (1990). DOI: 10.1115/1.2891191.

[183] Kim H Parker et al. "What stops the flow of blood from the heart?" In: *Heart and Vessels* 4.4 (1988), pp. 241–245. DOI: 10.1007/BF02058593.

[184] B Partsch and H Partsch. "Calf compression pressure required to achieve venous closure from supine to standing positions". In: *Journal of vascular surgery* 42.4 (2005), pp. 734–738. DOI: 10.1016/j.jvs.2005.06.030.

[185] Abdul Shokor Parwani et al. "Atrial fibrillation-induced cardiac troponin I release". In: *International Journal of Cardiology* 168.3 (2013), pp. 2734–2737. DOI: 10.1016/j.ijcard.2013.03.087.

[186] Iacopo Pasticci et al. "Determinants of the esophageal-pleural pressure relationship in humans". In: *Journal of Applied Physiology* 128.1 (2020), pp. 78–86. DOI: 10.1152/japplphysiol.00587.2019.

[187] O Paulson, S Strandgaard, and L Edvinsson. "Cerebral autoregulation". In: *Cerebrovascular and Brain Metabolism Reviews* 2.2 (1990), pp. 161–192. URL: http://europepmc.org/abstract/MED/2201348.

[188] Anne Pavy-Le Traon et al. "From space to Earth: advances in human physiology from 20 years of bed rest studies (1986–2006)". In: *European Journal of Applied Physiology* 101 (2007), pp. 143–194. DOI: 10.1007/s00421-007-0474-z.

[189] Lonnie G Petersen et al. "Gravitational effects on intraocular pressure and ocular perfusion pressure". In: *Journal of Applied Physiology* 132.1 (2022), pp. 24–35. DOI: 10.1152/japplphysiol.00546.2021.

[190] Lonnie G Petersen et al. "Mechanisms of increase in cardiac output during acute weightlessness in humans". In: *Journal of Applied Physiology* 111.2 (2011), pp. 407–411. DOI: 10.1152/japplphysiol.01188.2010.

[191] Lonnie Grove Petersen et al. "Postural influence on intracranial and cerebral perfusion pressure in ambulatory neurosurgical patients". In: *American Journal of Physiology-Regulatory, Integrative and Comparative Physiology* 310.1 (2016), R100–R104. DOI: 10.1152/ajpregu.00302.2015.

[192] Kristy Peterson et al. "Numerical simulation of the influence of gravity and posture on cardiac performance". In: *Annals of Biomedical Engineering* 30.2 (2002), pp. 247–259. DOI: 10.1114/1.1451075.

[193] Emy Philibert et al. "Impact Of Postural Position On Determination Of Aortic Stiffness And Central Blood Pressure". In: *Journal of Hypertension* 40 (2022), e129. DOI: 10.1097/01.hjh.0000836584.99789.80.

[194] Steven H Platts et al. "Cardiovascular adaptations to long-duration head-down bed rest". In: *Aviation, Space, and Environmental Medicine* 80.5 (2009), A29–A36. DOI: 10.3357/ASEM.BR03.2009.

[195] Albert A Pollack and Earl H Wood. "Venous pressure in the saphenous vein at the ankle in man during exercise and changes in posture". In: *Journal of applied Physiology* 1.9 (1949), pp. 649–662. DOI: 10.1152/jappl.1949.1.9.649.

[196] A Posch et al. "Sympathetic neural and hemodynamic responses to head-up tilt during isoosmotic and hyperosmotic hypovolemia". In: *Journal of Neurophysiology* 118.4 (2017), pp. 2232–2237. DOI: 10.1152/jn.00403.2017.

[197] Rajesh Pradhan, Ashok Chaudhary, and Anthony A Donato. "Predictive accuracy of ST depression during rapid atrial fibrillation on the presence of obstructive coronary artery disease". In: *The American journal of emergency medicine* 30.7 (2012), pp. 1042–1047. DOI: 10.1016/j.ajem.2011.06.027.

[198] Tiago Santos Prata et al. "Posture-induced intraocular pressure changes: considerations regarding body position in glaucoma patients". In: *Survey of Ophthalmology* 55.5 (2010), pp. 445–453. DOI: 10.1016/j.survophthal.2009.12.002.

[199] L Pstras et al. "The Valsalva manoeuvre: physiology and clinical examples". In: *Acta Physiologica* 217.2 (2016), pp. 103–119. DOI: 10.1111/apha.12639.

[200] Giacomo Pucci et al. "Age-Specific Acute Changes in Carotid–Femoral Pulse Wave Velocity With Head-up Tilt". In: *American Journal of Hypertension* 33.12 (2020), pp. 1112–1118. DOI: 10.1093/ajh/hpaa101.

[201] Bettina Pump et al. "Arterial pressure in humans during weightlessness induced by parabolic flights". In: *Journal of Applied Physiology* 87.3 (1999), pp. 928–932. DOI: 10.1152/jappl.1999.87.3.928.

[202] Luigi Quartapelle. *Numerical solution of the incompressible Navier-Stokes equations*. Vol. 113. Birkhäuser, 2013. DOI: 10.1007/978-3-0348-8579-9.

[203] A Quarteroni, A Manzoni, and C Vergara. "The cardiovascular system: mathematical modelling, numerical algorithms and clinical applications". In: *Acta Numerica* 26 (2017), pp. 365–590. DOI: 10.1017/S0962492917000046.

[204] Alfio Quarteroni and Silvia Quarteroni. *Numerical models for differential problems*. Vol. 2. Springer, 2009. DOI: 10.1007/978-88-470-1071-0.

[205] Alfio Quarteroni, Alessandro Veneziani, and Christian Vergara. "Geometric multiscale modeling of the cardiovascular system, between theory and practice". In: *Computer Methods in Applied Mechanics and Engineering* 302 (2016), pp. 193–252. DOI: `10.1016/j.cma.2016.01.007`.

[206] Sara Qvarlander et al. "Postural effects on intracranial pressure: modeling and clinical evaluation". In: *Journal of Applied Physiology* 115.10 (2013), pp. 1474–1480. DOI: `10.1152/japplphysiol.00711.2013`.

[207] Felix T Range et al. "Impaired myocardial perfusion and perfusion reserve associated with increased coronary resistance in persistent idiopathic atrial fibrillation". In: *European Heart Journal* 28.18 (2007), pp. 2223–2230. DOI: `10.1093/eurheartj/ehm246`.

[208] Xavier Repessé, Antoine Vieillard-Baron, and Guillaume Geri. "Value of measuring esophageal pressure to evaluate heart-lung interactions—applications for invasive hemodynamic monitoring". In: *Annals of Translational Medicine* 6.18 (2018). DOI: `10.21037/atm.2018.05.04`.

[209] P Reymond et al. "Validation of a one-dimensional model of the systemic arterial tree". In: *American Journal of Physiology-Heart and Circulatory Physiology* 297.1 (2009), H208–H222. DOI: `10.1152/ajpheart.00037.2009`.

[210] DR Roberts et al. "Structural brain changes following long-term 6 head-down tilt bed rest as an analog for spaceflight". In: *American Journal of Neuroradiology* 36.11 (2015), pp. 2048–2054. DOI: `10.3174/ajnr.A4406`.

[211] David R Rutkowski et al. "Sex differences in cardiac flow dynamics of healthy volunteers". In: *Radiology: Cardiothoracic Imaging* 2.1 (2020), e190058. DOI: `10.1148/ryct.2020190058`.

[212] Henry W Ryder, William E Molle, Eugene B Ferris, et al. "The influence of the collapsibility of veins on venous pressure, including a new procedure for measuring tissue pressure". In: *The Journal of Clinical Investigation* 23.3 (1944), pp. 333–341. DOI: `10.1172/JCI101499`.

[213] R Saborowski, D Vaitl, and R Stark. "Perception of posture and cerebral blood flow". In: *International Journal of Psychophysiology* 43.2 (2002), pp. 167–175. DOI: `10.1016/S0167-8760(01)00169-6`.

[214] Michel E Safar, Olivier Henry, and Sylvie Meaume. "Aortic pulse wave velocity: an independent marker of cardiovascular risk". In: *The American Journal of Geriatric Cardiology* 11.5 (2002), pp. 295–304. DOI: `10.1111/j.1076-7460.2002.00695.x`.

[215] K Sagawa et al. "End-systolic pressure/volume ratio: a new index of ventricular contractility". In: *The American Journal of Cardiology* 40.5 (1977), pp. 748–753. DOI: `10.1016/0002-9149(77)90192-8`.

[216] Andrea Saglietto et al. “A computational analysis of atrial fibrillation effects on coronary perfusion across the different myocardial layers”. In: *Scientific Reports* 12.841 (2022). DOI: `10.1038/s41598-022-04897-6`.

[217] Andrea Saglietto et al. “Higher ventricular rate during atrial fibrillation relates to increased cerebral hypoperfusions and hypertensive events”. In: *Scientific Reports* 9.1 (2019), p. 3779. DOI: `10.1038/s41598-019-40445-5`.

[218] Andrea Saglietto et al. “Increased beat-to-beat variability of cerebral microcirculatory perfusion during atrial fibrillation: A near-infrared spectroscopy study”. In: *EP Europace* 23.8 (2021), pp. 1219–1226. DOI: `10.1093/europace/euab070`.

[219] Andrea Saglietto et al. “Prognostic implications of atrial fibrillation in patients with stable coronary artery disease: a systematic review and meta-analysis of adjusted observational studies”. In: *Reviews in Cardiovascular Medicine* 22.2 (2021), pp. 439–444. DOI: `10.31083/j.rcm2202049`.

[220] Daiji Saito et al. “Effect of atrial fibrillation on coronary circulation and blood flow distribution across the left ventricular wall in anesihetized open-chest dogs”. In: *Japanese Circulation Journal* 42.4 (1978), pp. 417–423. DOI: `10.1253/jcj.42.417`.

[221] Laurent Sakka, Guillaume Coll, and Jean Chazal. “Anatomy and physiology of cerebrospinal fluid”. In: *European Annals of Otorhinolaryngology, Head and Neck Diseases* 128.6 (2011), pp. 309–316. DOI: `10.1016/j.anorl.2011.03.002`.

[222] Adriana Salatino et al. “Zero gravity induced by parabolic flight enhances automatic capture and weakens voluntary maintenance of visuospatial attention”. In: *npj Microgravity* 7.1 (2021), p. 29. DOI: `10.1038/s41526-021-00159-3`.

[223] S Scarsoglio et al. “Impact of atrial fibrillation on the cardiovascular system through a lumped-parameter approach”. In: *Medical & Biological Engineering & Computing* 52.11 (2014), pp. 905–920. DOI: `10.1007/s11517-014-1192-4`.

[224] Stefania Scarsoglio, Matteo Fois, and Luca Ridolfi. “Increased hemodynamic pulsatility in the cerebral microcirculation during parabolic flight: a computational investigation”. In: *Acta Astronautica* 211 (2023), pp. 344–352. DOI: `10.1016/j.actaastro.2023.06.018`.

[225] Stefania Scarsoglio et al. “Alteration of cerebrovascular haemodynamic patterns due to atrial fibrillation: an in silico investigation”. In: *Journal of The Royal Society Interface* 14.129 (2017), p. 20170180. DOI: `10.1098/rsif.2017.0180`.

[226] Stefania Scarsoglio et al. “Cerebral hemodynamics during atrial fibrillation: Computational fluid dynamics analysis of lenticulostriate arteries using 7 T high-resolution magnetic resonance imaging”. In: *Physics of Fluids* 34.12 (2022), p. 121909. DOI: `10.1063/5.0129899`.

[227] Stefania Scarsoglio et al. “Impaired coronary blood flow at higher heart rates during atrial fibrillation: Investigation via multiscale modelling”. In: *Computer Methods and Programs in Biomedicine* 175 (2019), pp. 95–102. DOI: `10.1016/j.cmpb.2019.04.009`.

[228] Todd T Schlegel et al. “Cardiovascular and Valsalva responses during parabolic flight”. In: *Journal of Applied Physiology* 85.5 (1998), pp. 1957–1965. DOI: `10.1152/jappl.1998.85.5.1957`.

[229] Todd T Schlegel et al. “Orthostatic intolerance and motion sickness after parabolic flight”. In: *Journal of Applied Physiology* 90.1 (2001), pp. 67–82. DOI: `10.1152/jappl.2001.90.1.67`.

[230] Renate B Schnabel et al. “50 year trends in atrial fibrillation prevalence, incidence, risk factors, and mortality in the Framingham Heart Study: a cohort study”. In: *The Lancet* 386.9989 (2015), pp. 154–162. DOI: `10.1016/S0140-6736(14)61774-8`.

[231] Patrick Segers, Ernst R Rietzschel, and Julio A Chirinos. “How to measure arterial stiffness in humans”. In: *Arteriosclerosis, Thrombosis, and Vascular Biology* 40.5 (2020), pp. 1034–1043. DOI: `10.1007/s10439-012-0688-z`.

[232] Patrick Segers and Pascal Verdonck. “Role of tapering in aortic wave reflection: hydraulic and mathematical model study”. In: *Journal of Biomechanics* 33.3 (2000), pp. 299–306. DOI: `10.1016/S0021-9290(99)00180-3`.

[233] Patrick Segers et al. “Three-and four-element Windkessel models: assessment of their fitting performance in a large cohort of healthy middle-aged individuals”. In: *Proceedings of the Institution of Mechanical Engineers, Part H: Journal of Engineering in Medicine* 222.4 (2008), pp. 417–428. DOI: `10.1243/09544119JEIM287`.

[234] Felix S Seibert et al. “The effect of microgravity on central aortic blood pressure”. In: *American Journal of Hypertension* 31.11 (2018), pp. 1183–1189. DOI: `10.1093/ajh/hpy119`.

[235] H Senzaki, C Chen, and D Kass. “Single-beat estimation of end-systolic pressure-volume relation in humans: a new method with the potential for noninvasive application”. In: *Circulation* 94.10 (1996), pp. 2497–2506. DOI: `10.1161/01.CIR.94.10.2497`.

[236] Ascher H Shapiro. “Steady flow in collapsible tubes”. In: *Journal of Biomechanical Engineering* 99.3 (1977), pp. 126–147. DOI: `10.1115/1.3426281`.

[237] Mark Shelhamer. “Parabolic flight as a spaceflight analog”. In: *Journal of Applied Physiology* 120.12 (2016), pp. 1442–1448. DOI: `10.1152/japplphysiol.01046.2015`.

[238] Makoto Shiraishi et al. “Comparison of acute cardiovascular responses to water immersion and head-down tilt in humans”. In: *Journal of Applied Physiology* 92.1 (2002), pp. 264–268. DOI: `10.1152/jappl.2002.92.1.264`.

[239] A Silvani et al. “Physiological mechanisms mediating the coupling between heart period and arterial pressure in response to postural changes in humans”. In: *Frontiers in Physiology* 8 (2017), p. 163. DOI: `10.3389/fphys.2017.00163`.

[240] Arthur J Sit et al. “Circadian variation of aqueous dynamics in young healthy adults”. In: *Investigative Ophthalmology & Visual Science* 49.4 (2008), pp. 1473–1479. DOI: `10.1167/iovs.07-1139`.

[241] J Smith, C Porth, and M Erickson. “Hemodynamic response to the upright posture”. In: *The Journal of Clinical Pharmacology* 34.5 (1994), pp. 375–386.

[242] R Sprangers et al. “Initial blood pressure fall on stand up and exercise explained by changes in total peripheral resistance”. In: *Journal of Applied Physiology* 70.2 (1991), pp. 523–530. DOI: `10.1152/jappl.1991.70.2.523`.

[243] RLH Sprangers et al. “Initial circulatory responses to changes in posture: influence of the angle and speed of tilt”. In: *Clinical Physiology* 11.3 (1991), pp. 211–220. DOI: `10.1111/j.1475-097X.1991.tb00452.x`.

[244] Sarah R St Pierre, Mathias Peirlinck, and Ellen Kuhl. “Sex matters: a comprehensive comparison of female and male hearts”. In: *Frontiers in Physiology* 13 (2022), p. 831179. DOI: `10.3389/fphys.2022.831179`.

[245] Claudia Stern et al. “Eye-brain axis in microgravity and its implications for Spaceflight Associated Neuro-ocular Syndrome”. In: *npj Microgravity* 9.1 (2023), p. 56. DOI: `10.1038/s41526-023-00300-4`.

[246] J Stewart and L Montgomery. “Regional blood volume and peripheral blood flow in postural tachycardia syndrome”. In: *American Journal of Physiology-Heart and Circulatory Physiology* 287.3 (2004), H1319–H1327. DOI: `10.1152/ajpheart.00086.2004`.

[247] Motoaki Sugawara et al. “Clinical usefulness of wave intensity analysis”. In: *Medical & Biological Engineering & Computing* 47.2 (2009), pp. 197–206. DOI: `10.1007/s11517-008-0388-x`.

[248] P Sundblad, J Spaak, and L Kaijser. “Time courses of central hemodynamics during rapid changes in posture”. In: *Journal of Applied Physiology* 116.9 (2014), pp. 1182–1188. DOI: `10.1152/japplphysiol.00690.2013`.

[249] A Tahvanainen et al. “The type of the functional cardiovascular response to upright posture is associated with arterial stiffness: a cross-sectional study in 470 volunteers”. In: *BMC Cardiovascular Disorders* 16.1 (2016), pp. 1–12. DOI: `10.1186/s12872-016-0281-8`.

[250] Giovanni Taibbi et al. “The effect of microgravity on ocular structures and visual function: a review”. In: *Survey of Ophthalmology* 58.2 (2013), pp. 155–163. DOI: `10.1016/j.survophthal.2012.04.002`.

[251] Alifia Tameem and Hari Krovvidi. “Cerebral physiology”. In: *Continuing Education in Anaesthesia, Critical Care & Pain* 13.4 (2013), pp. 113–118. DOI: `10.1093/bjaceaccp/mkt001`.

[252] H Tanaka, B Sjöberg, and O Thulesius. “Cardiac output and blood pressure during active and passive standing”. In: *Clinical Physiology* 16.2 (1996), pp. 157–170. DOI: `10.1111/j.1475-097X.1996.tb00565.x`.

[253] E Tansey et al. “Understanding basic vein physiology and venous blood pressure through simple physical assessments”. In: *Advances in Physiology Education* 43.3 (2019), pp. 423–429. DOI: `10.1152/advan.00182.2018`.

[254] Charles A Taylor and CA Figueroa. “Patient-specific modeling of cardiovascular mechanics”. In: *Annual Review of Biomedical Engineering* 11 (2009), pp. 109–134. DOI: `10.061807.160521`.

[255] “The muscle-vein pump”. In: *https://www.ofa-bamberg.com/en/knowledge/our-body/blood-circulation/veins/*. (). Accessed: 07.09.2023.

[256] K Toska and L Walløe. “Dynamic time course of hemodynamic responses after passive head-up tilt and tilt back to supine position”. In: *Journal of Applied Physiology* 92.4 (2002), pp. 1671–1676. DOI: `10.1152/japplphysiol.00465.2000`.

[257] J Truijen et al. “Orthostatic leg blood volume changes assessed by near-infrared spectroscopy”. In: *Experimental Physiology* 97.3 (2012), pp. 353–361. DOI: `10.1113/expphysiol.2011.061051`.

[258] M Ursino and C Lodi. “A simple mathematical model of the interaction between intracranial pressure and cerebral hemodynamics”. In: *Journal of Applied Physiology* 82.4 (1997), pp. 1256–1269. DOI: `10.1152/jappl.1997.82.4.1256`.

[259] Mauro Ursino and Massimo Giannessi. “A model of cerebrovascular reactivity including the circle of Willis and cortical anastomoses”. In: *Annals of Biomedical Engineering* 38 (2010), pp. 955–974. DOI: `10.1007/s10439-010-9923-7`.

[260] Dieter Vaitl, Horst Mittelstaedt, and Friedhelm Baisch. "Shifts in blood volume alter the perception of posture". In: *International Journal of Psychophysiology* 27.2 (1997), pp. 99–105. DOI: `10.1016/S0167-8760(97)00053-6`.

[261] Frans N Van de Vosse and Nikos Stergiopulos. "Pulse wave propagation in the arterial tree". In: *Annual Review of Fluid Mechanics* 43.1 (2011), pp. 467–499. DOI: `10.1146/annurev-fluid-122109-160730`.

[262] Ewout J Van Den Bos et al. "Minor elevations in troponin I are associated with mortality and adverse cardiac events in patients with atrial fibrillation". In: *European Heart Journal* 32.5 (2011), pp. 611–617. DOI: `10.1093/eurheartj/ehq491`.

[263] J Van Lieshout et al. "Stroke volume of the heart and thoracic fluid content during head-up and head-down tilt in humans". In: *Acta anaesthesiologica scandinavica* 49.9 (2005), pp. 1287–1292. DOI: `10.1111/j.1399-6576.2005.00841.x`.

[264] Angelique Van Ombergen et al. "Brain ventricular volume changes induced by long-duration spaceflight". In: *Proceedings of the National Academy of Sciences* 116.21 (2019), pp. 10531–10536. DOI: `10.1073/pnas.1820354116`.

[265] Kevin Verhoeff and Jamie R Mitchell. "Cardiopulmonary physiology: why the heart and lungs are inextricably linked". In: *Advances in Physiology Education* 41.3 (2017), pp. 348–353. DOI: `10.1152/advan.00190.2016`.

[266] Regitze Videbaek and Peter Norsk. "Atrial distension in humans during microgravity induced by parabolic flights". In: *Journal of Applied Physiology* 83.6 (1997), pp. 1862–1866. DOI: `10.1152/jappl.1997.83.6.1862`.

[267] P Vijaylakshmi, S Veliath, and M Mohan. "Effect of head-up tilt on cardiovascular responses in normal young volunteers". In: *Indian Journal of Physiology and Pharmacology* 44.4 (2000), pp. 467–472.

[268] D Vrachatis et al. "Effect of supine versus sitting position on noninvasive assessment of aortic pressure waveform: a randomized cross-over study". In: *Journal of Human Hypertension* 28.4 (2014), pp. 236–241. DOI: `10.1038/jhh.2013.101`.

[269] Donald E Watenpaugh. "Analogs of microgravity: head-down tilt and water immersion". In: *Journal of Applied Physiology* 120.8 (2016), pp. 904–914. DOI: `10.1152/japplphysiol.00986.2015`.

[270] M Wayson et al. "Suggested reference values for regional blood volumes in children and adolescents". In: *Physics in Medicine & Biology* 63.15 (2018), p. 155022. DOI: `10.1088/1361-6560/aad313`.

[271] Berend E Westerhof and Nico Westerhof. "Magnitude and return time of the reflected wave: the effects of large artery stiffness and aortic geometry". In: *Journal of Hypertension* 30.5 (2012), pp. 932–939. DOI: 10.1097/HJH.0b013e3283524932.

[272] Berend E Westerhof and Nico Westerhof. "Uniform tube models with single reflection site do not explain aortic wave travel and pressure wave shape". In: *Physiological Measurement* 39.12 (2018), p. 124006. DOI: 10.1088/1361-6579/aaf3dd.

[273] Berend E Westerhof et al. "Quantification of wave reflection in the human aorta from pressure alone: a proof of principle". In: *Hypertension* 48.4 (2006), pp. 595–601. DOI: 10.1161/01.HYP.0000238330.08894.17.

[274] N Westerhof et al. "Forward and backward waves in the arterial system". In: *Cardiovascular Research* 6.6 (1972), pp. 648–656. DOI: 10.1093/cvr/6.6.648.

[275] Nico Westerhof, Jan-Willem Lankhaar, and Berend E Westerhof. "The arterial windkessel". In: *Medical & biological engineering & computing* 47.2 (2009), pp. 131–141. DOI: 10.1007/s11517-008-0359-2.

[276] Nico Westerhof, Patrick Segers, and Berend E Westerhof. "Wave separation, wave intensity, the reservoir-wave concept, and the instantaneous wave-free ratio: presumptions and principles". In: *Hypertension* 66.1 (2015), pp. 93–98. DOI: 10.1161/HYPERTENSIONAHA.115.05567.

[277] Nicolaas Westerhof et al. "Cardiac Oxygen Consumption and Hemodynamics". In: *Snapshots of Hemodynamics*. Springer, 2010, pp. 129–134. DOI: 10.1007/978-1-4419-6363-5.

[278] Nicolaas Westerhof et al. *Snapshots of hemodynamics: an aid for clinical research and graduate education*. Vol. 7. Springer, 2010. DOI: 10.1007/978-3-319-91932-4.

[279] Richard S Whittle and Ana Diaz-Artiles. "Gravitational effects on carotid and jugular characteristics in graded head-up and head-down tilt". In: *Journal of Applied Physiology* 134.2 (2023), pp. 217–229. DOI: 10.1152/japplphysiol.00248.2022.

[280] Richard S Whittle and Ana Diaz-Artiles. "Modeling individual differences in cardiovascular response to gravitational stress using a sensitivity analysis". In: *Journal of Applied Physiology* 130.6 (2021), pp. 1983–2001. DOI: 10.1152/japplphysiol.00727.2020.

[281] Richard S. Whittle et al. "Gravitational Dose-Response Curves for Acute Cardiovascular Hemodynamics and Autonomic Responses in a Tilt Paradigm". In: *Journal of the American Heart Association* 11.14 (2022), e024175. DOI: 10.1161/JAHA.121.024175.

[282] Devy Widjaja et al. “Cardiovascular autonomic adaptation in lunar and martian gravity during parabolic flight”. In: *European Journal of Applied Physiology* 115.6 (2015), pp. 1205–1218. DOI: `10.1007/s00421-015-3118-8`.

[283] Rohan S Wijesurendra and Barbara Casadei. “Atrial fibrillation: effects beyond the atrium?” In: *Cardiovascular research* 105.3 (2015), pp. 238–247. DOI: `10.1093/cvr/cvv001`.

[284] Ian B Wilkinson et al. “The influence of heart rate on augmentation index and central arterial pressure in humans”. In: *The Journal of Physiology* 525.Pt 1 (2000), p. 263. DOI: `10.1111/j.1469-7793.2000.t01-1-00263.x`.

[285] N Williams et al. “Patient-specific modelling of head-up tilt”. In: *Mathematical Medicine and Biology: a Journal of the IMA* 31.4 (2014), pp. 365–392. DOI: `10.1093/imammb/dqt004`.

[286] Tom H Williamson and Alon Harris. “Ocular blood flow measurement.” In: *The British Journal of Ophthalmology* 78.12 (1994), p. 939. DOI: `10.1136/bjo.78.12.939`.

[287] Ke Xu, Mark Butlin, and Alberto Avolio. “Age-Related Effects Of Postural Changes On Aortic Pulse Wave Velocity”. In: *Journal of Hypertension* 29 (2011), e477–e478. DOI: `10.1097/00004872-201106001-01442`.

[288] Alex Yartsev. *The concept of venous return*. Accessed: 16.04.2021. 2016. URL: `https://derangedphysiology.com/main/cicm-primary-exam/required-reading/cardiovascular-system/Chapter%5C%200282/concept-venous-return`.

[289] Alex Yartsev. *Vertical gradient of pleural pressure*. Accessed: 16.04.2021. 2021. URL: `https://derangedphysiology.com/main/cicm-primary-exam/required-reading/respiratory-system/Chapter%5C%200356/vertical-gradient-pleural-pressure`.

[290] J Youde et al. “Reproducibility of circulatory changes to head-up tilt in healthy elderly subjects”. In: *Age and Ageing* 32.4 (2003), pp. 375–381. DOI: `10.1093/ageing/32.4.375`.

[291] Laurence R Young and Jeffrey P Sutton. *Handbook of Bioastronautics*. Springer, 2021. DOI: `10.1007/978-3-319-12191-8`.

[292] A Zaidi et al. “Haemodynamic effects of increasing angle of head up tilt”. In: *Heart* 83.2 (2000), pp. 181–184. DOI: `10.1136/heart.83.2.181`.

[293] Mair Zamir and RS Budwig. “Physics of pulsatile flow”. In: *Appl. Mech. Rev.* 55.2 (2002), B35–B35. DOI: `10.1115/1.1451229`.

[294] Li-Fan Zhang and Alan R Hargens. “Spaceflight-induced intracranial hypertension and visual impairment: pathophysiology and countermeasures”. In: *Physiological Reviews* 98.1 (2018), pp. 59–87. DOI: `10.1152/physrev.00017.2016`.

[295] Rong Zhang et al. “Effects of head-down-tilt bed rest on cerebral hemodynamics during orthostatic stress”. In: *Journal of Applied Physiology* 83.6 (1997), pp. 2139–2145. DOI: `10.1152/jappl.1997.83.6.2139`.

[296] X Zhang et al. “Gravitational effects on global hemodynamics in different postures: A closed-loop multiscale mathematical analysis”. In: *Acta Mechanica Sinica* 33.3 (2017), pp. 595–618. DOI: `10.1007/s10409-016-0621-z`.

[297] Xuan Zhang et al. “Invasive and noninvasive means of measuring intracranial pressure: a review”. In: *Physiological Measurement* 38.8 (2017), R143. DOI: `10.1088/1361-6579/aa7256`.

This Ph.D. thesis has been typeset by means of the TEX-system facilities. The typesetting engine was pdfLATEX. The document class was `toptesi`, by Claudio Beccari, with option `tipotesi=scudo`. This class is available in every up-to-date and complete TEX-system installation.